EPFL

Uncovering interactions between Descending Neurons as a functional principle of behavioural control

Jonas Friedrich BRAUN

■ École
polytechnique
fédérale
de Lausanne

2024

"If you work on something a little bit every day, you end up with something that is massive."
— *Sisyphos* [I]

"I have no special talent. I am only passionately curious."
— *The head of the NSA* [II]

"Research is what I'm doing when I don't know what I'm doing."
— *Boris Johnson* [III]

[I] In the interest of scholarly correctness, I herewith correct the above humorously misattributed quote: Correctly, this quote is to be attributed to Kenneth Goldsmith.

[II] In the interest of scholarly correctness, I herewith correct the above humorously misattributed quote: Correctly, this quote is to be attributed to Albert Einstein.

[III] In the interest of scholarly correctness, I herewith correct the above humorously misattributed quote: Correctly, this quote is to be attributed to Wernher von Braun.

Acknowledgements

First and foremost, I want to express my gratitude to **Prof. Pavan Ramdya** for the opportunity to join his laboratory and for his trust in my abilities. Thank you for striking the balance between giving me the freedom to explore and guiding my path with constructive feedback. Thank you for mentoring and supporting me not only in my academic endeavours but also in my personal aspirations.

I am thankful to my academic mentors throughout my Master's degree, **Prof. Jakob Macke**, **Prof. Chethan Pandarinath**, and **Prof. Simon Jacob**, who supported my development as a scientist and provided valuable advice to choose a PhD position. I would like to thank my Jury members **Prof. Brian McCabe**, **Prof. Carl Petersen**, **Dr. Jan Ache**, and **Dr. Salil Bidaye** for taking their time to evaluate my work and provide feedback. I would like to thank the **Boehringer Ingelheim Fonds** for their support of my PhD. Beyond the financial support I am particularly grateful for the precious opportunity to be part of the BIF network and meet many inspiring people.

I cannot thank my colleagues in the Neuroengineering laboratory enough for the inspiring, collaborative, and supporting environment they have created over the years[IV]: Thank you, **Femke**, for our exciting collaboration, pushing my project to new spheres, and cheering me up when I feel low. Thank you, **Sibo**, for helping out with computational challenges of my project, for bringing the best random facts to our discussions, and being a point of trust. Thank you, **Laura**, for our motivating collaboration and supporting me when I was doubting. Thank you, **Gizem**, for making the lab a lively place when you joined after the pandemic. Thank you, **Jasper**, for being very generous with your time when it comes to helping me and others. Thank you, **Victor**, for always being available and knowledgeable to help in every possible way. Thank you, **Israel**, for being my lab companion throughout the pandemic. Thank you, **Matthias**, for asking the big-picture questions. Thank you, **Florian**, for laying the foundation for many analysis tools in the lab. Thank you, **Alfie**, for bringing motivation and fresh perspectives to the lab. Thank you, **Daniel** and **Chin-Lin**, for helping me to get started with experiments. Thank you, **Stefanie**, for being a reliable constant and a source of order in the lab. Thank you, **Kate**, for making every organisational matter seem smooth. You all have made my PhD worthwhile and even helped me catch the thief of my bike (and documented the latter on Instagram). Thank you also to the motivated students I had the pleasure of supervising. I learned even more from you than I hope I was

---

[IV]The list of lab members is in no particular order.

able to teach you.

Abstract

Animals, including humans, exhibit a remarkable variety of complex behaviours. How the nervous system controls all these behaviours ranging from simple, stereotyped movements to flexible, adaptive actions is a central questions of neuroscience. One of the key steps is the transformation from intentions into actions: Movement instructions must pass from the brain to downstream motor circuits through Descending Neurons (DNs). These include small sets of command-like neurons that are sufficient to drive behaviours and specific populations of DNs that are active during different behaviours. Currently it is unclear whether and how different DNs interact with each other to control behaviours.

In this thesis, I present two important, synergistic advances for our understanding of the descending control of behaviour. First, we developed a micro-engineered toolkit to enable long-term recording of the *Drosophila* ventral nerve cord and cervical connective for up to a month. We demonstrate its utility by visualising sensory neuron degradation after leg injury and by studying the effect of different foods on Ascending and Descending Neuron dynamics. This toolkit will facilitate future studies of DNs across different internal states and throughout motor adaptation.

Second, we studied whether and how DNs interact with each other to control behaviours using a combination of optogenetics, functional population recordings, and connectome analysis. We show that command-like DNs in *Drosophila* directly recruit networks of additional DNs to orchestrate flexible behaviours. Specifically, we found that optogenetic activation of command-like DNs, previously thought to drive behaviours alone, in fact co-activate larger populations of DNs. Connectome analysis revealed that this functional recruitment can be explained by direct excitatory connections between command-like DNs and networks of interconnected DNs in the brain. The size of downstream DN networks is predictive of whether descending population recruitment is necessary to generate a complete behaviour: DNs with many downstream descending partners require network recruitment to drive flexible behaviours, while neurons with fewer partners can alone drive stereotyped behaviours and simple movements. These results support a mechanism for command-like descending control whereby a continuum of stereotyped to flexible behaviours are generated through the recruitment of increasingly large DN networks which likely construct a complete behaviour by combining multiple motor subroutines.

Key words: Descending Neurons, motor control, two-photon fluorescence imaging, optogenetics, connectome analysis, long-term imaging

Zusammenfassung

Tiere, einschließlich Menschen, zeigen eine bemerkenswerte Vielfalt komplexer Bewegungen. Wie das Nervensystem all diese Bewegungen kontrolliert ist eine zentrale Frage der Neurowissenschaften. Um Intentionen in Aktionen zu übersetzen, müssen Bewegungsanweisungen vom Gehirn durch Deszendierende Neuronen (DNs) zu nachgelagerten Schaltkreisen zur Bewegungskontrolle gelangen. Dazu gehören kleine Gruppen von befehlsähnlichen Neuronen, die suffizient sind, um Bewegungen zu aktivieren, sowie spezifische Populationen von DNs, die während unterschiedlicher Bewegungen aktiv sind. Gegenwärtig ist unklar, ob und wie verschiedene DNs miteinander interagieren um Bewegungen zu kontrollieren.

In dieser Doktorarbeit präsentiere ich zwei wichtige, synergetische Fortschritte die zum Verständnis der Bewegungskontrolle durch DNs beitragen. Zuerst haben wir eine mikroingenieurtechnische Toolbox entwickelt, die es ermöglicht, neuronale Aktivität im Strickleiternervensystem und Schlundkonnektiv der *Drosophila* über einen Zeitraum von bis zu einem Monat aufzunehmen. Wir haben den Nutzen dieser Toolbox demonstriert, indem wir die Degeneration von sensorischen Neuronen nach einer Beinverletzung visualisieren und den Einfluss unterschiedlicher Nahrungsmittel auf die Dynamik von Aszendierenden und Deszendierenden Neuronen studieren. Diese Toolbox kann in Zukunft eingesetzt werden um die Rolle von DNs in internen Zuständen und während der Bewegungsanpassung zu erforschen.

Zweitens haben wir untersucht, ob und wie DNs miteinander interagieren, um Bewegungen zu kontrollieren. Dabei haben wir eine Kombination aus Optogenetik, funktionellen Populationsmessungen und Konnektomanalyse verwendet. Wir haben gezeigt, dass befehlsähnliche DNs in *Drosophila* Netzwerke zusätzlicher DNs rekrutieren. Die Konnektomanalyse ergab, dass diese funktionale Rekrutierung durch direkte exzitatorische Verbindungen zwischen befehlsähnlichen DNs und DN-Netzwerken im Gehirn erklärt werden kann. Die Größe der rekrutierten DN-Netzwerke sagt voraus, ob die Rekrutierung von DN-Populationen erforderlich ist, um ein vollständige Bewegung zu erzeugen: DNs mit vielen DN Partnern erfordern die Rekrutierung von Netzwerken um flexible Bewegungen zu steuern während Neuronen mit weniger Partnern alleine stereotypische, einfache Bewegungen auslösen können. Diese Ergebnisse unterstützen einen Mechanismus für die befehlsähnliche deszendierende Kontrolle, bei dem ein Kontinuum von stereotypen bis zu flexiblen Bewegungen durch die Rekrutierung zunehmend großer DN-Netzwerke erzeugt wird, die wahrscheinlich eine vollständiges Bewegung durch die Kombination mehrerer motorischer Teilroutinen konstruieren.

Stichwörter: Deszendierende Neuronen, Bewegungskontrolle, Zwei-Photonen Fluoreszenzmikroskopie, Optogenetik, Konnektomanalyse, Langzeitbildgebung

Résumé

Les animaux, y compris les humains, présentent une variété remarquable de comportements complexes. La manière dont le système nerveux contrôle tous ces comportements est une question centrale en neurosciences. Pour transformer les intentions en actions, les instructions de mouvement doivent passer du cerveau aux circuits moteurs en aval par des neurones descendants (DN). Ceux-ci comprennent certains neurones de type dits 'commandants', dont l'activité suffit à déclencher des comportements spécifiques ; ainsi que des sous-ensembles de DNs qui sont actifs pendant un mouvement donné. À présent, on ne sait pas très bien si et comment ces différents DN interagissent pour contrôler les comportements.

Dans cette thèse, je présente deux avancées importantes et synergiques pour notre compréhension du contrôle descendant du comportement. Premièrement, nous avons développé un ensemble d'outils de micro-ingénierie pour permettre l'enregistrement à long terme de la corde nerveuse ventrale et du connecteur cervical de la *drosophile* pendant une durée allant jusqu'à un mois. Nous démontrons son utilité en visualisant la dégradation des neurones sensoriels après une lésion de la jambe et en étudiant l'effet de différents aliments sur la dynamique des neurones ascendants et descendants. Cet ensemble d'outils facilitera les futures études des DN dans différents états internes et tout au long de l'adaptation motrice. Deuxièmement, nous avons étudié si et comment les DNs interagissent pour diriger les comportements en utilisant une combinaison d'optogénétique, d'enregistrements fonctionnels de populations de neurones et d'analyse du connectome. Nous avons montré que les DNs de type commandant chez la *drosophile* recrutent directement des réseaux de DNs supplémentaires. L'analyse du connectome a révélé que ce recrutement fonctionnel peut s'expliquer par des connexions excitatrices directes entre les DN de type commandant et les réseaux de DN interconnectés dans le cerveau. La taille des réseaux de DN connectés permet de prévoir si le recrutement d'une population descendante est nécessaire pour générer un comportement complet : Les DN ayant de nombreux partenaires descendants nécessitent un recrutement en réseau pour générer des comportements flexibles, tandis que les neurones ayant moins de partenaires peuvent à eux seuls générer des comportements stéréotypés et des mouvements simples. Ces résultats plaident en faveur d'un mécanisme de contrôle descendant par lequel un continuum de comportements stéréotypés à flexibles est généré par le recrutement de réseaux de DN de plus en plus grands qui construisent probablement un comportement complet en combinant de multiples sous-programmes moteurs.

Mots clefs : neurones descendants, contrôle moteur, imagerie de fluorescence à deux photons, optogénétique, analyse du connectome, imagerie à long terme

Contents

List of figures

List of tables

List of videos

1 Introduction

1.1 A hierarchical point of view on motor control

Actively moving our body is central to many aspects of life: We express ourselves through articulation of muscles in our vocal tract and face, we interact with the world by touching and moving objects with our hands, and we locomote by rhythmically swinging our legs. Different animals have evolved unique body morphologies to solve these tasks but what they have in common is that the brain must send neuronal signals to the body to control and coordinate many muscles at once. This grand task of motor control can be decomposed into a hierarchy of different control problems, ranging from low-level control of individual muscle fibres to high-level control of changing between different actions. Nikolai Bernstein's levels of construction of movement were one of the first such hierarchical decompositions [1][I] and inspire researchers until today [2–5]. He posited that motor control was divided into four levels, each having evolved on top of the previous level and acting upon the next lower level. The lowest and oldest level of control — the 'tonus' — describes the interface between the nervous system and the muscles, responsible for maintenance of posture. The second one — the level of 'synergies' — acts upon the first one and describes the coordination between different muscles. Both the third level — 'space' — referring to goal-directed interactions with the environment and the fourth and highest one — 'action' — responsible for coordinating and adapting sequences of movements, can act upon and influence the second level.

Since Bernstein's proposition, anatomical structures relating to individual levels of his hierarchy have been studied in detail: Individual motor neurons and muscles fibres are connected through synapses in the neuromuscular junction [6] and form motor units [7], which may control the lowest hierarchical level of the 'tonus'. Local circuits in the vertebrate spinal cord, or invertebrate ventral nerve cord (VNC) may control the level of 'synergies'. While early studies made the case for synergistic activation of motor units [8], the existence of such motor synergies is now more debated [9]; More recent work suggests that motor units are flexibly controlled instead of in fixed synergies [10]. Nevertheless, muscle activation

---

[I]originally published in Russian in 1947, then translated to English in 1996

is coordinated across different muscles both within and across limbs, potentially owing to central pattern generators in the spinal cord/VNC [11]. The activation of muscles can also be described as a dynamical system [12]. Reaching movements are often studied as an example of goal-directed interactions with the environment and may be related to Bernstein's level of 'space'. Here, motor and premotor cortex are implicated in the movement control [13] and, again, dynamical systems are used to describe the cortical control of movements [14, 15]. Finally, the highest level of 'actions' is more complex to delineate and is thought to be implemented in a more distributed fashion in the brain. Thalamocortical loops have been implicated in motor sequencing [16] and sequence representations have been found in premotor and parietal cortices [17]. In *Drosophila*, a range of brain mechanism for motor sequencing have been discovered [18–20] and in *C. elegans*, motor sequences have been found to be embedded in global brain dynamics [21].

Hierarchical control was also described as an architecture to flexibly control robotic systems [22]. Recently, Merel et al. further elaborated on the idea of hierarchical motor control as a principle shared by animals and robots with a particular focus on the signals sent between different hierarchical levels [23].

1.2   Descending neurons as an anatomical bottleneck in motor control

While understanding individual levels of the hierarchy of motor control is important, it is equally critical to understand the signals in between the different levels. These are composed of both feed-forward signals — ones that are sent from a higher to a lower level — and feed-back signals — sent from a lower to a higher level. The interface connecting the 'action' and 'space' layers with the 'synergies' layer is particularly tractable to study because abstract brain signals about intentions have to be transformed into instructions understandable by lower level motor circuits. Because of the anatomical separation of brain and spinal cord/VNC, these feed-forward signals have to be sent through a limited set of neurons, the Descending Neurons (DNs). DNs have their cell body in the brain and send an axon to the spinal cord/VNC. On the contrary, Ascending Neurons (ANs) have their cell bodies in the spinal cord/VNC and project to the brain to convey feed-back signals. In the following, I will primarily focus on DNs, but will further discuss implications of ANs on DN signalling in Section 5.3.2.

1.2.1   DNs in cortex and cerebral ganglia

In mammals, cortex and brainstem connect to the spinal cord through DNs in the pyramidal and extrapyramidal tracts, respectively **(Figure 1.1a)**. There are >1 million neurons in the human pyramidal tract (also including the corticobulbar tract that projects to the brainstem but not the spinal cord) [25] and ~70,000 DNs in the mouse corticospinal tract (CST) [26]. The CST is composed of the axons of layer V cortical neurons — also referred to as
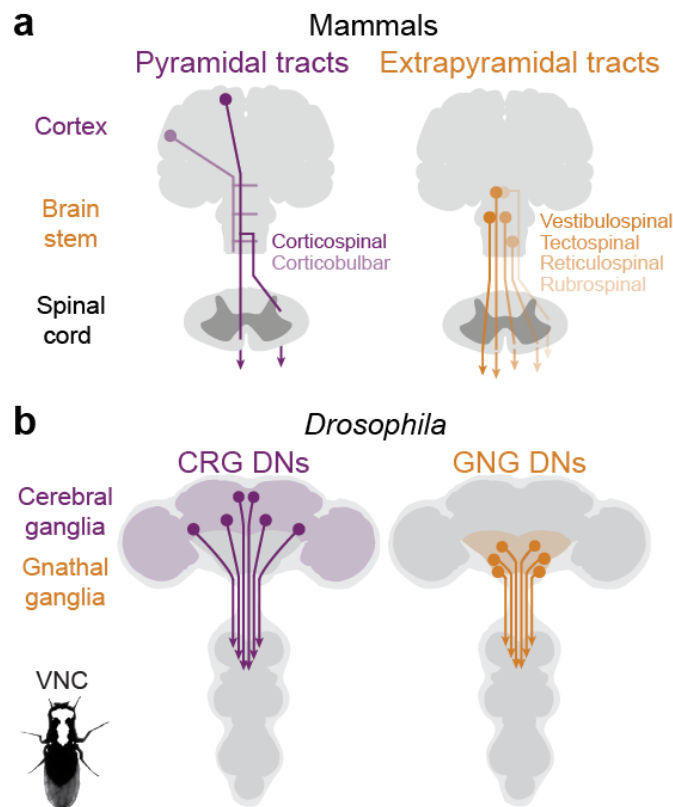
Figure 1.1: Descending Neurons in Mammals and Drosophila. (a) Pyramidal and extrapyramidal tracts, respectively, connect mammalian cortex and brainstem to the spinal cord (graphic modified from [24]). **(b)** Cerebral ganglia DNs and gnathal ganglia DNs connect the *Drosophila* brain to the ventral nerve cord (VNC).

upper motor neurons — and is involved in voluntary control, in particular skilled and precise movements of the limbs [27]. Consistently across different mammalian species, the cortical origin determines the projection pattern of CST neurons along the dorso-ventral axis of the spinal cord [28]: In mice ventrally projecting motor cortex DNs and dorsally projecting sensory cortex DNs are involved in different aspects of skilled reaching movements [29]. While in primates and postnatal rodents, some CST neurons synapse directly onto motor neurons in the spinal cord, most commonly, CST neurons project onto spinal interneurons [30]. CST neurons are also one of the prime targets of neurodegeneration observed in amyotrophic lateral sclerosis (ALS) [31].

In insects, DNs originating in the cerebral ganglia (CRG) are the closest equivalent to CST neurons **(Figure 1.1b)**. CRG DNs receive synaptic inputs from many different brain areas, but not the mushroom body and central complex [32], which are thought to be involved in learning [33] and spatial navigation [34], respectively. This may be analogous to mammalian higher order brain regions such as prefrontal cortex not having any direct projections to the spinal cord. Similarly to mammals, most DNs target VNC interneurons — only 8 % of all post-synaptic partners in the VNC are motor neurons [35].

1.2.2   DNs in brainstem and gnathal ganglia

In mice, only about a quarter of all DNs are of cortical origin — the majority of all DNs have their cell body in the brainstem. Most of them are located in the tegmental, reticular, and red nuclei [36]. The brainstem DNs are mostly thought to "exert control over the initiation, speed, termination, and direction of locomotor bouts" [37]. However, populations of brainstem neurons in the lateral rostral medulla, that project onto the reticular formation (where many brainstem DNs are located) have also been implicated in skilled forelimb movements [38, 39]. Arber and Costa propose a model where the brainstem functions to combine, enhance, or veto behavioural intentions received from basal ganglia or cortical inputs before those signals are sent to the spinal cord [40].

In *Drosophila*, the majority of DNs have their cell body in the gnathal ganglia (GNG), the most caudal region of the fly brain **(Figure 1.1b)**. Akin to the brainstem, the GNG is a multi-sensory processing region. It receives gustatory, mechanosensory, and auditory afferents from the proboscis, the maxillary palps, the head capsule, and the Johnston's organ [41–44]. Interestingly, 85 % of all DNs, irrespective of whether they have their cell body in the cerebral ganglia or GNG, have synaptic outputs in the GNG [32], making the GNG a prime candidate to study interactions between DNs. This is analogous to projections from the cerebral cortex to the brainstem through the corticobulbar tract and axon collaterals of corticospinal DNs projecting to the brainstem [28, 45, 46]. Additionally, the GNG receives a majority of the ascending input conveying sensory and behavioural state information from the VNC [47, 48]. Similarly to the brainstem being the root of ten out of twelve cranial nerves [49], the GNG controls head and proboscis movements, in particular through the ten pairs of neck motor neurons [50] and 18 pairs of proboscis motor neurons [51]. The GNG DNs are the predominant input to the leg (in particular, front leg) neuropils, whereas cerebral DNs are the predominant input to the more dorsal VNC neuropils (tectulum, neck, wing, haltere) [32]. This front-leg dominance is analogous to direct projections of DNs in the brainstem nucleus medullary reticular formation ventral part onto forelimb-innervating motor neurons in the spinal cord [38]. All of these inputs and outputs predestine the GNG to be involved in sensorimotor transformation [52, 53] and action selection, particularly in decisions related to feeding [54].

The anatomical distance of the GNG to other parts of the nervous system varies across insects. In *Drosophila* adults, the GNG is fused to the cerebral ganglia around the esophagus, but physically separated from the VNC by the cervical connective (see **Figure 1.1b**). However in *Drosophila* larvae, the caudal part of the GNG is directly attached to the first thoracic neuromere [55]. In hemimetabolous insects, such as locusts and cockroaches, the GNG is a ganglion separated from the cerebral ganglia by the esophagus and only connected by the circumesophageal connectives [56, 57]. This physical separation provides the experimental advantage of being able to ablate the cerebral ganglia and GNG separately: Cockroaches with ablated cerebral ganglia, but intact GNG have postures similar to intact animals and walk spontaneously with intact inter-leg coordination, whereas animals missing only the GNG or both ganglia do not walk shortly after the lesion and have a hyper-extended

posture [58, 59]. Based on these results, it has been suggested that the GNG and its DNs are involved in leg coordination [57]. This is analogous to the involvement of the brainstem in locomotion [37] and decerebrate cats being able to locomote upon stimulation of the mesencephalic locomotor region of the brainstem [60]. Additionally, the GNG also houses circuits responsible for grooming with the front legs [61], analogous to brainstem involvement in skilled forelimb movements [38]. Irrespective of the species and the nature of their physical attachment, the brainstem and the GNG integrate information from many sources and are the last opportunity to modulate descending signals before they reach low-level motor circuits in the spinal cord or VNC. While circuits within the brainstem have been studied intensively in the past years, how individual DNs within the brainstem function to give rise to different behaviours remains largely unknown. In *Drosophila* it is currently unknown whether CRG or GNG DNs have specific functions that the respective other population of DNs cannot fulfil.

1.3 Activation of DNs triggers movements

A popular way to study the function of neurons is to selectively activate them and observe the effect of their activation on animal behaviour [62]. This approach is powerful because manipulations of neuron function may lead to a causal understanding of their role in behavioural control. Based on experiments where stimulation of neurons elicited specific behaviours, many neurons, in particular DNs have been designated as 'command neurons'.

1.3.1 Concept of a command neuron

The term 'command neuron' was first coined in 1964 [63], but in 1978, Kupfermann and Weiss introduced a more rigorous definition [64]: They defined a command neuron as being "both necessary and sufficient for the initiation of a given behaviour". Verifying this requires three experimental results: (1) the neuron being active during a stereotypical behavioural response to a sensory stimulus, (2) the absence of said behavioural response upon deletion of the neuron, and (3) the triggering of said behavioural pattern upon artificial but "normal" activation of the neuron. This formal definition is often too strict for any neuron to fulfil it. Thus, in practice, the term 'command-like neuron' has proven useful to describe cells that are sufficient to activate a certain behaviour, but not strictly necessary [65]. In the following, I will continue to use the term 'command-like neurons'.

1.3.2 Command-like DNs across different species

Command-like neurons provide a simple, low-dimensional communication channel for higher order brain circuits to convey context-independent signals to lower-order motor circuits. Thus, it is not surprising that among the command-like neurons found, many project from the brain to the spinal cord/VNC and thus are classified as DNs. The first command-like DNs were discovered in the late 20th century: A single action potential in the crayfish giant

fibres is sufficient to elicit a tail-flip escape response [63]. Two specific DNs in *C. elegans* — the AVA and AVB neurons — are sufficient to drive backward and forward locomotion, respectively, and their ablation reduces the probability of the behavioural response to touch stimulation [66]. The Mauthner cell is a reticulospinal command neuron that initiates escape sequences in goldfish [67]. Finally in crickets, a command-like DN controls male singing [68].

In mammals, several studies identified DNs that could trigger specific behaviours. Importantly, they are not single neurons, but genetically defined small populations of neurons. Early studies showed that electrical or pharmacological stimulation of different brainstem regions induces locomotor behaviour [69, 70]. However, because of the lack of genetic targeting, stimulation could not be restricted to individual nuclei or even DNs in particular. During the last decade, sub-populations have been delineated based on neurotransmitter identity or connection patterns and were found to initiate [71] or stop locomotion [71, 72]. Interestingly, the locomotion initiation commands are symmetric, i.e., unilateral activation in the brainstem causes straight locomotion [73]. In order to turn, another population of inhibitory DNs, which project to the spinal cord unilaterally, cause mice to turn ipsilaterally upon unilateral activation [74].

With the conception of the split-GAL4 system [75] that allows to genetically target sparse sets of *Drosophila* neurons and the generation of genetic lines targeting over 400 separate DNs [32, 44], a wave of research on DNs in *Drosophila* has begun. Numerous studies used those tools for activation [61, 76–87], silencing [76, 79, 85, 88, 89], and electrophysiological [76–78, 87, 90–94] or optical [52, 79, 80, 87, 92, 95, 96] recordings of individual DNs. Among those DNs, many have a command-like function: The giant fibres are large diameter DNs that elicit rapid escape take-off [90] similar to giant fibre systems in squid [97] or crayfish [63]. The moonwalker DNs (MDN) integrate visual information [98] and tactile sensory signals from Ascending Neurons [99] and are sufficient and necessary to elicit backward walking in adult flies [86] or backward crawling in larvae [100, 101]. Various GNG DNs elicit different types of anterior grooming (antennal DN/aDN, DNg11, DNg12) [61, 83]. Yet other DNs trigger egg-laying (oviDN) [89], a sequence of courtship actions (aSP22) [78], or the production of courtship song (pIP10) [88]. Some DNs act in a command-like fashion, but are state-dependent: DNp07 and DNp10 drive leg extension for landing, but only if the fly was previously flying [76]. DNp09 — known to drive forward walking [79] — induces running or freezing depending on the current walking speed [85]. In general, numerous command-like DNs have been found in different species highlighting that this mechanisms of descending control may be evolutionarily conserved.

1.4   DN functions beyond commanding behaviours

However, with the amount of 1300 DNs in total in *Drosophila* [50] and even more in larger animals, not every single pair of DNs can be implicated in the activation of a large-scale behaviour. This is particularly evident in the optogenetic activation screen of Cande et al.,

where many DNs do not have a clear behavioural phenotype associated with them [81]. The question arises, what their role may be? In 1999, Edwards et al. postulated that "animals possess a spectrum of premotor organisation" that range from "patterns of activity of a population of premotor interneurons [in] parallel distributed networks" responsible for "shifts in motor pattern" to command systems and command neurons responsible for stereotyped behaviours [102]. More recent studies in *Drosophila* have in fact found that many DNs do not act alone, but in populations: A population of 15 DNs can modulate wing beat amplitude [80] and strength of the opto-motor response [103]. The activation of individual DNs has a lower probability of driving take-off than co-activation of multiple DNs [77]. Aymanns et al. found that different populations of DNs in the cerebral ganglia are co-active during walking and grooming [96], similar to distributed activation of DNs in zebrafish for complex behaviours [104]. Consistent with this mode of action, brainstem DNs can modulate walking speed [71] and ablation of specific DN populations in larval zebrafish reduces the maximum swimming speed [105]. In adult zebrafish, different DNs encode start and duration of locomotion events vs. sudden changes in speed and their respective ablation selectively impacts slow and fast swimming [106]. The authors argue that having different DN pathways to modulate slow and fast swimming contributes to behavioural flexibility. In primates, some corticospinal DNs directly synapse onto motor neurons to facilitate dexterous control of hand and finger muscles [107]. Similarly, in *Drosophila* some DNs control specific limb gestures during turning [87].

Counterintuitively, individual insect DNs have been found to encode sensory information, including pheromones [108], sugar taste [52], odours [96], and tactile information [96, 109]. Analogously, many DNs in the mammalian corticospinal tract originate from sensory cortices [28]. In insects, a fraction of DNs does not use fast-acting neurotransmitters, but instead release slow-acting neuromodulators: Some dopaminergic DNs are active during leg movements, but are not sufficient to elicit leg movements [94]. Some octopaminergic DNs in stick insects modulate sensory-evoked motor activity [110].

Overall, DNs fulfil diverse functions: They command discrete behaviours, act in populations to modulate motion parameters, facilitate flexible and dexterous movement control, release neuromodulatory signals, and encode sensory information. The last few years have seen significant advances in our understanding of the descending control of movements, but many open questions remain. One of the most burning questions is how to unify the observations that single DNs may be sufficient to elicit a behaviour, but many DNs are involved in its regulation. Understanding, whether and how different DNs interact with each other will contribute to resolving this question.

1.5 Goal of this thesis

In the next chapter, I will describe common technologies used to study DNs and will put the methods we deployed into context. Afterwards, I present two important advances to further our understanding of descending signals. In Chapter 3 we developed a method

that allows long-term recording of neuronal activity in the VNC and cervical connective of *Drosophila*. We demonstrate how this toolkit may be used to study the dynamics of ANs and DNs over extended time spans and across different internal states. By analysing neuronal activity in the cervical connective before, during, and after feeding, we observed that ingestion of high doses of caffeine lead to waves of activity in all ANs and DNs. In Chapter 4 we used optogenetic activation and functional population recordings of DNs to discover that DNs recruit each other for flexible behavioural control. Based on the analysis of DN connectivity in the brain, we show how DNs interact with each other in networks. We make the prediction that connectivity predicts functional properties of DNs and verify this prediction experimentally. Finally, in Chapter 5 I discuss conceptual implications and technological limitations of our studies and describe potential future directions, including the deployment of our long-term imaging toolkit to study Descending Neurons, and the influence of Ascending Neurons on Descending Neurons.

2 Technical background

Our studies rely on a combination of multiple experimental and computational techniques. Some of those techniques look back at decades of incremental improvements but breakthroughs within the last few years have enabled us to perform a set of experiments that were thought to be impossible for a long time: Activating and recording specific neurons in a behaving animal, and additionally studying the connectivity of said neurons with all other neurons in the brain. In the following, I will describe the recent technical developments that this work builds on and show how the methods have been used in related studies. I will focus on techniques to (1) quantify animal behaviour, (2) record neuronal activity, (3) stimulate neurons while recording neuronal activity, (4) use *Drosophila* as a genetic model organism, and (5) investigate connections between neurons.

2.1 Quantifying animal behaviour

To understand behavioural control through neuronal circuits, one must inevitably quantify animal behaviour [111]. Quantifying animal behaviour often consists of three steps: (1) recording behaviour, (2) tracking the animal(s), and then (3) extracting behavioural variables of interest. While in earlier days, all of the above had to be done manually by observing and scoring behaviour, multiple technological advances have facilitated those steps.

Videographic recording of behaviour have become fast (up to 1 kHz frame rate) and affordable because of CMOS camera systems [112]. The simplest way to extract movements from such videographic recordings is to track specific key-points across time and space. In research with humans and larger model organisms, the use of reflective markers applied to specific body parts of interest provided an early solution to this challenge (e.g., [113]). More recently, tracking key-points on experimental animals has become possible without applying markers, thanks to solutions using deep neural networks [114, 115]. Extensions of these tools now allow to perform pose-estimation in both 2D and 3D on various animals, including *Drosophila* [116–118].

These pose-estimation datasets provide rich sources of high-dimensional information. The challenge that remains is to extract behavioural variables of interest. Classically, supervised machine learning and deep-learning techniques have been used to classify specific behaviour into different categories (e.g., boosted decision trees in [119, 120], or a ResNet in [121]). These methods are useful because they allow to detect events with similar statistical structure and can be easily tailored to specific problems. However, they require significant amounts of manually labelled data points and are subject to user biases [122]. Berman et al. have pioneered an unsupervised approach that does not rely on external labels, but instead compresses high-dimensional behavioural data into a two-dimensional behavioural space [81, 123]. Unsupervised approaches allow to detect new behaviours, do not suffer from experimenter biases, and remove the need to label data, but ultimately are harder to interpret. Whiteway et al. used a combination of supervised and unsupervised training to create a classifier of fly behaviour using only few labelled frames [124]. Interestingly, they made use of an additional "soft classification" loss using experimenter-defined heuristics, for example that if the animal moves its front legs, but not its hind legs, it may be grooming. Overall, multiple different approaches have emerged in parallel to solve specific problems and may be chosen and adapted based on the problem at hand. In our studies, we used a system consisting of seven cameras surrounding the fly [116] to record behaviour and performed 2D [117] and 3D pose estimation [116]. We classified behaviours using simple and intuitive heuristics to maximise the interpretability of different behavioural categories.

2.2   Recording neuronal activity

Recording the activity of neurons is key to understanding their function. Signal propagation inside of neurons happens electrically through the flux of ions, which ultimately leads to changes in voltage across the cell membrane. Thus, neuronal activity can be measured using electrical probes or — more indirectly — through recording of the concentration of specific ions.

The first neuronal activity recordings date back to the 1920s, when Edgar Adrian recorded electrical "impulses in sensory nerve fibres" [125]. Since then, multiple different recording techniques have been developed. Electrophysiological recordings are the most direct measures of neuronal activity and permit to observe action potentials in individual or multiple neurons. Electrical activity is commonly recorded extracellularly using single wires [126], tetrodes [127], or, more recently, silicon probes with up to thousands of recording sites [128]. In smaller model organisms, such as *Drosophila*, extracellular recordings are uncommon, and spiking activity is usually recorded using intracellular recordings [129]. However, electrophysiological recordings are challenging to perform for large numbers of neurons and are often agnostic to the genetic identity of the recorded neurons.

Complementary to electrophysiological recordings, measuring the Calcium concentration in neurons has become increasingly popular. Calcium ions flow into the cell through voltage-gated ion channels upon depolarisation, for example during an action potential,

making them an indirect read-out of neuronal activity. By fusing a fluorescent protein with a Calcium binding domain (calmodulin), that undergoes conformational change in the presence of Calcium, changes in the concentration of Calcium ions can be converted into changes of fluorescence [130]. These changes in fluorescence can then be recorded without penetrating neuronal tissue using fluorescence microscopy. Developments in recent years have afforded drastic improvements in signal-to-noise ratio and speed of those Calcium indicators [131, 132], most notably the family of GCAMP indicators [133–135]. By design, Calcium indicators are an indirect measure of neuronal activity and limited in temporal resolution by slow dynamics of Calcium binding and release (e.g., GCaMP6s has a half decay time in the order of 1s [133, 134].). More recently, fluorescent indicators of voltage [136–138] and specific neurotransmitters [139, 140] have been developed to overcome some of those limitations, but also introduce other challenges.

Most commonly, fluorescent indicators of neuronal activity are imaged using two-photon microscopy [141] due to its high resolution, excellent optical sectioning and ability to record from deep tissues. A focused infrared laser beam is point-scanned across the field of view using movable mirrors and only the coincident arrival of two photons at a given position leads to the excitation of a fluophore. Because of the point-scanning mechanism, the speed of two-photon microscopy is limited, especially for volumes and larger field of views recorded at high spatial resolution. Microscopy techniques that acquire an entire 2D plane at once can be used instead: In recent years, light-sheet microscopes, such as the SCAPE microscope [142, 143], have been proposed for functional imaging of neuronal activity. Instead of a single point, an entire 2D plane of tissue is illuminated and is then projected onto the pixel array of a high-speed camera for simultaneous acquisition. A SCAPE microscope allows to record from an entire fly brain at around 10 volumes per second at single-cell resolution [144][I]. However, these microscopes are not as widely available and standardised as two-photon microscopes yet and the resolution deteriorates in deeper tissues because they use single photon excitation. Conventional widefield epifluorescence microscopes have been re-introduced a simple means for functional imaging to acquire large fields of view (e.g., covering the entire mouse brain [145]) by compromising on optional sectioning and single-cell resolution. They allow to compare neuronal activity between different brain areas [145], for example. Alternatively, they allow voltage imaging of small ROIs at up to 5 kHz frame rates [136].

Finally, to gain optical access to the nervous system, specific surgeries and dissection protocols have been developed for rodent brain [146] and spinal cord [147], and *Drosophila* brain [148] and ventral nerve cord [95] to allow optical recording of neuronal activity in behaving animals. Recording from translucent animals such as *C. elegans* [149], *Drosophila* larvae [150], zebrafish larvae [105], or *Danionella* [151] eliminates the need for a dissection. In our studies, we recorded GCaMP6 fluorescence [133] in the *Drosophila* VNC [95] using *in-vivo* two-photon microscopy (see Chapters 3 and 4) and developed an approach that permits recordings up to a month (see Chapter 3).

[I]This is a $\sim 12x$ higher number of pixels per second than the two-photon recordings we perform in Chapter 4.

2.3   Simultaneous activation and recording of neurons

To create causal insights about the function of the nervous system, one must not only record neuronal activity, but also be able to manipulate it. Naturally, neurons are activated (i.e., depolarised) because of the influx of positive ions. This effect can be mimicked by breaking into the cell membrane and injecting positive current or by inserting light sensitive ion channels into the membrane.

During intracellular recordings, current injections provide a way to activate the cell while recording its spiking activity. However, as soon as multiple neurons and their interaction are to be studied, this technique becomes very challenging because one has to gain intracellular access to multiple cells at once. Similar effects can be achieved by genetically adding ion channels that can be controlled through remote signals without physical contact to the cell: The thermosensitive cation channel TrpA1 [152] can be expressed in specific cells using the GAL4 system in *Drosophila*. When flies are heated to around 30 °C, those specific cells are activated because the ion channel becomes permeable [86]. More commonly, light sensitive ion channels derived from opsins found in algae, such as ChannelRhodopsin-2 [153, 154] are genetically inserted into cells of interest. Upon exposure to light of a specific wavelength, the cation channels open and the cells are depolarised. Other light activatable ion channels have been found to hyperpolarise cells [155] and a combination of those two can be used to excite cells with red light, but inhibit them with blue light [156].

Combining optogenetic stimulation of a specific cell type with electrophysiological recordings in different cells can allow to study the connectivity between those cells, including whether the synaptic effect is excitatory or inhibitory (e.g., [157]). Alternatively, optical recording of a Calcium indicator can be combined with optical activation of an opsin to allow for more flexible recordings while compromising the ability to observe inhibition. However, care has to be taken to avoid cross-talk between the two optical pathways for stimulation and recording. Most commonly, this is achieved by spectrally segregating stimulation and imaging light. Green Calcium indicators, such as GCaMP [133–135], are excitable using blue ($\sim$488 nm) light (or $\sim$930 nm light for two-photon excitation), and emit green photons ($\sim$525 nm). They can be used in conjunction with red-shifted opsins, such as CsChrimson [154], which is activatable at wavelengths around 600nm. One of the caveats of CsChrimson is that it is still activated by 488 nm light at around 30 % of its peak activation [154]. The use of the UV excitable version of the XCaMP indicators [132] could improve the spectral separation. Alternatively, one can use red calcium indicators [131, 132, 158, 159] in combination with blue-light activated opsins [153, 154]). Despite its superior division of the optical spectrum, this combination is less-often used, because green Calcium indicators are much further developed than red ones, and red light used for activation of CsChrimson penetrates deeper into tissue than shorter wavelength blue light.

The problem of spectral overlap can also be alleviated by spatially constraining optogenetic excitation and imaging (e.g., stimulation of the leg using an optical fibre and recording from the VNC in [157]). Most recently, cell-specific optical activation and optical recordings can

be combined inside a single microscope using two separate light paths by spatially targeting the stimulation light through a spatial light modulator (SLM) [160, 161]. Additionally, bi-directional opsins [156] can be combined with voltage indicators for an "all-optical closed-loop voltage clamp" [162]. In our study in Chapter 4 we used two-photon imaging of GCaMP6s [133] in conjunction with genetically and spatially targeted one-photon activation of CsChrimson [154] using a 640 nm laser.

2.4 Drosophila as a genetic model system

Very often, answering systems neuroscience questions require invasive experimental techniques. Thus, animal model organisms are used with the hope that findings translate to humans. One particular strength of using certain model organisms is that defined cells can be genetically modified. This allows for example to target fluorescent indicators of neuronal activity and optogenetic channels to manipulate neuronal activity to genetically defined sets of neurons in mice (e.g., [163]), zebrafish (e.g., [164], and *Drosophila* (e.g., [92]).

The *Drosophila* research community has developed particularly versatile genetic toolboxes. Three independent, binary expression systems are available: GAL4 [165], LexA [166], and QUAS [167]. The GAL4 system is the most frequently used system. Being a binary expression system, it consists of two parts that can be flexibly combined: The first part is a GAL4 driver line — a transgenic fly line — that expresses the GAL4 gene coding for a yeast-derived transcription factor under the control of a promoter of interest. The second part is a so-called activator line, where a target gene of interest (e.g., coding for GCaMP), flanked by an upstream activation sequence (UAS), is inserted. These two fly lines are then crossed and selected off-spring may contain both transgenes. When both GAL4 and UAS are present in a specific cell — which only happens in cells that express the promoter of interest —, the GAL4 protein produced in this cell binds to the UAS sequence and activates expression of the target gene of interest. By fragmenting the GAL4 gene into two parts and expressing each part under a different promoter, an intersectional strategy (the split-GAL4 system [75]) was developed. This system now allows to target gene expression to even smaller subsets of cells, down to single pairs of neurons. On the contrary, driver lines targeting Hox genes allow to target expression to large segments of the body [168].

The power of *Drosophila* as a genetic model system also stems from its short generation time of about 10 days. Most commonly, transgenes are inserted in specific docking sites and single-mutant flies are created. Using simple crossing schemes, animals carrying multiple transgenes can be flexibly created from single-mutant flies within a few weeks. This approach is powerful, but limited by the number of six usable chromosomes (The fourth chromosome pair is very short and not commonly used to create transgenic animals [169].). If more transgenes are to be expressed, more complex crossing schemes designed around the non-deterministic occurrence of homologous recombination can be used to stably combine two transgenes on one chromosome [169]. In Chapter 4 we developed a flexible genetic approach allowing to optogenetically activate specific neurons of choice while recording

Calcium activity from a defined population of neurons. This approach involved a combined use of the GAL4 and LexA expression systems and the creation of transgenic flies with up to six transgenes spread over four chromosomes.

2.5 Connectomics: Studying connections between neurons and their relation to circuit function

Knowing the connectivity between neurons of interest is crucial to understanding the function of a particular circuit. Combined this knowledge with functional recordings allows to put neuronal activity into the context of the circuit that a given neuron is connected to.

The morphology of individual neurons and all their synapses with other neurons can be reconstructed from electron microscopy (EM) volumes of nervous system tissue. Both the EM recording and the reconstruction are very time consuming, which is why the first 'connectome' of an entire nervous system was the one of the nematode *C. elegans* with only 302 neurons in 1986 [170]. Since then, multiple small volumes of the mouse brain [171, 172] or the *Drosophila* brain [173, 174] have been reconstructed. In the last few years, entire brain connectomes of the *Drosophila* larva [175] and adult [50], as well as the adult ventral nerve cord [176, 177] have been generated and an entire *Drosophila* nervous system dataset is on the horizon.

Excitingly, the last few years have seen a transition from purely anatomical studies of a single connectome to the pursuit of understanding the link between anatomy and function. As with the generation of connectomes, studies on *C. elegans* lead the way of what is technically possible and provide inspiration for future studies in larger animals: Comparison of multiple connectomes of *C. elegans* showcased the changes of information processing during development [178] and the convergence of sexually dimorphic circuits [179]. By matching brain-wide functional recordings in behaving animals to the *C. elegans* connectome, researchers found that a few local connectivity motifs support global brain dynamics [149] and that neurons that are closely connected encode similar behaviours [180]. Shiu et al. combined connectomics with optogenetic activation and functional imaging to study multi-layer processing in a *Drosophila* sensorimotor circuit [52] and showed that they could accurately predict functional properties of neurons in a simulation of the entire *Drosophila* brain connectome [181]. Mammalian connectomics research still focuses on small regions of the brain: Lee et al. showed that neurons with similar tuning in V1 have more synapses to one-another [182]. Wanner et al. discovered how reciprocal inhibition within the zebrafish olfactory bulb mediates whitening of odour stimuli [183]. Interestingly, a recent study compared connectomes across different species: Haber et al. inferred overarching design principles of neuronal circuits from three different connectomes [184]. In the future, it will be inevitable to complement the functional study of a specific circuit with its exact connectivity. In our study of Descending Neurons (DNs) in Chapter 4, we complemented our stimulation and neuronal population recording experiments with the analysis of connectivity patterns of identified DNs. We found that DN connectivity predicts functional properties and that DNs connect in behaviour-specific excitatory networks.

3 Microengineered devices enable long-term imaging of the ventral nerve cord in behaving adult Drosophila

Laura Hermans[1], Murat Kaynak[1], **Jonas Braun**, Victor Lobato Ríos, Chin-Lin Chen, Adam Friedberg, Semih Günel, Florian Aymanns, Mahmut Selman Sakar[2], Pavan Ramdya[2]. "Microengineered devices enable long-term imaging of the ventral nerve cord in behaving adult *Drosophila*", *Nature Communications* 13, 5006 (2022).
The article can be found here: https://doi.org/10.1038/s41467-022-32571-y
[1] These authors contributed equally.
[2] These authors contributed equally.

My contribution: I developed the neural data processing pipeline used in this article. This pipeline has become the standard software of the laboratory to process neural and behavioural data from two-photon imaging experiments and also forms the foundation of the data analysis in Chapter 4. It adapts and integrates multiple approaches in one package: motion-correction [95], denoising [185], semi-automated ROI detection, $\Delta F/F$ computation of neuronal signals; ball movement tracking using two different approaches [186, 187], 2D and 3D pose-estimation using different approaches [116, 117], external stimulus processing, and synchronisation of all of the variables above.
I analysed and visualised functional recordings of population neural activity during different feeding states (**Figures 3.4** and **S3.13** and **Videos** 3.10 to 3.13)
Finally, I contributed to data curation, writing, and editing.

3.1 Abstract

The dynamics and connectivity of neural circuits continuously change on timescales ranging from milliseconds to an animal's lifetime. Therefore, to understand biological networks, minimally invasive methods are required to repeatedly record them in behaving animals. Here we describe a suite of devices that enable long-term optical recordings of the adult *Drosophila melanogaster* ventral nerve cord (VNC). These consist of transparent, numbered windows to replace thoracic exoskeleton, compliant implants to displace internal organs, a precision arm to assist implantation, and a hinged stage to repeatedly tether flies. To validate and illustrate our toolkit we (i) show minimal impact on animal behavior and survival, (ii) follow the degradation of chordotonal organ mechanosensory nerve terminals over weeks after leg amputation, and (iii) uncover waves of neural activity caffeine ingestion. Thus, our long-term imaging toolkit opens up the investigation of premotor and motor circuit adaptations in response to injury, drug ingestion, aging, learning, and disease.

3.2 Introduction

Neural tissues are remarkably plastic, adapting to changes in internal states and in response to repeated exposure to salient environmental cues. In neuroscience, physiological studies of long timescale phenomena, including memory formation and neurodegeneration, have often relied on comparing data pooled across animals sampled at multiple time points. However, resolving differences across conditions with this approach suffers from inter-individual variability. Thus, longitudinal recordings of the same animal would be ideal to uncover adaptive changes in the functional and structural dynamics of neural circuits. Important technical challenges must be overcome to perform long-term studies in individual animals, including the minimization of experimental insults.

With the advent of microscopy-based neural recordings, most notably two-photon calcium imaging [188], it has become possible to chronically record brain circuits *in vivo* in a minimally invasive manner. Cranial window technologies were first developed to study mouse neocortex [189] and have since been improved to acquire larger [190] and deeper [191] imaging fields-of-view, as well as longer duration recordings [192]. Similar to rodents, brain imaging can also be performed in the behaving adult fly, *Drosophila melanogaster* [186, 193], a popular model organism that is (i) genetically tractable, (ii) has a small nervous system with few neurons, and (iii) generates complex social, navigation, and motor behaviors [194–197].

Recent approaches have enabled long-term chronic recordings of neurons in the fly brain [198–200]. Similar to imaging the neocortex of rodents with a cranial window [201], the fly brain can be made optically accessible by removing head capsule cuticle and underlying tissues [186]. To perform long-term or repeated imaging, this hole can be covered with UV-curable glue [199], two-component silicon [202], or manually-cut coverglass [198]. However, the techniques and technologies used to perform long-term imaging in the brains

of mice and flies are not suitable to record motor circuits in the mammalian spinal cord, or insect ventral nerve cord (VNC). Like the spinal cord, which is obscured by vertebral bone, muscle, and dorsal lamina [203], optical access to the VNC requires the removal of overlying organs and tissues including the flight muscles, fat bodies, gut, and trachea. Invasive surgeries on the spinal cord permit the implantation of a chamber [204], or a clamp [147]. However, the small size of the fly limits the use of conventional implantable devices, representing an important challenge for uncovering general principles for motor control through the investigation of the experimentally tractable VNC—a nervous tissue that is coarsely organized like the mammalian spinal cord [47], and whose control principles resemble those found in vertebrates [205, 206].

We recently developed a dissection approach that gives optical access to the VNC in tethered, behaving animals by surgically and genetically—in the case of the indirect flight muscles—removing overlying tissues [95]. However, this technique is invasive, requiring the resection of thoracic organs and leaving open the thoracic cavity. This precludes recordings that last beyond a few hours. Consequently, it has been impossible to perform repeated measurements of premotor and motor circuits in the same fly to shed light on how these circuits adapt over time. Existing tools for long-term brain imaging are insufficient for long-term VNC imaging. Unlike for brain imaging, one cannot glue [199], or manually cut coverslips [198] to cover the thoracic hole following dissection. Instead, one needs a more precise, reproducible approach that ensures that hemolymph does not leak from the thorax. Additionally, to gain optical access to the VNC one must gently but firmly displace large overlying thoracic organs and tissues without disrupting their function.

Here, we describe a suite of microengineered devices that address all of these challenges to permit long-term and repeated recordings of the *Drosophila* VNC for more than one month. These devices address the unique challenges associated with studying small model organisms (the fly is ∼2-3 mm long) that require extremely gentle manipulation. Specifically, we designed (i) a manipulator ('arm') that allows us to move aside and temporarily hold in place thoracic organs, (ii) flexible implants that eliminate the need to surgically remove thoracic organs to gain optical access to the VNC, (iii) a transparent polymer window that encloses the thoracic cavity and is numbered, allowing individual flies to be distinguished from one another across imaging sessions, and (iv) a remounting stage that allows flies to be gently yet firmly tethered for repeated recordings. We provide detailed descriptions of how to fabricate and use all of these tools, to facilitate their replication and adoption by other laboratories.

We demonstrate that implants and windows have minimal impact on animal survival and locomotion, and that they permit neural recordings across at least one month. Then we illustrate use-cases of our long-term imaging toolkit in two proof-of-concept studies. First, we longitudinally measure the degradation of limb mechanosensory neuron innervation of the VNC over two weeks following leg removal. Second, we illustrate how—by leaving thoracic organs intact—one can measure the impact of drug ingestion on neural population dynamics. Thus, our long-term thoracic imaging toolkit enables the repeated, longitudinal

study of structural and functional neural dynamics in premotor and motor circuits. These tools may more generally also be used to study other thoracic tissues including indirect flight muscles, gut, and trachea.

3.3 Results

3.3.1 Long-term recording toolkit and experimental workflow

We developed microengineered devices and associated micromanipulation protocols that enable optical access to the fly's VNC for more than one month. Implanted flies exhibit no obvious deficits in their ability to feed, walk, lay eggs, or interact with others. (**Figure 3.1**a and **Video** 3.1). Optical access depends on two main components: a compliant and transparent implant (**Figure 3.1**b) and a transparent thoracic window (**Figure 3.1**c). The fabrication of windows must be reproducible and they must be large enough to securely seal the thoracic opening to prevent hemolymph leakage. Solutions developed for long-term brain imaging such as sealing with UV-curable glue [199] or a manually cut piece of coverglass [198] do not address these challenges. We designed and microfabricated a custom window using a biocompatible polymer, SU-8, through photolithography (**Figure S3.1**). Because implants are not required for long-term brain imaging, these had to be designed *de novo* and without inspiration from previous approaches. Our earliest implants were rigid structures intended to protect VNC imaging regions-of-interest from occlusion by thoracic tissues (**Figure S3.2**, 'iterations 1 and 2'). Later iterations attempted to combine thoracic windows with protective pillars (**Figure S3.2**, 'iterations 3 and 4'). However, both of these initial prototypes yielded prohibitively low survival rates. We achieved a breakthrough by taking a completely different approach: we designed compliant (polymer-based), mechanically compressible V-shaped implants. Through several iterations and testing, we converged upon the specific size and angle of V-shaped implants, ultimately resulting in a very high post-implantation survival rate. We fabricated these V-shaped implants *en masse* using soft lithography, a technique that is based on rapid prototyping and replica molding (**Figure S3.3** and **Figure S3.4**).

To use these tools, we developed a manipulation protocol illustrated in **Video** 3.2. Briefly, we first mount animals onto a surgical dissection stage using UV-curable glue (**Figure 3.1**d) [95]. Next, we cut a square-shaped hole into the dorsal cuticle using a 30G syringe needle (**Figure 3.1**e - left panel). The indirect flight muscles (IFMs) are subsequently removed to create a thoracic opening for the implant. To minimize the impact of the microsurgery, we work with animals expressing the apoptosis-inducing protein, Reaper, specifically in IFMs (*Act88F:Rpr*). Expressing Reaper results in rapid degradation of the muscle tissue [95], the remainder of which can easily be removed with the syringe needle. However, this genetic line is not strictly required to make use of these tools. Having exposed the thoracic tissues, we then use a fine glass needle and forceps to unilaterally detach tracheal fibers that connect the gut and left salivary gland. We designed a custom manipulation arm (**Figure S3.5**) to push internal organs—gut, salivary gland and trachea—to the right side of the thoracic cavity (**Figure 3.1**e - left panel). This allows one to insert the implant, in a closed state,
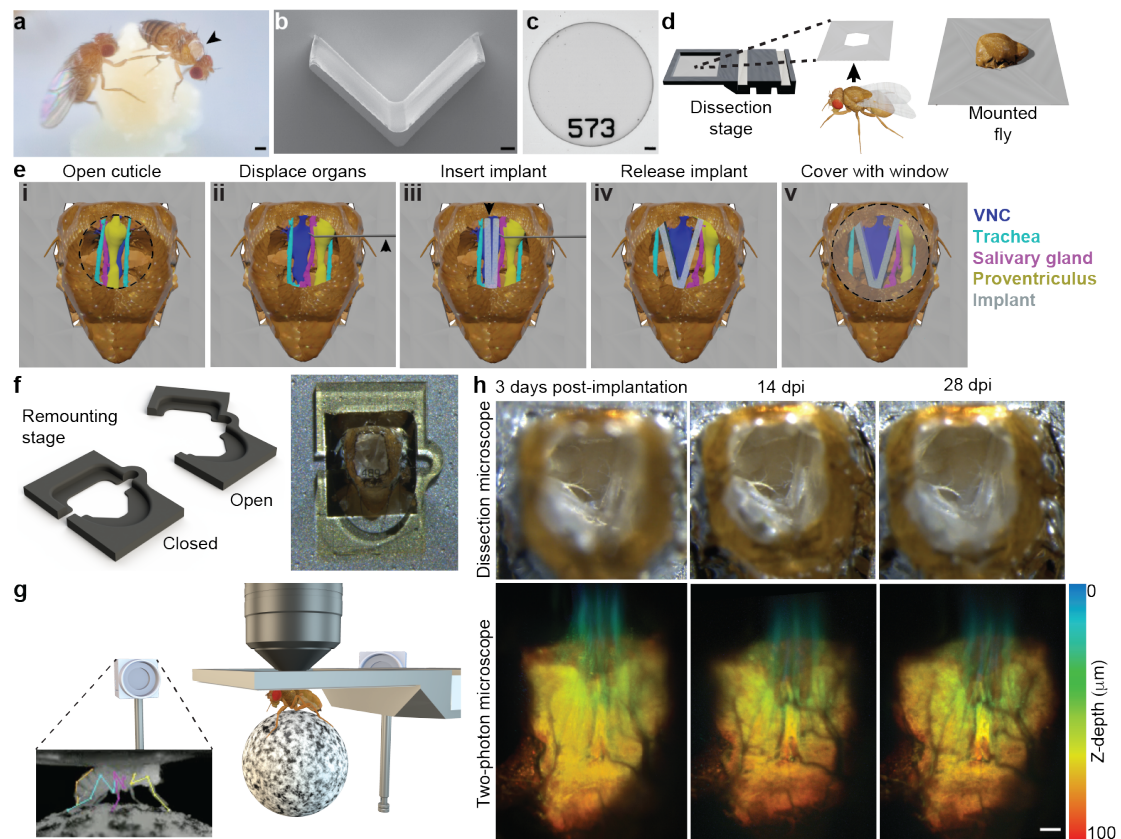
Figure 3.1 - See Figure Legend on next page.

into the newly accessible thoracic cavity (**Figure 3.1**e - middle panel and **Figure S3.4**). Upon release, the implant gradually opens, holding the organs against the thoracic wall after the manipulation arm is retracted (**Figure 3.1**e - right panel). We seal the exposed thoracic cavity by gluing a transparent polymer window to the cuticle (**Figure 3.1**e - right panel). These windows have unique numbers engraved on their surfaces, making it possible to identify and distinguish between implanted animals. We can then detach animals by removing the UV-curable glue holding the scutellum to the dissection stage, allowing them to behave freely.

To facilitate repeated, gentle tethering of implanted flies, we printed a remounting stage (**Figure 3.1**f and **Figure S3.6**) using two-photon polymerization [207]. This manufacturing process has the accuracy required to fabricate 3D features that reliably hold animals in place. When mounted, we studied animals using a two-photon microscope system surrounded by a multi-camera array. This system enables simultaneous recordings of neural activity in the VNC [95] as well as markerless 3D body part tracking [116] (**Figure 3.1**g). In the vast majority of cases, our implantation protocol was successful. Infrequently, implanted animals exhibited specific movements of respiratory, or digestive tissues that could occlude the VNC during imaging (**Figure S3.7**). Successful implantation permitted optical access to the VNC that remained largely unchanged over one month. This allowed repeated

Figure 3.1: Long-term recording technologies, workflow, and experimental validation.
(a) Implanted adult flies can be raised in complex environments. An implanted animal—see
dorsal thoracic window (black arrow)—interacts with a non-implanted animal. Scale bar is
0.5mm. **(b)** A mechanically compliant, transparent implant microfabricated from Ostemer
220. Scale bar is 50 µm. **(c)** A numbered, transparent thoracic window microfabricated
from SU-8. Scale bar is 50 µm. **(d)** For implantation, an animal is first mounted, thorax
first, into a hole in a steel shim within a dissection stage. **(e)** A multi-step dissection permits
long-term optical access to the ventral nerve cord (VNC). (**left**) A hole is cut into the dorsal
thoracic cuticle, revealing the proventriculus (yellow), trachea (cyan), and salivary gland
(magenta) overlying the ventral nerve cord (VNC, dark blue). The indirect flight muscles
(IFMs) were degraded by tissue-specific expression of Reaper (*Act88F:Rpr*) [95]. Then,
using a custom-designed manipulator arm, thoracic organs are displaced, revealing the VNC.
(**middle**) Next, the implant is placed within this thoracic hole in a narrow, mechanically
closed configuration. (**right**) The arm is removed and the implant is released, causing
it to open and mechanically push aside organs covering the VNC. Finally, a transparent
window is sealed to enclose the thoracic hole. **(f)** A 3D nanoprinted remounting stage
permits mounting and dismounting of animals for repeated two-photon imaging. (**left**)
The monolithic mechanism is actuated around a compliant hinge. (**right**) Sample image
of an animal tethered to the remounting stage, seen from above. **(g)** Implanted animals
tethered to the remounting stage are placed under a two-photon microscope surrounded by
a camera array. This configuration permits simultaneous recordings of neural activity and
animal behavior. Inset shows one camera image superimposed by deep learning-based 2D
poses estimated using DeepFly3D [116]. **(h)** (**top row**) The dorsal thorax of an implanted
animal, seen from the dissection microscope, and (**bottom row**) its VNC, visualized using
two-photon microscopy. This animal expresses GFP throughout the nervous system and is
recorded at (**left**) 3 dpi, (**middle**) 14 dpi, and (**right**) 28 dpi. Z-stacks are depth color-coded
(100 µm). Scale bar is 25 µm.

---

studies of the structure (**Figure 3.1**h and **Video** 3.3) and functional dynamics of neural
populations in female (**Video** 3.4) and male (**Video** 3.5) flies. Our long-term recording
tools could also be applied to recording genetically-identifiable pairs of neurons. We
illustrate this by imaging the activity of a pair of DNa01 descending neurons over three
days (1, 3, and 5 days-post-implantation (dpi)). This activity correlates with locomotor
turning [95](**Figure S3.8** and **Video** 3.6). Although here we focused on gaining optical
access to the VNC's cervical connective and prothoracic (T1) neuromere (**Figure 3.1**h), our
approach is general, permitting the redesign and microfabrication of implants that enable
the imaging of other regions of the VNC. As a proof-of-concept, we modified an implant,
making it possible to restrain tissue in the posterior thorax and to gain optical access to T2
and T3 neuromeres (**Figure S3.9**).

3.3.2 Impact of long-term imaging technologies on lifespan and behavior

To validate our long-term recording approach, we first studied the potential impact of implantation on lifespan. Specifically, we measured the longevity of three groups of animals (n = 40 per group): (i) flies that were not manipulated ('Intact'), (ii) animals that endured cold anesthesia, mounting onto the dissection stage, and wing removal ('Sham implanted'), or (iii) flies that underwent the full implantation procedure ('Implanted'). For this experiment, 73% of implanted animals survived more than 4 h following surgery. Because the surgical and implantation procedure for a single fly takes approximately 40 min from start to finish. Total throughput—a combination of this implantation time and acute survival rate—was one implanted animal per 55 min. Among flies that survived more than 4 h after implantation, we observed a maximum survival of up to 88 days. However, implanted flies exhibited higher mortality than intact animals in the first days following implantation (**Figure 3.2**a). Notably, sham implanted flies had similarly increased mortality in the first days, suggesting that pre-implantation animal handling, and not implantation itself, was responsible for increased mortality. We obtained similar survival rates for implanted versus intact male flies examined over 20 days (**Figure S3.10**a).

Next, although implantation did not dramatically affect longevity, we reasoned that placing a microfabricated object within the thorax might negatively impact walking, possibly due to the perturbation of leg-related musculature, or simply the additional load. Investigating this possibility is difficult because flies use a variety of diverse gaits at different walking speeds and maneuvers [208]. Therefore, to be able to perform a quantitative analysis of walking, we drove stereotypical backward walking through optogenetic activation of the light-gated cation channel, CsChrimson [154] expressed in Moonwalker Descending Neurons (MDNs) [86, 98]. We stimulated animals in a custom-built arena (**Figure 3.2**b) repeatedly over the course of one month. This allowed us to quantify and compare the walking trajectories of intact, sham implanted, or implanted flies. We first recorded spontaneous behaviors for 30 s, and then delivered three consecutive flashes of 590 nm orange light for 3 s each (**Figure 3.2**c, pink and **Figure S3.11**a) with an inter-stimulus interval of 10 s. These experiments were performed on the same animals at three periods of time over one month (1-3 days post implantation (dpi), 14-16 dpi, and 28-30 dpi). Upon optogenetic stimulation, we observed that animals generated fast backward walking that gradually slowed and rapidly returned to baseline when the light was turned off (**Video** 3.7). Over all recording sessions, we did measure a small significant difference in the initial backward acceleration (**Figure 3.2**d) between the intact group and the sham implanted group ($P=$ 0.044 Kruskal-Wallis with post-hoc Conover test) and between the 'intact' group and the 'implanted' group ($P=$ 0.044), no statistical difference were observed in the translational velocities of intact, sham implanted, and implanted animals in terms of the total backward walking distance traveled (**Figure 3.2**e), and the maximum backward walking velocity (**Figure 3.2**f). Similar results were obtained when comparing age-restricted cohorts. Specifically, we did not observe a difference between the intact and implanted groups in the initial backward acceleration for any age cohort (1-3 dpi, 14-16 dpi, or 28-30 dpi). Intact flies had a slightly slower backward acceleration (this may be because of contact between
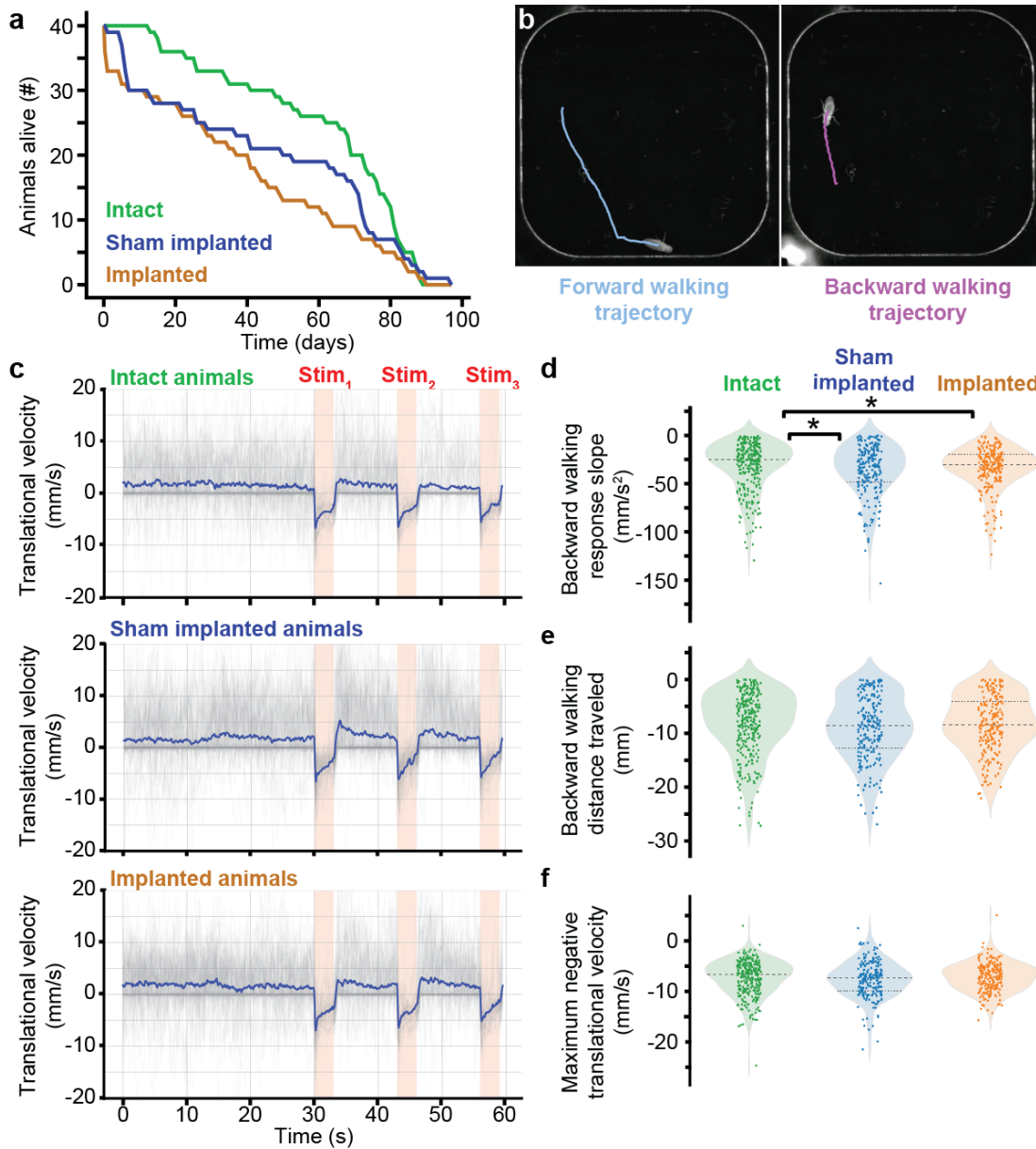
Figure 3.2 - See Figure Legend on next page.

the legs and wings due to Act88F:Rpr expression). We, noted a significant difference between both control groups at 14–16 dpi (**Figure S3.11**b-c) for (i) the backward walking response slope ($P= 0.009$), (ii) the backward walking distance traveled ($P= 0.0008$), and (iii) the maximum negative translational velocity ($P= 0.003$). Spontaneous walking was also qualitatively unchanged in male implanted versus intact flies (**Video** 3.8). Taken together, these results suggest that locomotion is not significantly affected by implantation.

Figure 3.2: Impact of long-term imaging technologies on lifespan and behavior. (a)
Survival curves for genetically-identical sibling animals that were (i) not experimentally
manipulated (green, 'Intact'), (ii) tethered, cold anaesthetised, and had their wings removed
(blue, 'Sham implanted'), or (iii) prepared for long-term imaging by implantation and the
addition of a thoracic window (orange, 'Implanted'). Source data are provided as a Source
Data file. **(b)** Behaviors were compared by analyzing the dynamics of optogenetically
activated backward walking within a rounded square-shaped arena. Locomotion was
computationally analyzed and plotted, showing the animal's initial forward trajectory (cyan)
and subsequent optically evoked backward walking trajectory (purple). **(c)** Translational
velocities of intact (**top**), sham implanted (**middle**), and implanted (**bottom**) animals during
30 s of spontaneous behavior, followed by three optogenetic stimulation periods of 3 s each
(pink, 'Stim'). Here, we pooled data recorded at three time periods over one month. Shown
are raw (grey) and mean (blue) traces. From these time-series, each stimulation event is one
data point from which we calculated summary statistics (intact group, n=286 events; sham
implanted group, n=208 events; implanted group, n=213 events) including **(d)** the initial
negative slope in translational velocity—backward walking—upon optogenetic stimulation,
(e) the backward walking distance traveled over the entire optogenetic stimulation period,
and **(f)** the peak negative translational velocity over the entire optogenetic stimulation
period. One asterisk (*) indicates $P < 0.05$. Source data are provided as a Source Data file.

3.3.3 Quantifying long-term nerve degradation in the VNC following limb amputation

Neuronal circuits retain a capacity for structural rearrangement throughout adulthood [209,
210]. This enables adaptations in response to nervous system injury [211–213], and stroke
[214]. Similarly, in flies, locomotor gaits reorganize following leg amputation [215]. However,
the impact of amputation on limb control circuits remains unexplored because uncovering
these changes requires imaging the VNC of amputated animals across days, or weeks.
Although, in principle, one could instead pool data across multiple animals at specific days
following leg amputation, this has two major shortcomings. First, inter-animal variability
would limit the ability to resolve the degeneration of specific neural structures. Second, this
approach would be more time consuming, requiring many more experiments and animals
per timepoint of interest. By contrast, longitudinal imaging is ideally suited for uncovering
dynamic changes in neuronal structures using relatively few animals. To illustrate this
possibility, we followed the degradation of primary proprioceptive mechanosensory afferents
in the VNC following leg amputation. Specifically, we visualized the axon terminals of
amputated proprioceptive leg femoral chordotonal organs (*Act88F-Rpr/+; iav-Gal4/UAS-
GFP; +/+*) in the T1 neuromere of the VNC. Flies were implanted on the first day
post-eclosion (dpe). Then, one day post-implantation (1 dpi), we performed volumetric
two-photon imaging of T1. Volumes consisted of 100 images taken at 1 μm depth intervals.
Then, at 2 dpi, the front left leg of each experimental animal was amputated near the
thorax-coxa joint (**Figure 3.3**a).
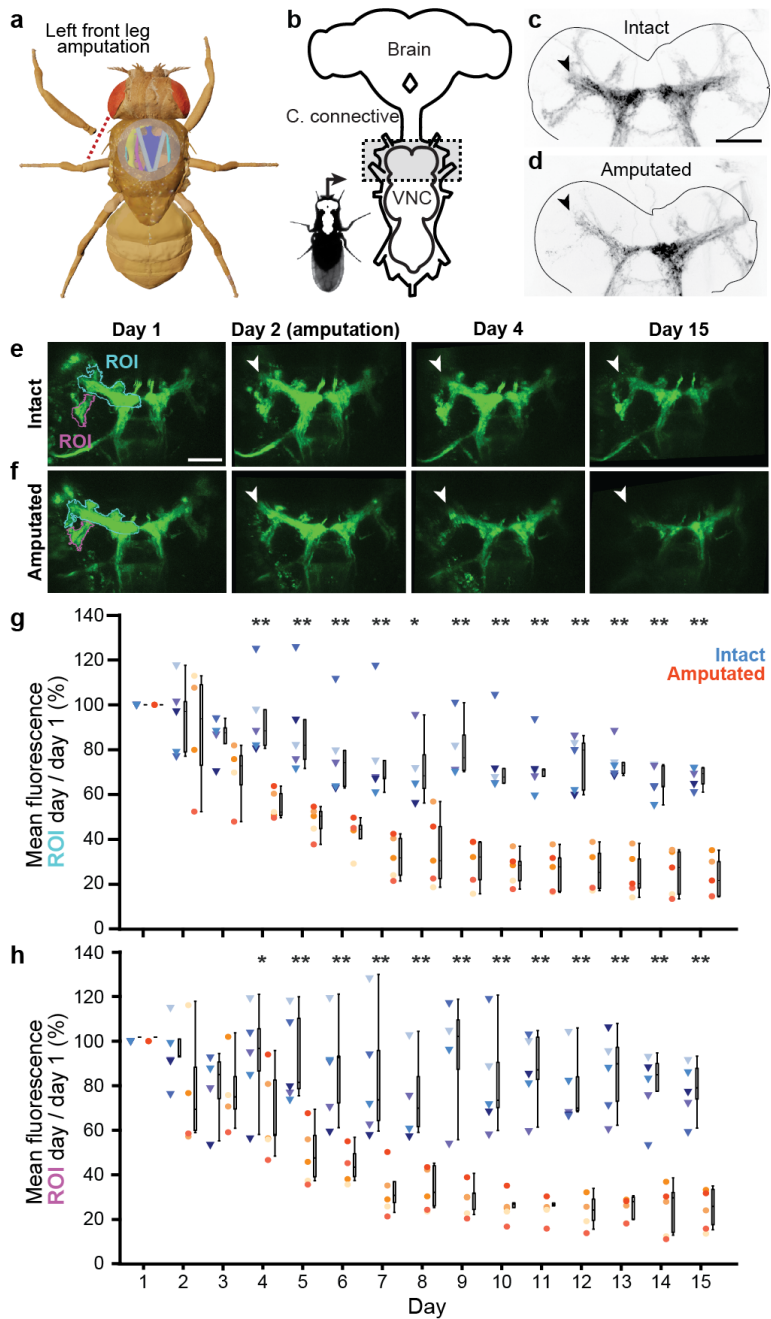
Figure 3.3 - See Figure Legend on next page.

Implanted flies tolerated leg amputation and generated normal behaviors with the remaining five legs (as in [215]). Every day for 15 days, we collected T1 volumes (**Figure 3.3**b) from control animals ('Intact'), and from animals with their front left leg removed ('Amputated'). We performed VNC dissection, staining, and confocal imaging 18 days after leg removal to confirm that mechanosensory innervation of the VNC's T1 neuromere persisted in intact animals (**Figure 3.3**c) but degraded in amputated animals (**Figure 3.3**d). Close examination of two-photon microscope image volumes revealed that, in control animals, some

Figure 3.3: Long-term imaging of mechanosensory nerve degradation in the VNC following leg amputation. (a) In experimental animals, the front left leg was amputated at the thorax-coxa joint at 2 dpi. **(b)** Fly nervous system schematic. The VNC region imaged is highlighted (gray). **(c,d)** Standard deviation z-projection of confocal imaging volumes recorded from flies that were either **(c)** left intact, or **(d)** amputated at 2 dpi (nc82 stained neuropil outlined in grey; GFP fluorescence in black). Tissues were taken from implanted animals whose front left legs were amputated. VNC tissue was removed and stained at 20 dpi. Black arrowhead indicates VNC region exhibiting greatest difference between intact and amputated proprioceptor innervation. Scale bar is 50 μm. **(e,f)** Maximum intensity projections of z-stacks recorded from **(e)** an intact (control), or **(f)** amputated animal. Data were acquired using two-photon microscopy of implanted animals. Shown are images taken at 1, 2, 4, and 15 dpi. Images are registered to the 1 dpi image. Scale bar is 50 μm. White arrowheads indicate degrading axon terminals in the VNC of amputated animals. **(g,h)** Fluorescence measured across days using two-photon microscopy from intact (n=5; blue triangles), or amputated animals (n=5; orange-red circles). Measurements indicate mean fluorescence within the **(g)** cyan, or **(h)** purple region-of-interest (ROI) as in panels e and f, normalized and divided by the mean fluorescence at 1 dpi. Box plots indicate median, first and third quartiles. Statistical comparisons performed with a Mann-Whitney U Test (two-sided) for which one asterisk (*) indicates $P<0.05$ and two asterisks (**) indicate $P<0.01$. For panel **g**, $P = 0.006$ (day 4); 0.006 (day 5); 0.009 (day 6); 0.006 (day 7); 0.018 (day 8); 0.009 (day 9); 0.006 (day 10); 0.006 (day 11); 0.009 (day 12); 0.006 (day 13); 0.006 (day 14); 0.006 (day 15). For panel **h**, $P = 0.03$ (day 4); 0.006 (day 5); 0.009 (day 6); 0.006 (day 7); 0.009 (day 8); 0.009 (day 9); 0.006 (day 10); 0.006 (day 11); 0.009 (day 12); 0.006 (day 13); 0.006 (day 14); 0.006 (day 15). Source data are provided as a Source Data file.

photobleaching occurred in the imaging region over days (**Figure 3.3**e). However, this decline in fluorescence was not nearly as profound as the reduction in signal observed in chordotonal organ axon terminals of the left T1 neuropil in amputated animals (**Figure 3.3**f; **Figure S3.12** and **Video** 3.9). By quantifying changes in signal intensity within specific regions of interest (ROIs) of chordotonal axon innervations within the VNC [216], we measured a highly reproducible and significant fluorescence reduction in amputated versus intact animals (Mann-Whitney U Test, * indicates $P<0.05$ and ** indicates $P<0.01$)(**Figure 3.3**g,h).

3.3.4 Capturing neural population dynamics associated with drug ingestion

In addition to being morphologically adaptable across days and weeks, neural circuits also continuously modulate their dynamics on shorter timescales depending on the internal state of an animal. In *Drosophila*, as in vertebrates, these states include hunger [217], fatigue [218], sexual arousal [219], aggression [220], and defensive arousal [221]. Internal states can also change following the ingestion of psychoactive substances including caffeine [222–224]. Continuous monitoring of the nervous system is crucial to uncover how circuits reconfigure during these changing states.
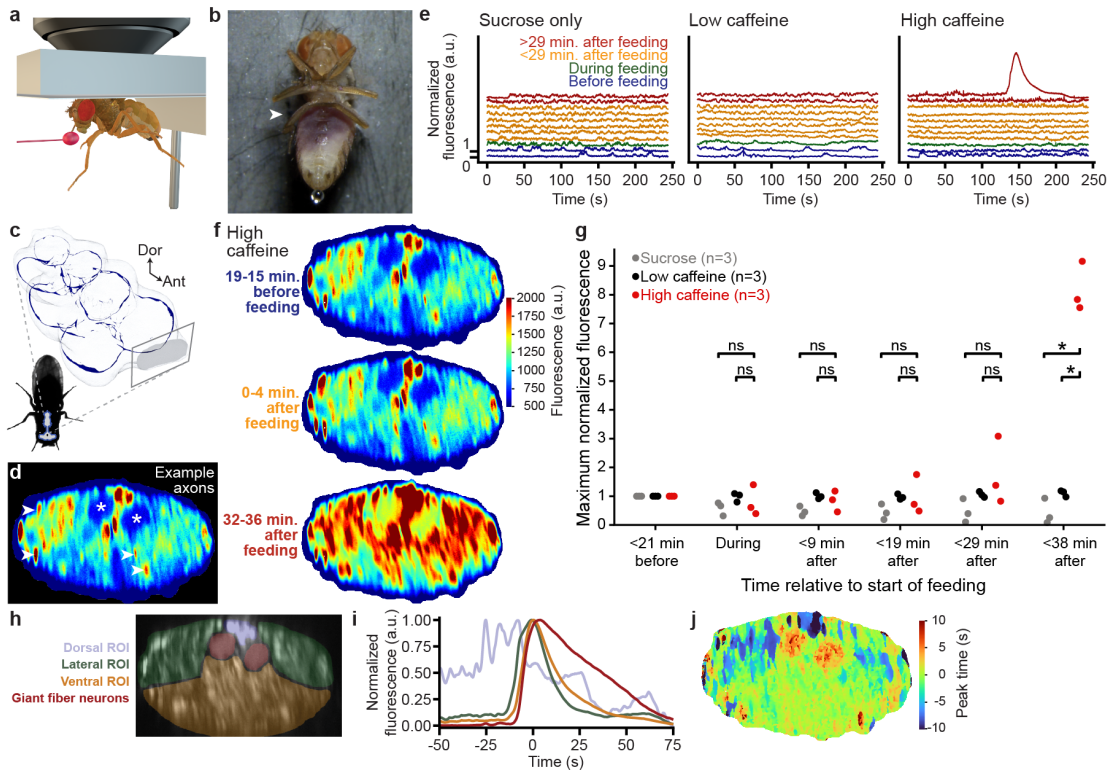
Figure 3.4 - See Figure Legend on next page.

Our previous technique for studying VNC neural dynamics in behaving animals [95] required the removal of large sections of gut, reducing the longevity of animals and making long-term recordings that capture changes in internal states impossible. Furthermore, although taste responses can be studied in the brain [225], removing the gut precludes feeding, and, consequently, does not allow one to investigate how satiety, or the ingestion of psychoactive substances modulate neural dynamics in the VNC. Our long-term imaging toolkit preserves the gut, making it possible for animals to be fed during two-photon microscopy. Therefore, we next asked to what extent our technologies could be used to uncover the impact of drug ingestion on neural dynamics.

Flies exposed to low doses of caffeine have reduced sleep [222, 223] and increased locomotor activity [224]. Here, we asked to what extent caffeine ingestion might also drive global changes in neural population dynamics. To test this, we first starved animals for 21-23 h to encourage feeding. Then, after implantation, we recorded neural activity in the cervical connective ('Before feeding'). While continuing to record neural activity, animals were then fed (**Figure 3.4**a) either a control solution ('Sucrose only') containing 8 mg/ml sucrose and 1 mg amaranth dye (to confirm feeding [226]) (**Video** 3.10), or an experimental solution that also contained 8 mg/ml, or 40 mg/ml caffeine: 'Low caffeine' (**Video** 3.11), or 'High caffeine' (**Video** 3.12), respectively. We continued to record neural activity and behavior for the next 38 minutes. Feeding was confirmed by post-hoc evaluation of abdominal coloration from dye ingestion (**Figure 3.4**b). During imaging, we examined the activity of

Figure 3.4: Continuous imaging of neural population dynamics before, during, and after ingestion. (a) Digital rendering of a fly being fed while neurons are recorded using a two-photon microscope. **(b)** Photo of an implanted animal after ingesting a high-concentration caffeine solution during two-photon microscopy. White arrowhead indicates purple coloration of the abdomen, confirming digestion of a caffeine-sucrose solution mixed with Amaranth dye. **(c)** Schematic of the ventral nerve cord indicating the imaging region in the neck connective. **(d)** Color-coded mean neural activity during all non-locomotor periods for a fly before feeding (same data as top panel in f) including annotations of individual axons passing through the neck connective (arrowheads). Asterisks indicate location of giant fiber axons. **(e)** Normalized fluorescence across all axons passing through the thoracic neck connective during four minute recordings either before (blue), during (green), soon after (orange), or long after (red) feeding. Flies were fed with a solution containing either only sucrose (**left**), sucrose and a low-dose (**middle**), or high-dose of caffeine (**right**). **(f)** Color-coded mean neural activity during all non-locomotor periods for a fly either before (**top**), immediately after (**middle**), or long after (**bottom**) ingestion of a high-concentration caffeine solution. **(g)** Statistical analysis indicating the presence of activity waves. Neural activity is normalized using parameters computed on pre-feeding activity (Methods). Maximum normalized activity is shown for three flies per condition before, during, and after feeding. Maximum activity is only significantly increased > 29min after feeding with a high concentration caffeine solution (one-sided Mann-Whitney-U tests, $*$ indicates $P < 0.05$, $P=0.04$ for both $*$ reported, ns indicates not significant). Source data are provided as a Source Data file. **(h)** The cervical connective in one implanted animal is segmented into four regions-of-interest (ROIs). These are overlaid onto a standard-deviation time-projection image. **(i)** Neural activity normalized to peak fluorescence during a wave of activity. Traces are color-coded as in panel h. The peak of mean fluorescence across all regions is centered on 0 s. **(j)** Pixel-wise time of peak activity. The peak of mean activity across the entire neck connective set as 0 s.

ascending and descending neurons whose axons pass through the cervical connective linking the brain and VNC. To do this, we performed coronal cross-section two-photon imaging of the thoracic cervical connective (**Figure 3.4**c)[95] in flies expressing the genetically encoded calcium indicator, GCaMP6f, as well as the anatomical marker, tdTomato, throughout the nervous system (*Act88F-Rpr/+; GMR57C10-Gal4/UAS-opGCaMP6f; UAS-tdTomato/+*). To overcome image deformation and translation occurring during animal behaviors, we registered imaging data using an optic flow-based algorithm (see Methods) [95]. After image registration, our coronal imaging data reveals the activity of axons belonging to descending neurons that drive actions [32, 81], and ascending neurons that convey ongoing behavioral states to the brain [48]. These axons are apparent as ellipses in our two-photon microscopy images (**Figure 3.4**d, white arrowheads). These pan-neuronal regions-of-interest (ROIs) are consistent with those we observed when imaging neural activity in very sparse sets of descending [95] and ascending [48] neurons. This is most apparent for the pair of large Giant Fiber descending neuron axons [227] that pass through the dorsal midline of the cervical connective (**Figure 3.4**d, white asterisks).

Across all three experimental conditions—before, during, and shortly after feeding—we observed fluctuations in neural activity that were associated with epochs of walking (**Figure 3.4**e, blue, green, and orange traces; **Figure S3.13**c, Fly 7 and **Videos** 3.10 to 3.12). However, more than 29 min after feeding, we observed large waves of activity uniquely in flies fed the high concentration caffeine solution (**Figure 3.4**e, red traces). Waves were much larger in amplitude than neural activity fluctuations associated with spontaneous locomotion. Activity waves spread across the entire connective (**Figure 3.4**f) and were associated with an overall rigid pose accompanied by micromovements (**Video** 3.13). To quantify the presence and amplitude of waves at different time points and between experimental conditions, we normalized neural activity across the cervical connective relative to that observed before feeding for each fly. We then computed the maximum normalized fluorescence (upper bound of the 99% percentile) for periods before, during and after feeding. Up to approximately 29 minutes after feeding, the maximum activity level of flies fed with a high concentration of caffeine was not significantly different from flies fed with sucrose, or a low caffeine solution (Mann-Whitney-U tests, $P > 0.05$). By contrast, between 29 and 38 minutes after feeding, the maximum activity of each fly fed with high caffeine solution was significantly higher than the other conditions (Mann-Whitney-U tests, $P = 0.040$), due to the wave of neural activity (**Figure 3.4**g). The temporal evolution of these waves was also reproducible: activity began in the dorsalmedial (blue), then dorsolateral (green), and then ventral (orange) connective. The Giant Fiber neurons (red)[227] were last to become active and sustained high activity for longer periods of time (**Figure 3.4**h-j and **Figure S3.13**d-i). These data illustrate that our long-term imaging toolkit can be used to investigate how food or drug ingestion influences internal states and global neural dynamics.

3.4   Discussion

Here we have described microengineered devices that open up the comprehensive and longitudinal investigation of motor control in behaving animals. Specifically, we enable long-term two-photon recordings of tissues in the adult *Drosophila* thorax including premotor/sensory and motor circuits targeting and residing within the VNC, respectively. Our toolkit is designed to address the unique challenges of long-term recording of the VNC as opposed to simpler approaches that enable longitudinal recordings of neurons in the brain [198, 199]: it consists of (i) a micromanipulator arm, (ii) a polymer-based soft implant for displacing thoracic organs, (iii) a numbered, transparent polymer window that can be fabricated in a reproducible manner to seal the thoracic opening, and (iv) a compliant tethering stage that permits gentle, repeated mounting around the thorax of animals for two-photon imaging. Together, these tools expand the neural recording time window from only a few hours [95] to more than one month, without markedly reducing the lifespan of implanted animals, or significantly perturbing their locomotor behavior. We have illustrated several use cases for our long-term imaging approach including (i) weeks-long recordings of neural morphology, pan-neuronal activity, and sparse neural activity, (ii) weeks-long degradation of limb sensory neuron projections to the VNC from an amputated limb, and (iii) global changes in neural activity following drug ingestion.

Our longevity experiments confirmed that the lifespans of implanted flies was similar to those of intact animals. The survival curves were, however, shifted for implanted and sham implanted flies due to excess mortality within the first few days following surgery. This suggests that those initial losses might be due to surgical handling and not specifically linked to implantation. Consistent with this, our studies of backward walking revealed no clear changes in locomotor metrics between control and implanted animals. However, in the future, it would be important to confirm the minimal impact of implantation on more complex behaviors like courtship and gap-crossing.

In a first case study of our toolkit, we investigated the anatomical degradation of chordotonal projections to the VNC over two weeks following leg amputation. There, we observed a marked degradation of mechanosensory neuron terminals in the first week following amputation. The time evolution of this degradation was heterogeneous across ROIs, consistent with the existence of distinct chordotonal cell populations [228] which may have varying levels of robustness to degradation. Alternatively, some terminals might arise via ascending projections from T2 (midleg) or T3 (hindleg) and thus are not directly affected by foreleg amputation. *Drosophila* has been previously used in numerous studies as a model of nerve injury [229], where it has been shown that axonal degradation following injury can be similar to Wallerian degeneration in mammals [230]. Thus, our long-term imaging toolkit might in the future be used to test for pharmacological interventions that can slow down or prevent injury-induced axonal degeneration in motor circuits.

When analyzing the activity of descending and ascending neurons in the thoracic cervical connective following caffeine ingestion, we did not observe large changes in neural activity in the low-concentration caffeine condition, despite previously reported behavioral changes [224]. On the other hand, we observed large waves of neural activity following ingestion of a high-concentration caffeine solution. Some flies had several of these waves, suggesting that they are not due to calcium release from a terminal cell death process. However, the origin of these calcium dynamics remains unclear. For example, caffeine has been shown to induce cytoplasmic release of internal stores of Ca^{2+} [231]. Although this may be unlikely in the case of caffeine ingestion, whether temporally propagating activity waves result from such a mechanism or profound neural firing remains unclear and could be the focus of future studies using these tools. Notably, we observed that animals did not recover after feeding on our high concentration caffeine solution. Nevertheless, this proof-of-concept illustrates how long-term imaging in *Drosophila* may be used in the future to screen for the impact of drug ingestion on neural dynamics in behaving animals.

Based on these successful case studies, we envision that our microengineered long-term imaging devices can be leveraged to study a variety of additional questions and challenges. For example, one might apply these devices to record the progression of cell death in *Drosophila* models of neuronal disorders like Parkinson's disease [232]. Our implant fabrication pipeline is also generalizable. Therefore, implant shapes could be adapted to address other experimental challenges including the targeting of abdominal ganglia circuits that regulate mating receptivity in females [233]. Furthermore, implants might be modified

to store and release active components that, for example, deliver compounds into the hemolymph in a controlled manner. Finally, additional steps might be taken to automate implantation by, for example, opening the thoracic cuticle using a UV-excimer laser [234], or developing robotic manipulation techniques to automatically displace thoracic organs, position the implant, and seal the thoracic hole with a window [235].

In summary, the technological developments presented in this work permit a variety of experiments on individual flies across a wide range of time scales, opening up an understanding of how biological systems—in particular premotor and motor circuits—change during aging or disease progression, following injury, learning, or social experiences, in response to shifts in internal state, or as a consequence of food or drug ingestion. These data, in turn, can inspire the development of more adaptive controllers for artificial systems that have the capacity to shift in form and function to accommodate continuously changing capabilities and needs.

3.5 Methods

3.5.1 Fabrication of thoracic windows with engraved numbers

Thoracic windows (transparent polymer disks) were fabricated using photolithography [236]. All exposure steps were performed on a mask aligner (MJB4 , Süss MicroTec, Germany) using i-line illumination. Chrome masks were fabricated using a direct laser writer (VPG-200, Heidelberg Instruments, Germany) and an automatic mask processor (HMR900, HamaTech, Germany). The dimensions of microfabricated structures were measured using an optical microscope (DM8000 M, Leica Microsystems, Switzerland) or a mechanical surface profiler (Dektak XT, Bruker Corporation, USA). The protocol began with treating the surface of a 4-inch silicon wafer with a plasma stripper (PVA TePla 300, PVA AG, Germany) at 500 W for 7 min to reduce its wettability. An aqueous solutions of 20% (wt/vol) Dextran (MP Biomedicals, MW 60k-90k g/mol) was spun at 1000 rpm (WS-650-23, Laurell Technologies Corporation, USA), and baked at 150 C for 2 mins to form a 1 μm thick water-soluble sacrificial layer. This layer permits windows to be gently released at the end of the fabrication process (**Figure S3.1**a-i). A negative photoresist (SU-8 3025, Kayaku Advanced Materials, USA) was directly spin-coated on the sacrificial layer and soft-baked (**Figure S3.1**a-ii). Notably, at this thickness, SU-8 has a transmittance of greater than 95% [237] (https://kayakuam.com/wp-content/uploads/2020/07/KAM-SU-8-3000-Datasheet-7.10-final.pdf). After exposure, the windows were post-baked and uncured resist was removed with a developer (Propylene glycol methyl ether acetate (PGMEA, 1-methoxy-2-propanol acetate), Sigma-Aldrich, Germany) (**Figure S3.1**a-iii). Next, the wafer with SU-8 windows was coated with a 20 μm thick layer of positive photoresist (AZ 40XT) using an automated processing system (ACS200 Gen3, Süss MicroTec, Germany). This extra layer of polymer serves as a physical mask during the metal deposition process. A second chrome mask was fabricated to pattern unique identifiers onto the windows using photolithography. Next, the wafer was coated with Ti and Au films

[238] using physical vapor deposition (EVA 760, Alliance-Concept, France) at a thickness of 3 nm and 15 nm, respectively (**Figure S3.1**a-iv). The development of the negative photoresist (Remover 1165, Kayaku Adv. Mat., USA) removed all the layers on top of the windows except for the numbers that serve as markers. Finally, the labelled windows were released by dissolving the sacrificial layer in DI water (**Figure S3.1**a-vi). The windows were filtered, dried at room temperature, and sterilized prior to use in experiments. The resulting windows were optically transparent (**Figure S3.1**b) and of the appropriate size to seal thoracic openings (**Figure S3.1**c).

3.5.2   Fabrication of polymer molds that are used to cast implants

We developed a two-level microfabrication technique to maximize throughput, protect master molds from excessive use, and facilitate technology dissemination [239, 240]. Briefly, implants were cast within elastomer templates that were fabricated from an etched wafer serving as a master mold. First, a four-inch silicon test wafer (100/P/SS/01-100, Siegert Wafer, Germany) was treated with hexamethyldisilazane (HMDS) (CAS number: 999-97-3, Sigma-Aldrich, Germany) and dehydrated at 125°C to enhance adhesion to its surface. The wafer was then spin-coated with an 8 µm thick film of positive photoresist (AZ 9260, Microchemicals GmbH, Germany) using an automatic resist processing system (EVG 150, EV Group, Germany)(**Figure S3.3**a-i). After baking, exposure, and development steps, the wafer was then processed using deep reactive ion etching (DRIE), specifically a Bosch process, [241] (AMS 200 SE, Alcatel) to obtain nearly vertical walls with a high aspect ratio (**Figure S3.3**a-ii). The remaining positive resist was stripped in a remover (Remover 1165, Kayaku Advanced Materials, USA) at 70°C and cleaned by rinsing with water and air drying (**Figure S3.3**a-iii). The elastomer templates were fabricated by replica molding using polydimethylsiloxane (PDMS). The replica molding process began with vapor deposition of silane (trichloro(1H,1H,2H,2H-perfluorooctyl) Silane, Sigma-Aldrich, Germany) onto the surface of the master mold in a vacuum chamber for 6 h. Silanizion was only performed once because it forms a permanent silane layer. PDMS was prepared as a mixture (10:1, wt/wt) of the elastomer and the curing agent (GMID number: 01673921, Dow Europe GmbH, Germany) and poured onto the wafer in a petri dish. To release any bubbles trapped inside the high aspect ratio wells, the mold was degassed using a vacuum pump (EV-A01-7, Swiss Vacuum Technologies SA, Switzerland) in a vacuum desiccator (F42020-0000, SP Bel-Art Labware & Apparatus, USA). Finally, the elastomer was cured at 65°C for 5 h in an oven (UF30, Memmert GmbH, Germany) and the PDMS slab was peeled off (**Figure S3.3**b). Using alignment markers as a guide, the slab was then cut into several pieces with a razor blade to serve as templates with which one could then fabricate implants (**Figure S3.3**c).

3.5.3   Fabrication of implants

Flexible implants were fabricated from a photocurable polymer (Ostemer 220, Mercene Labs AB, Sweden). Polymerization occurs when a mixture of two components (Part A and Part B) are exposed to UV light (**Figure S3.4**a-i). The PDMS template was silanized

(trichloro(1H,1H,2H,2H-perfluorooctyl) silane, Sigma-Aldrich, Germany) for 1 h in a vacuum desiccator (**Figure S3.4**a-ii). Part A was warmed at 48°C overnight to make sure there were no undissolved crystals remaining in the solution. Part B and the container were also heated up to 48°C before mixing. Parts A and B were then mixed thoroughly and the mixture was degassed in a vacuum chamber for 5 min. A 200 µL drop of the mixture (1.86:1, wt\wt) was poured onto the template (**Figure S3.4**a-iv) and the template was mechanically sandwiched between two glass slides using two clips. The glass slide touching the implant polymer was previously plasma treated (PDC-32G, Harrick Plasma,USA) at 29 W for 1 min to facilitate implant release by improving the adhesion between the glass and implants. The solution was exposed to UV light (365 nm, UV9W-21, Lightning Enterprises, USA) for 10 min for polymerization (**Figure S3.4**a-v). The samples were rotated several times during UV exposure to ensure a homogeneous reaction throughout the template. The implants were released by mechanically agitating the templates in isopropyl alcohol (IPA) using a sonicator (DT 100 H, Bandelin Sonorex Digitec, Germany)(**Figure S3.4**a-vi). This whole process yielded a wafer with 100 implants (**Figure S3.4**b,c) that were subsequently cut out using a razor blade prior to implantation.

3.5.4 Fabrication of a manipulator arm that temporarily displaces thoracic organs

We designed and constructed a manipulator arm to temporarily displace thoracic organs during implantation (**Figure S3.5**a,b). To construct the arm, we first 3D printed a mold that allowed us to glue a dissection pin (26002-10, Fine Science Tools, Germany) to the tip of a syringe needle (15391557, Fisher Scientific, USA) in a reproducible manner (**Figure S3.5**c). The pin is inserted into the needle until its tip touches the end of the mold. We glued the pin to the needle using a UV-curable adhesive (Bondic, Aurora, ON Canada). The arm was then bent using forceps and guided by a second 3D printed mold (**Figure S3.5**d). The pin was first bent coarsely and then adjusted more finely using the 3D printed mold. Another 3D printed piece was then used to connect the syringe needle to a 3-axis micromanipulator (DT12XYZ, ThorLabs, USA) and to an extension stage (**Figure S3.5**a). The whole structure was then attached to a breadboard (MB1224, ThorLabs, USA) (**Figure S3.5**b).

3.5.5 Fabrication of a remounting stage

We used direct laser writing [242] to fabricate a custom compliant mechanism that holds flies in place during two-photon microscopy. The mechanism was designed using 3D CAD software (SolidWorks 2021, Dassault Systèmes, France). A 25 mm x 25 mm diced silicon wafer was used as the substrate upon which structures were printed. The surface of the substrate was plasma treated at 500 W for 7 min and coated with an aqueous solution of 10% (wt/vol) Poly(acrylic acid) (MW 50000, Polysciences, USA) at 2000 rpm for 15 s using a spin-coater (WS-650-23, Laurell Technologies Corporation, USA) (**Figure S3.6**a-i-iii). The mechanism was fabricated using a direct laser writer (Photonic Professional GT+,

Nanoscribe GmbH, Germany) that controls two-photon polymerization (**Figure S3.6**a-iv). A polymer (IP-S, Nanoscribe GmbH, Germany) was chosen as the print material due to its Young's modulus of 4.6 GPa [243] and the resolution at which structures could be printed. The overall design was segmented into multiple frames because the maximum laser scan area provided by a 25X objective (NA 0.8, Zeiss) is 400 µm. This approach results in fine printing over a relatively large layout. The objective was dipped into liquid photoresist during printing. At the end of the printing process, the uncured polymer was removed using a developer (PGMEA, Sigma-Aldrich, Germany) for 20 min (**Figure S3.6**a-v). Finally, the PGMEA was rinsed using IPA. The mechanism was released from the substrate by dissolving the sacrificial layer in DI water (**Figure S3.6**a-vi). This yielded a microfabricated structure large enough to contain the thorax of the fly (**Figure S3.6**b,c). The remounting stage was completed by attaching the mechanism onto a laser-cut aluminum frame using UV-curable glue (Bondic, Aurora, ON Canada).

The materials and equipments required to fabricate our microengineered devices are summarized in Table 3.3 and Table 3.4.

3.5.6   Implantation procedure

The steps required to prepare flies for long-term VNC imaging are described here. See **Video** 3.2 for more details.

Tethering flies onto the dissection stage

A fly was cold anesthetized for 5 min. Then it was positioned onto the underside of a dissection stage and its wings were removed near their base using forceps. The thorax was then pressed through a hole (Etchit, Buffalo, MN) in the stage's steel shim (McMaster-Carr, USA; 0.001" Stainless Steel, type 316 soft annealed; Part #2317K11). Afterwards, the stage was turned upside down and a tiny drop of UV-curable glue (Bondic, Aurora, ON Canada) was placed onto the scutellum, to fix the fly in place.

Opening the thoracic cuticle

The stage was filled with saline solution (Table 3.2). A 30 G syringe needle was then used to cut a small rectangular hole (smaller than the 600 µm diameter window) into the dorsal thoracic cuticle. The hole was made by inserting the needle into the posterior thorax close to the scutellum. Then three lines were cut into the lateral and anterior thorax. A final line was cut to complete a rectangular opening. The resulting piece of cuticle was then removed using forceps.

Clearing out thoracic tissues

Residual degraded IFMs were removed from the opened thorax using forceps. Then, a pulled (P-1000, Sutter instrument, USA) glass needle (30-0018, Harvard Apparatus, USA) was used to detach small tracheal links between a large piece of trachea and the left side of the gut. The left salivary gland was then also removed using forceps.

Displacing thoracic organs using the manipulator arm

The manipulator arm was positioned on top of the stage with its tip visible. The dissection stage was positioned with the fly's head pointing toward the experimenter. The arm tip was then inserted into the thorax using a 3-axis manipulator (DT12XYZ, ThorLabs, USA). The tip of the arm was then inserted to the (experimenter's) right side of the gut near the middle of the proventriculus. The tip was inserted deep enough to be below the crop and salivary glands but not to touch the VNC. Once the tip of the arm was on the right side of the salivary gland, crop, and gut, it was pulled towards the left side of the thoracic cavity, making a space for the closed implant.

Positioning the implant

Once the flies' organs were held securely onto the left side of the thoracic cavity by the manipulation arm, the implant was closed in the air using forceps and then transferred into the saline solution filling the dissection stage. The closed implant was then positioned in front of the fly on the stage. A thinner pair of forceps was next used to insert the implant into the animal's thorax. Finally, a glass needle was used to adjust the location of the implant and to keep it at the appropriate height, allowing it to open passively. Once open, the glass needle was used to gently press the left side of the implant towards the bottom of the thorax while the arm was removed, and to remove any bubbles on the implant.

Sealing the thoracic hole with a numbered, transparent window

Once the implant was well positioned, a syringe needle (15391557, Fisher Scientific, USA) was used to remove saline solution from the stage. A window was then positioned on top of the cuticular hole and centered with the identification number on the posterior of the thorax, near the scutellum. A wire was then used to add tiny drops of UV curable glue between the window and the surrounding thoracic cuticle, beginning from the right side of the scutellum and finishing on the left side. Saline solution was then added back to the stage. The cured UV glue, previously tethering the fly to the stage, was removed using a needle. The saline solution was then also removed and the window was fully sealed by placing and curing UV glue onto the fly's posterior cuticle near the scutellum.

Dismounting flies from the dissection stage

Once the thoracic hole was fully sealed by a transparent window, the fly was dismounted from the dissection stage by gently pushing the front of the thorax through the hole in the steel shim. The fly was then returned to a vial of food to recover.

3.5.7   Drosophila melanogaster experiments

All flies were raised on standard cornmeal food on a 12h light:12h dark cycle. Experiments for each particular study were performed at a consistent time of day to exclude the possibility of circadian-related confounding factors. No specific ethical approval is required for *Drosophila* experiments in Switzerland. For most experiments, female flies were used because they are larger in size. This increases the ease of dissection, implantation, and tethering. It also facilitates computational image processing and neural region-of-interest detection.

3.5.8   Long-term study of survival and locomotion

Female flies expressing CsChrimson in Moonwalker Descending Neurons (MDNs) [86](*UAS-CsChrimson / Act88F-Rpr; VT50660.p65AD(attp40) /+; VT44845.Gal4DBD(attp2) /+*)(**Figure 3.2**) were implanted at five days-post-eclosion (dpe). For this experiment, before implantation, implants were dipped in a 30 mg/ml dextran solution (#31392, Sigma-Aldrich, Switzerland) while mechanically closed. Implants were then taken out of the solution and dried using a twisted Kimwipe (5511, Kimberly-Clark, USA). This step was performed to fix implants in a closed position. However, we later discovered that dextran is not required to close implants and we removed this step. Implants were then positioned in the fly's thorax as described above. The number of days following implantation is denoted as 'days-post-implantation' (dpi). Age and gender-matched control animals were selected from the same parental cross. For longevity studies, flies were housed individually in food vials and assessed every 1-2 days.

Studies of locomotion were performed at 1-3 dpi, 14-16 dpi, and 28-30 dpi. Animals were individually cold-anaesthetized and then transferred to rounded square arenas for optogenetic activation and video recording. Each recording consisted of 30 s of spontaneously generated behaviors (primarily walking and grooming), followed by three 3 s periods of optogenetic stimulation at 590 nm (6 mW / cm^2) with 10 s interstimulus intervals. Therefore, each recording session was 59 s long.

To process video data, flies' centroids were tracked using a customized version of Track-tor [244]. Their orientations were then extracted using a neural network (implemented in PyTorch [245]) that was trained on hand-labeled data. The network consisted of two convolutional layers followed by three fully connected layers. All layers, except for the final one, were followed by a ReLU activation function [246]. We also applied dropout after the first two fully connected layers with 0.2 probability [247]. To train the network, we

hand annotated a total of 300 samples in three orientations (head up, head down, and sideways). The grayscale images were then cropped using Tracktor centroid locations and resized to 32×32 pixels. During training, we randomly applied affine transformations (20 degrees of rotation, 5 pixels of translation, and 0.2 scaling factor), horizontal, and vertical flip augmentations with a 0.5 probability. We used PyTorch's torchvision package for all data augmentation. The network was trained with cross-entropy loss using 80% of the data. We used an Adam optimizer with a learning rate of 0.001, without weight decay and learning rate drop [248]. We trained for 1000 epochs and selected the weights with the best test error.

Translational velocities were computed by applying a second order Savitzky-Golay filter with a first-order derivative to centroid positions. The sign for the velocity values was set to negative for movements counter to the animal's heading direction. Flies that collided with the arena's walls for more than 0.3 s during the stimulation period were excluded from analysis. Flies that were dorsally flipped (i.e., walking on the sigma-coated ceiling) during the stimulation period were also excluded from analysis. The 'Backward walking response slope' metric was calculated as the acceleration from the beginning of each stimulation period to the minimum velocity (maximum backward speed) reached on that period. The 'Backward walking distance traveled' metric was computed as the left Riemann sum of the velocity curves during each stimulation period. We only considered frames where the velocity was negative. Finally, the 'Maximum negative translational velocity' is the minimum velocity value reached on each stimulation period.

For studies of male survival and behavior, animals expressing Reaper in their indirect flight muscles (*Act88F-Rpr; UAS-GFP; +/+*) were implanted at 1 day-post-eclosion (dpe). Age and gender-matched control ('Intact') animals were selected from the same parental cross. Flies were housed individually in food vials and flipped every day into a new food vial while assessing their longevity (**Figure S3.10**). Spontaneous behavior was recorded for three males per group. These males were individually cold-anaesthetized and then transferred to rounded square arenas for video recordings. Each recording consists of 60 s of spontaneously generated behaviors.

3.5.9 Long-term pan-neuronal anatomical imaging in the VNC

Female flies expressing GFP throughout the nervous system (*Act88F-Rpr/+; GMR57C10-Gal4/UAS-GFP; +/+*) (**Figure 3.1**h) were implanted at 4-6 dpe and kept individually in food vials. At 1-3 dpi, 14-16 dpi, and 28-30 dpi, flies were tethered onto a remounting stage and 25 imaging volumes of 100 μm depth (1 μm stepsize) were acquired using a two-photon microscope (Bergamo II microscope, ThorLabs, USA) and a 930 nm laser (MaiTai DeepSee, Newport Spectra-Physics, USA) with 20 mW of power at the sample location. We acquired 0.1 volumes-per-second (vps) using a Galvo-Resonance scanner [95]. The 25 images per depth were then registered to one another using the HyperStackReg module in Fiji [249] and a rigid body transformation. These registered images were next projected along the time axis into one standard deviation image. The resulting volume was then depth color-coded using Fiji's Temporal-Color macro.

For experiments in male flies, we imaged animals expressing GFP throughout the nervous system (*Act88F-Rpr; GMR57C10-Gal4/UAS-GFP; +/+*) (**Figure S3.10**). These animals were implanted at 1 dpe and kept individually in food vials. At 1 dpi, 5 dpi, and 10 dpi, flies were tethered and a volumetric recording of the VNC was performed using a two-photon microscope at 930 nm with 11 mW of laser power. Flies were anesthetized using carbon dioxide (1.3l/min) applied ventrally while recording imaging volumes. Volumes consisted of 512x512 pixel frames taken every 1 µm over a total depth of 100 µm. Z-projections were then generated with depth color-coding using Fiji's 'Temporal-Color' macro.

3.5.10   Long-term pan-neuronal functional recording in the VNC

Flies expressing GCaMP6f and tdTomato throughout the nervous system (*Act88F-Rpr/+; GMR57C10-Gal4/UAS-GCaMP6f; UAS-tdTomato/+*) were implanted at 5 dpe (female), or 1 dpe (male) and then mounted onto the two-photon imaging stage at 1, 5 and 10 dpi (Female, **Video** 3.4; male, **Video** 3.5). One horizontal imaging plane of the prothoracic neuromere was acquired using a two-photon microscope at 930 nm with 25 mW of power. Three horizontal z-plane images were acquired using a Galvo-Resonance scanner and averaged into one frame at an imaging rate of 10.7 fps. Behavior frames were acquired simultaneously (as in [95]) at a rate of 80 fps.

3.5.11   Long-term sparse functional recording in the VNC

A female fly expressing GCaMP6f and tdTomato in DNa01 descending neurons [32, 95](*Act88F-Rpr/+; GMR22C05-AD-spGal4/UAS-GCaMP6f; GMR56G08-DBD-spGal4 / UAS-tdTomato*) was implanted at 3 dpe. The same fly was then mounted onto the two-photon microscope stage at 1, 3 and 5 dpi. One horizontal imaging plane of the prothoracic neuromere was acquired using a two-photon microscope at 930 nm with 28 mW of laser power. Horizontal plane images were acquired using a Galvo-Galvo scanner at an imaging rate of 5.6 fps. Behavior frames were acquired simultaneously (as in [95]) at a rate of 80 fps. AxoID was used to detect the neurons as regions-of-interest (ROIs) in two-photon microscope images and extract their fluorescence values [48]. The semi-automated neural fluorescence event classifier described in [48] was used to detect neural activity events from fluorescence traces. These were then correlated to spherical treadmill rotations.

3.5.12   Modifying the implant to image the VNC T2 and T3 neuromeres

To illustrate how other implant designs could be used to gain optical access to posterior regions of the VNC (**Figure S3.9**), a female fly expressing GFP throughout the nervous system (*Act88F-Rpr/+; GMR57C10-Gal4/UAS-GCaMP6f; UAS-tdTomato/+*) was dissected at 3 dpe. A drop of UV glue was cured onto the tip of an implant. Implantation was also slightly modified: once inserted in the fly's thorax, the implant was pushed posterior with the cured glue resting against the interior cuticle of the scutellum, fixing the implant

into position. The fly was then closed using a transparent window. An imaging volume (576x576 pixels and 100 μm deep) of the VNC was recorded using a two-photon microscope with a Galvo-Galvo scanner at 930 nm with 22 mW of laser power.

3.5.13 Long-term study of chordotonal organ degradation in the VNC following leg amputation

Female flies expressing GFP in their chordotonal organs (*Act88F-Rpr/+; iav-Gal4/UAS-GFP; +/+*) (**Figure 3.3**) were implanted at 1 dpe. A z-stack of the VNC was recorded at 1 dpi, using a two-photon microscope at 930 nm with 55 mW of laser power. Flies were anesthetized with carbon dioxide (1.8l/min) supplied ventrally while recording z-stacks. Z-stacks consisted of 576x384 pixel frames taken every 1 μm over a total depth of 100 μm (i.e., 100 frames per volume). The front left leg was then removed at the thorax-coxa joint using dissection scissors (#15300-00, Fine Science Tools, Germany). A second z-stack was then immediately recorded. Flies were kept individually in food vials and imaged every day using the same recording parameters until 15 dpi. Fiji's linear stack alignment with the SIFT registration plugin [250] was then used to register all the projected z-stacks to the first z-stack. A custom Python script was then used to draw and extract the mean fluorescence of specific regions of interest. Mean fluorescence within these regions were measured for each day and normalized across animals by dividing them by the mean fluorescence on the first day.

Flies' nervous systems were dissected and fixed with paraformaldehyde (441244, Sigma-Aldrich, USA) at 20 dpi. Samples were stained against nc82 with mouse anti-nc82 primary antibody diluted at 1:20 in PBST solution and then followed by goat anti-mouse Alexa 633 conjugated secondary antibody diluted at 1:500 (detailed procedure described in [95]). This allowed us to acquire confocal images that included both neuropil landmarks and endogenous GFP expression. Zen 2011 14.0 software was used to acquire confocal images. Confocal laser intensities and PMT gains were manually selected to avoid pixel saturation. These confocal z-stacks were then projected into 2D using Fiji's standard deviation projection. The standard deviation projection of GFP expression is shown as an inverted image (**Figure 3.3**c,d). A custom python script was written to detect the VNC's boundaries using the standard deviation projection of nc82 images. This contour was detected using the Open CV library and then drawn onto GFP standard deviation projection images.

3.5.14 Recording neural population activity before, during, and after feeding

Female flies (5 dpe) expressing a calcium indicator, GCaMP6f, and an anatomical marker, td-Tomato, throughout the nervous system (*Act88F-Rpr/+; GMR57C10-Gal4/UAS-GCaMP6f; UAS-tdTomato/+*) (**Figure 3.4**) were starved for 21-23 h on a wet Kimwipe (5511, Kimberly-Clark, USA). They were then implanted without a thoracic window, and kept on the dissection stage (the remounting stage was not used here) to limit the number of interventions. Animals were then positioned under a two-photon microscope where they

could walk on a spherical treadmill consisting of an air-supported (0.8 L/min) foam ball (Last-A-Foam FR7106, General Plastics, USA) with a diameter of 1cm [48]. Coronal cross-sections of their cervical connective were then imaged at 930 nm with a laser power of 15 mW. We achieved a 16 frames-per-second (fps) imaging rate by using a Galvo-Resonance scanner. In parallel, the behavior of the flies was recorded using seven cameras at 80 fps. Ball rotations were also measured along three axes using two optic flow sensors [95, 186]. We recorded neural activity and behavior in trials of approximately four minutes each. First, four trials were recorded. Then, the foam ball was lowered and recording continued while flies fed on a solution consisting of either (i) 1 ml deionized water, 8 mg of sucrose (A2188.1000, Axon Lab, Switzerland) and 1 mg of Amaranth dye (A1016, Sigma-Aldrich, USA), (ii) a low concentration caffeine solution consisting of 1 ml deionized water, 8 mg caffeine (C0750, Sigma-Aldrich, USA), 8 mg of sucrose and 1mg of Amaranth, or (iii) a high concentration supersaturated caffeine solution consisting of 1 ml deionized water, 40 mg caffeine, 8 mg of sucrose and 1mg of Amaranth. Animals were fed using a pulled glass needle (P-1000, Sutter instrument, USA; puller parameters- Heat: 502; Pull:30; Velocity: 120; Time: 200; Pressure: 200). A tiny drop of UV curable glue (Bondic, Aurora, ON Canada) was added near the tip of the needle to prevent the solution from travelling up on the needle. The needle was positioned in front of the flies using a manipulator (uMp-3, Sensapex, Finland). After feeding, the spherical treadmill was repositioned below the fly and eight more imaging trials were acquired.

Motion correction of two-photon imaging data

We used custom Python code unless otherwise indicated. For all image analysis, the y-axis is ventral-dorsal along the fly's body, and the x-axis is medial-lateral. Image and filter kernel sizes are specified as (y, x) in units of pixels. Recordings from the thoracic cervical connective suffer from large inter-frame motion including large translations, as well as smaller, non-affine deformations. Because calcium indicators (e.g., GCaMP6f) are designed to have low baseline fluorescence, they are challenging to use for motion correction. Therefore, we relied on signals from the co-expressed red fluorescent protein, tdTomato, to register both the red (tdTomato) and the green (GCaMP6f) PMT channel images. First, we performed center-of-mass (COM) registration of each recorded frame to remove large translations and cropped the background regions around the neck connective (from 480x736 to 352x576). Then, we computed the motion field of each red frame relative to the first recorded frame using optic flow and corrected both red and green frames for the motion using bi-linear interpolation. The algorithm for optic flow motion correction was previously described in [95]. We only used the optic flow component to compute the motion fields and omitted the feature matching constraint. We regularized the gradient of the motion field to promote smoothness ($\lambda = 800$). Python code for the optic flow motion correction (ofco) package can be found at https://github.com/NeLy-EPFL/ofco.

Correction for uneven illumination

We observed that absolute fluorescence values were slightly lower on the right side of the
connective than the left side, likely due to scattering by thoracic organs that are pushed to
the right by the implant. To correct for this uneven absolute fluorescence, we computed
the mean of all motion corrected frames across time. We then median filtered and low-pass
filtered the resulting image (median filter: (71,91), Gaussian filter: $\sigma = 3$) to remove
the features of individual neurons and retain only global, spatial changes in fluorescence.
We then computed the mean across the y axis to obtain a fluorescence profile in the x
(left - right) axis and fit a straight line to the most central 200 pixels. To correct for the
decrease in fluorescence towards the right side, we multiplied the fluorescence with the
inverse value of this straight line fit to the x-axis profile. Note that this correction only aids
in the visualisation of fluorescence, and does not have any impact on the computation of
$\Delta F/F$ because, for a given pixel, both the fluorescence at each time point, and its baseline
fluorescence are multiplied by the same constant factor.

Denoising calcium imaging data

To denoise registered and corrected data, we used an adapted version of the DeepInter-
polation algorithm [185]. Briefly, DeepInterpolation uses a neuronal network to denoise
a microscopy image by "interpolating" it from temporally adjacent frames. A U-Net is
trained in an unsupervised manner using 30 frames (around 2s) before and 30 frames after
the target frame as an input and the current frame as an output. Thus, independent
noise is removed from the image and components that dynamically evolve across time are
retained. We modified the training procedure to fit one batch into the 11GB RAM of a
Nvidia GTX 2080TI graphics card: rather than use the entire frame (352x576 pixels), we
used a subset of the image (352x288 pixels) during training. We randomly selected the x
coordinate of the subset. During inference, we used the entire image. We verified that using
different images sizes during training and inference did not change the resulting denoised
image outside of border regions. We trained one model for each fly using 2000 randomly
selected frames from one of the trials before feeding and applied it to all of subsequent
frames. Training parameters are outlined in Table 3.1. The adapted DeepInterpolation
algorithm can be found on the "adapttoR57C10" branch of the following GitHub repository:
https://github.com/NeLy-EPFL/deepinterpolation

Generating $\Delta F/F$ videos

We show fluorescence values as $\Delta F/F$ (**Videos** 3.10 to 3.12). This was computed as
$\Delta F/F = \frac{F - F_0}{F_0}$, where F is the time varying fluorescence and F_0 is the pixel-wise fluorescence
baseline. To compute F_0, we applied a spatial Gaussian filter ($\sigma = 10$) to images and
convolved each pixel with a temporal window of 10 samples (around 0.6s). We then
identified the minimum fluorescence of each pixel across all trials.

Table 3.1: Training parameters for DeepInterpolation.

Parameter	Value
Number of training frames	2000
Number of frames pre/post current frames	30
Omission of frames pre/post current frame	0
Number of iterations through training data	1
Learning rate	0.0001
Learning decay	0
Batch size	4
Steps per epoch	5
Number of GPUs	1
Number of workers	16

Optic flow processing and classification of stationary periods

Optic flow sensors have been used to measure spherical treadmill rotations [95, 186] but they are inherently noisy. Therefore, we computed the moving average across 80 samples (around 200ms). From preprocessed sensor values, we computed the forward, sideways and turning velocities [186]. We classified stationary periods (no movements of the ball) as periods when the absolute optic flow values of spherical treadmill rotation velocities were below a threshold of $0.31 \mathrm{m\,s^{-1}} \cong 0.01$ rotations/s and at least 75% of the frames within the time ± 0.5s of the sample were below this threshold. The latter criterion ensured that short stationary periods between bouts of walking would be excluded.

Synchronisation of two-photon, optic flow, and camera data

We recorded three different data modalities at three different sampling frequencies: two-photon imaging data was recorded at approximately 16Hz, behavioral images from seven cameras were acquired at 80Hz, and ball movements using two optical flow sensors were measured at nearly 400Hz. Therefore, to synchronise these measurements for further analysis, we down-sampled all measurements to the two-photon imaging frame rate by averaging all behavioral and ball rotation samples acquired during one two-photon frame.

Data analysis for caffeine ingestion experiment

To compute normalized fluorescence traces for each trial—as shown in **Figure 3.4**e—we averaged the fluorescence across the entire cervical connective and computed the 99% percentile of this time series during trials before feeding. We then normalized the time series of all trials recorded from that fly to the 99% pre-feeding percentile. To perform statistical analysis, we used normalized fluorescence and computed the maximum (upper boundary of the 99% percentile) within certain time periods before, during, and after feeding. Before feeding, the maximum normalized fluorescence is unity for each of the 9 flies, as expected

from the percentile normalisation. For periods during, $< 9min$ after, < 19 min after, < 29 min after, and < 38 min after feeding, we performed Mann-Whitney-U tests to determine whether the maximal neural activity after high caffeine ingestion was significantly different from the maximal activity after sucrose, or low caffeine ingestion (**Figure 3.4**G). Aiming to apply the least amount or pre-processing necessary, until this point, we used fluorescence data that was not denoised using DeepInterpolation. However, in this case, to analyze the precise timing of the waves, we applied DeepInterpolation as described above. This reduces background fluorescence and high frequency noise. To analyze the temporal progression of fluorescence waves, we first identified the time of peak fluorescence across the entire cervical connective T_{peak}. All times are given relative to the time of that peak permitting an analysis of precise timing differences. We then computed the mean fluorescence across time within manually selected regions of interest (dorsal, lateral, and ventral connective, as well as giant fiber neurons) and represent them normalised to their minimum and maximum values. We smoothed the time series with a Gaussian filter ($\sigma = 3 \widehat{=} 0.18$s). To identify the peak time for each pixel, we applied a temporal Gaussian filter ($\sigma = 10 \widehat{=} 0.62$s) and spatial Gaussian filter ($\sigma = 1$) and searched for the maximum fluorescence value within $T_{peak} \pm 10$s. In **Figure 3.4**f we show the mean fluorescence during periods when the fly was stationary (i.e., not moving the ball).

3.6   Supplementary Tables

Table 3.2: Saline solution

Chemical	mM
NaCl	103
KCl	3
NaHCO3	26
NaH2PO4	1
CaCl2 (1M)	4
MgCl2 (1M)	4
Trehalose	10
TES	5
Glucose	10
Sucrose	2

Table 3.3: Main materials for long-term imaging tool fabrication

Device	Material	Part number	Company
Implant	Silicon Wafer	100/P/SS/01-100	Sigert Wafer, Germany
	HMDS	999-97-3	Sigma Aldrich, Germany
	Positive resist	AZ9260	Microchemicals GmbH, Germany
	Remover	Remover1165	Kayaku Advanced Materials, USA
	Silane	448931	Sigma Aldrich, Germany
	PDMS	01673921	Dow Europe GmbH, Germany
	Polymer	Ostemer 220	Mercene Labs AB, Sweden
Window	Silicon Wafer	100/P/SS/01-100	Sigert Wafer, Germany
	Dextran	205195	MP Biomedicals, USA
	Negative resist	SU8-3025	Kayaku Advanced Materials, USA
	Developer	PGMEA	Sigma Aldrich, Germany
	Positive resist	AZ40XT	Microchemicals GmbH, Germany
	Remover	Remover1165	Kayaku Advanced Materials, USA
Remounting stage	Silicon Wafer	100/P/SS/01-100	Sigert Wafer, Germany
	Poly(Acrylic acid)	9003-01-4	Polysciences, USA
	Polymer	IP-S	Nanoscribe GmbH, Germany
	Developer	PGMEA	Sigma Aldrich, Germany
	Glue	Bondic glue	Bondic, Aurora, Canada
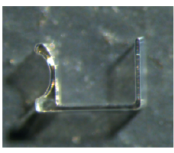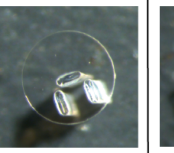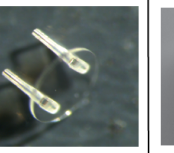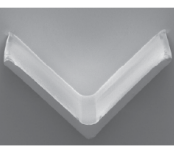
Table 3.4: Main equipment for long-term imaging tool fabrication

Device	Equipment	Part number	Company
Implant	Resist processing system	EVG 150	EV Group, Germany
	Etcher	AMS 200 SE	Alcatel, France
	Vacuum Pump	EV-A01-7	Swiss Vacuum Tech. SA, Switzerland
	Vacuum desiccator	F42020-0000, SP	Bel-Art, USA
	Oven	UF30	Memmert GmbH, Germany
	Plasma Cleaner	PDC-32G	Harrick Plasma, USA
	UV Light	UV9W-21	Lightning Enterprise, USA
	Sonicator	DT 100 H	Bandelin Sonorex Digitec, Germany
Window	Mask aligner	MJB4	Süss MicroTec, Germany
	Direct laser writer	VPG-200	Heidelberg Instruments, Germany
	Automatic mask processor	HMR900	HamaTech, Germany
	Optical microscope	DM8000 M	Leica Microsystems, Switzerland
	Mechanical surface profiler	Dektak XT	Bruker Corporation, USA
	Plasma stripper	PVA TePla 300	PVA AG, Germany
	Spin coater	WS-650-23	Laurell Technologies Corporation, USA
	Automated processing system	ACS200 Gen3	Süss MicroTec, Germany
	Vacuum Evaporation Machine	EVA 760	Alliance-Concept, France
Remounting stage	CAD Software	SolidWorks 2021	Dassault Systèmes, France
	Plasma stripper	PVA TePla 300	PVA AG, Germany
	Spin coater	WS-650-23	Laurell Technologies Corporation, USA
	3D writer	Photonic Professional GT+	Nanoscribe GmbH, Germany

3.7   Supplementary Figures
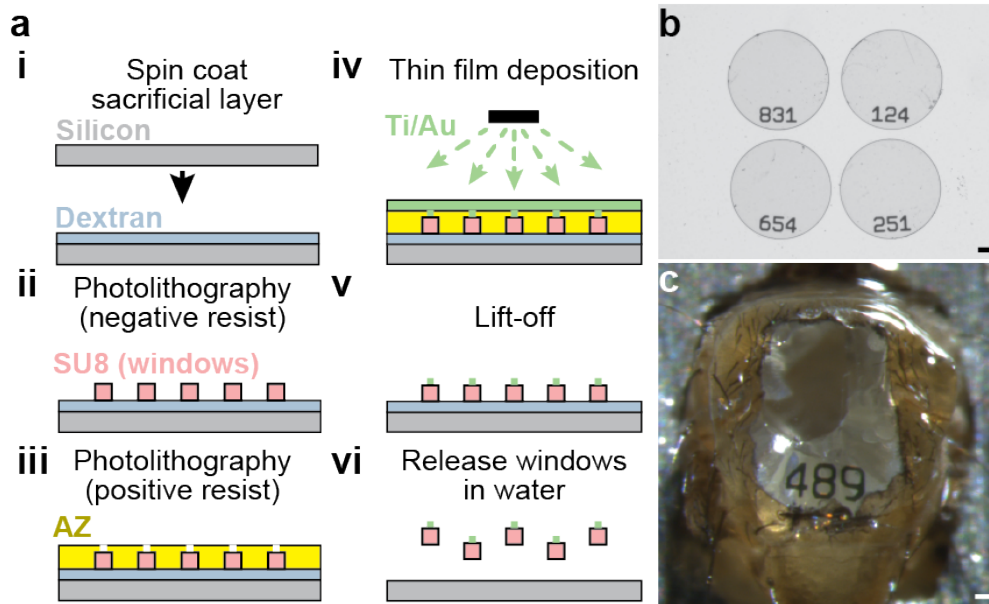
Supplementary Figure S3.1: Fabrication of numbered, optically transparent thoracic windows. **(a)** Thoracic windows are fabricated by performing the following steps. **(i)** A sacrificial layer of dextran is spin-coated onto a silicon wafer. **(ii)** SU-8 windows are structured onto the sacrificial layer, using photolithography. **(iii)** A positive resist, AZ, is cross-linked to mark number openings. **(iv)** Ti/Au is vapor deposited. **(v)** The AZ layer is lifted off. **(vi)** Finally, the numbered windows are released in water. **(b)** This process yields transparent SU-8 windows with thin Ti/Au numbers. Scale bar is 100 μm. **(c)** A window on an implanted animal, permitting a view of thoracic organs and tracking of this animal's identity. Scale bar is 50 μm.

Iteration (#)	1	2	3	4	Final
Implant					
CAD drawing					
Implant type	Rigid	Rigid	Rigid	Rigid	Flexible
Survival rate	Low	Low	Low	2%	73%

Supplementary Figure S3.2: Design iterations of implants used to displace thoracic tissues and enable long-term VNC imaging. Early designs were rigid (SU-8 based), with an open shape used to protect imaging regions of interest from invading tissues (iterations 1 and 2). Later rigid designs combined the thoracic window with protective pillars (iterations 3 and 4). All of these early iterations yielded single-digit survival rates. A major breakthrough was in the fabrication of compliant (Polymer-based) V-shaped implants. Through iterative testing of V-shaped implant sizes and angles that displace but do not squeeze internal organs, we converged upon the reported solution (iteration 'Final') with a high survival rate.
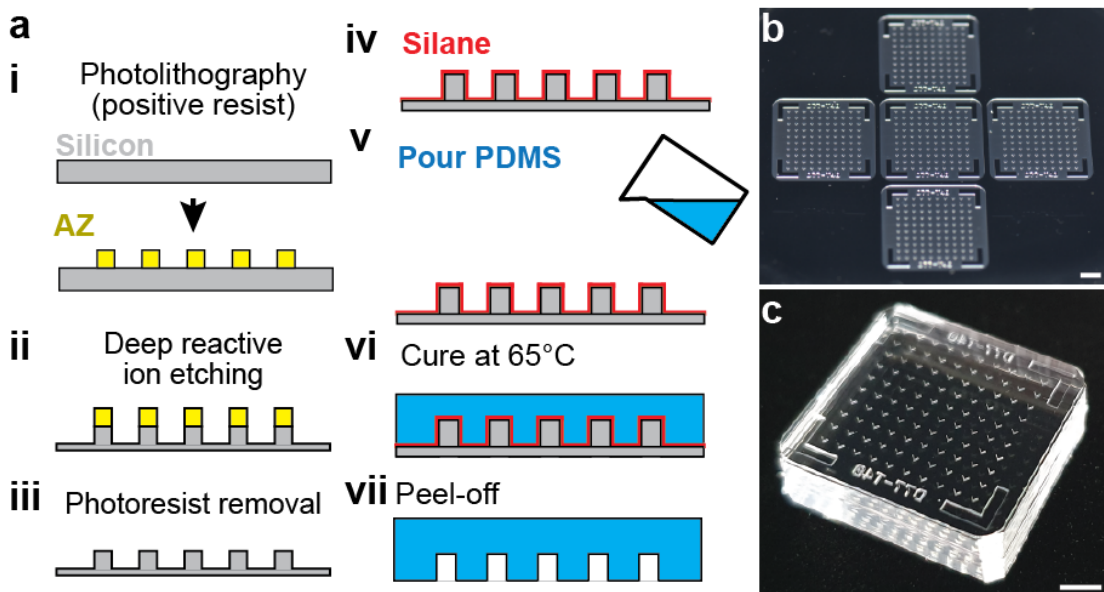
Supplementary Figure S3.3: Fabrication of molds used to cast implants. (a) Implant molds are fabricated by performing the following steps. **(i)** Through photolithography, a positive resist, AZ, is cross-linked onto a silicon wafer to form a temporary mask. **(ii)** Deep reactive ion etching is used to sculpt the silicon wafer. **(iii)** The photoresist is removed. **(iv)** Subsequently, this silicon piece is silanized. **(v)** PDMS is then poured, **(vi)** cured, and **(vii)** peeled off. **(b)** This process yields a single large piece. Scale bar is 0.5 cm. **(c)** This large piece is cut into five individual implant molds. Scale bar is 0.5 cm.
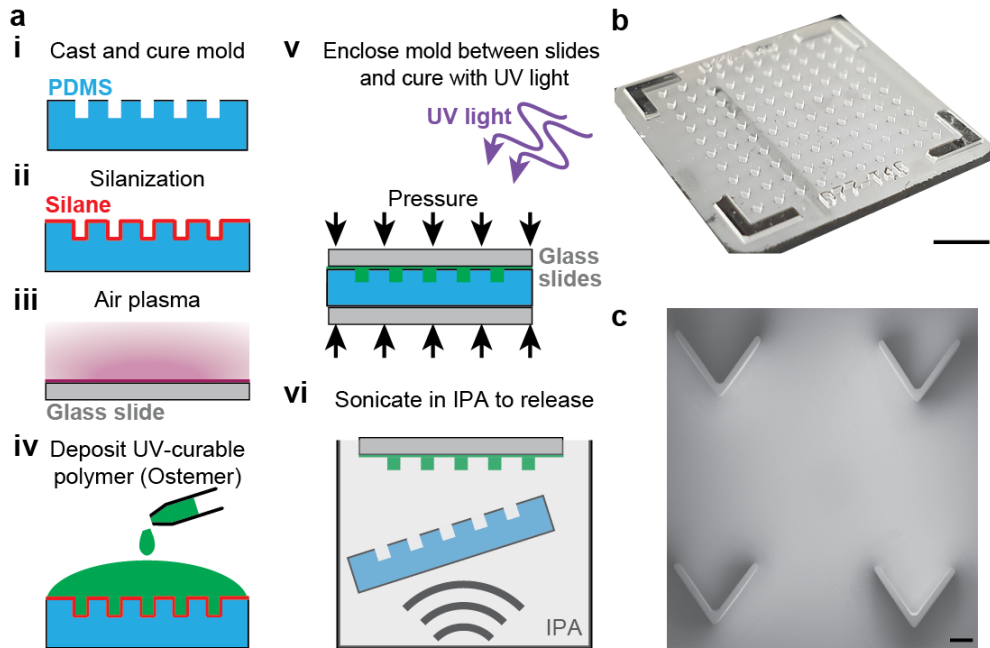
Supplementary Figure S3.4: Fabrication of implants. (a) Implants are fabricated by performing the following steps. **(i)** PDMS molds are cast, cured, and cut into pieces. **(ii)** PDMS molds are silanized. **(iii)** A glass slide is plasma treated to promote adhesion. **(iv)** A UV curable polymer is deposited onto the PDMS mold. **(v)** This composite is sandwiched between glass slides and exposed to UV light. **(vi)** The mold is sonicated to release in IPA. **(b)** This high-throughput process yields 100 implants in a single mold. Scale bar is 0.5 cm. **(c)** A scanning electron microscopy image confirms the precision of implant fabrication. Scale bar is 200 μm.
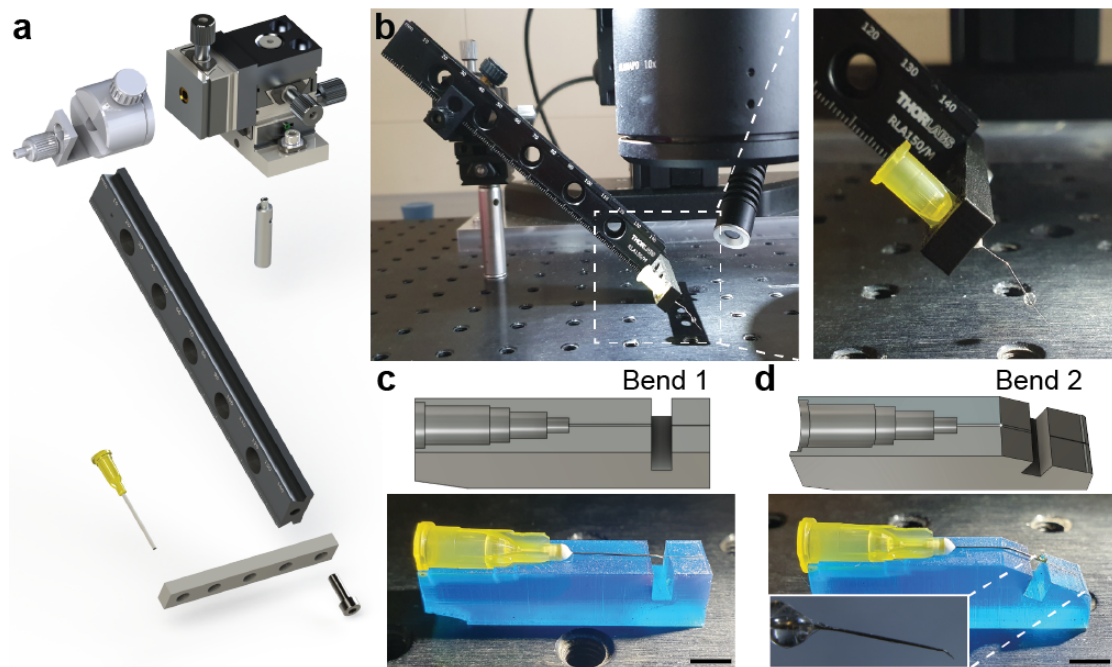
Supplementary Figure S3.5: Fabrication of a manipulator arm to temporarily displace thoracic organs. (a) Exploded view of the manipulator arm and its component parts. **(b)** (**left**) View of the manipulator arm mounted near the dissection microscope. (**right**) Zoomed in view of the inset (dashed white lines) highlighting the bent needle tip. **(c)** 3D printed piece used to guide gluing of the pin to the syringe needle. Scale bar is 0.5 cm. **(d)** 3D printed piece used to guide bending the manipulator arm tip. Inset shows a zoomed-in view of the arm's tip.

a

i Deposit PAA   **ii** Spin coat   **iii** Evaporate solvent

iv 3D print via 2PP   **v** Develop   **vi** Release in water

b

c
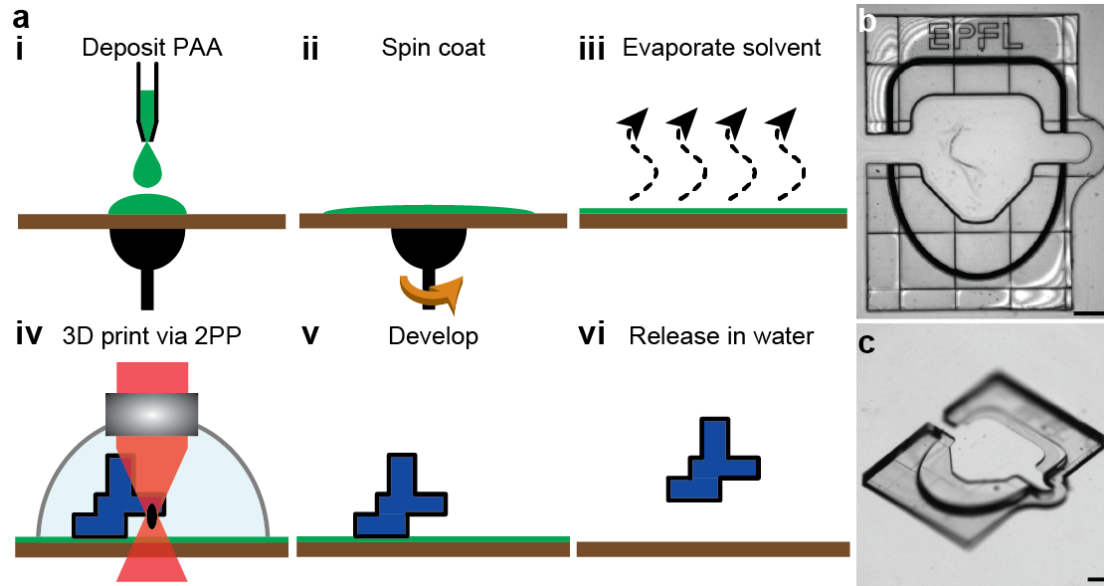
Supplementary Figure S3.6: Fabrication of a remounting stage. (a) A water soluble sacrificial solution is **(i)** deposited and **(ii)** spin-coated to ensure a thin layer. **(iii)** The water in the solution is evaporated, leaving a dry water soluble layer. **(iv)** The remounting stage is 3D printed using two-photon polymerization (2PP). **(v)** This is followed by development in a solvent. **(vi)** Finally, the piece is released in water. **(b)** A microscope image of the remounting stage before releasing it in water. Scale bar is 0.25 mm. **(c)** Another view of the remounting stage illustrating its ergonomic design for fly tethering. Scale bar is 0.25 mm.
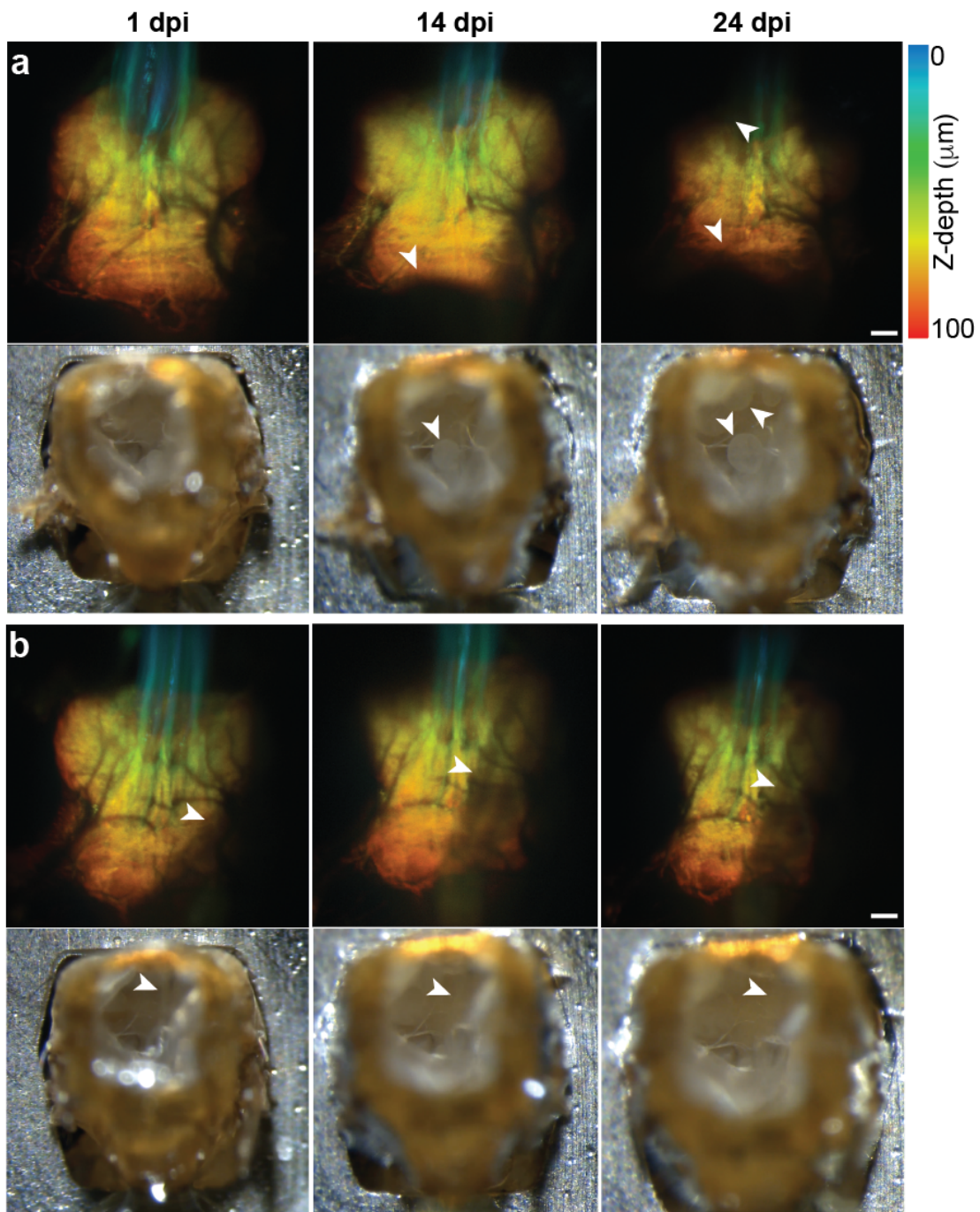
Supplementary Figure S3.7: Potential organ movements within the thorax after implantation. Two implanted animals at (**left**) 1 dpi, (**middle**) 14 dpi, and (**right**) 24 dpi. Highlighted are image-obscuring movements of the **(a)** fat bodies, or **(b)** salivary glands. **(top row)** Two-photon images of the animal's VNC expressing GFP throughout the nervous system. White arrowheads indicate **(a)** fat bodies, or **(b)** salivary glands that shift over time obscuring the view of the VNC. Z-stacks are depth color-coded (100 μm). Scale bar is 25 μm. (**bottom row**) The same animal's dorsal thorax, visualized using a dissection microscope.
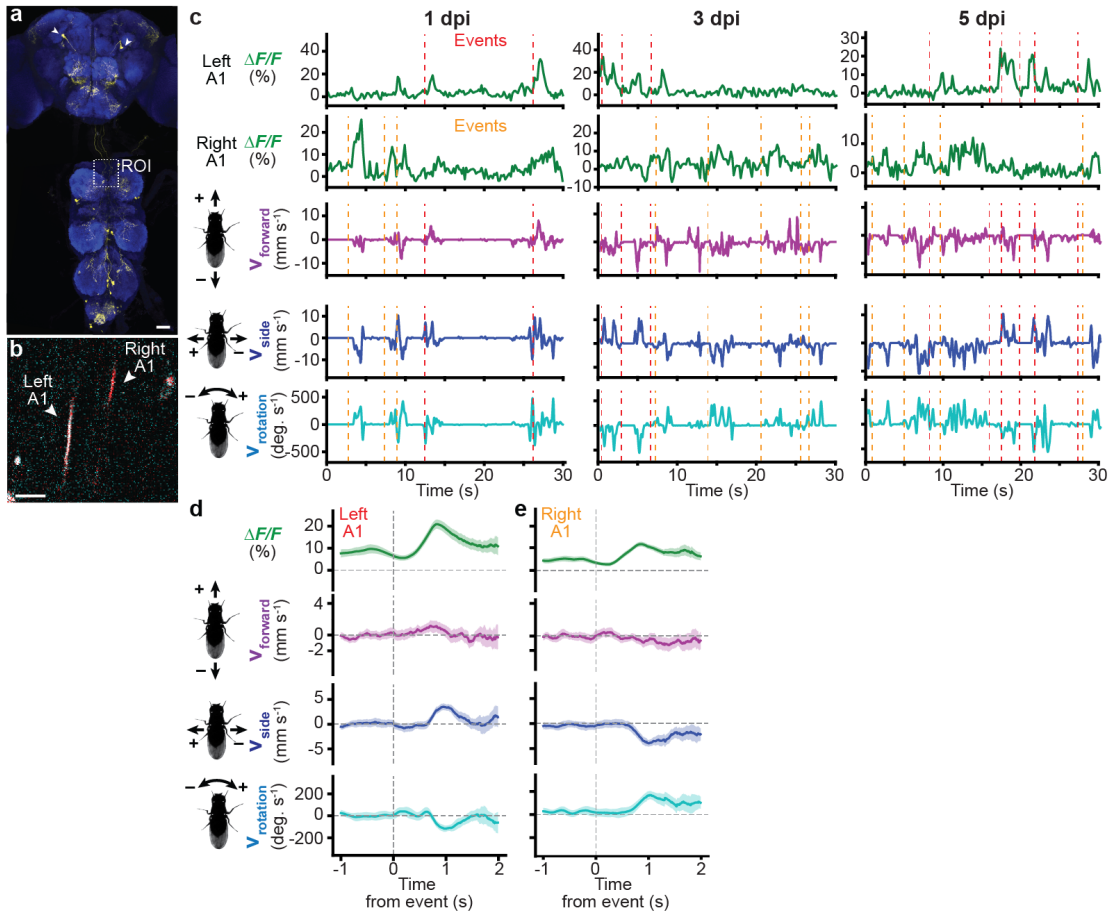
Supplementary Figure S3.8: Repeated neural recordings of a pair of DNa01 descending neurons. (a) Confocal image of DNa01-Gal4 driver line expression in the brain and VNC. Scale bar is 40 ⁻m. Shown are neuronal GFP (yellow) and neuropil (nc82, blue). A dashed white box highlights the VNC imaging region of interest ('ROI'). Image is modified from [251]. **(b)** One two-photon horizontal image of the cervical connective. Indicated are the left and right DNa01 neuron axons (white arrow heads). Scale bar is 16 ⁻m. **(c)** Activities of the left (**first row**) and right (**second row**) DNa01 neuron are synchronized with the fly's (**third row**) forward, (**fourth row**) sideways, and rotational (**fifth row**) velocities as measured by spherical treadmill ball rotations. Neural activity 'events' are indicated for left (red) and right (yellow) DNa01 neurons. Traces for one fly are shown for recordings at 1 (**left**), 3 (**middle**) and 5 (**right**) dpi. **(d,e)** All DNa01 **(d)** left and **(e)** right neuron activity events aligned at 0s. Solid lines and shaded regions show the mean and 95% confidence interval, respectively.
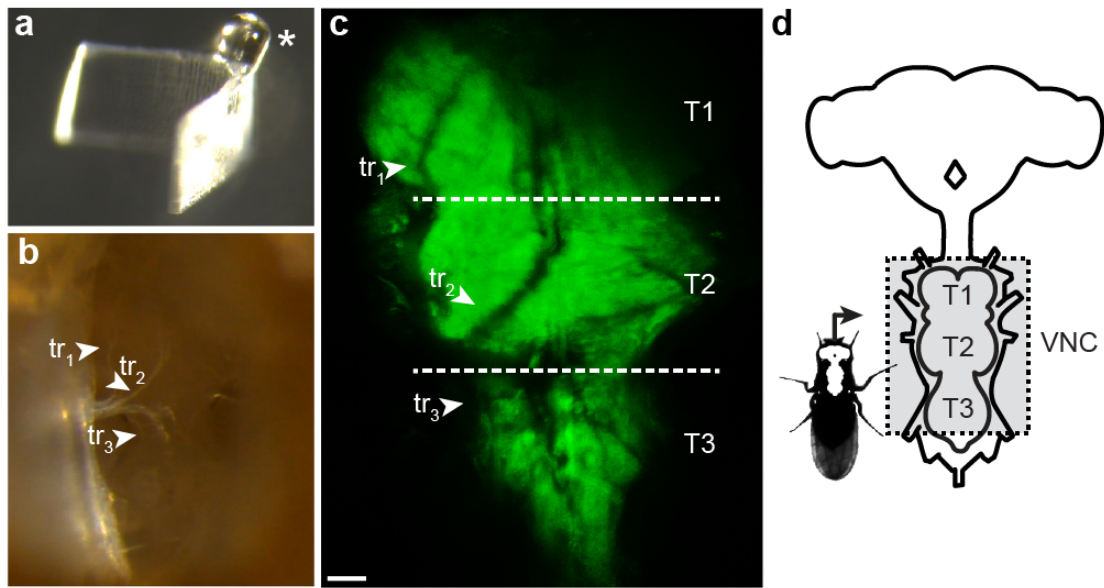
Supplementary Figure S3.9: Recording posterior regions of the VNC. (a) Prototype modified implant, with a drop of UV glue cured onto the apex of an implant. **(b)** Dissection microscope view through the dorsal thoracic window, revealing posterior positioning of the implant. Highlighted are tracheal fibers innervating the VNC (white arrowheads)(n=1). **(c)** Z-projected two-photon microscopy imaging volume of the VNC for the animal expressing GFP throughout the nervous system in panel B. Indicated are the same tracheal innervations from panel B (white arrowheads) as well as the newly visible T2 and T3 VNC neuromeres. Scale bar is 30 ⁻m. **(d)** A schematic of the VNC region imaged in panel C.
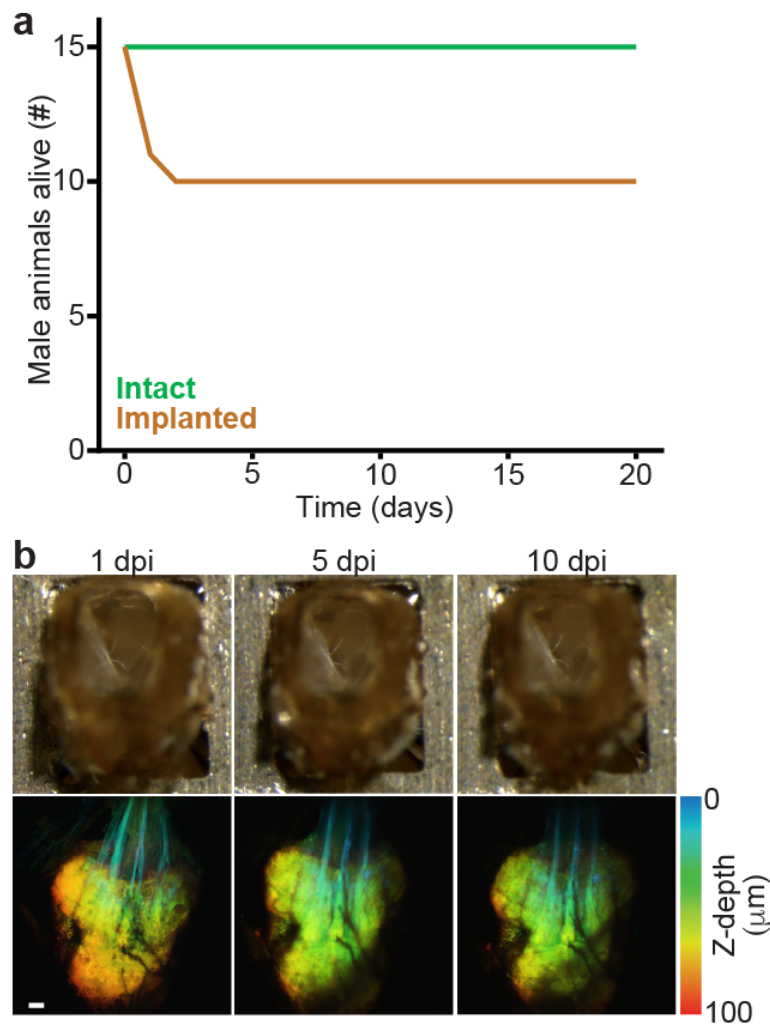
Supplementary Figure S3.10: Implanted male fly survival and long-term anatomical imaging. (a) Survival curves for genetically-identical sibling male flies that were either (i) not experimentally manipulated (green, 'Intact'), or (ii) prepared for long-term imaging by implantation and the addition of a thoracic window (orange, 'Implanted'). Source data are provided as a Source Data file. **(b)** The dorsal thorax of an implanted animal, as seen from the dissection microscope (**top row**), and the corresponding z-projected volumetric image of the VNC, visualized using a two-photon microscope (**bottom row**). This animal expressed GFP throughout the nervous system. Recordings were performed at (**left**) 1, (**middle**) 5, and (**right**) 10 dpi. Z-stacks are depth color-coded (100 ¯m). Scale bar is 20 ¯m.
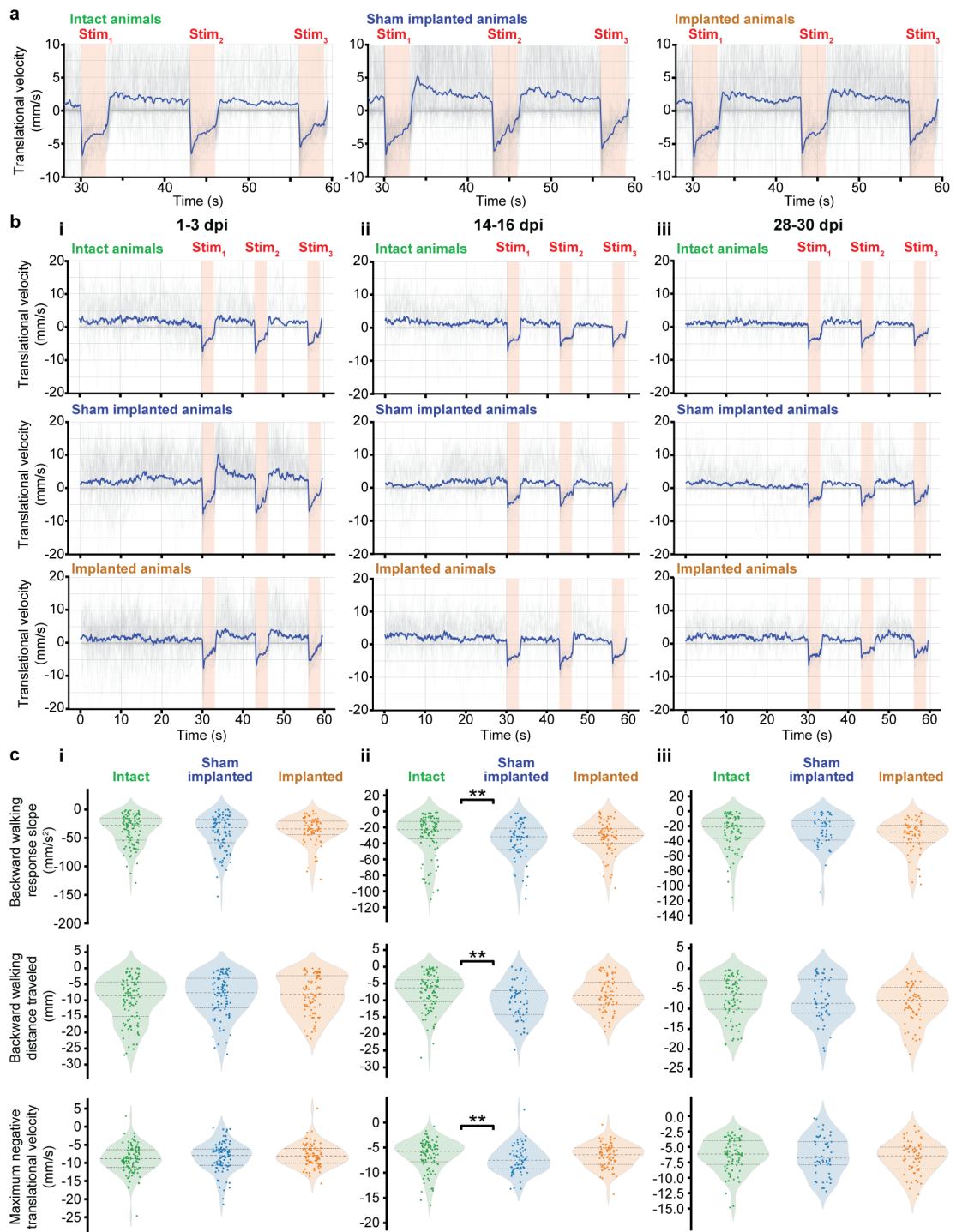
Figure S3.11 - See Figure Legend on next page.

Supplementary Figure S3.11: Impact of implantation and windows on behavior, separated by age post-implantation. (a) Zoomed in traces of translational velocities shown in Figure 2 for (**left**) intact, (**middle**) sham implanted, and (**right**) implanted flies including three recordings taken over one month. **(b)** Translational velocities of intact (**top**), sham implanted (**middle**), and implanted (**bottom**) animals during 30 s of spontaneous behavior, followed by three optogenetic stimulation periods of 3 s each (pink, 'Stim'). Shown are the raw (grey) and mean (blue) traces arranged by age: **(i)** 1-3 dpi, **(ii)** 14-16 dpi, or **(iii)** 28-30 dpi. **(c)** From these time-series data, we used each stimulation event as one data point for calculating summary statistics (1-3 dpi - intact group, n=103; sham implanted group, n=90, implanted group, n=81. 14-16 dpi - intact group, n=101, sham implanted group: n=66, implanted group: n=71; 28-30 dpi - intact group, n=82, sham implanted group, n=52, implanted group, n=61). Summary statistics include (**top**) the initial negative slope in translational velocity—backward walking—upon optogenetic stimulation, (**middle**) the integrated translational velocity over the entire optogenetic stimulation period, and (**bottom**) the peak negative translational velocity over the entire optogenetic stimulation period. Data are sorted by age as in panel B. A Kruskal-Wallis statistical test was used to compare behaviors across the three groups. A post-hoc Conover's test with a Holm correction was used to perform pairwise comparisons. Significant differences were found at 14-16 dpi between the two control groups: 'Sham implanted' and 'Intact'. One asterisk (*) indicates $P< 0.05$ and two asterisks (**) indicate $P< 0.01$. Source data are provided as a Source Data file.
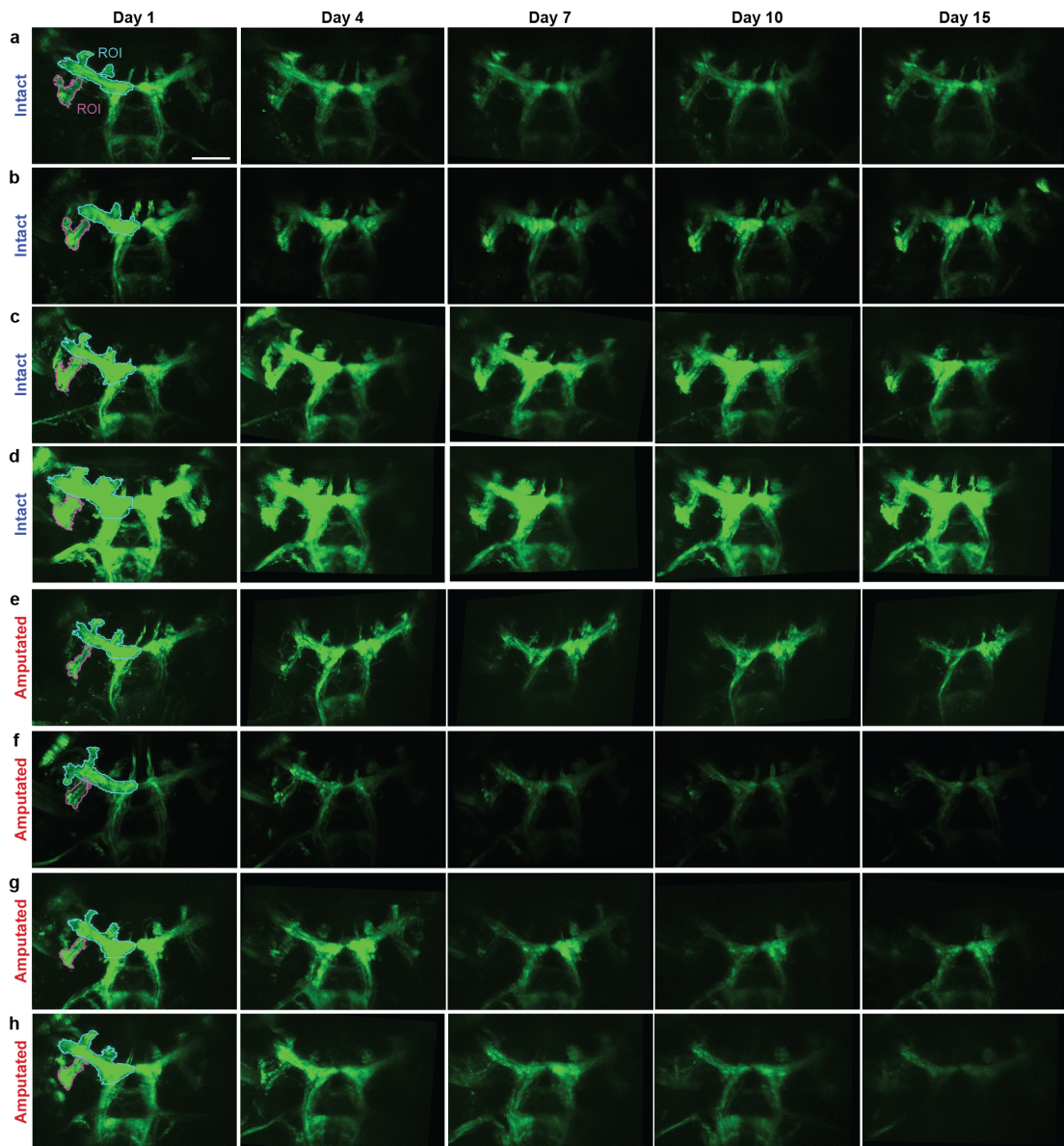
Supplementary Figure S3.12: Long-term imaging of front leg chordotonal organs axon terminals in the VNC in intact or amputee animals. Maximum intensity projections of z-stacks taken at 1, 4, 7, 10 and 15 dpi. Data are registered to images at 1 dpi. Scale bar is 50µm. Cyan and pink ROIs used for quantification in Figure 3 are indicated. Data are for **(a-d)** four control animals with intact legs and **(e-h)** four animals whose front left legs were amputated at 2 dpi.
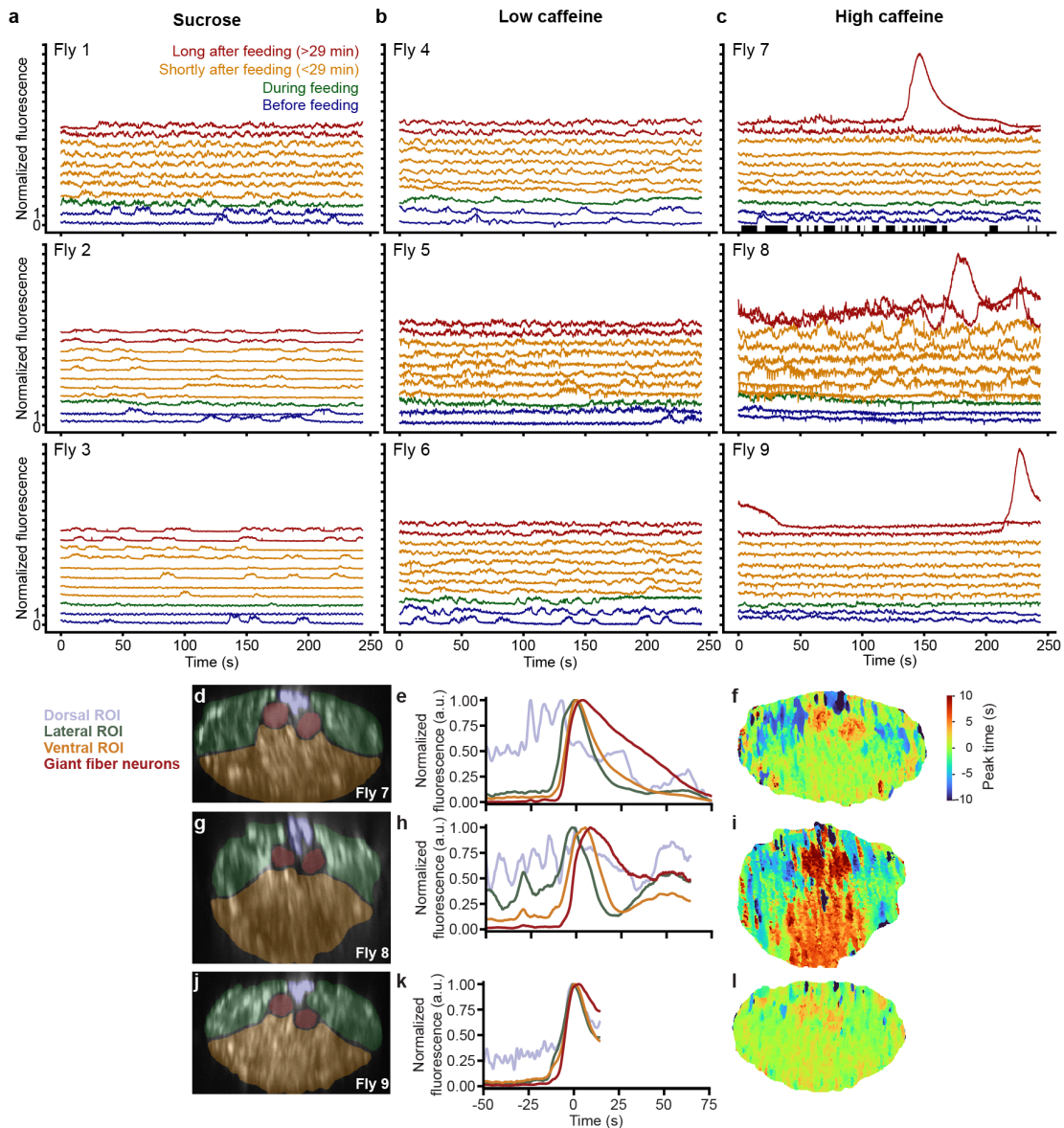
Supplementary Figure S3.13: Waves of neural activity observed across three animals following ingestion of high-concentration caffeine. (a-c) Normalized fluorescence across all axons passing through the thoracic neck connective over four minute recordings either before (blue), during (green), shortly after (orange), or long after (red) feeding. Three flies per condition were fed a solution containing either only sucrose **(a)**, or sucrose and **(b)** a low-dose, or **(c)** high-dose of caffeine. Flies 1, 4, and 7 are shown in Figure 4e. Black bars below Fly 7 traces show times when the fly was stationary during first trial. The Pearson correlation coefficient between the normalized fluorescence and time-series of stationary periods is $r = -0.67$, indicating that spontaneous fluctuations are strongly linked to changes in behavioral state. **(d,g,j)** Thoracic cervical connectives from three animals. ROIs overlaid on top of standard-deviation time-projected images. **(e,h,k)** Neural activity over time for each ROI (color-coded) normalized to the peak fluorescence during the wave of activity. Shown are three waves from three animals. Time is aligned to the peak of the mean fluorescence across all ROIs. **(f,i,l)** Pixel-wise time of peak activity (color-coded) relative to the peak of mean activity across the entire neck connective.

3.8 Supplementary Videos

Supplementary Video 3.1: Interactions among implanted and intact freely behaving animals. Two implanted animals—identifiable by visible thoracic windows—and one intact animal interact near a morsel of food. Video is real-time.
https://www.dropbox.com/s/b5ui7z7uotrnoql/video_1.mov?dl=0

Supplementary Video 3.2: Protocol to prepare animals for long-term neural recordings. A step-by-step visualization of how a fly is outfitted with an implant and window for long-term two-photon microscope recordings.
https://www.dropbox.com/s/tpegdzdu80tno4x/video_2.mov?dl=0

Supplementary Video 3.3: Repeatedly recording VNC anatomy across one month. Two-photon z-stacks of an animal's VNC at 1, 14, and 28 days post-implantation (dpi). This animal expressed GFP throughout the nervous system (*GMR57C10-Gal4*). Z-stack images progress from the dorsal to ventral VNC.
https://www.dropbox.com/s/efntyidl1gnx5aw/video_3.mov?dl=0

Supplementary Video 3.4: Repeatedly recording VNC neural activity in female flies across ten days. Two-photon imaging of a female animal's VNC at 1, 5, and 10 days post-implantation (dpi). This animal expressed a genetically-encoded calcium indicator, GCaMP6f, and an anatomical fiduciary, tdTomato, throughout the nervous system (*Act88F:Rpr; GMR57C10-Gal4 / UAS-GCaMP6f; UAS-tdTomato*). Neural data are averaged across three cumulatively acquired two-photon microscope images. Activity are related to foreleg-dependent grooming.
https://www.dropbox.com/s/4z3bztl88rwm9sl/video_4.mov?dl=0

Supplementary Video 3.5: Repeatedly recording VNC neural activity in male flies across ten days. Two-photon imaging of a male animal's VNC at 1, 5, and 10 days post-implantation (dpi). This animal expressed a genetically-encoded calcium indicator, GCaMP6f, and an anatomical fiduciary, tdTomato, throughout the nervous system (*Act88F:Rpr; GMR57C10-Gal4 / UAS-GCaMP6f; UAS-tdTomato*). Neural data are averaged across three cumulatively acquired two-photon microscope images. Activity are related to forward walking.
https://www.dropbox.com/s/bnqk4udfujeu626/video_5.mov?dl=0

Supplementary Video 3.6: Long-term imaging of DNa01 descending neuron axons. Two-photon horizontal imaging of DNa01 neuron axons within an animal's (*Act88F-Rpr/+; GMR22C05-AD-spGal4 / UAS-GCaMP6f; GMR56G08-DBD-spGal4 / UAS-tdTomato*) thoracic cervical connective at 1, 3, and 5 days post-implantation (dpi).
https://www.dropbox.com/s/h4g547ic3yth09o/video_6.mov?dl=0

Supplementary Video 3.7: Optogenetically elicited backward walking of intact, sham implanted, and implanted female flies. Representative videos of three female flies driven to walk backward through optogenetic activation of Moonwalker Descending Neurons. Columns are experimental dates (1, 14, and 28 dpi). Rows are experimental groups (Intact, Sham implanted, and Implanted). A light appears on the bottom-left of each arena, indicating times of orange light illumination and CsChrimson activation. Trajectories are shown for forward walking (cyan) and backward walking (purple).
https://www.dropbox.com/s/05x5cekrut9gec5/video_7.mov?dl=0

Supplementary Video 3.8: Spontaneous behaviors of intact and implanted male flies. Representative videos of two male flies behaving spontaneously. Columns are experimental dates (1, 5, 10, and 20 dpi). Rows are experimental groups (Intact and Implanted). Trajectories are shown for forward walking (cyan) and backward walking (purple).
https://www.dropbox.com/s/ooclrch2428d9rx/video_8.mov?dl=0

Supplementary Video 3.9: Repeatedly recording the anatomy of proprioceptive inputs to the VNC for 15 days before and after forelimb amputation. Two-photon z-stacks of two animals' VNCs at 1, 7, and 15 days-post-implantation (dpi). These animals expressed GFP in limb chordotonal organs (*iav-Gal4*). Z-stack images progress from the dorsal to ventral VNC. Top row shows data from an animal with an intact leg. Bottom row shows an animal whose front left leg was amputated at 2dpi.
https://www.dropbox.com/s/lmxsl323qhprots/video_9.mov?dl=0

Supplementary Video 3.10: Repeatedly recording thoracic cervical connective neural activity before, during, right after, and long after feeding with a sucrose solution. Two-photon imaging of a cross-section of the thoracic cervical connective including neurons descending from and ascending to the brain. Columns are data acquired before (left), during (middle-left), right after (middle-right), and 25 minutes (right) after feeding with a sucrose solution. Rows are behavioral videography (top), $\Delta F/F$ (middle) and motion-corrected raw (bottom) two-photon calcium imaging data. This animal expressed GCaMP6s and tdTomato, throughout the nervous system.
https://www.dropbox.com/s/7zzb2n4570m6ris/video_10.mov?dl=0

Supplementary Video 3.11: Repeatedly recording thoracic cervical connective neural activity before, during, right after, and long after feeding with a low-concentration caffeine and sucrose solution. Two-photon imaging of a cross-section of the thoracic cervical connective including neurons descending from and ascending to the brain. Columns are data acquired before (left), during (middle-left), right after (middle-right), and 25 minutes (right) after feeding with a low-concentration caffeine and sucrose solution. Rows are behavioral videography (top), $\Delta F/F$ (middle) and motion-corrected raw (bottom) two-photon calcium imaging data. This animal expressed GCaMP6s and tdTomato, throughout the nervous system.
https://www.dropbox.com/s/rn8cas5lxtnyzxs/video_11.mov?dl=0

Supplementary Video 3.12: Repeatedly recording thoracic cervical connective neural activity before, during, right after, and long after feeding with a high-concentration caffeine and sucrose solution. Two-photon imaging of a cross-section of the thoracic cervical connective including neurons descending from and ascending to the brain. Columns are data acquired before (left), during (middle-left), right after (middle-right), and more than 25 minutes (right) after feeding with a high-concentration caffeine and sucrose solution. Rows are behavioral videography (top), $\Delta F/F$ (middle) and motion-corrected raw (bottom) two-photon calcium imaging data. This animal expressed GCaMP6s and tdTomato, throughout the nervous system.
https://www.dropbox.com/s/28qcd329mhykeu6/video_12.mov?dl=0

Supplementary Video 3.13: Neural activity waves following high-concentration caffeine ingestion. Two-photon imaging of a cross-section of the thoracic cervical connective including neurons descending from and ascending to the brain. Columns are different occurrences of neural activity waves observed across three animals (here flies '1-3' are flies '7-9' in Supplementary Figure 13) more than 25 minutes after feeding with a sucrose and high-concentration caffeine solution. The second wave of fly 1 occurred in a later trial that is not included in Supplementary Figure 13). Rows are behavioral videography (top), $\Delta F/F$ (middle) and motion-corrected raw (bottom) two-photon calcium imaging data. These animals expressed GCaMP6s and tdTomato, throughout the nervous system.
https://www.dropbox.com/s/84abk0emwsm4klz/video_13.mov?dl=0

3.9   Data availability

The raw data generated in this study have been deposited on a public repository available at:
https://dataverse.harvard.edu/dataverse/long_term_imaging_vnc_drosophila
Source data are provided with this paper.

3.10   Code availability

Custom made codes used to analyse the raw data are available at:
https://github.com/NeLy-EPFL/Long-Term-Imaging-VNC-Drosophila
https://doi.org/10.5281/zenodo.6826488

3.11 Acknowledgments

3.12 Author Contributions

L.H. - Conceptualization, Methodology, Software, Validation, Formal analysis, Investigation, Data acquisition, Data curation, Writing - Original Draft Preparation, Writing - Review & Editing, Visualization.
M.K. - Methodology, Software, Validation, Formal analysis, Writing - Original Draft Preparation, Writing - Review & Editing, Visualization.
J.B. - Methodology, Software, Formal analysis, Data curation, Writing - Review & Editing, Visualization.
V.L.R. - Methodology, Software, Formal analysis, Data curation, Writing - Review & Editing, Visualization.
C.-L. C. - Data acquisition, Data curation, Writing - Review & Editing
A.F. - Methodology, Writing - Review & Editing
S.G. - Methodology, Software, Data curation, Writing - Review & Editing.
F.A. - Methodology, Software, Writing - Review & Editing.
M.S.S. - Conceptualization, Methodology, Resources, Writing – Original Draft Preparation, Writing - Review & Editing, Supervision, Project Administration, Funding Acquisition.
P.R. - Conceptualization, Methodology, Resources, Writing – Original Draft Preparation, Writing - Review & Editing, Supervision, Project Administration, Funding Acquisition.

3.13 Competing interests

The authors declare that no competing interests exist.

4 Networks of descending neurons transform command-like signals into population-based behavioral control

My contribution: I <u>conceived this study</u> under the supervision of Prof. Pavan Ramdya. I generated stable transgenic *Drosophila* lines and developed an approach to amend a two-photon microscope set-up with an optogenetic stimulation laser. I <u>performed all functional recording experiments</u> (**Figures 4.2** and **S4.2**), all <u>decapitation experiments</u> in **Figure 4.4**, some of the experiments to test predictions (**Figures S4.3** and **4.5**), all control experiments (**Figure S4.1**). Moreover, I <u>performed all analyses and visualisation of functional imaging data</u> (**Figures 4.2** and **S4.2**), pioneered anlyses of DN connectivity in the brain (**Figure 4.3**), and performed all analyses and visualisation of decapitation experiments in **Figure 4.4** and most analyses and visualisation of prediction testing experiments (**Figures S4.3** and **4.5**). Furthermore, I <u>designed all schematics</u> used to visualise concepts, generated the initial draft of all figures, <u>wrote the initial draft</u> of the paper, and <u>coordinated the work</u> of my co-authors.
I am very grateful to Femke Hurtak, who joined the project to systematically analyse connectivity between DNs in the brain connectome (**Figure 4.3**). She also performed many of the experiments and analyses to create and test predictions (**Figures S4.3** and **4.5**). She conceived, analysed and visualised clusters of DNs (**Figure 4.6**). I am very grateful to Sibo Wang-Chen, who joined the project to systematically analyse connectivity between DNs in the brain connectome (**Figure 4.3**). I am very grateful to Prof. Pavan Ramdya, who supervised the project and contributed substantially to the main text and the layout of the figures.

4.1 Abstract

To transform intentions into actions, movement instructions must pass from the brain to downstream motor circuits through descending neurons (DNs). These include small sets of command-like neurons that are sufficient to drive behaviors—the circuit mechanisms for which remain unclear. Here, we show that command-like DNs in *Drosophila* directly recruit networks of additional DNs to orchestrate flexible behaviors. Specifically, we found that optogenetic activation of command-like DNs previously thought to drive behaviors alone in fact co-activate larger populations of DNs. Connectome analysis revealed that this functional recruitment can be explained by direct excitatory connections between command-like DNs and networks of interconnected DNs in the brain. The size of downstream DN networks is predictive of whether descending population recruitment is necessary to generate a complete behavior: DNs with many downstream descending partners require network recruitment to drive flexible behaviors, while neurons with fewer partners can alone drive stereotyped behaviors and simple movements. Finally, DN networks reside within behavior-specific clusters that inhibit one another. These results support a mechanism for command-like descending control whereby a continuum of stereotyped to flexible behaviors are generated through the recruitment of increasingly large DN networks which likely construct a complete behavior by combining multiple motor subroutines.

4.2 Introduction

Animals, including humans, are capable of generating a remarkable variety of behaviors. For example, they can navigate rugged terrain and manipulate objects in their environments by coordinating their limbs. These movements ultimately arise from motor circuit dynamics in the vertebrate spinal cord or invertebrate ventral nerve cord. Nevertheless, the selection, initiation, and control of behaviors often depends on ongoing commands sent from the brain to downstream motor circuits via a relatively small population of brain neurons called descending neurons (DNs).

We still lack mechanistic understanding of how DNs as a population drive and coordinate flexible behaviors that require ongoing feedback (e.g., goal-directed walking or reaching for an object) as well as those which are more stereotyped (e.g., escape). This is in part due to the technical difficulty of comprehensively recording and manipulating DNs in behaving mammals: there are >1 million in the human pyramidal tract [25] and ~70,000 in the mouse corticospinal tract [26]. By contrast, the adult fly, *Drosophila melanogaster*, has approximately 1,300 DNs linking the brain to motor centers in the ventral nerve cord (VNC) [50]. Despite this numerical simplicity, flies can generate a variety of complex behaviors including walking over challenging terrain [195], flight [252], courtship [197], and aggression [253]. Recently, it has become possible to quantify the synaptic connectivity of every neuron—including DNs—in the brain [50] and the VNC [35, 176]. Importantly, in flies DNs can be repeatedly targeted across individual animals for experimental recordings (electrophysiological [90] or optical [92]) or manipulations (e.g., activation [81] or silencing [76]) using genetic lines that drive transgene expression in small sets of DNs [32, 44].

One notable discovery that was derived using these tools was the observation that, despite the abundance of DNs in the fly brain, artificial activation of very small sets (2-4 neurons) of so-called 'command-like' DNs can be sufficient to drive a complete behavior (but not strictly necessary as for 'command' neurons [64]). For example, DNs have been identified whose artificial activation triggers forward walking (DNp09) [79], anterior grooming (antennal DNs / aDN, DNg11, DNg12) [61, 83], backward walking (moonwalker DNs / MDN) [86], escape (giant fiber neurons / GF) [90], egg-laying (oviDN)[89], and aspects of courtship (pIP10, aSP22) [78, 88]. The capacity of some DNs to act as command-like neurons appears to be general across species including other invertebrates (e.g., crayfish giant escape neurons [63] and cricket song neurons [254]) and mammals (e.g., neurons which halt locomotion in mice [72]). This framework of command-like descending control—using simple, low-dimensional brain signals to drive downstream distributed motor circuits—has been formalized into controllers for bio-inspired robots that can walk and swim [255].

The concept of command-like control raises a fundamental question: To what extent does every pair or small set of DNs drive a distinct behavior? Several lines of evidence refute this possibility. Most directly, for many DNs, sparse optogenetic activation does not clearly and reliably drive a distinct, coordinated behavior [81]. Additionally, even during one behavior—forward walking and turning—we have observed that populations of many DNs in the cerebral ganglia become co-active [96]. This is in line with the observation that a population of 15 DNs can modulate wing beat amplitude [80] and that the activation of individual DNs has a lower probability of driving take-off than co-activation of multiple DNs [77]. Beyond controlling kinematics, it has also been shown that DNs can convey sensory information [96, 109] and that they may be modulatory [94, 103, 106, 110]. All of these observations suggest that, rather than being low-dimensional, DN control of behavior is population-based or high-dimensional: the brain flexibly engages larger populations of DNs to construct and mediate complete behaviors.

At first glance, these two models—command-like versus population-based DN behavioral control—appear to be incompatible. However, we can envision at least two means of unifying these seemingly disparate observations. On one hand, command-like or non-command-like DNs may simply target different downstream motor circuits (i.e., in the spinal cord or VNC) that can or cannot generate complete behaviors, respectively. On the other hand, command-like DNs might be privileged in that they can recruit additional DN populations to drive complete behaviors. This latter possibility is supported by the fact that, in addition to projecting to the VNC, 85 % of all DNs have axon collaterals in the brain's gnathal ganglia (GNG), where the majority of DNs also originate [32]. Thus, the GNG may function as a locus where command-like DNs engage other DNs to construct complex behaviors from simpler motor primitives.

Here we investigated the degree to which command-like DNs and other DNs interact with one another in the brain to drive complete behaviors. While optogenetically activating three sets of command-like DNs driving a range of distinct actions, we observed the co-activation of additional DN populations in the GNG. The degree of this functional recruitment covaries

with and can be explained by excitatory monosynaptic connections between command-like DNs and downstream DN networks. Through decapitation experiments, we show that this engagement of DN networks is necessary to drive complete flexible behaviors like forward walking and grooming but not for stereotyped behaviors like backward walking. This predicts that command-like DNs driving larger DN networks require their downstream partners in the brain to execute a behavior while DNs with smaller networks do not—a prediction we validate for six additional sets of DNs. Finally, a comprehensive analysis of all DN-to-DN interconnectivity in the brain revealed that DN networks form clusters that are linked to distinct behaviors and that largely inhibit one another. These findings can reconcile the two dominant models of DN control: Command-like DNs drive behaviors by recruiting additional DN populations—the extent to which depends on the flexibility versus stereotypy of the behavior in question. These DN populations likely construct complete behaviors by combining multiple DN-driven motor subroutines.

4.3 Results

4.3.1 An optogenetic approach to investigate the relationship between command-like DNs and DN population activity

We set out to explore the relationship between two prominent models for how DNs control behavior. In the first model, the artificial activation of a few 'command-like' DNs ('comDNs')—a simple high-level descending signal—engages downstream motor circuits in the VNC and is thus sufficient to drive a complete behavior (e.g., walking or grooming) **(Figure 4.1a, left 'comDNs')**. In the second model, a larger population of DNs must become co-active to drive a given behavior. Each DN within this population would be responsible for controlling or modulating a particular motor primitive. The combined activity of the entire population would yield a complete behavior **(Figure 4.1a, right 'popDNs')**.

These two scenarios can be distinguished by the degree to which activation of command-like DNs further activates other downstream DNs. We tested this by devising an all-optical experimental strategy in *Drosophila melanogaster*, where we could optogenetically activate command-like DNs while recording the activity of DN populations within the GNG (GNG-DNs), the most caudal region of the fly brain. We selected GNG-DNs because ∼60% of all DNs have their cell bodies in the GNG and ∼85% of all DNs have axonal output in this region[32] **(Figure 4.1b, right)**. To explore the range of DN control, we performed this experiment across three sets of command-like DNs driving diverse behaviors. First, we stimulated forward walking, a flexible, goal-directed behavior that can employ closed-loop control [256] (DNp09-spGAL4, green). Second, we studied anterior grooming, a somewhat flexible behavior that consists of the sequential control of multiple sub-behaviors [20] (aDN2-spGAL4, red), and backward walking, a stereotyped behavior that, although kinematically as complex as forward walking, has been shown to arise principally from stereotyped oscillations of the hindlegs [82] (MDN3-spGAL4, cyan) **(Figure 4.1b, left)**. We artificially activated these command-like DNs via cell-specific expression of the light-activated ion channel, CsChrimson [154] (comDN-spGAL4 > UAS-CsChrimson; **Figure S4.1a,d**).
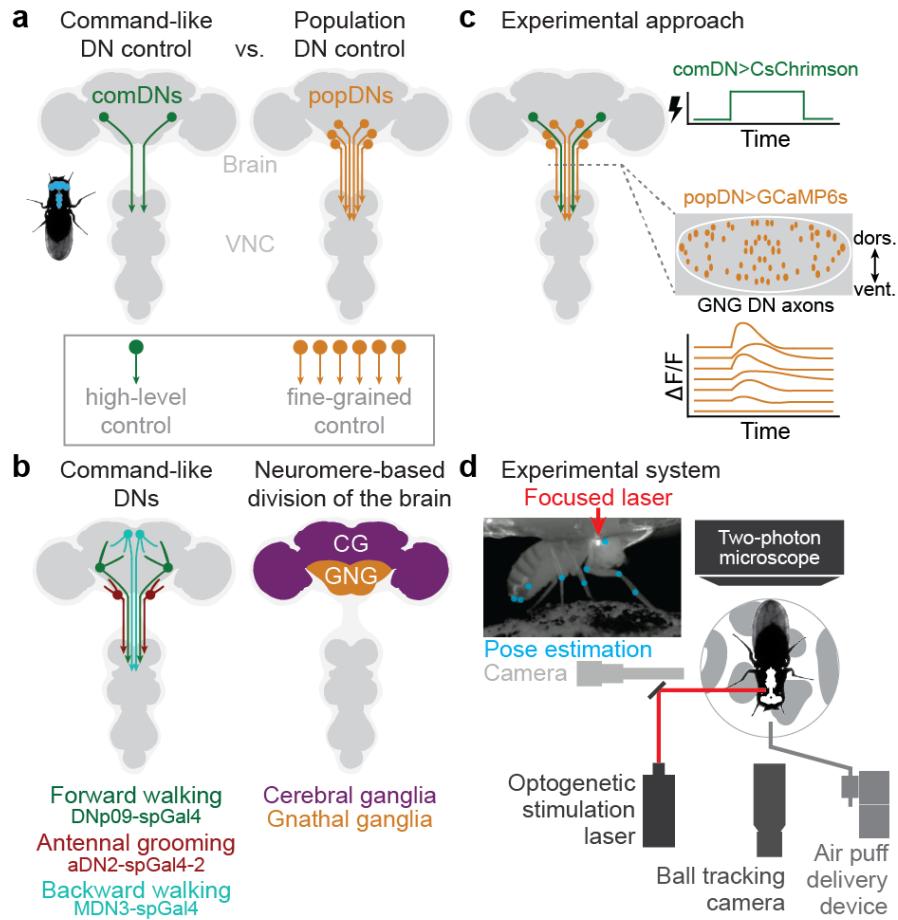
Figure 4.1 - See Figure Legend on next page.

While stimulating these command-like DNs, we recorded neural activity in GNG DN populations by expressing the genetically-encoded calcium indicator GCaMP6s [133] in cells positive for the Hox-gene Deformed (Dfd) [168] (*Dfd*-LexA > LexAOp-opGCaMP6s). This yields selective expression of GCaMP in the GNG **(Figure S4.1a,b)** and in the proboscis. To further restrict our neural recordings to DNs, we performed two-photon microscopy of DN axons passing through the thoracic cervical connective, as in [96] **(Figure 4.1c)**. To increase the specificity of command-like DN optogenetic activation, we designed a stimulation system that focuses a 640 nm laser onto the animal's neck connective **(Figure 4.1d, red)**. This reduced the degree to which our laser light might also activate other brain and VNC neurons **(Figure S4.1e,f)**.

Figure 4.1: Optical approach to probe the relationship between command-like descending neurons and populations of descending neurons in behaving animals. (a, left) Schematic of the *Drosophila* nervous system showing a pair of descending neurons (DNs) which project from the brain to motor circuits in the ventral nerve cord (VNC). Activation of small sets of command-like DNs ('comDNs', green) can drive complete actions like walking and grooming. Thus, command-like DNs are thought to send simple, high-level control signals to the VNC, where they are transformed into complex, multi-joint movements. **(a, right)** However, much larger populations of DNs ('popDNs', orange) are known to become active during natural walking and grooming. Therefore, in another model, individual DNs contribute to complex behaviors by sending low-level signals to control the fine-grained movements of individual or sparse sets of joints. **(b, left)** A schema illustrating three sets of DNs which exemplify command-like control for limb-dependent behaviors. These elicit (i) forward walking (DNp09, green) [32, 79], (ii) antennal or anterior grooming (aDN2, red) [61], or (iii) backward walking (MDN, cyan) [86]. Indicated is the approximate location of DN cell bodies within the brain. VNC targets are not schematized. **(b, right)** Two coarse subdivisions of the adult *Drosophila* brain are the cerebral ganglia (CG) and gnathal ganglia (GNG). These are delineated by neuromere boundaries [56]. The majority of all DNs and their brain targets are predominantly found in the GNG [32]. Our neural recordings were restricted to DNs within the GNG (GNG-DNs). **(c)** To uncover the relationship between command-like and population-based DN control, we recorded neural activity in the axons of GNG-DN populations (orange) while optogenetically activating different sets of command-like DNs (green). Indicated (dashed gray line) is the coronal imaging region-of-interest in the thoracic cervical connective. Small orange ellipses represent the cross-sections of descending neuron axons. **(d)** To accomplish these experiments, we used a behavior and neural recording system from [96] and added an optogenetic stimulation laser (640 nm) that was focused onto DN axons passing through the neck connective. Cartoon schema is not to scale. Inset shows a real camera image of a fly on the spherical treadmill with focused laser light shining on the neck (red arrow). Measured body and leg keypoints for pose estimation are superimposed (light blue).

4.3.2 Activation of command-like DNs recruits additional DN populations

Using these tools we examined whether additional DNs in the GNG might be recruited upon optogenetic activation of command-like DNs. We used an open-loop trial structure in which 5 s periods with optogenetic stimulation of command-like DNs were interleaved with 10 s periods of spontaneous animal behavior. This approach elicited robust behavioral responses which could be trial-averaged for quantification **(Figure 4.2a)**. Similar to what we observed when recording from DNs in the cerebral ganglia [96], many GNG-DNs were active during spontaneous behavior in the absence of optogenetic stimulation. Thus, to distinguish between GNG-DN activity due to command-like stimulation versus the initiation of spontaneous behaviors, we only analyzed trials for which flies were walking immediately prior to optogenetic stimulation.
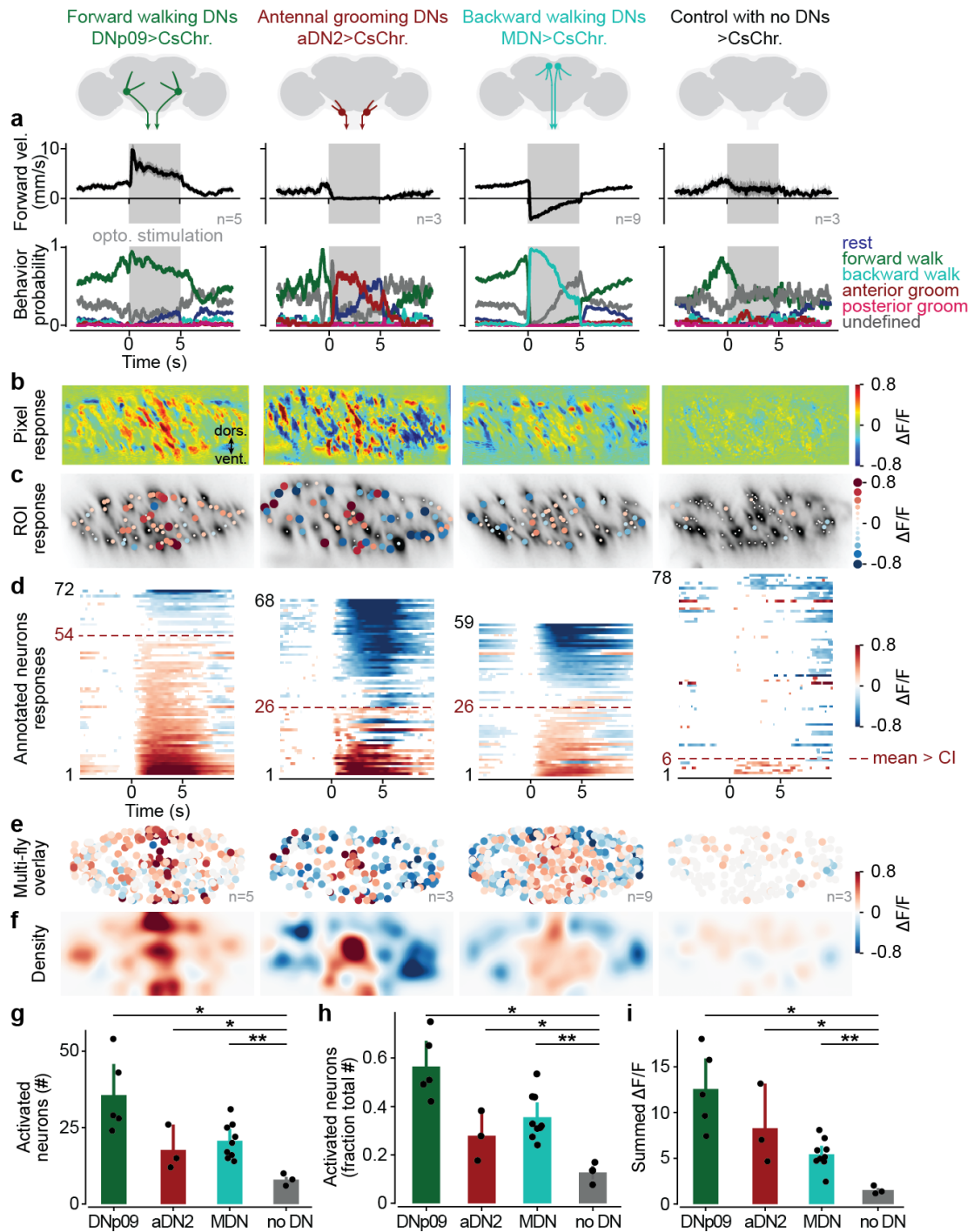
Figure 4.2 - See Figure Legend on next page.

When we trial-averaged the change in neural activity upon optogenetic stimulation of command-like DNs, we observed a clear increase in GNG-DN activity during the stimulation of any of the three sets of command-like DNs in individual animals: DNp09 **(Video 4.1)**, aDN2 **(Video 4.2)**, and MDN **(Video 4.3) (Figure 4.2b-d)**. This was also consistent across multiple animals **(Figure 4.2e-f)**. Importantly, we did not observe such a pronounced

Figure 4.2: Activation of command-like DNs recruits larger, distinct DN populations.
Three command-like DN driver lines were optogenetically stimulated. DNp09 drove forward walking (n=5 flies, total of 120 stimulation trials), aDN2 drove anterior grooming (n=3 flies, total of 34 stimulation trials), and activating MDN drove backward walking (n=9 flies, total of 271 stimulation trials). Control animals without DN expression were also optically stimulated (n=3 flies, total of 47 stimulation trials). **(a)** Shown are forward walking velocities inferred from spherical treadmill rotations (top) and the probability of generating each classified behavior (bottom) during optogenetic stimulation (grey epoch). Shaded area indicates 95 % confidence interval of the mean across all trials. **(b)** Processed two-photon microscopy images illustrating the activation of GNG-DN populations upon command-like DN stimulation. One example animal is shown per driver line (the flies and color scheme are the same as in **Videos 4.1 to 4.3**; n=33, 10, 97, and 10 trials for DNp09, aDN2, MDN, and control flies, respectively). The same flies are shown in **c** and **d**. **(c)** Single neuron / region-of-interest (ROI) response magnitude to command-like DN stimulation. Each circle is scaled and color-coded to represent the maximum change in fluorescence (normalized $\Delta F/F$) of one detected DN axon/ROI relative to the level of activity 1 s prior to stimulation. Small white dots are shown if the response magnitude is smaller than the 95% confidence interval of the mean across trials. The background image is a standard-deviation projection across time of raw fluorescence microscopy data. **(d)** Trial-averaged single neuron/ROI responses across time, aligned to stimulus onset and ordered by response magnitude. Data are color-coded according to the magnitude of activity, or white if the response is smaller than the 95% confidence interval of the mean. Indicated are the number of neurons/ROIs with a positive response magnitude larger than the 95% confidence interval of the mean across trials (horizontal red line). **(e-f)** A **(e)** registered overlay or **(f)** density visualization of the data from multiple flies analyzed in the same manner as in **c**. The number of flies and trials are the same as in **a**. **(g)** Statistical comparison of the number of activated neurons/ROIs (i.e., the red dashed line as in **d**) using Mann-Whitney-U tests (p-values: DNp09 vs. control = 0.018, aDN2 vs. control = 0.040, MDN vs. control = 0.008). **(h)** Statistical comparison of the fraction of activated neurons (i.e., data from **g** divided by the total number of visible neurons/ROIs per fly) using Mann-Whitney-U tests (p-values: DNp09 vs. control = 0.018; aDN2 vs. control = 0.040; MDN vs. control = 0.008). **(i)** Statistical comparison of the strength of activation (i.e., the sum of normalized $\Delta F/F$ for positively activated neurons) using Mann-Whitney-U tests (p-values: DNp09 vs. control = 0.018; aDN2 vs. control = 0.040; MDN vs. control = 0.008). Error bars in (g)-(i) represent 95% confidence interval of the mean.

recruitment of GNG-DNs in control animals lacking a spGAL4 transgene **(Video 4.4, Figure 4.2b-f, far-right)**. This confirms that these populations became active due to command-like DN stimulation. Statistical comparisons confirmed that, for all three sets of command-like DNs, the number and fraction of GNG-DNs activated were significantly higher than for control animals **(Figure 4.2g-h**; DNp09: p=0.018, aDN2: p=0.040, MDN: p=0.008**)**.

Interestingly, we found that GNG-DNs were recruited in a spatially distinct manner across the cervical connective depending on which command-like DNs were optogenetically activated **(Figure 4.2e-f)**. The activation of forward walking (DNp09) and anterior grooming (aDN2) command-like DNs increased activity among DNs localized to distinct regions of the medial cervical connective: the entire dorsal-ventral axis for forward walking, and the central and ventral connective for grooming. Activation of backward-walking command-like DNs led to weaker GNG-DN recruitment in the central connective.

We quantified the strength of GNG-DN recruitment as the summed responses of neurons that were positively activated during optogenetic stimulation **(Figure 4.2i)**. The summed response was significantly higher for the stimulation of command-like DNs compared with control animals (DNp09: p=0.018, aDN2: p=0.040, MDN: p=0.008). Intriguingly, we also observed a recruitment gradient among command-like DNs: DNp09 stimulation resulted in very strong recruitment of GNG-DNs, aDN2 slightly weaker recruitment, and MDN the weakest. We note that reduced GNG-DN activity **(Figure 4.2b-f, blue neurons and regions)** likely does not reflect inhibition (which is not robustly observed using calcium imaging) but rather reduced drive in DNs that were previously active during spontaneous forward walking prior to optogenetic stimulation. Consistent with this, additional experiments in animals that were resting prior to optogenetic stimulation showed fewer DNs with reduced activity **(Supporting Information File 1)**.

To address the possibility that recruitment of GNG-DNs by optogenetic stimulation may be non-ethological rather than reflecting a natural process, we compared the activity of GNG-DN populations in the same animal both during optogenetic stimulation and during the corresponding natural behavior. Specifically, in individual animals we compared neural activity during DNp09 stimulation to bouts of spontaneous forward walking **(Figure S4.2a, Video 4.5)**, aDN2 stimulation to air puff-induced anterior grooming **(Figure S4.2b, Video 4.6)**, and MDN stimulation to spontaneous backward walking on a cylindrical treadmill **(Figure S4.2c, Video 4.7, see Methods)**. In each of these cases, we observed that populations of GNG-DNs were recruited during both optogenetic and natural conditions. For backward walking, these patterns were largely similar across optogenetic and natural conditions **(Figure S4.2c)**. However, for forward walking **(Figure S4.2a)** and to a lesser extent for anterior grooming **(Figure S4.2b)**, there were some differences. DNp09 stimulation consistently and strongly activated a small subset of DNs located in the medial-dorsal and medial-ventral connective. These were not active during spontaneous forward walking **(Figure S4.2d-f)**. However, the remaining largest fraction of DNs were active in a similar fashion during optogenetic stimulation and during spontaneous walking **(Figure S4.2e, white region)**.

Taken together, these data reveal that the stimulation of command-like DNs leads to the recruitment of many additional DNs in the GNG in a manner that is similar to DN population activity during natural behaviors. This framework can reconcile the two observations that only a few command-like neurons are sufficient to drive behaviors but that larger DN populations are active during spontaneous behaviors.
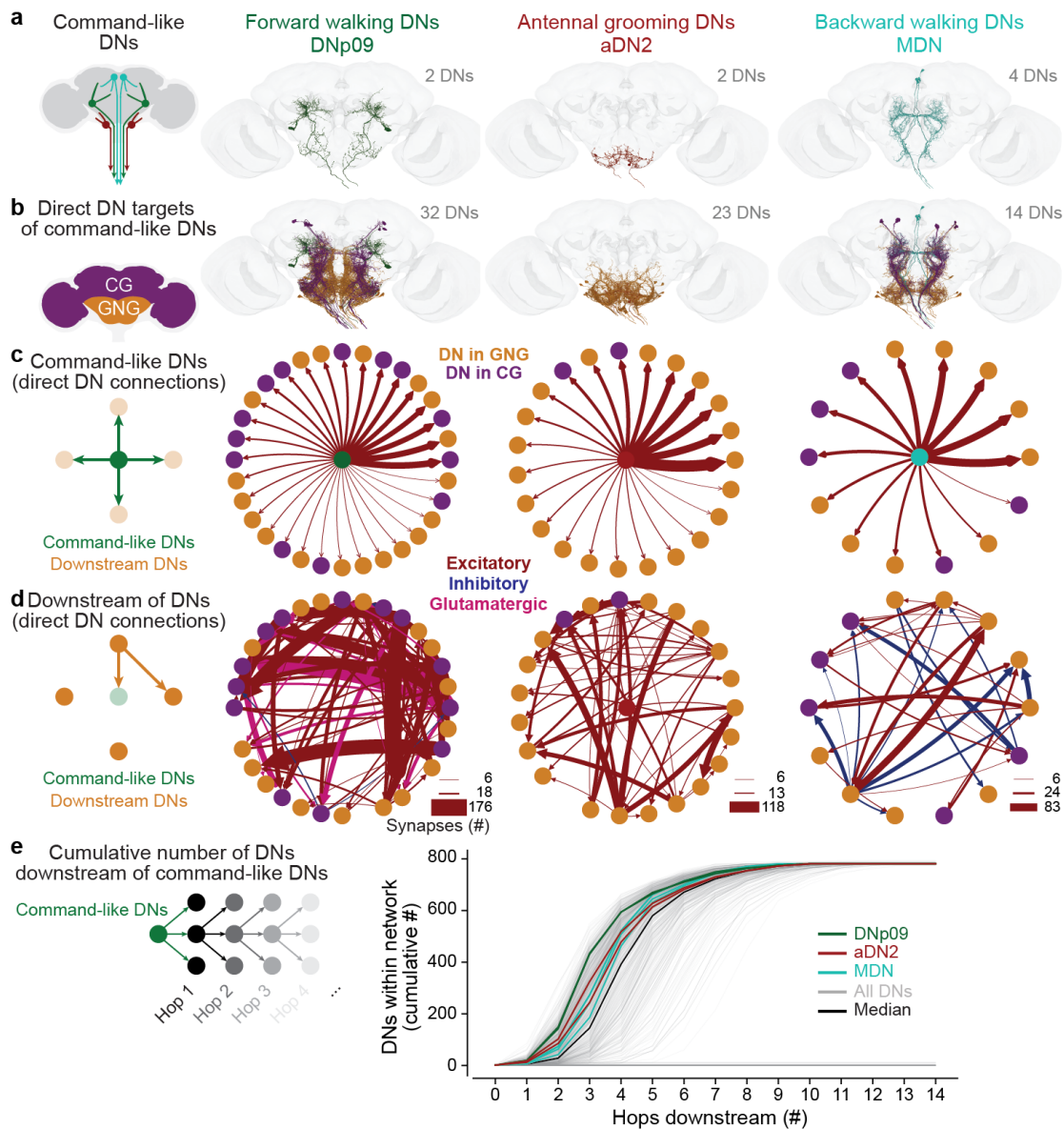
Figure 4.3 - See Figure Legend on next page.

4.3.3 Command-like DNs connect to recurrent DN networks in the brain

The functional recruitment of GNG-DNs by command-like DNs could arise from a variety of circuit mechanisms. Broadly speaking, it might either result from direct, monosynaptic excitatory connections, or indirect polysynaptic connectivity via local brain circuits, or via ascending neurons in the VNC. To investigate these possibilities, we examined DN connectivity within the female adult fly brain connectome [50, 257]. There, we found our three sets of command-like DNs—DNp09, aDN2, and MDN **(Figure 4.3a)**—and identified all of their downstream DN partners. We observed that each command-like DN has direct, monosynaptic connections to DNs with somata in both the cerebral ganglia (CG, purple) and the GNG (orange) **(Figure 4.3b)**.

Networks of Descending Neurons transform command-like signals
into population-based behavioral control
Chapter 4

Figure 4.3: Command-like DNs synapse onto other DNs, forming larger DN networks.
(a) The neuronal morphologies of three sets of command-like DNs—**(left)** DNp09, **(middle)** aDN2, and **(right)** MDN in the female adult fly brain connectome [50]. **(b)** The location and morphologies of DNs directly (monosynaptically) targeted by command-like DNs. DNs are color-coded based on their cell body localization in the GNG (orange) or CG (purple). Command-like neurons are color-coded as in **a**. **(c)** Command-like DNs form monosynaptic excitatory connections to downstream DN targets. Edge weights reflect the number of synapses as shown in **d**, with consistent scaling across all plots. Edge colors denote excitatory (red), inhibitory (blue), or glutamatergic (pink) which can be excitatory or inhibitory depending on receptor type [258]. DNs are color-coded as in **b**. **(d)** Network connectivity among downstream DNs shows strong recurrence and minimal feedback to command-like DNs (only in aDN2). **(e)** The cumulative number of downstream DNs that three sets of command-like neurons—DNp09 (green lines, 2 DNs), aDN2 (red lines, 2 DNs), MDN (cyan lines, 4 DNs) connect to across an increasing number of DN-DN synapses ('hops'). This is compared to the number of DNs accessible over an increasing number of hops for all DNs (grey lines) and the median of all DNs (black line). The maximum number of recruited neurons (~ 800) is smaller than the total number of DNs because 455 neurons receive inputs from maximally one other DN. Note that many DNs do not connect to any other DN, even across 14 hops.

Based on predictions from EM images, our command-like DNs are cholinergic [50, 259] and the connections they form with downstream DNs are most likely excitatory **(Figure 4.3c, red arrows)**. These connections are predominantly feedforward with only sparse feedback connections for aDN2 **(Figure 4.3d)**. By contrast, among downstream DNs, we observed strong recurrent interconnectivity, including some inhibition **(Figure 4.3d, blue arrows)**. Notably, command-like DNs connect to a variable numbers of downstream DNs that mirrors the differential recruitment of GNG-DNs in our functional imaging experiments **(Figure 4.2i)**: those for forward walking (DNp09) have the most downstream DNs (32), while those for antennal grooming (aDN2) have fewer (23), and those for backward walking (MDN) have the fewest (14). This ordering also holds for multi-synaptic connections to downstream DNs **(Figure 4.3e)**. All three command-like DNs, in particular DNp09, form more short connections (one to six synapses away) to the remaining DN population than the median DN **(Figure 4.3e)**. These data support a mechanism whereby command-like DNs engage additional DN populations in the brain via direct excitatory connections.

4.3.4   Behavioral requirement for DN population recruitment

We next asked to what extent the recruitment of additional DN populations is necessary for command-like DNs to drive complete behaviors. We can envision at least four possibilities. First, it may be that these additional DNs are required because command-like DNs only control a small subset of the required behavioral kinematics. Second, additional DNs may be modulatory, controlling behavioral vigor or persistence. Third, additional DNs may 'gate' a behavior that is initiated by command-like DNs. Fourth, DN recruitment may be relatively inconsequential: activating command-like DNs alone may be sufficient to drive a complete behavior.

To distinguish between these possibilities, we needed to stimulate command-like DNs while preventing the recruitment of additional DN populations. We achieved this by carefully decapitating flies and sealing their exposed neck. It has been shown that flies can survive and generate behaviors for hours following decapitation [260]. In this way we could identify which elements of behavioral kinematics directly result from optogenetic activation of command-like DNs alone (i.e., a low-dimensional signal coming from the brain), without the recruitment of other DNs in the brain **(Figure 4.4a, right)**. Notably, a less invasive approach—acute optogenetic inhibition of GNG-DNs using the anion channelrhodopsin, GtACR1 [155] (Dfd-LexA > LexAop-GtACR1)—would achieve inhibition of only a fraction of all DNs and, when tested, caused animals to groom at even low light intensities, obstructing any analysis of command-like DN-driven behaviors.

We compared the behaviors of intact and headless animals upon optogenetic activation of command-like DNs. As in our previous experiments, stimulation of DNp09, aDN2, and MDN in intact animals drove forward walking **(Video 4.8)**, anterior grooming **(Video 4.9)**, and backward walking **(Video 4.10)**, respectively **(Figure 4.4b-d, black traces)**. Control animals with no DN driver did not reliably generate specific behaviors upon laser stimulation but were more aroused **(Video 4.11)** resulting in a decreased probability of resting **(Figure 4.4e, black traces)**.

After decapitation of the same animals, we found that the activation of MDN in headless flies still drove backward walking. This confirms that decapitation does not trivially impair movement generation **(Figure 4.4d**; $p = 0.265$ comparing the backward walking probabilities of headless versus intact flies). By contrast, decapitation had a different effect on the other two command-like DNs: DNp09 and aDN2 stimulation in headless animals did not generate forward walking **(Figure 4.4b**; $p = 0.006$) or anterior grooming **(Figure 4.4c**; $p = 0.006$), respectively. Importantly, headless animals could still behave. Outside of optogenetic stimulation periods we observed episodes of spontaneous grooming in headless flies that resembled those generated by intact animals. This confirms that local VNC circuits required to generate coordinated movements were still intact. Additionally, although optogenetic stimulation of DNp09 and aDN2 in headless flies did not drive complete forward walking or anterior grooming, respectively, it reliably elicited more subtle movements: stereotyped abdomen contraction for DNp09 **(Figure 4.4f**; $p = 0.006$ comparing headless DNp09 versus headless control animals) and front leg approach for aDN2 animals **(Figure 4.4g**; $p = 0.030$ comparing the distance between the tibia-tarsus joint and neck in headless aDN2 versus headless control animals).

In summary, these data lead us to posit that differences in optogenetically-driven behaviors between intact and headless flies result from the failure to recruit additional, downstream DN pathways in the brain. These results also show that the functional recruitment of populations of DNs is necessary for command-like DNs to drive more flexible (DNp09 and aDN2), but not stereotyped (MDN) behaviors, suggestive of different modes of DN-driven behavioral control that we next set out to explore.
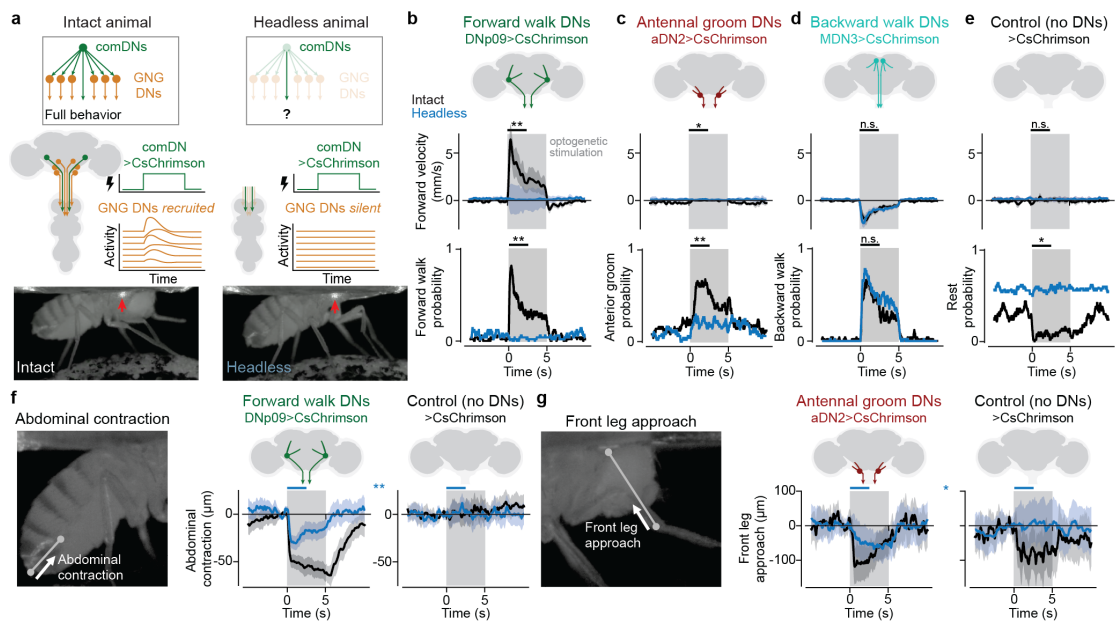
Figure 4.4: Recruited DN networks are required for forward walking and grooming, but not for backward walking. (a) In intact animals, the activation of a command-like DN (green) recruits other DNs (orange) and leads to the execution of a complete behavior (left). In headless flies, the axons of command-like DNs (green) can still be activated in the VNC. However, other DNs (orange) cannot be recruited in the brain and will remain silent (right). This comparison between intact and headless animals allows one to isolate the contribution of full DN networks versus command-like DNs alone to behavioral output. **(b-e)** Forward walking velocities and behavior probabilities for **(b)** DNp09, **(c)** aDN2, **(d)** MDN, or **(e)** control flies. Mann-Whitney-U tests compare the difference between the means of the first 2.5 s of optogenetic stimulation across intact (black traces) versus headless animals (blue traces). **(f)** DNp09 stimulation in both intact and headless animals leads to abdominal contractions. This is quantified as the change in Euclidian distance between the anal plate and ventral side of the most posterior stripe compared to 1 s prior to stimulation. Mann-Whitney-U test compares the mean of the first 2.5 s of stimulation (blue bars) for headless DNp09 versus headless control animals (two blue traces). **(g)** aDN2 stimulation in both intact and headless animals leads to front leg approach. This is quantified as the change in Euclidian distance between the front leg tibia-tarsus joint and the neck compared to 1 s prior to stimulation. Mann-Whitney-U test compares the first 2.5 s of stimulation (blue bars) between headless aDN2 and headless control animals (two blue traces). All plots in **b**-**g** show data from 5 flies with 10 trials each. Statistical tests compare the trial mean across different flies. *** = p<0.001, ** = p<0.01, * = p<0.05, n.s. = p>0.05. For exact p-values, see Methods.
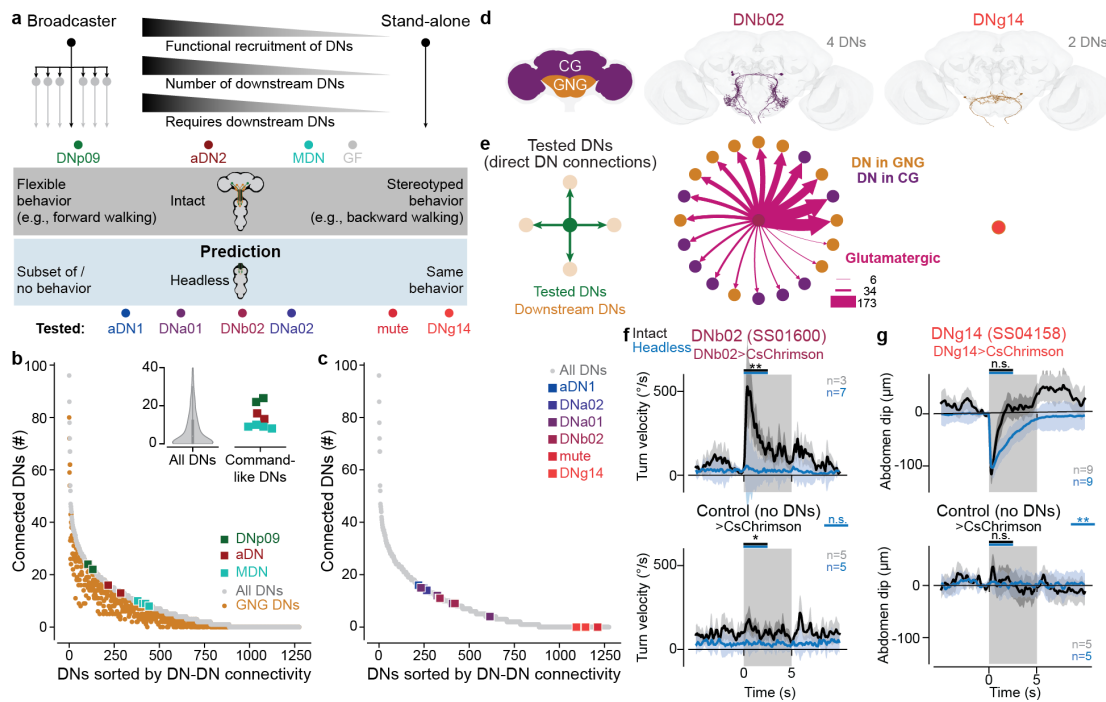
Figure 4.5 - See Figure Legend on next page.

4.3.5 Descending neuron connectivity predicts the necessity for DN recruitment to drive behavior

Our results thus far reveal a correlation between three properties of command-like DNs **(Figure 4.5a, top)**: the functional recruitment of other DNs **(Figure 4.2)**, monosynaptic connectivity to downstream DNs **(Figure 4.3)**, and the necessity of downstream DNs to generate complete optogenetically-driven behaviors **(Figure 4.4)**. For example, for DNp09, optogenetic stimulation activates many other DNs, DNp09 has many downstream DN partners, and they cannot drive forward walking in headless animals. By contrast, for MDN, optogenetic stimulation activates fewer GNG-DNs, MDN has fewer direct downstream DN partners, and they alone are sufficient to drive backward walking in headless animals. Thus, we propose that command-like DNs lay on a continuum between 'broadcaster' DNs like DNp09, which have a large number of downstream DNs that are recruited and required to execute flexible behaviors, and 'stand-alone' DNs which do not have any downstream DNs and are by themselves sufficient to drive stereotyped movements **(Figure 4.5a, gray box)**. This hypothesis suggests that the strength of a DN's connectivity to other DNs is predictive of the behavioral outcome of optogenetic stimulation in intact versus headless animals. Specifically, broadcaster or stand-alone DNs should exhibit a strong or weak degradation of a flexible or stereotyped behavior, respectively, following decapitation **(Figure 4.5a, light blue box)**.

Figure 4.5: Network connectivity accurately predicts the necessity for other DNs and flexibility of DN-driven behaviors. (a) For the three command-like DNs investigated three properties covary: (i) the number of functionally recruited DNs, (ii) the number of directly connected downstream DNs, and (iii) the requirement of downstream DNs to generate a complete behavior. This implies a continuum across DNs that spans from 'broadcaster' DNs like DNp09—which recruit large networks of DNs that are required to drive flexible behaviors—to 'stand-alone' DNs—which recruit no other DNs to drive stereotyped behaviors. We include giant fiber neurons (GF, grey) in this category based on previous studies of headless animals [84, 261] and their small number of downstream DNs. These findings predict the requirement and behavioral flexibility of other, untested DNs. Namely, that optogenetically activating a broadcaster DN with many directly connected downstream DNs should drive more flexible behaviors that are lost in headless animals. Conversely, optogenetically activating a stand-alone DN with few directly connected downstream DNs should drive relatively simple behaviors that are retained in headless animals. Schematized along this continuum are our three tested command-like DNs (DNp09, aDN2, and MDN), as well as six additional untested neurons for which we make connectome-based predictions: aDN1, DNa01, DNb02, DNa02, Mute, and DNg14. Their positions on the horizontal continuum are coarsely defined. **(b)** The number of all (grey circles) or GNG-based (orange circles) DNs monosynaptically downstream of each individual *Drosophila* DN. Command-like DNs of interest are color-coded as elsewhere. Inset shows the median, 25 %, and 75 % quantile of DNs targeted for all DNs (left violin plot) and the number of DNs targeted by three sets of command-like DNs (DNp09, aDN2, MDN). **(c)** The number of DNs directly downstream of six sets of additional DNs (color-coded circles as in **a**) for which we make connectome-based predictions. All DNs are shown for reference as in **b** (grey circles). **(d)** The morphology in the female adult fly brain connectome of two sets of DNs (DNb02, DNg14) for which we test connectome-based predictions. **(e)** Monosynaptic connectivity for the two tested DNs. DNb02 has many connections, akin to the 'broadcaster' DN class, whereas DNg14 does not connect to any other DNs in the brain, akin to the 'stand-alone' DN class. Edge weights denote the number of synapses. Edge colors denote excitatory (red), inhibitory (blue), or glutamatergic (pink) which can be excitatory or inhibitory depending on receptor type [258]. **(f)** Absolute turn velocity for DNb02 (top) and control (bottom) animals upon optogenetic stimulation. This magnitude of the turn velocity is not directed (i.e., leftward or rightward). **(g)** Abdomen dipping for DNg14 (top) and control (bottom) animals upon optogenetic stimulation. Abdomen dipping is quantified as the change in vertical position of the anal plate. In **f** and **g**, shown are data for intact (black traces) and headless (blue traces) animals. The number of animals are indicated for each condition. Each animal was optogenetically stimulated 10 times. Thus, the traces show the average and 95 % confidence interval of the mean across $n * 10$ trials. Shown are Mann-Whitney U tests comparing the trial mean of intact and headless animals (black bars) or comparing headless experimental with headless control flies (blue bars, result shown between top and bottom plot). *** = p<0.001, ** = p<0.01, * = p<0.05, n.s. = p>0.05. For exact p-values, see Methods.

Chapter 4
Networks of Descending Neurons transform command-like signals
into population-based behavioral control

To test these predictions, we sought additional broadcaster and stand-alone DNs by examining direct DN-DN connectivity for all DNs in the brain connectome. There, we observed a continuum of DN-DN connectivity for DNs across the entire brain **(Figure 4.5b, gray)** that was also present in GNG-based DNs specifically **(Figure 4.5b, orange)**. A few DNs have dozens of DN partners while hundreds of DNs have no downstream DNs. Our three sets of command-like DNs are in the middle of this continuum with higher connectivity than most DNs (median number of connected DNs: 4; MDN: 9; aDN2: 15; DNp09: 23; **Figure 4.5b, inset**). Notably, consistent with our hypothesis, giant fiber neurons (GF) have only a few DN partners (three and four for the left and right GFs, respectively; **Figure 4.5a, gray**) and are known to drive stereotyped, ballistic escape in both intact and headless animals [84, 261].

We selected six sets of DNs along this continuum **(Figure 4.5c, colored squares)** by identifying those with available genetic driver lines [32, 44] and that fulfilled additional criteria (see Methods). We optogenetically stimulated these sets of DNs in animals that were either intact or headless. Data from these six experiments confirmed our predictions: DNs driving more flexible behaviors in intact animals and with many downstream DNs lost their behavior in headless animals while DNs without any downstream partners elicited stereotyped movements that were maintained in headless animals.

Among broadcasters, this was most profound for DNb02. These DNs synapse upon 20 other DNs **(Figure 4.5d-e)** and drive turning in intact animals. In headless animals, DNb02 stimulation does not elicit turning **(Figure 4.5f**, $p = 0.001$ comparing intact and headless flies) but instead drives flexion of the front legs at stimulation onset **(Video 4.12)**. This is noticeable as a small spike in forward velocity in headless animals **(Figure S4.3c)**. Similarly, turning was lost in DNa01 **(Figure S4.3b, Video 4.13)** and DNa02 **(Figure S4.3d, Video 4.14)**) animals. aDN1 animals retained only partial behaviors—anterior grooming became uncoordinated front-leg movements in headless animals **(Figure S4.3a, Video 4.15)**).

Among stand-alone DNs, the maintenance of stereotyped behaviors was most clear for DNg14. These DNs do not directly synapse upon any other DN **(Figure 4.5e)** and their activation triggers a subtle dip and vibration of the abdomen in both intact and headless animals **(Figure 4.5g**, $p = 0.144$, **Video 4.16)**. Similarly, ovipositor extension was retained in headless Mute animals **(Figure S4.3f, Video 4.17)**).

Thus, our hypothesis that DN downstream connectivity is predictive of the kind of DN-driven behavior (flexible versus stereotyped) and its requirement for network recruitment is supported by experiments on ten DNs spanning the continuum from those driving flexible behaviors (DNp09-induced forward walking, DNa01/DNa02/DNb02 induced turning, and aDN1/aDN2-induced grooming) to those driving stereotyped (giant fiber-induced escape jump [261], and MDN-induced backward walking) behaviors and movements (DNg14-induced abdominal dipping/vibration, and Mute-induced ovipositor extension).

4.3.6   DN networks cluster as a function of associated behaviors

Our investigation of the brain connectome revealed that DN-DN connectivity lies on a continuum: a few DNs have very high, hub-like connectivity (e.g., >80 downstream DNs), while 567 (44 %) target only two or fewer DNs **(Figure 4.5b)**. Hub-like DNs of high-degree connectivity suggest an overall structure of DN networks that would have implications on how information flows between neurons. Therefore, we next examined the large-scale structure of the entire DN network. To do this, we compared the DN network derived from the fly brain connectome with a shuffled DN network having the same number of neurons and the same number of overall connections between neurons, but with individual connections randomly assigned. We found that the connectivity degree distribution (i.e., the distribution of how many other DNs each DN connects to) is indeed dramatically different ($R^2 = -0.04$ comparing connectivity distributions) between the original DN network (**Figure 4.6a, black**) and the shuffled network (**Figure 4.6a, red**). This is largely because very strongly connected DNs (>30 partners) and very weakly connected ones (<5 partners) only appear in the original connectome DN network but not in the shuffled network. The original DN network can be fit better by an exponential ($R^2 = 0.92$, green) or a power law ($R^2 = 0.79$, blue) degree distribution, indicative of intrinsic structure. A power law connectivity degree distribution is the defining feature of a scale-free network [262, 263] and hints at an underlying structure of DNs linked through well-connected 'hub' neurons.

Inherent structure within this network may be indicative of sub-networks, or clusters, with unique properties. In the case of DNs, our initial analysis of command-like DNs downstream partners suggest the existence of non-overlapping networks for forward walking (DNp09) versus anterior grooming (aDN2). To further explore this possibility, we identified clusters of DNs within the entire fly brain and applied the Louvain method—a community detection algorithm [264]—to the undirected network of DNs (i.e., connections between two neurons are scaled by their synaptic strength and neurotransmitter identity, but the directionality of the connection is not taken into account; see Methods). Indeed, we could reliably identify multiple clusters of DNs with strong inter-connectivity **(Figure 4.6b, gray boxes)**. Importantly, when we applied the same algorithm to our shuffled network with the same size, same number of neurons, same connection weights, but randomly shuffled connections, we only inconsistently found small clusters **(Figure 4.6c, gray boxes)**. This was clear by quantifying the number of DNs in the five largest clusters for the original DN-DN network (726 ± 42 neurons) versus the shuffled DN-DN network (581 ± 51 neurons; mean $\pm$ std, $p < 0.001$ comparing 100 repetitions of the Louvain method).

Within clusters we observed predominantly strong excitatory connections **(Figure 4.6d, diagonal elements)**. By contrast, between clusters we observed predominantly inhibition **(Figure 4.6d, off-diagonal elements)**, localized between specific clusters. In the shuffled DN-DN network, this inhibition was weaker and more uniformly distributed **(Figure 4.6e, off-diagonal elements)**.
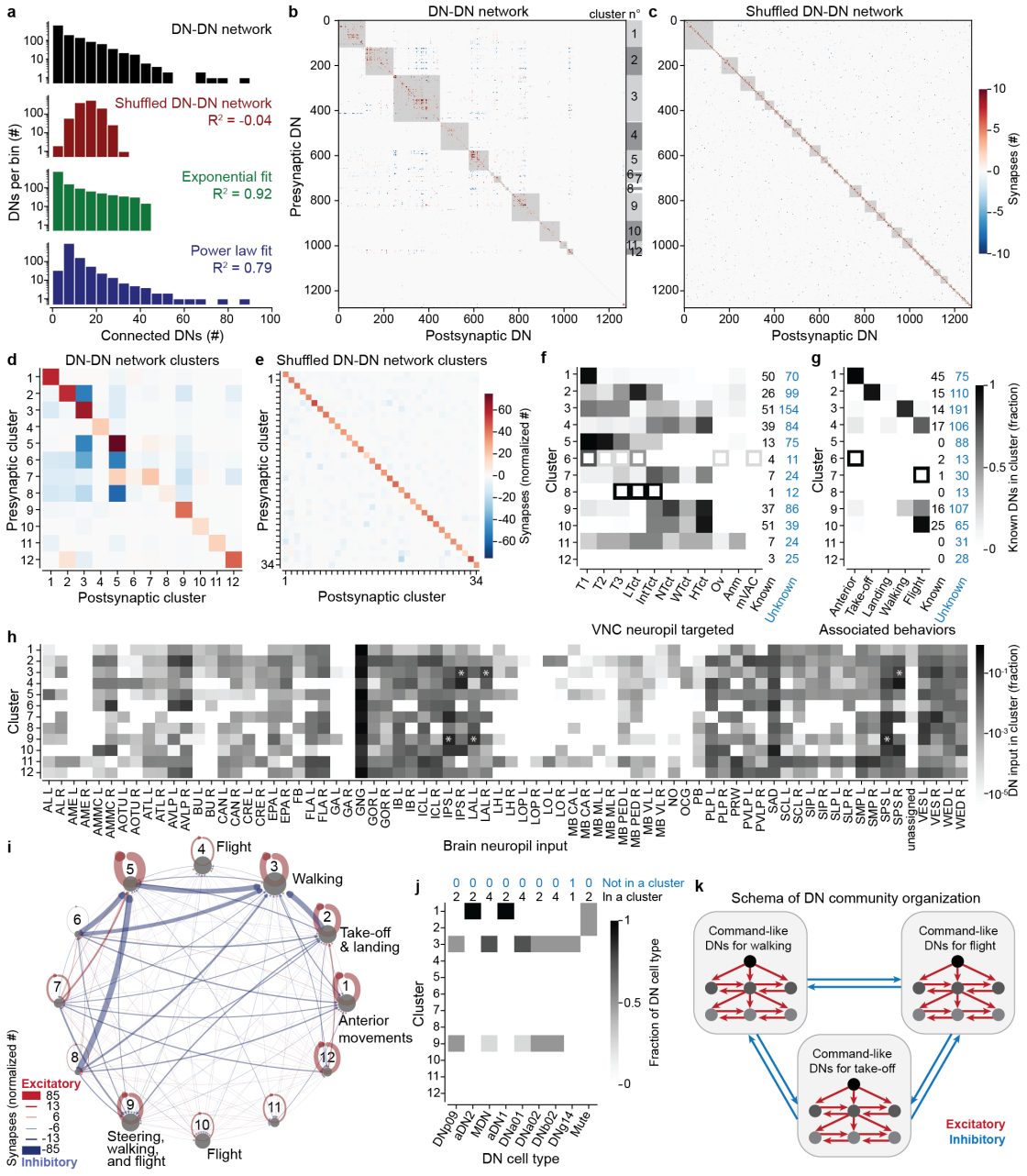
Figure 4.6 - See Figure Legend on next page.

Distinct excitatory clusters could imply parallel pathways of descending neurons with distinct anatomical and/or functional properties. We examined this possibility by first investigating whether DN clusters (with similar connectivity in the brain) connect to similar targets in the VNC. Specifically, we studied the projections of known DNs [32, 86] within the VNC connectome of an adult male fly [35]. This analysis revealed very specific connectivity patterns including, for example, that cluster 1 projects predominantly to regions controlling the front leg (T1 neuropil), cluster 2 predominantly to the lower tectulum (LTct), clusters 3 and 5 most strongly to the leg neuropils (T1, T2, T3) and clusters 4, 7, 9 and 10

Networks of Descending Neurons transform command-like signals
into population-based behavioral control
Chapter 4

Figure 4.6: Networks of DNs for similar behaviors excite one another and inhibit those for other behaviors. (a) The connectivity degree distribution of (black) the DN-DN network as a histogram (bin width 5) on a logarithmic scale and (red) the same data after shuffling individual connections between DNs. Shown as well are the best exponential (green) or power-law degree distribution (blue) fits to the DN-DN network data. **(b)** A community detection algorithm applied to the DN connectivity matrix yields large clusters (grey squares). DNs are sorted based on detected clusters. Excitatory (red) and inhibitory (blue) connectivity between individual DNs from row (presynaptic) to column (postsynaptic) are color-coded. Numbers on the right side map onto cluster numbers in **d,f,g,h,i,j**. **(c)** Equivalent analysis to **b**, but for a network with shuffled DN-DN network connectivity. **(d)** The number of synapses between any two clusters normalized by the number of DNs in the postsynaptic cluster. Only clusters with 10 or more DNs are considered. Synapse weights are summed such that one excitatory synapse and one inhibitory synapse is shown as no synapse. **(e)** Equivalent analysis to **d**, but for the shuffled network in **c**. **(f)** For each cluster, the fraction of known DNs projecting to different neuropil regions within the VNC (T1,T2,T3: leg neuropils, LTct: lower tectulum, IntTct: intermediate tectulum, NTct: neck tectulum, WTct: wing tectulum, HTct: haltere tectulum, Ov: ovoid, Anm: abdominal neuromere, mVAC: medial ventral association center) is shown. Data are taken from [35] (**Supporting Information File 1**). The number of known (black) versus unknown (blue) DNs per cluster is indicated (right). Empty squares indicate clusters containing fewer than five known DNs. **(g)** For each cluster, the fraction of known DNs associated with different behaviors (anterior movements, take-off, landing, walking, flight) is shown. The number of known (black) and (blue) unknown DNs per cluster is indicated (right). Data are taken from the literature (**Supporting Information File 2**). Empty squares indicate clusters containing fewer than five known DNs. **(h)** For each cluster, the fraction of DN input synapses from different brain neuropils. Asterisks indicate a left-right imbalance among inputs to clusters 3 and 9 from the IPS, SPS and LAL. Note that these data are shown on a log scale. Neuropil names are described in Methods. **(i)** A network visualization of clusters in **d**. Overlaid are associated behavior annotations from **g**. Edge weights indicate the relative strength of excitatory (red) or inhibitory (blue) connectivity. **(j)** The distribution of optogenetically investigated DNs across DN clusters. The number of DNs inside (black) and outside (blue) the 12 clusters is indicated (top). **(k)** A summary model of the proposed organization among DN networks. There are predominantly excitatory (red) connections within each DN cluster. Each cluster may have its own hierarchical network sub-structure, with command-like DNs recruiting other DNs in a excitatory fashion. There are inhibitory (blue) connections between DN clusters.

predominantly to dorsal neuropil regions involved in wing, haltere, and neck control (WTct, HTct, NTct) **(Figure 4.6f)**.

These results strongly imply that excitatory DN clusters may also regulate distinct behaviors. We examined this possibility by identifying 132 known DNs which are shown or predicted to be involved in anterior movements, walking, take-off, flight, and landing (see **Supplementary Data File 2** and Methods for details). Indeed, we found that the clusters included DNs with known links to specific behaviors **(Figure 4.6g)**. For example, as might be expected,

DNs related to anterior grooming were predominantly in cluster 1 which targets T1 (e.g., DNg10 [83], DNg12 [83], aDN1 [61], aDN2 [61]). All DNs involved in take-off and, more weakly, landing were in the cluster 2 (e.g., giant fiber/DNp01 [90], DNp02 [77], DNp04 [77], DNp10 for landing [76], DNp11 [77], DNp35 [35]). Many DNs related to walking were in cluster 3 with strong projections to T1-T3 (e.g., DNp09 [79], DNa01 [95], DNa02 [91], DNb02 [265], DNg13 [35], MDN [86]). This cluster also receives strong inhibition, particularly from cluster 2 related to take-off **(Figure 4.6i)**. Cluster 5 also mainly projects to the leg neuropils (T1-T3), but the behavioral phenotype of its constituent DNs are unknown. DNs related to flight were also localized to clusters 4 (e.g. DNa10 [35], DNg02 [80], DNp20 [93]) and 10 (e.g. DNg02 [80], DNg07 [80], DNp31 [35]). Some additional flight-related neurons involved in steering are in cluster 9 (e.g. DNp03 [35], DNg02 [80]), grouped with walking DNs known to be involved in turning.

The command-like DNs we studied experimentally were part of behavioral consistent clusters as well **(Figure 4.6j)**. aDN1, aDN2 in the 'anterior movement' cluster 1 and DNp09, MDN, DNa01, DNa02, DNb02 in the 'walking' or 'steering' clusters 3 & 9, with neurons in the right hemisphere being assigned mainly to cluster 3 and those of the left hemisphere being assigned to cluster 9. This split of DNs associated with walking between clusters 3 and 9 was due to differences in connectivity between the two brain hemispheres, both in terms of bilateral symmetry in the brain as well as from the localization of the inputs coming from the inferior posterior slope (IPS), superior posterior slope (SPS) and the lateral accessory lobe (LAL) **(Figure 4.6h, white asterisks)**.

Taken together, these data support a model in which complete behaviors are orchestrated by specific excitatory DN subnetworks which, in turn, inhibit other subnetworks driving potentially conflicting behaviors **(Figure 4.6k)**.

4.4   Discussion

Here, by combining optogenetic activation, functional imaging, and brain connectome analysis, we have resolved two seemingly conflicting observations: The activation of a few command-like DNs is sufficient to drive complete behaviors like forward walking, nevertheless many DNs are active when the same behavior is generated spontaneously. To explain this discrepancy, we propose a model in which command-like DNs recruit additional DN networks. This network recruitment is required for flexible forward walking but less critical for more stereotyped backward walking. Indeed, brain connectivity analyses suggest that all DNs generally lie along a continuum in which those driving more flexible behaviors recruit and require the activity of large DN networks, whereas those driving stereotyped behaviors and movements have dispensable connections to only a few downstream DNs. This model makes predictions which we confirmed through experiments on additional DNs. Finally, DN networks at a larger scale form excitatory clusters with specific behavioral roles and downstream targets in the motor system. These functionally distinct clusters inhibit one another, providing a potential mechanism for action selection in the brain.

4.4.1   Circuit mechanisms giving rise to DN networks

There are a number of circuit motifs that could give rise to DN-DN interactions. Although we focus on monosynaptic connectivity, we have also shown that command-like DNs (DNp09, aDN2 and MDN) ultimately reach—and may potentially activate—hundreds of other DNs within only a few synapses. Thus, DN populations recruited by the activation of command-like DNs in our functional studies may also be multiple synapses away. Although the temporal limitations of calcium imaging preclude the ability to distinguish between mono- or polysynaptic recruitment, in the future it may be possible to map the identity of recruited DNs onto the connectome by taking advantage of volumetric anatomical recordings of the cervical connective and anterior VNC along with computational approaches to register functional recording data to an anatomical template [266].

Most of the monosynaptic connections between DNs are in the GNG. Akin to the mammalian brain stem, the GNG is a multi-sensory processing region [41–44] that controls head and proboscis movements [50, 51]. The presence of numerous DN inputs and outputs also make the GNG well-positioned as a locus for action selection [53]. In line with this possibility, we found predominantly excitatory clusters of DNs that mediate distinct behaviors and inhibit one another.

Interestingly, the GNG also receives a large number of inputs from ascending neurons (ANs) that project from the VNC to the brain [47, 48]. Among these are a set of ANs involved in deciding between locomotion and feeding [267]. Connections from ANs may thus allow DNs to integrate motor information from the VNC potentially to regulate switching during a sequence of actions. DN-DN recruitment could also potentially arise indirectly through ANs in a DN-AN-DN 'zigzag' motif that has previously been observed in low numbers in the *Drosophila* larval connectome [175] (i.e., a DN targets an AN in the VNC which projects back to the brain and to a different DN). Our headless fly experiments cannot discriminate the contribution of ANs (decapitation eliminates both DN-DN and putative DN-AN-DN connections). ANs encompass 17 % of all DN post-synaptic partners in the VNC [35] and 10 % of all DN pre-synaptic partners in the brain. Efforts aiming to bridge the existing brain and VNC connectomes [50, 176, 177] and to generate complete adult nervous system connectomes will further reveal the extent of DN-AN-DN circuit motifs in adult flies.

Alternatively, DN recruitment might arise indirectly via sensory feedback during a change in behavioral state: Active DNs may drive a new behavior which results in sensory feedback that in turn may be transmitted through ANs to influence other DNs. We would expect to see such sensory-induced DN activation in spontaneous occurrences of the behavior. However, we instead observed that, in general, fewer DNs are strongly activated during spontaneous behaviors compared with during optogenetically elicited behaviors. This argues that strong GNG-DN activation is a specific response to optogenetic stimulation of command-like DNs. In particular, we observed that the 10 most active neurons during DNp09 stimulation are not active during spontaneous forward walking. These results suggest that DN recruitment likely does not result from sensory feedback arising during optogenetically-induced changes in behavioral state.

In addition to excitatory interactions among DNs, on a larger scale, we observed that DN clusters related to distinct behaviors inhibit one another. Direct DN-DN connectivity is rare in the VNC (only 2 % of all DN post-synaptic partners in the VNC are DNs [35]) compared to strong and prominent DN-DN connections within the brain (32 % of all DN post-synaptic partners in the brain are DNs). This inhibition is thus likely restricted to the brain because these DN clusters mostly project to different downstream targets within the VNC. Most DNs project either to the dorsal neuropils (wing, neck, haltere), or to the ventral leg neuropils. Only a few DNs, related to behaviors like take-off and landing—which require the coordination of both legs and wings—project to both of these regions [32, 35]. Additionally, a preliminary examination of how DNs in this study connect to one another in the male VNC connectome [35, 177] shows that DNp09, giant fiber, DNa01, DNa02, and DNg14 do not synapse onto other DNs in the VNC. MDN and DNb02 connect to one and two DN cell types in the VNC, respectively. Thus, we can conclude that DN-DN interactions in the VNC are rare.

4.4.2 The utility of DN networks

We have shown that precise stimulation of multiple classes of command-like DNs recruits activity in many additional DNs. Thus, the 'command' signal is not only conveyed directly to the VNC, but can also be sent to other brain neurons that, in parallel, convey additional descending signals. Interestingly, the strength of this DN recruitment varies across command-like DNs in a manner that correlates with behavioral flexibility as well as the necessity of these connections to generate a complete behavior. These results are most consistent with a descending control model in which most DNs drive relatively simple body part kinematics. Then, some privileged DNs (e.g., command-like DNs) directly recruit other DNs that, together, act as building blocks to construct a full behavior. This is in line with earlier observations in other insects that suggest that descending fibers may 'act in consensus' to assemble a complete behavior from different 'subroutines' [268]. For example, DNp09 is connected to and requires the actions of a large number of DNs to drive elaborate movements of the six legs for goal-directed walking during courtship [79]. Both DNp09 (for forward walking) and MDN (for backward walking) synapse upon DNa01 and DNa02, two other DNs involved in turning [91, 95]. Turning may therefore represent a behavioral building block that is used to construct both forward or backward walking. Notably, we found that DNa01 and DNa02 also synapse onto other DNs and that their activation alone (in headless animals) is not sufficient to drive turning. Thus, they may also sit higher in a hierarchy of DN recruitment activating yet other DNs which control specific movements required for turning. In the extreme case, such building blocks may be single degree-of-freedom movements like the lowering of the abdomen driven by DNg14—a pair of DNs that do not have any downstream DNs, but receive inputs from twelve upstream DNs.

These behavioral building blocks are analogous to 'motor primitives'—fundamental elements for generating flexible behaviors in both vertebrates and invertebrates [269]. In mammals it has been posited that complex behaviors are learnt by flexibly combining such motor

primitives [270] potentially through a motor cortical network gain modulation mechanism [271] and in vertebrates, frogs can combine motor primitives stored in the spinal cord [272]. Combining different motor primitives at the level of DNs may thus be a mechanism to ensure flexible descending control [10].

By contrast, other DNs can act alone to drive relevant downstream motor circuits and behaviors. These include the giant fiber which connects to a very small number of DNs and triggers a stereotyped and ballistic escape behavior. Similarly, MDNs with few downstream DNs drive backward walking. Neural activity during spontaneous and optogenetically-elicited backward walking was very similar, confirming that the control of backward walking is highly stereotyped. Both giant fiber and MDN are sufficient to drive their respective behaviors and do not rely on other DNs. Such a distinction between the mechanisms of descending control for flexible (walking) versus stereotyped (stridulation) behaviors has been proposed from studies in Orthoptera [273]. This continuum of well-connected (DNp09) to largely disconnected (giant fiber) command-like DNs demonstrates that the classification of a DN as 'command-like' lies not only in its DN-DN connectivity. Instead, command-like DNs can drive complete behaviors through two distinct mechanisms: either by relying strongly on co-recruitment of other DNs in the brain or solely through their actions on VNC circuits.

In general, a descending control framework in which DNs can potentially recruit additional DNs, each of which control simple movements, provides an effective substrate for the evolutionary modification of behaviors (e.g., diversification of species-specific courtship displays), or the generation of entirely new behaviors through the *de novo* coupling or uncoupling of DNs. Thus, it is likely that a similar mechanism is leveraged for descending control in other species including mammals [72, 270] and may be used to inspire the design of better artificial controllers in engineering and robotics [22].

4.5 Methods

4.5.1 Fly stocks and husbandry

All experiments were performed on female adult *Drosophila melanogaster* raised at 25°C and 50 % humidity on a 12 hr light–dark cycle. The day before optogenetic experiments (22-26 h before), we transferred experimental and control [274] flies to a vial containing food covered with $20\mu l$ of all trans-retinal (ATR) solution (100mM ATR in 100 % ethanol; Sigma Aldrich R2500, Merck, Germany) and wrapped in aluminium foil.

Functional imaging and behavior experiments

We generated transgenic flies expressing LexAop-opGCaMP6s (generous gift from Orkun Akin [275]) under the control of a Dfd-LexA driver (generous gift from Julie Simpson [168]) and having a copy of UAS-CsChrimson (Bloomington ID 55135): **(Table 4.1, ID 1)** We also generated flies that additionally expressed LexAop-tdTomato (Bloomington ID 77139):

(Table 4.1, ID 2). For most experiments we used the flies lacking tdTomato expression. MDN-spGAL4 flies (also known as MDN3 from [86]) were used to drive backward walking. aDN2-spGAL4 flies (also known as aDN2-spGAL4-2 from [61]) were used to drive antennal grooming. DNp09 spGAL4 flies (from [79]) were used to drive forward walking. Their genotypes are listed at the top of **Table 4.2**.

For all experiments in **Figure 4.2 and Figure 4.4** we crossed those spGAL4 flies or wild type flies (PR - Phinney Ridge flies, Dickinson lab) with one of our stable transgenic driver lines for imaging **(Table 4.1, ID 1 or 2)**. For experiments in **Figure 4.2** flies were 2-9 days post-eclosion at the time of experiments and experiments were performed at Zeitgeber time ZT 7-13. For experiments in **Figure 4.4** flies were 2-9 days post-eclosion at the time of experiments and experiments were performed at Zeitgeber time ZT 4-7. For experiments in **Figure 4.5, Figure S4.3** we crossed spGAL4 lines with 20XUAS-CsChrimson.mVenus (attP40) flies (Bloomington ID 55135). The exact genotypes of the split lines and the source stock are listed in the **Table 4.2**. All experiments were performed on flies 4-8 days post-eclosion (dpe), at Zeitgeber time ZT 4-7.

Confocal imaging experiments

We generated flies with stable Dfd expression of membrane-targeted tdTomato, or nuclear-targeted mCherry based on flies generated by the Laboratory of Neural Genetics and Disease (McCabe laboratory, EPFL): **(Table 4.1, ID 3 and 4)**. For the three split-GAL4 driver lines targeting command-like DNs (MDN, DNp09, aDN2), we generated stable lines expressing UAS-CsChrimson: **(Table 4.1, ID 5,6, and 7)**. We crossed flies expressing a red fluorescent protein variant with flies expressing CsChrimson in a split GAL4 driver line to visualise the expression patterns using confocal imaging (**Figure S4.1**).

ID	Chromosome X	Chromosome II	Chromosome III
1		20xUAS-CsChr.mVenus (attP40), 13xLexAop-opGCaMP6s (su(Hw)attP5)	DfdLexA / TM6B
2		20xUAS-CsChr.mVenus (attP40), 13xLexAop-opGCaMP6s (su(Hw)attP5)	13xLexAop-CD4-tdTomato (VK00033), DfdLexA / TM6B
3		LexOp-myr-TdTomato / CyO	DfdLexA / TM6B
4		LexOP-H2B::mCherry / CyO	DfdLexA / TM6B
5	20xUAS-CsChr. [mVenus]attP18	VT023490-p65.AD	VT44845.GAL4DBD
6	20xUAS-CsChr. [mVenus]attP18	R76F12-AD	R18C11-DBD
7	20xUAS-CsChr. [mVenus]attP18	VT023490-p65.AD	R38F04-GAL4.DBD

Table 4.1: Transgenic fly lines generated in this study.

DN	Split	Ref.	Source Stock	Stock n°	AD	DBD
MDN	SS03131	[86]	Janelia	n.a.	VT023490	VT44845
aDN2	n.a.	[61]	Julie Simpson	n.a.	R76F12	R18C11
DNp09	SS01540	[79]	Bloomington	75903	VT023490	R38F04
DNa01	SS00731	[32]	Bloomington	75862	R22C05	R56G08
DNa02	SS00730	[32]	Janelia	n.a.	75C10	87D07
aDN1	n.a.	[61]	Julie Simpson	n.a.	18C11	R71D01
Web	SS41434	[44]	Janelia	n.a.	VT023750	VT043284
DNb02	SS01600	[32]	Bloomington	75901	R59B10	R21F05
Mute	SS42606	[44]	Janelia	n.a.	26C03	84D10
DNp24	SS01046	[32]	Bloomington	75821	VT048835	R24C07
DNg30	SS02378	[32]	Bloomington	75872	R61A01	R13B05
DNg14	SS04158	[32]	Bloomington	75812	R53D12	VT018689

Table 4.2: SpGAL4 lines used in this study.

Recording from DNs using a Dfd driver line

We leveraged a genetic-optical intersectional approach to selectively record from GNG-DNs. We chose to record from GNG-DNs because we found that 73 % of all DN-DN synapses in the brain connectome are in the GNG. Additionally, the GNG houses 60% of all DNs and 85% of all DNs have axonal output in the GNG[32]. However the Hox gene Dfd does not include the entirety of all GNG-DNs as it excludes those driven by the Hox gene Sex combs reduced (Scr) [276]. Sterne et al.[44] estimate that 550 cells in the GNG are Dfd positive and 1100 Scr positive, with only a small fraction expressing both. We show, for example, that aDN2, while localized to the GNG, is Dfd negative and thus most likely Scr positive **(Figure S4.1c)**. In our hands, functional imaging of DNs using an Scr driver line proved to be difficult because Scr expression extends into the neck and anterior VNC [168]. Specifically, we observed strong expression of GCaMP in the tissues surrounding the thoracic cervical connective (potentially ensheathing glia [277]), making it very hard to record the activity of DN axons. We expect that some Scr-positive DNs will be recruited by command-like DNs as for Dfd-positive DNs. Thus, we likely under-report the number of recruited GNG DNs.

Limitations of selected spGAL4 driver lines

In addition to descending neurons, our aDN2 spGAL4 driver line (*aDN2-GAL4.2* [61]) contains two groups of additional neurons. One pair is on the anterior surface of the brain and, based on our control experiments, likely is not or is only weakly activated by targeted optical stimulation of the neck (and not at all activated by the thoracic stimulation). Another is a set of neurons in the anterior VNC. Because other driver lines targeting aDN2 neurons with more, other off-target neurons have the same behavioral phenotype as our aDN2 driver [61], we are more confident that the effects we observe are due to stimulating the aDN2 neurons themselves.

Different studies report variable behavioral phenotypes for stimulating the DNp09-spGAL4 driver line: Some saw forward walking [79], while others observed stopping or freezing [81, 85]. We observed both: at our standard 10μW optogenetic stimulation power, heterozygous animals mostly walked forward. Occasionally flies would only transiently walk forward and then stop, or alternate rhythmically between walking and stopping. With higher expression levels of CsChrimson (i.e., DNp09-spGAL4 > UAS-CsChrimson homozygous animals) we observed mostly freezing. We used heterozygous animals for our study.

4.5.2   Immunofluorescence tissue staining and confocal imaging

We dissected brains and VNCs from 3–6 dpe female flies as described in [48].

For samples in **Figure S4.1**a,c, we fixed flies in 4 % PFA (Paraformaldehyde, 441244-1KG, Sigma Aldrich, Merck, Germany) in 0.1M PBS (Gibco PBS, pH 7.4, 10010-015, ThermoFisher Scientific, Switzerland). We then washed them six times for 10 min with 1 % Triton (Triton X-100, X100-100ML, Sigma Aldrich, Merck, Germany) in PBS (thereafter named 1 % PBST) at room temperature (RT). We then transferred them to a solution of 1 % PBST, 5 % Natural Goat Serum (Goat serum from controlled donor herd, G6767-100ML, Sigma Aldrich, Merck, Germany) and primary antibodies (see **Table 4.3**) and left them overnight at 4°C. We then washed the samples six times for 10 min with 1 %PBST at RT. We then transferred them to a solution of 1 % PBST, 5 % Natural Goat Serum and secondary antibodies (see **Table 4.3**) and left them for two hours at RT. We then washed the samples six times for 10 min with 1 % PBST at RT. We mounted the samples on glass slides using SlowFade (SlowFade Gold Antifade Mountant, S36936, ThermoFisher Scientific, Switzerland) and applied a cover slip. To space the slide and the cover slip, we applied a small square of two layers of double-sided tape at each edge. We sealed the edges of the coverslip with nail polish.

For samples in **Figure S4.1**b we fixed flies in 4 % PFA in PBS and transferred them to 1 % PBST and left them overnight at 4 °C. We then washed the samples 3 times for 15 min with 1 % PBST at RT. We then transferred them to a solution of 1 % PBST, 5 % Natural Goat Serum and primary antibodies (see **Table 4.3**) and left them overnight at 4 °C. We then washed the samples 3 times for 15 min with 1 % PBST at RT. We then transferred them to a solution of 1 % PBST, 5 % Natural Goat Serum and secondary antibodies (see **Table 4.3**) and left them overnight at 4 °C. We then washed the samples 3 times for 15 min with 1 % PBST at RT. We mounted the samples on glass slides using SlowFade and applied a cover slip. To space the slide and the cover slip, we applied a small square of two layers of double-sided tape at each edge. We sealed the edges of the coverslip with nail polish.

We imaged samples using a Leica SP8 Point Scanning Confocal Microscope with the following settings: 20x, 0.75 NA HC PL APO dry objective, 2× image averaging, 1024x1024 pixels, 0.52×0.52μm pixel size, 0.57μm z-step interval; green channel 488nm excitation, 500-540nm emission bandpass; red channel (imaged separately to avoid cross-contamination)

figure	type	AB name	dilution	company	AB ID
a,b,c	1°	Anti-Bruchpilot (mouse) NC82	1:20	Dev. Studies Hybridoma	NC82 1ml supernatant
a,c	1°	GFP Tag Rabbit	1:500	ThermoFisher	G10362
a,b,c	2°	Goat anti-Mouse Alexa 633	1:500	ThermoFisher	A21052
a,c	2°	Goat anti-Rabbit Alexa 488	1:500	ThermoFisher	A11008
b	1°	Living Colors DsRed	1:500	Takara	632496
b	1°	Chicken to GFP Anti-GFP	1:1000	abcam	ab13970
b	2°	Goat Anti-Rabbit (Cy3)	1:500	abcam	ab6939
b	2°	Goat Anti-Chicken (Alexa 488)	1:500	abcam	ab150169

Table 4.3: List of antibodies used for immunofluorescence tissue staining.

552nm excitation, 570-610nm emission bandpass; infrared channel (nc82, imaged in parallel to green channel) 638nm excitation, 650-700nm emission bandpass. We summed the confocal image stacks in the z-axis and rotated and translated the images to center the brain/VNC using Fiji [249].

4.5.3 Optogenetic stimulation system and approach

We used a 640nm laser (Coherent OBIS 1185055 640nm LX 100mW, Edmund Optics, US) as an optogenetic excitation light source. We reduced the light intensity using neutral density filters (Thorlabs, Germany) and controlled the light intensity using mixed analogue and digital control signals coming from an Arduino with custom software. A digital signal was used to turn the laser on and off. An analogue signal (PWM output from Arduino and RC-low pass filtered) was used to modulate the power. Both of those signals were sent in parallel to the laser and an acquisition board and were recorded alongside the two-photon microscope signals using ThorSync 3.2 Software (Thorlabs, Germany). The light was directed towards the fly using multiple mirrors. Fine control of the target location was achieved using a kinematic mount (KM100, Thorlabs, Germany) and a galvanometric mirror (GVS011/M, Thorlabs, Germany). We manually optimized targeting of the laser onto the neck/thorax before each experiment. The light was focused onto the fly using a plano-convex lens with $f = 75.0$ mm (LA1608, Thorlabs, Germany) placed at the focal distance from the fly.

We note that, although command-like DNs have axon collaterals in the GNG, none of the command-like DNs in this study were among the DN populations we imaged: DNp09-spGAL4 and MDN-spGAL4 lines drive expression in neurons with cell bodies in the cerebral ganglia and not in the GNG **(Figure S4.1a)**. The DN cell bodies of the aDN2-spGAL4 line are within the GNG but do not overlap with Dfd driver line expression **(Figure S4.1c)**. Thus, we could be certain that any active DNs would be recruited through synaptic connections and not optogenetically. We identified laser light intensities that could elicit robust forward walking, anterior grooming, and backward walking **(Figure 4.2a, Figure S4.1d)**.

We used different laser intensities to stimulate MDN (10 μW), DNp09 (10 μW), and aDN2 (20 μW) animals, respectively, because 10 μW stimulation power mostly causes aDN2 animals to stop **(Figure S4.1d)**. Activation of MDN in the head, neck, and thorax were sufficient to trigger backward walking **(Figure S4.1e)**. Although some tissue scattering of laser light can be expected, in control experiments we found that activation of the head capsule, but not the thorax, could strongly elicit forward walking in the brain's "Bolt protocerebral neurons" (BPNs)—these neurons are known to drive robust and fast forward walking [79]**(Figure S4.1f)**. 10 μW stimulation was more specific than 20 μW, which is why we selected 10 μW stimulation for MDN and DNp09 as well as the spGAL4 lines tested in **(Figure 4.5f-g, Figure S4.3)**. We regularly calibrated the laser intensity by measuring it with a power meter (PM100D, Thorlabs, Germany) and adjusting the analogue gain of the laser.

4.5.4   In vivo two-photon calcium imaging experiments

We performed two-photon microscopy with a ThorLabs Bergamo II two-photon microscope augmented with a behavioral tracking system as described in [96]. Briefly, we recorded a coronal section of the thoracic cervical connective using galvo-resonance scanning at around 16Hz frame rate. Additionally, optogentic stimulation was performed as described above. We only recorded the green PMT channel (525 ± 25 nm) because the red PMT channel would be saturated by red laser illumination of the fly. In parallel, we recorded animal behavior at 100 frames per second (fps) using two infrared (IR) cameras placed in front of and to the right of the fly.

Flies were dissected to obtain optical access to the VNC and thoracic cervical connective as described in [95]. Briefly, we mounted the fly to a custom stage by gluing its thorax and anterior head to the holder and removed its wings. Then, we opened the dorsal thorax using a syringe needle and waited for indirect flight muscles to degrade for ~ 1.5 h. We pushed aside the trachea and resected the gut and salivary glands. For some flies, where the trachea was obstructing the view, we placed a V-shaped implant [278] into the thoracic cavity to push the trachea to the side. We then placed the fly over an air-suspended spherical treadmill marked with a pattern visible on IR cameras for ball tracking (air flow at 0.6 l/min). While the fly was adapting to this new environment, the imaging region was identified and the optogenetic stimulation laser was centered onto the neck (~ 15 min).

We then recorded 10000 microscopy frames (around 10 min) while also recording behavioral data using cameras placed around the fly and presenting optogenetic stimuli. During a typical 10 min recording session, we presented 40 stimuli (5 s stimulation and 10 s inter-stimulus interval). Whenever the recording quality was still good enough (many neurons were visible and the fly still behaved healthily), we recorded multiple sessions to increase the number of stimulation trials.

4.5.5 Investigating natural behaviors

In **Figure S4.2** we compared optogenetically-elicited neural activity to activity observed during natural behaviors: forward walking, anterior grooming, and backward walking. Natural forward walking is frequently spontaneously generated by the flies. By contrast, we needed to stimulate the antennae with 5 s puffs of humidified air to increase the probability of natural grooming **(Figure S4.2b)**. We provided humidified air puffs with an olfactometer (220A, Aurora Scientific, Canada) using the following parameters: 80 ml/min air flow, 100 % humidity, 5 s duration, 20 s inter-stimulus interval. In order to have humid air puffs (i.e., an abrupt change in flow rate) instead of a switch from dry air to humidified air—the default olfactometer configuration—we only connected the "Odor" tube to the final valve and not the "Air" tube. Furthermore, to increase the likelihood of spontaneous backward walking **(Figure S4.2c)**, we replaced the spherical treadmill with a custom cylindrical treadmill that we found increases the motivation to backward walk. Specifically, we designed a 10 mm diameter, 80 mg 3D printed wheel (RCP-30 resin) and printed it using stereolithography through digital light processing (Envisiontec Perfactory P4 Mini XL). This wheel was mounted on a low-friction jewel-bearing holder (ST-3D sapphire shafts, VS-40 sapphire bearings, Freudiger SA, Switzerland). We marked the sides of the wheel with IR-visible dots to facilitate IR camera tracking of the wheel and calculations of velocity to classify bouts of backward walking. When using the wheel, we used an additional third IR camera to the left of the wheel, where dot markers were visible

4.5.6 Behavioral experiments in headless animals

For behavioral experiments, we mounted flies to the same stages used for two-photon imaging, but without gluing the anterior part of the head to the holder. Then, without further dissection, we placed animals onto the spherical treadmill. After recording 10 trials of responses to optogenetic stimulation in intact animals, we decapitated the fly by inverting the holder and pushing a razor blade onto the neck. To achieve this, we mounted a splinter of the razor blade onto the tip of a pair of dissection forceps for finer control. We took care not to injure the fly's legs and to make a clean cut without pulling out thoracic organs passing through the neck connective. To limit desiccation, we then sealed the stump of the neck with a drop of UV-curable glue. We only continued experiments on flies if their limbs were moving following decapitation. We then placed the headless flies onto the spherical treadmill and let them recover for at least 10 min. Then, we recorded 10 trials of responses to optogenetic stimulation on the spherical treadmill and 10 trials in which the fly was hanging from the holder without contacting the spherical treadmill. In experiments for testing connectome-based predictions, we slightly modified this experimental procedure. Because intact control animals become aroused by optogenetic stimulation, to avoid false positives and to discover behavioral phenotypes for less well-studied DNs, we attempted to reduce the spontaneous movements of flies. First, instead of 10 s between optogenetic stimulation trials, we used 20 s. Second, we filled the fly holder with room-temperature saline solution to buffer heating from IR illumination.

4.5.7 Data exclusion

We manually scored the quality of neural recordings (signal-to-noise ratio, occlusions, etc.) and the behavior of the fly (rigidity, leg injury, etc.) on a scale from 1 to 6 (where 1 is very good, 3 is satisfying, 6 is insufficient) for each 10 min recording session. We only retained sessions in which both criteria were at least at a satisfying quality level. Unless indicated otherwise, we analyzed trials where the fly was walking before stimulus onset. Thus, we did not retain data from flies with less than ten trials of walking before stimulation. We chose to do this for several reasons: (1) GCaMP6s decays very slowly. Even if the fly was moving ~2 s before stimulation, we still observed residual fluorescence signals, increasing the variability of changes upon stimulation. There were only very few instances where the animal was robustly resting for >2 s making the inverse analysis impossible. (2) We observed that control flies became aroused upon laser light stimulation. Thus, they may begin moving if they were resting prior to stimulation, indirectly driving DN activity and making it harder to discriminate between optogenetically-induced versus arousal-induced activity. We nevertheless provide data from flies that were resting before stimulation in **Supplementary File 1**, noting that the recruitment patterns, while not identical, are largely similar. DNp09 shows strong activation in the medial cervical connective (as for when the fly was walking prior to stimulation) and additional activation in lateral regions. The central neurons characteristic of aDN2 activation in animals that were previously walking are also active in animals that were previously resting. Additionally, we observe more widespread, weaker activation. DN signals upon MDN activation were slightly more spread out when the fly was resting prior to stimulation.

For experiments with headless animals, we excluded data from flies where one of the legs was visibly immobile after decapitation or when the abdomen was stuck to the spherical treadmill such that other movements became impossible.

4.5.8 Behavioral data analysis

For analysis, we used custom Python code unless otherwise indicated. Code for behavioral data pre-processing can be found in the 'twoppp' Python package on GitHub previously used in [278]. Code for more detailed analysis can be found in the GitHub repository for this paper.

Velocity computation

As a proxy for walking velocities, we tracked rotations of the spherical treadmill using Fictrac [187]. Data from an IR camera placed in front of the fly was used for these measurements as described in [96]. Raw velocity traces acquired at 100 Hz were noisy and thus low pass filtered with a median filter (width $= 5 = 0.05$ s) and a Gaussian filter ($\sigma = 10 = 0.1$ s).

Behavior	v_{abs} (mm/s)	v_{forw} (mm/s)	fr. leg height	ME front	ME mid	ME hind
Rest	≤ 0.75	n.a.	> 0	≤ 0.75	≤ 0.75	≤ 0.75
Forward walk	n.a.	> 1	n.a	n.a	n.a	n.a
Backward walk	n.a.	≤ -1	n.a	n.a	n.a	n.a
Anterior grooming 1	≤ 0.75	n.a.	≤ 0	n.a.	≤ 0.75	≤ 0.75
Anterior grooming 2	≤ 0.75	n.a.	> 0	> 0.75	≤ 0.75	≤ 0.75
Posterior grooming	≤ 0.75	n.a.	> 0	≤ 0.75	n.a.	> 0.75

Table 4.4: Parameters used for behavior classification.

The velocity of the cylindrical treadmill was computed as follows. First, the wheel was detected in a camera on the left side of the fly using Hough circle detection. For each frame, we extracted a line profile along the surface of the wheel showing the dot pattern painted on its side. We then compared this line profile to the line profile of the previous frame to determine the most likely rotational shift. We converted this shift to a difference in wheel angle and then transformed this into a linear velocity in mm/s to make it comparable to quantification of spherical treadmill rotations. This image processing was prone to high frequency noise. Therefore, we filtered raw velocities with a Gaussian filter ($\sigma = 20 = 0.2s$).

2D Pose estimation using SLEAP

We tracked nine keypoints from a camera on the right side of the fly: anal plate, ovipositor, most posterior stripe, neck, front leg coxa, front leg femur tibia joint, front leg tibia tarsus joint, mid leg tibia tarsus joint, hind leg tibia tarsus joint (see **Figure 4.1d**) using SLEAP version 1.3.0 [279]. All leg key-points were of right-side limbs on the fly.

Behavior classification

We classified behaviors using an interpretable classifier based on heuristic thresholds of the walking velocity, limb motion energy (ME), and front leg height. For example, we classified forward and backward walking as having a forward velocity > 1 mm/s and ≤ -1 mm/s, respectively. All parameters are shown in **Table 4.4**. If none of the conditions were fulfilled, we classified the behavior as undefined.

Anterior grooming was composed of a logical 'OR' of two conditions: (1) The front leg was lifted up high, or (2) the front leg was moving with high motion energy. Front leg height was computed as the vertical distance between the front leg tibia-tarsus joint and the median position of the coxa. Pixel coordinates start from the top of the image. Thus, it is positive when the front leg is low (e.g., during resting) and negative when the front leg is high (e.g., during head grooming). Motion energy of the front, mid, and hind legs was computed based on the movements of the respective tibia-tarsus joint as follows: $ME = \sqrt{(\Delta x_t)^2 + (\Delta y_t)^2}$, where Δx_t and Δy_t are the difference in x and y between two consecutive frames. We then computed the moving average of the motion energy within a 0.5 s (i.e., 50 samples) window to focus on longer time-scale changes in motion energy.

4.5.9 Two-photon microscopy image analysis

We used custom Python code unless otherwise indicated. For all image analysis, the y-axis is dorsal-ventral along the fly's body, and the x-axis is medial-lateral. Image and filter kernel sizes are specified as (y, x) in units of pixels. Code for two-photon data pre-processing can be found in the 'twoppp' Python package on GitHub previously used in [278]. Code for more detailed analysis can be found in the GitHub repository for this paper.

Motion correction

Recordings from the thoracic cervical connective suffer from large inter-frame motion including large translations, as well as smaller, non-affine deformations. Contrary to motion correction procedures used before for similar data [278], here we made use of the high baseline fluorescence seen in Dfd>LexAop-GCaMP6s animals instead of relying on an additional, red color channel for motion correction. Thus, we performed motion correction directly on the green GCaMP channel. We compared the performance for data where a red channel was available and could only find negligible differences in ROI signals. Importantly, whether a neuron was encoding walking or resting was unchanged irrespective of whether we used the GCaMP channel or recordings from an additional red fluorescent protein.

We performed center of mass registration on every microscopy frame to compensate for large cervical connective translations. We then cropped the microscopy images (from 480x736 to 320x736 pixels). Then, we computed the motion field for each frame relative to one selected frame per fly using optic flow. We corrected the frames for this motion using bi-linear interpolation. The algorithm for optic flow motion correction was previously described in [95]. We only used the optic flow component to compute the motion fields and omitted the feature matching constraint. We regularized the gradient of the motion field to promote smoothness ($\lambda = 800$).

ROI detection

For each pixel, we computed the standard deviation image across time for the entire recording. This gives a good proxy of whether a pixel belongs to a neuron—it has high standard deviation, because the neuron was sometimes active—or not. We used this image as a spatial map of the recording to inform ROI detection. Example standard deviation images are also used as the background image for **Figure 4.2**c.

We applied principal component analysis on a subset of all pixels in the two-photon recording. We then projected the loadings of the first five PCs back into the image space. This gave us additional spatial maps integrating functional information to identify neurons. We then used a semi-automated procedure to detect ROIs: we performed peak detection in the standard deviation map. We visually inspected these peaks for correctness by looking at both the standard deviation map and the PCA maps. We manually added ROIs that the

peak detection algorithm had missed, for example because the neuron was only weakly active. The functional PCA maps allowed us to discriminate between nearby neurons with dissimilar functions. They might show up as one big peak in the standard deviation map, but would clearly be assigned to different principal components. We were able to annotate between 50 and 80 ROIs for each fly. The number of visible neurons varies due to GCaMP6s expression levels, dissection quality, recording quality, and the behavioral activity level of the fly.

4.5.10   Neural signal processing

We extracted fluorescence values for each annotated ROI by averaging all pixels within a rhomboid shape placed symmetrically over the ROI center (11 px high and 7 px wide). This gave us raw fluorescence traces across time for each neuron/ROI. We then low-pass filtered those raw fluorescence traces using a median filter (width$= 3 =\sim$ 0.185 s) and a Gaussian filter ($\sigma = 3 =\sim$ 0.185 s).

$\Delta F/F$ **computation**

Because of variable expression levels among cells, GCaMP fluorescence is usually reported as a change in fluorescence relative to a baseline fluorescence. Here, we were mostly interested whether neurons were activated or not. To have a quantification that was comparable across neurons, we also normalised fluorescence of each neuron to its maximum level. Thus, we computed $\Delta F/F = \frac{F-F_0}{F_{max}-F_0}$, where F is the time-varying fluorescence of a neuron, F_0 is its fluorescence baseline and F_{max} is its maximum fluorescence. We computed F_{max} as the 95 % quantile value of F across the entirety of the recording. In rare instances, neurons would get occluded, or slight glitches of the motion correction algorithm would result in some residual movement. Both of these make it challenging to estimate the minimum fluorescence. When the fly is resting, nearly all neurons are at their lowest levels (aside from several [96]) and there is usually less movement of the nervous system. Thus, we computed F_0 as a 'resting baseline' as follows. First, using our behavioral classifier we identified the onsets of prolonged resting (at least 75 % of 1 s after onset classified as resting and at least 1 s after the previous onset of resting) outside of optogenetic stimulation periods. For each neuron, we then computed the median fluorescence across repetitions aligned to resting onset. We then searched for the minimum value in time over the 2 s following rest onset. Taking the median across multiple instances of resting provided a more stable way to compute the baseline than by simply taking the minimum fluorescence. The normalization using F_0 and F_{max} provided a way to compare fluorescence across multiple neurons with similar units. Thus, whenever we report absolute $\Delta F/F$, a value of 0 refers to neural activity during resting and 1 refers to the 95 % quantile of neural activity. When we report $\Delta F/F$ relative to pre-stimulus values **(Figure 4.2b-f,i, Figure S4.2)**, then the unit of $\Delta F/F$ persists and a value of 0.5 means that the neuron has changed its activity level half as much as when it would go from a resting state to its 95 % quantile state.

Video data processing

To process the raw fluorescence videos shown in the **Videos 4.1 to 4.7** and **Figure 4.2b**, we first low-pass filtered the data with the same temporal filters as for ROI signals (median filter width=3=~ 0.185 s, Gaussian filter $\sigma = 3 =\sim 0.185$ s). Additionally, we applied spatial filters (median filter width=(3,3) px, Gaussian filter $\sigma = (2, 2)$ px). We then applied the same $\Delta F/F$ computation method described above, but for each individual pixel instead of for individual ROIs. Thus, the units used in the videos are identical to the units used for ROI signals in **Figure 4.2, Figure S4.1**.

Synchronization of two-photon and camera data

We recorded two different data modalities at two different sampling frequencies: two-photon imaging data was recorded at approximately 16.23Hz, behavioral images from cameras were acquired at 100Hz. We synchronized these recordings using a trigger signal acquired at 30kHz. When it was necessary to analyse neural and behavioral data at the same sampling rate (e.g., **Videos 4.1 to 4.7**), we down-sampled all measurements to the two-photon imaging frame rate by averaging all behavioral samples acquired during one two-photon frame. In the figures, we report data at its original sampling rate.

4.5.11   Stimulus-triggered analysis of neural and behavioral data

We proceeded in the same way irrespective of whether the trigger was the onset of optogenetic stimulation **(Figure 4.2, Figure 4.4, Figure 4.5, Figure S4.1, Figure S4.3)** or the onset of a natural (spontaneous, or puff-elicited) behavior **(Figure S4.2)**. To compute stimulus-triggered averages, we aligned all trials to the onset of stimulation and considered the times between 5 s prior to the stimulus onset and 5 s after stimulus offset. In **Figure 4.2** we only considered trials where the fly was walking in the 1 s prior to stimulation (behavior classification applied to the mean of the 1 s pre-stimulus interval). We only considered flies with at least 10 trials of walking before stimulation. Behavioral responses in **Figure 4.2a, Figure 4.4b-g, Figure 4.5f-g, Figure S4.1d-f, Figure S4.2a-c, Figure S4.3** show the average across all trials (including multiple animals) and the shaded area indicates the 95 % confidence interval of the mean across trials. When behavioral probabilities are shown, the fraction of trials that a certain behavior occurs at a specific time after stimulus onset is shown. Neural responses over time in **Figure 4.2d, Figure S4.2a-c** show average responses across all trials of one animal. In order to visualise the change in neural activity upon stimulation, the mean of neural activity in the 1 s prior to stimulation is subtracted for each neuron. If the absolute value of the mean across trials for a given neuron at a given time point was less than the 95 % confidence interval of the mean, the data was masked with 0 (i.e., it is white in the plot). This procedure allowed us to reject noisy neurons with no consistent response across trials. Because we subtracted the baseline activity before stimulus onset, we also observed DNs that became less active upon optogenetic stimulation (neurons appearing blue). However, GCaMP6s fluorescence does not reliably reflect neural

inhibition. Thus, we cannot claim that this reduced activation in some neurons is due to inhibition. Instead, because the flies were walking before stimulation onset, those neurons most likely encode walking and became less active when the fly stopped walking forward.

Individual neuron responses in **Figure 4.2c, Figure S4.2a-c,f** show the maximum response of a single neuron/ROI. We detected the maximum response during the first half of the stimulus (2.5 s). We then computed the mean response of this neuron during 1 s centered around the time of its maximum response. If during at least half of that 1 s the mean was confidently different from 0 (i.e., $|mean| > CI$), we considered the neuron to be responsive, otherwise we masked the response to zero to reject noisy neurons with no consistent response across trials. **Figure 4.2b** shows the same as **Figure 4.2c**, but with this processing applied to pixels rather than individual neurons/ROIs. Contrary to previous ROI processing, pixels are not masked to 0 in case they are not responsive. **Figure 4.2e** shows an overlay of **Figure 4.2c** for multiple flies. Data from each of these flies were registered to one another by aligning the y-coordinates of the most dorsal and ventral neurons, as well as the x-coordinate of the most lateral neurons. **Figure 4.2f** is a density visualization of **Figure 4.2e**. To compute the density, we set the individual pixel values where a neuron was located to its response value and summed this across flies. We then applied a Gaussian filter ($\sigma = 25$ px, kernel normalized such that it has a value of 1 in the center to keep the units interpretable) and divided by the number of flies to create an 'average fly'. **Figure S4.2d** was generated in the same manner.

Statistical tests

Figure 4.2g-i include a statistical analysis of neural responses. We quantified the number of activated neurons for each fly **(g)** as the neurons whose response value was positive (as in **Figure 4.2c**). We quantified the fraction of activated neurons for each fly **(h)** by dividing the number of activated neurons by the number of neurons detected in the recording. In **(i)**, we quantified the summed $\Delta F/F$ as the sum of the response values of neurons that were positively activated (see red line in **Figure 4.2d**). Here, we ignored neurons with negative response values because reductions in GCaMP fluorescence should not be interpreted as reflecting inhibition (see above). We used two-sided Mann–Whitney U tests ($scipy.stats.mannwhitneyu$ [280]) to statistically analyze these comparisons. Sample sizes and p-values are described in the figure legends. The Mann–Whitney U test is a ranked test. Thus, comparing three samples against three samples (e.g., aDN2 versus control), where all samples are at identical relative positions (i.e., ranks), will yield the same p-value, even if the absolute values are slightly different. This leads the p-values to be identical across **Figure 4.2g-i** reflecting the conservative choice of a rank test that does not assume an underlying distribution.

Figure 4.4b-e, Figure 4.5f,g, Figure S4.3 show statistical tests comparing the behavioral responses of intact and headless flies. **Figure 4.4f,g, Figure 4.5f,g, Figure S4.3** show statistical tests comparing the behavioral responses of headless experimental flies with headless control flies. In each case, we used two-sided Mann–Whitney U tests

Figure	GAL4	Variable	Comparison	N	P-value
Figure 4.4b	DNp09	forw. vel.	intact/headless	5	0.006
Figure 4.4b	DNp09	forw. prob.	intact/headless	5	0.006
Figure 4.4c	aDN2	forw. vel.	intact/headless	5	0.018
Figure 4.4c	aDN2	groom prob.	intact/headless	5	0.006
Figure 4.4d	MDN	forw. vel.	intact/headless	5	0.500
Figure 4.4d	MDN	back prob.	intact/headless	5	0.265
Figure 4.4e	control	forw. vel.	intact/headless	5	0.500
Figure 4.4e	control	rest prob.	intact/headless	5	0.018
Figure 4.4f	DNp09 v. control	abd. contr.	headless/headless	5	0.006
Figure 4.4g	aDN2 v. control	fr. leg appr.	headless/headless	5	0.030
Figure 4.5f	DNb02	turn vel.	intact/headless	3/7	0.001
Figure 4.5f	control	turn vel.	intact/headless	5	0.047
Figure 4.5f	DNb02 v. control	turn vel.	headless/headless	7/5	0.313
Figure 4.5f	DNg14	abd. dip	intact/headless	9	0.144
Figure 4.5f	control	abd. dip	intact/headless	5	0.072
Figure 4.5f	DNg14 v. control	abd. dip	headless/headless	9/5	0.003
Figure S4.3a	aDN1	fr. leg motion	intact/headless	5	0.002
Figure S4.3a	control	fr. leg motion	intact/headless	5	0.006
Figure S4.3a	aDN1 v. control	fr. leg motion	headless/headless	5	0.006
Figure S4.3a	aDN1	FeTi angle	intact/headless	5	0.008
Figure S4.3a	control	FeTi angle	intact/headless	5	0.417
Figure S4.3a	aDN1 v. control	FeTi angle	headless/headless	5	0.148
Figure S4.3a	aDN1	fr. leg appr.	intact/headless	5	0.149
Figure S4.3a	control	fr. leg appr.	intact/headless	5	0.072
Figure S4.3a	aDN1 v. control	fr. leg appr.	headless/headless	5	0.030
Figure S4.3b	DNa01	turn vel.	intact/headless	6	0.003
Figure S4.3b	control	turn vel.	intact/headless	5	0.047
Figure S4.3b	DNa01 v. control	turn vel.	headless/headless	6/5	0.206
Figure S4.3b	DNa01	side vel.	intact/headless	6	0.003
Figure S4.3b	control	side vel.	intact/headless	5	0.047
Figure S4.3b	DNa01 v. control	side vel.	headless/headless	6/5	0.392
Figure S4.3c	DNa02	turn vel.	intact/headless	6	0.002
Figure S4.3c	control	turn vel.	intact/headless	5	0.047
Figure S4.3c	DNa02 v. control	turn vel.	headless/headless	6/5	0.158
Figure S4.3c	DNa02	side vel.	intact/headless	6	0.003
Figure S4.3c	control	side vel.	intact/headless	5	0.047
Figure S4.3c	DNa02 v. control	side vel.	headless/headless	6/5	0.085
Figure S4.3d	DNb02	turn vel.	intact/headless	3/7	0.001
Figure S4.3d	control	turn vel.	intact/headless	5	0.047
Figure S4.3d	DNb02 v. control	turn vel.	headless/headless	7/5	0.313
Figure S4.3d	DNb02	forw. vel.	intact/headless	3/7	0.028
Figure S4.3d	control	forw. vel.	intact/headless	5	0.500
Figure S4.3d	DNb02 v. control	forw. vel.	headless/headless	7/5	0.313
Figure S4.3e	DNg14	abd. dip	intact/headless	9	0.144
Figure S4.3e	control	abd. dip	intact/headless	5	0.072
Figure S4.3e	DNg14 v. control	abd. dip	headless/headless	9/5	0.003
Figure S4.3f	Mute	ovi. ext.	intact/headless	3	0.500
Figure S4.3f	control	ovi. ext.	intact/headless	5	0.338
Figure S4.3f	Mute v. control	ovi. ext.	headless/headless	3/5	0.117

Table 4.5: Exact p-values for statistical tests in headless animal experiments.

($scipy.stats.mannwhitneyu$ [280]) to compare the average value within the first 2.5 s after stimulus onset. We averaged across technical replicates (trials) and only compare biological replicates (individual flies) using statistical tests. Exact p-values rounded to three digits are indicated in **Table 4.5**.

Figure S4.2a-c (right),e show the Pearson correlation between neural responses to optogenetic stimulation and neural activity during natural (spontaneous or puff-elicited) behaviors. The significance of the correlation is measured as the probability that a random sample has a correlation coefficient as high as the one reported ($scipy.stats.pearsonr$ [280]).

In all figures showing statistical tests, significance levels are indicated as follows: *** = p<0.001, ** = p<0.01, * = p<0.05, n.s. = p≥0.05.

4.5.12   Brain connectome analysis

Loading connectome data

We used the female adult fly brain (FAFB) connectomics dataset [50] from Codex [281] (version hosted on Codex as of 3 August 2023, FlyWire materialization snapshot 630, https://codex.flywire.ai/api/download) to generate all figures. We merged the "Neurons", "Morphology Clusters", "Connectivity Clusters", "Classification", "Cell Stats", "Labels", "Connections", and "Connectivity Tags" tables. We then found DNs by filtering for the attribute *super_class=descending*. We identified DNs with known, named (e.g., DNp09) genetic driver lines from Namiki et al.[32] by checking the 'Cell Type', 'Hemibrain Type' and 'Community Labels' attributes (in this priority) and using the following rules. Otherwise, we used the consensus cell type [282] (e.g. DNpe078). We semi-automatically assigned names using the following rules:

1. Special neurons: we manually labelled root IDs 720575940610236514, 720575940640331472, 720575940631082808, and 720575940616026939 as MDNs based on community labels from Salil Bidaye (consensus cell type DNpe078); root IDs 720575940616185531 and 720575940624319124 as aDN1 based on community labels from Katharina Eichler and Stefanie Hampel (consensus cell type DNge197); and root IDs 720575940624220925 and 720575940629806974 as aDN2 based on community labels from Katharina Eichler and Stefanie Hampel (consensus cell type DNge078). We verified visually that the shape of the neurons corresponded to published light-level microscopy images [61, 86].

2. Otherwise, if both the *hemibrain_type* attribute and the *cell_type* attribute followed the Namiki format ("DN{1 lowercase letter}{2 digits}" , eg. "DNp16"), and they are identical, we used this as the cell name. If they are both in this format but are not identical, we marked this neuron for manual intervention.

3. Otherwise, if the *hemibrain_type* attribute follows the Namiki format, we used this as the cell name. In addition, if the *hemibrain_type* attribute follows the Namiki format, but the the *cell_type* attribute has a different value following the consensus cell type format ("DN{at least 1 lowercase letter}{at least 1 digit}" , like 'DNge198'), we marked the cell as requiring manual attention.

4. Otherwise, if the *cell_type* attribute follows the Namiki format, we used this as the cell name.

5. Otherwise, if the *cell_type* attribute follows the consensus cell type format, we used this as the cell name.

6. Otherwise, we marked the cell as requiring manual intervention.

7. Wherever manual intervention was required (mostly where the *hemibrain_type* is the Namiki format, but the *cell_type* is in the consensus cell type format), we manually assigned the consensus cell type. However, we assigned the Namiki type if there was no other DN in this Namiki cell type or if the cell type was still missing a pair of DNs[32].

Next, we stored the connectome as a graph using SciPy sparse matrix [280] and NetworkX DirectedGraph [283] representations. We identified DNs with somas in the GNG by checking the third letter of the consensus cell type to be 'g' (i.e., DNgeXXX)[282].

Analyzing connectivity

We only considered neurons with at least five synapses to be connected and computed the number of connected DNs based on this criterion **(Figure 4.3, Figure 4.5b,c,e, Figure 4.6a-c, Figure S4.3)**. This is the same value as the default in Codex, the connectome data explorer provided by the FlyWire community [257, 281]. Analysis of connectivity across three brain hemispheres (2 brain halves from the FAFB dataset [50] and one from the hemibrain dataset [173]) revealed that connections "stronger than ten synapses or 1.1 % of the target's inputs have a greater than 90 % change to be preserved" [282]. We visualized all DNs connected to a given DN **(Figure 4.3a,b, Figure 4.5d, Figure S4.3)** using the neuromancer interface and manually colored neurons depending on whether they are in the GNG or not.

Neurotransmitter identification was available from the connectome dataset based on classification of individual synapses with an average accuracy of 87 % [259]. Here, we report neurotransmitter identity for a given presynaptic-postsynaptic connection. To define neurotransmitter identity for a given presynaptic-postsynaptic pair, we asserted that the neurotransmitter type would be unique using a majority vote rule. This was chosen as a tradeoff between harmonizing neurotransmitters for a neuron (especially GABA, acetylcholine and glutamate [284]) and avoiding the propagation of classification errors.

DN network visualisations and DN hierarchy

We used the networkx library [283] to plot networks of DNs in **Figure 4.3c,d, Figure 4.5e, Figure S4.3**. Again, we considered neurons to be connected if they had at least five synapses. In the circular plots we show summed connectivity of multiple DNs. For example, the network for DNp09 in **Figure 4.3c** shows only one green circle in the center representing two DNp09 neurons. All connections shown as arrows are the sum of those two neurons. DNs are considered excitatory if they have the neurotransmitter acetylcholine and inhibitory if they have the neurotransmitter GABA. Whether glutamate is excitatory or inhibitory is unclear—this depends on the receptor subtype [258] which is unknown in most cases. To emphasize this, we highlight glutamatergic network edges in a different color (pink).

In figure **Figure 4.3e** we show the cumulative distribution of the number of DNs reachable within up to N synapses. Statistics on DN connectivity across multiple synapses were computed using matrix multiplication with the *numpy* library on the adjacency matrix of the network. Colored lines represent a DN network traversal starting at specific command-like DNs. The black trace represents the median of all neurons. Only a maximum of approximately 800 DNs can be reached because the others have maximally one DN input. In **Figure 4.5b,c** we sorted DNs by the number of monosynaptic connections they make to other DNs. In **Figure 4.5b**, the same sorting is applied to show the number of connected GNG DNs (orange).

Fitting network models to connectivity degree distribution

In **Figure 4.6a**, we generated a shuffled network of the same size by keeping the number of neurons constant and keeping the number of connections constant. Then, we randomly shuffled (i.e., reassigned) those connections. Here, we only considered the binary measure of whether a neuron was connected or not (number of synapses >5) and not its synaptic weight. We then fit a power-law or an exponential to the connectivity degree distribution using the *scipy.optimize* [280] library. Histograms of the degree distributions for all four distributions are shown in **Figure 4.6a** using constant bin widths of 5 neurons. The quality of the fits are quantified using linear mean squared error (R^2).

Detection of DN clusters

We applied the Louvain method [264] with resolution parameter $\gamma = 1$ to detect clusters. Briefly, the Louvain method is a greedy algorithm that maximizes modularity (i.e., the relative density of connections within clusters compared to between clusters). To simplify the network during the optimization, we do not consider the directionality of connections between neurons. If there is reciprocal connectivity between neurons, we add up the number of synapses (positive if excitatory, negative if inhibitory; here glutamate is considered inhibitory and neuromodulators are disregarded for the sake of simplicity). The Louvain method finds different local optima of cluster assignments due to its stochastic initialization

and greedy nature. Therefore, we ran the algorithm 100 times. Based on the outcomes of these 100 runs, we define a co-clustering matrix: The matrix has the same size as the connectivity matrix (*number of DNs × number of DNs*). Each entry represents how often two DNs end up in the same cluster. This matrix assigns each pair of DNs a probability to be in the same cluster. We then applied hierarchical clustering to this matrix (using the 'ward' optimization method from the *scipy.cluster.hierarchy* library [280]) to get the final sorting of DNs shown in **Figure 4.6**b. Using this meta-clustering, we could be sure that the sorting of DNs we find through clustering is not a local optimum and that it is reproducible. We then used the final sorting to detect the clusters shown in grey in **Figure 4.6b** as follows: We started from one side of the sorted DNs and sequentially grew the cluster. If the next DN was in the same Louvain clusters at least 25 % of the time, we assigned it to the same cluster as the previous DN. If not, we started a new cluster with this DN and kept testing subsequent DNs as to whether they fulfill the criteria for this new cluster. Finally, we only kept clusters that had at least 10 neurons. This yielded 12 clusters (grey squares). We applied the same meta-clustering technique to a shuffled network (same number of DNs, same number of connections, same number of synapses, but shuffled connections). On this shuffled network, we found 34 clusters of much smaller size **(Figure 4.6c)**, hinting at a better clustering in our network than in a shuffled control (*modularity* = 0.27 for the original network and *modularity* = 0.12 for the shuffled network). The number of synapses is shown as positive values (red) if it is excitatory and as negative values (blue) if it is inhibitory.

We then analyzed the connectivity within and between clusters. To do this, we accumulated the number of synapses between two clusters (positive for excitatory, negative for inhibitory). In order to be able to compare this quantity between clusters of different sizes, we divided this number of synapses by the number of DNs in the cluster that receives the synaptic connections. This quantity is visualized in **Figure 4.6d** for the original DN-DN network clusters and **Figure 4.6e** for the shuffled network as the 'normalized number of synapses'. If positive (red), then connections from one cluster to another are predominantly excitatory. If negative (blue) connections are predominantly inhibitory.

Statistical comparison of original versus shuffled DN-DN clusters

As detailed above, we applied the Louvain algorithm 100 times to increase the robustness of clustering. We computed statistics on the clustering of this dataset (mean and standard deviation) specifically on metrics including the size and number of clusters. We then compared these distributions with those for the shuffled graph using one-sided t-tests (*scipy.stats.ttest_ind* [280]). The resulting statistics are a conservative quantification of the difference between the original network and the shuffled control, as each data point is taken independently. When performing the hierarchical clustering across 100 iterations, the large clusters from the biological network are preserved whereas the random associations of the shuffled network become incoherent. In practice, the difference in cluster sizes reported statistically underestimates the difference between the resulting matrices shown in

Figure 4.6b,c. The 100 iterations result from random seed initialization, on the condition that the algorithm converges. We restarted it whenever the convergence criteria was not reached within 3 s. Indeed we observed empirically that when the algorithm would not converge in 3 s it would not do so for at least 30 min and was, therefore, terminated.

Identifying DNs to test predictions

Based on the cell type data associated with each neuron in FAFB (see above), we were able to find many DNs from refs.[32, 44, 61] in the connectome database. We then checked which of them have either a very high number of synaptic connections to other DNs or a very low number. We then filtered for lines where a clean split-GAL4 line was available. Additionally, we focused on lines whose major projections in the VNC were outside of the wing neuropil, because we removed the wings in our experimental paradigm and thus might not be able to see optogenetically-induced behaviors. This left us with ten additional DNs to test our predictions. DNp01 (giant fiber) activation was reported to trigger take-off in intact and headless flies [84, 261] so we did not repeat those experiments. This left us with nine lines to test. The source and exact genotypes of those fly lines are reported in **Table 4.2**. We then performed experiments with those nine lines. Because intact control flies become aroused by laser illumination, but not headless control animals, to avoid false positives we only analyzed DN lines that either had a known optogenetic behavior in intact flies (i.e., aDN1, DNa01, DNa02), or that had a clear phenotype in headless flies (i.e., DNb02, DNg14, Mute). Thus, we excluded Web, DNp24, and DNg30 as they did not fulfill either of these criteria and only analyzed the remaining six driver lines in **Figure 4.5** and **Figure S4.3** .

Analyzing DN-DN connectivity in the VNC

We used the neuprint website to interact with the male adult nerve cord (MANC) connectome dataset [35, 177]. There, we searched neurons based on their name (MDN, DNp09, etc.) and checked whether there were any DNs among the neurons that are postsynaptic. We found all neurons that we used from [32] (i.e., DNp09, DNa01, etc.), and MDN. We were not able to find aDN2, aDN1, Mute and Web.

Analyzing VNC targets of DN clusters

We used data shown in Cheong et al.[35] Figure 3 - Supplement 2 to define whether a DN known from Namiki et al.[32] was projecting to a particular VNC neuropil. Briefly, a DN is considered as projecting to a given neuropil if at least 5 % of its presynaptic sites are in that region. We manually found the MDNs in the MANC dataset and determined the regions they connect to using the same criterion. To generate **Figure 4.6f**, for each cluster, we accumulated the number of known DNs that project to a given VNC region. We then divided this by the number of known DNs to obtain the fraction of known DNs

within a cluster that project to a given region. The number of unknown DNs per cluster is also shown next to the plot. The raw data of associations between DNs and VNC neuropils is shown in **Supplementary Data File 2**.

Analyzing behaviors associated with DN clusters

We examined the literature [35, 61, 76, 79–81, 83, 86, 90, 91, 93, 95, 265, 285] to identify behaviors associated with DNs and grouped them into broad categories (anterior movements, take-off, landing, walking, flight). This literature summary is available in the **Supporting Information File 2**. Of the 34 DN types annotated, we found conflicting evidence for only two: DNg11 is reported to elicit foreleg rubbing [83] while targeting mostly flight-related neuropils [35]; DNa08 targets flight power control circuits [35] but has been reported to be involved in courtship under the name aSP22 [78]. In **Figure 4.6g** we assigned DNg11 to 'anterior' and DNa08 to 'flight'. We accumulated the number of known DNs that are associated with a given behavior for each cluster. We then divided by the number of known DNs in the respective cluster to get a fraction of DNs within a cluster that have a known behavior. The number of unknown DNs per cluster is also shown next to the plot. The raw data of associations between DNs and behaviors is shown in **Supplementary Data File 2**.

Analyzing brain input neuropils for each DN cluster

We used data from FAFB to identify the brain input neuropils for each DN cluster based on the neuropil annotation for each DN-DN synapse. Thus, localization information is given by the position of each synaptic connection and not the cell body of the presynaptic partner. This allows us to account for local processing and modularity of neurons. The acronyms of brain regions are detailed in **Table 4.6**, with 'L' and 'R' standing for the left and right brain hemispheres respectively. Results are reported as the fraction of synapses made in a neuropil out of all the post-synaptic connections made by DNs of a given cluster.

Acronym	Neuropil	Region
AL	antennal lobe	Antennal Lobe
AME	accessory medulla	Optic Lobe
AMMC	antennal mechanosensory and motor center	Periesophageal Neuropils
AOTU	anterior optic tubercle	Ventrolateral Neuropils
ATL	antler	Inferior Neuropils
AVLP	anterior VLP (ventrolateral protocerebrum)	Ventrolateral Neuropils
BU	bulb	Lateral Complex
CAN	cantle	Periesophageal Neuropils
CRE	crepine	Inferior Neuropils
EPA	epaulette	Ventromedial Neuropils
FB	fanshaped body	Central Complex
FLA	flange	Periesophageal Neuropils
GA	gall	Lateral Complex
GNG	gnathal ganglia	Gnathal Ganglia
GOR	gorget	Ventromedial Neuropils
IB	inferior bridge	Inferior Neuropils
ICL	inferior clamp	Inferior Neuropils
IPS	inferior posterior slope	Ventromedial Neuropils
LAL	lateral accessory lobe	Lateral Complex
LH	lateral horn	Lateral Horn
LOP	lobula plate	Optic Lobe
LO	lobula	Optic Lobe
MB_CA	pedunculus	Mushroom Body
MB_ML	vertical lobe	Mushroom Body
MB_PED	medial lobe	Mushroom Body
MB_VL	calyx	Mushroom Body
NO	noduli	Central Complex
OCG	ocellar ganglion	Ocelli
PB	fanshaped body	Central Complex
PLP	posteriorlateral protocerebrum	Ventrolateral Neuropils
PRW	prow	Periesophageal Neuropils
PVLP	posterior VLP (ventrolateral protocerebrum)	Ventrolateral Neuropils
SAD	saddle	Periesophageal Neuropils
SCL	superior clamp	Inferior Neuropils
SIP	superior intermediate protocerebrum	Superior Neuropils
SLP	superior lateral protocerebrum	Superior Neuropils
SMP	superior medial protocerebrum	Superior Neuropils
SPS	superior posterior slope	Ventromedial Neuropils
UNASGD	unassigned	
VES	vest	Ventromedial Neuropils
WED	wedge	Ventrolateral Neuropils

Table 4.6: Acronyms for the brain neuropils used in **Figure 4.6h** based on [50]

4.6 Supplementary Figures
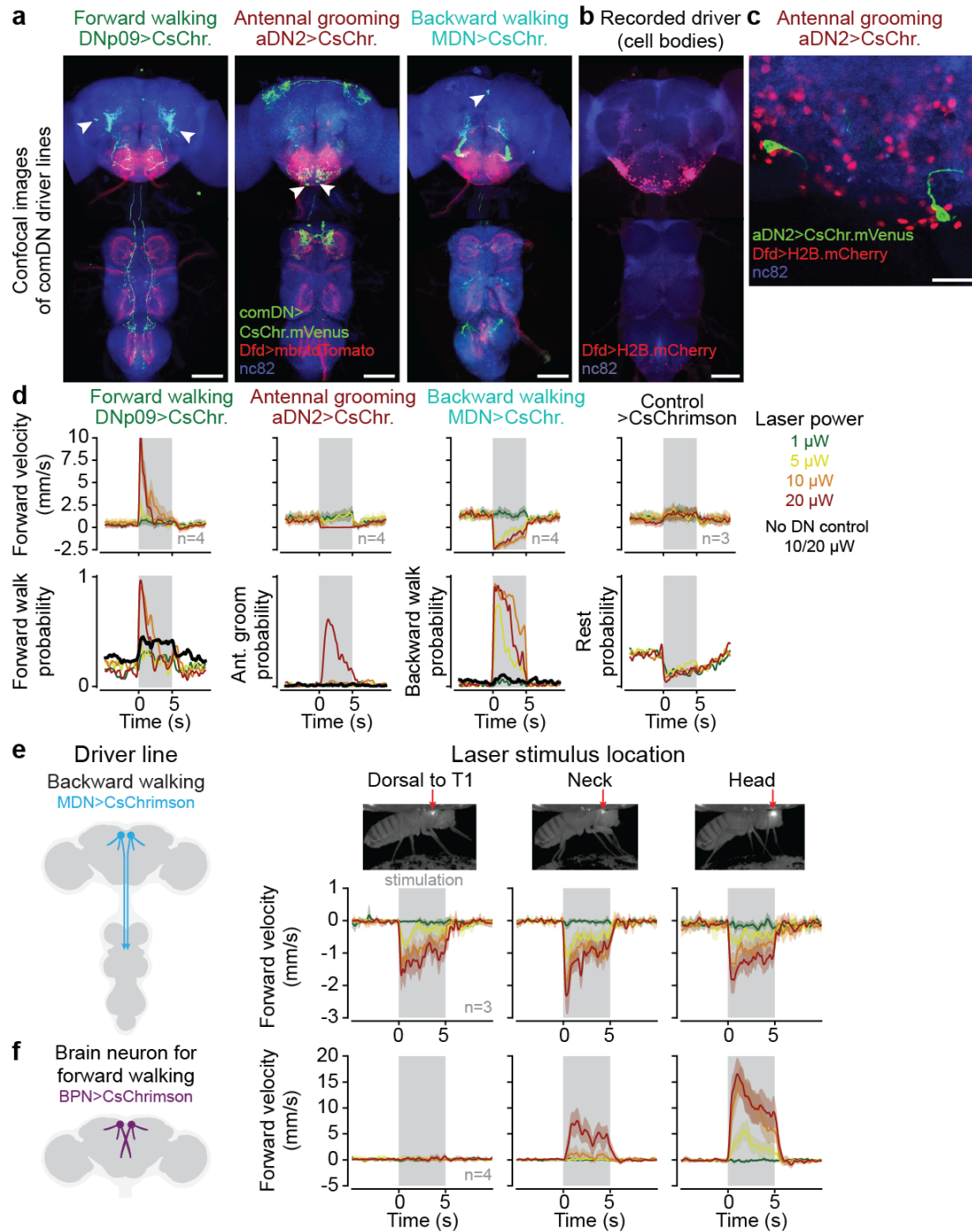
Figure S4.1 - See Figure Legend on next page.

Supplementary Figure S4.1: DN driver lines and optogenetic stimulation strategy. (a) Z-projected confocal images of the brain (top) and VNC (bottom) show the expression of UAS-CsChrimson.mVenus (green) in command-like DNs, membrane-bound tdTomato in the Dfd driver line (red), and neuropil ('nc82', blue). The location of command-like DN cell bodies is indicated (white arrowheads). Scalebars are 100 μm. **(b)** Z-projected confocal image of Dfd driver line expression of soma-targeted mCherry. Only brain neurons in the GNG are labeled. Scalebar is 100 μm. **(c)** Confocal image of the posterior GNG with Dfd driver line expression of soma-targeted mCherry and aDN2 expression of UAS-CsChrimson.mVenus (green). The two GNG-DNs in the aDN2 driver line are not targeted by the Dfd driver line. Scalebar is 20 μm. **(d)** Behavioral responses to optogenetic stimulation of the neck connective at different laser intensities for DNp09 (left; 4 flies, total 49 trials per condition), aDN2 (left-middle; 4 flies, total 60 trials per condition), MDN (right-middle; 4 flies, total 50 trials per condition), and no DN control (right; 3 flies, total 60 trials per condition) animals. Flies reliably (i) walk forward upon DNp09 stimulation for stimuli $\geq$ 10 μW, (ii) groom upon aDN2 stimulation only for the highest stimulation power (20 μW) but rest at 10 μW, and (iii) backward walk upon MDN stimulation for stimuli $\geq$ 5 μW. For all stimulation intensities, control flies walk more and rest less. Thus, we selected 10 μW as our default laser stimulation power and 20 μW for aDN2 stimulation specifically. **(e)** MDN stimulation with focused laser light elicits backward walking when shining light at the anterior dorsal thorax (left, as in **Figure 4.4** and **Figure 4.5)**, at the neck (middle, as in **Figure 4.2**), and at the head (right). 3 flies, total 30 stimulation trials per condition. **(f)** Stimulation of a brain-specific neuron ('Bolt protocerebral neurons' or BPN) known to drive forward walking [79] with focused laser light elicits forward walking when shining light on the head (right), but not on the thorax (left). Laser light focused on the neck (middle) can only elicit weak forward walking at 20 μW. 4 flies, total 40 stimulation trials per condition. All traces in this figure show mean $\pm$ 95 % confidence interval of the mean across stimulation trials.

Figure S4.2 – See Figure Legend on next page.

Supplementary Figure S4.2: Comparison of GNG-DN population neural activity during optogenetic stimulation versus corresponding natural behaviors. (a-c) For **(a)*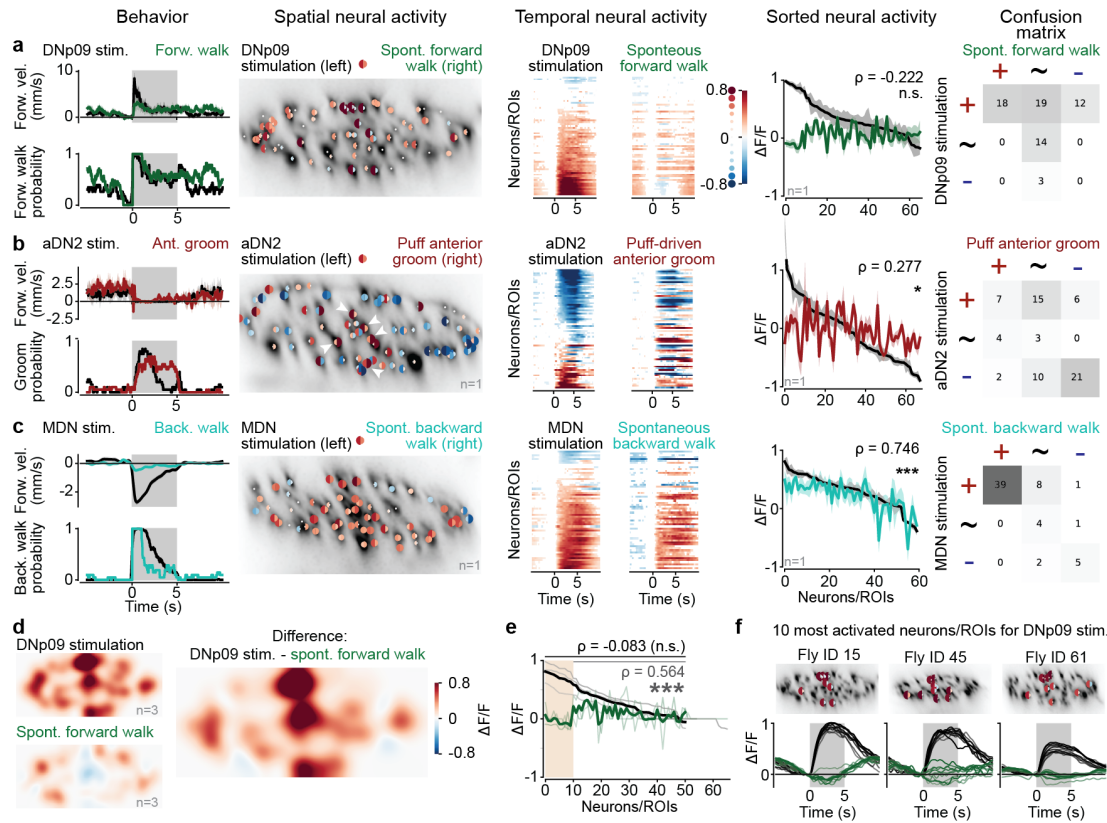* DNp09 and forward walking, **(b)** aDN2 and anterior grooming, or **(c)** MDN and backward walking: **(left)** behavioral responses to optogenetic stimulation of command-like DNs (black) versus natural occurrences of the behavior in question (color); **(middle left)** single neuron/ROI responses (analyzed as in **Figure 4.2c**). Here the left half-circle reflects the response to optogenetic activation and the right half-circle the activity during natural behavior; **(middle)** single neuron average responses as in **Figure 4.2d**; **(middle right)** Comparing the activity of individual neurons between optogenetic stimulation (black) and natural behavior (color). Neurons/ROIs are sorted by the magnitude of response to optogenetic activation. Shaded areas indicate 95% confidence interval of the mean across trials. Pearson correlation between optogenetic and spontaneous response and significance of test against null-hypothesis (the two variables are uncorrelated, see Methods) are shown; **(right)** Confusion matrix comparing the number of active neurons/ROIs that were more active (+), similar ($\sim$), or less active (-) upon optogenetic stimulation versus during natural behavior. **(a)** DNp09: for one fly n=23 optogenetic stimulation trials (not forward walking before stimulus) and 28 instances of spontaneous forward walking in which the fly was not walking forward for at least 1 s and then walking forward for at least 1 s (correlation: $\rho = -0.022, p = 0.356$). **(b)** aDN2: for one fly, n=20 optogenetic stimulation trials (pre-stimulus behavior not restricted) and 16 instances of anterior grooming elicited by a 5 s humidified air puff (correlation: $\rho = 0.277, p = 0.022$). Indicated are central neurons/ROIs with strong activation during aDN2 stimulation of the neck cervical connective as in **Figure 4.2f**. **(c)** MDN: for one fly, n=80 optogenetic stimulation trials (pre-stimulus behavior not restricted) and 21 instances of spontaneous backward walking on a cylindrical treadmill in which the fly was not walking backward for 1 s and then walked backward for at least 1 s (correlation: $\rho = 0.746, p < 0.001$). **(d)** Density visualisation (as in **Figure 4.2f**) of neural responses to DNp09 stimulation and spontaneous forward walking across three animals. The difference in responses is primarily localized to the central but not lateral regions of the connective. To maximize comparability, only trials where the fly was not walking forward before stimulus onset were selected. **(e)** Same plot as in **a, middle right** but for three animals with DNp09 stimulation and forward walking. Indicated are the correlation values when including ($\rho = -0.083, p = 0.564$) or excluding ($\rho = 0.564, p < 0.001$) the ten neurons most activated by optogenetic stimulation (orange region). **(f)** The locations of ten neurons indicated in **e** within the connective of three flies (top) and their single neuron responses to optogenetic stimulation (bottom, black traces) or during natural backward walking (bottom, green traces).
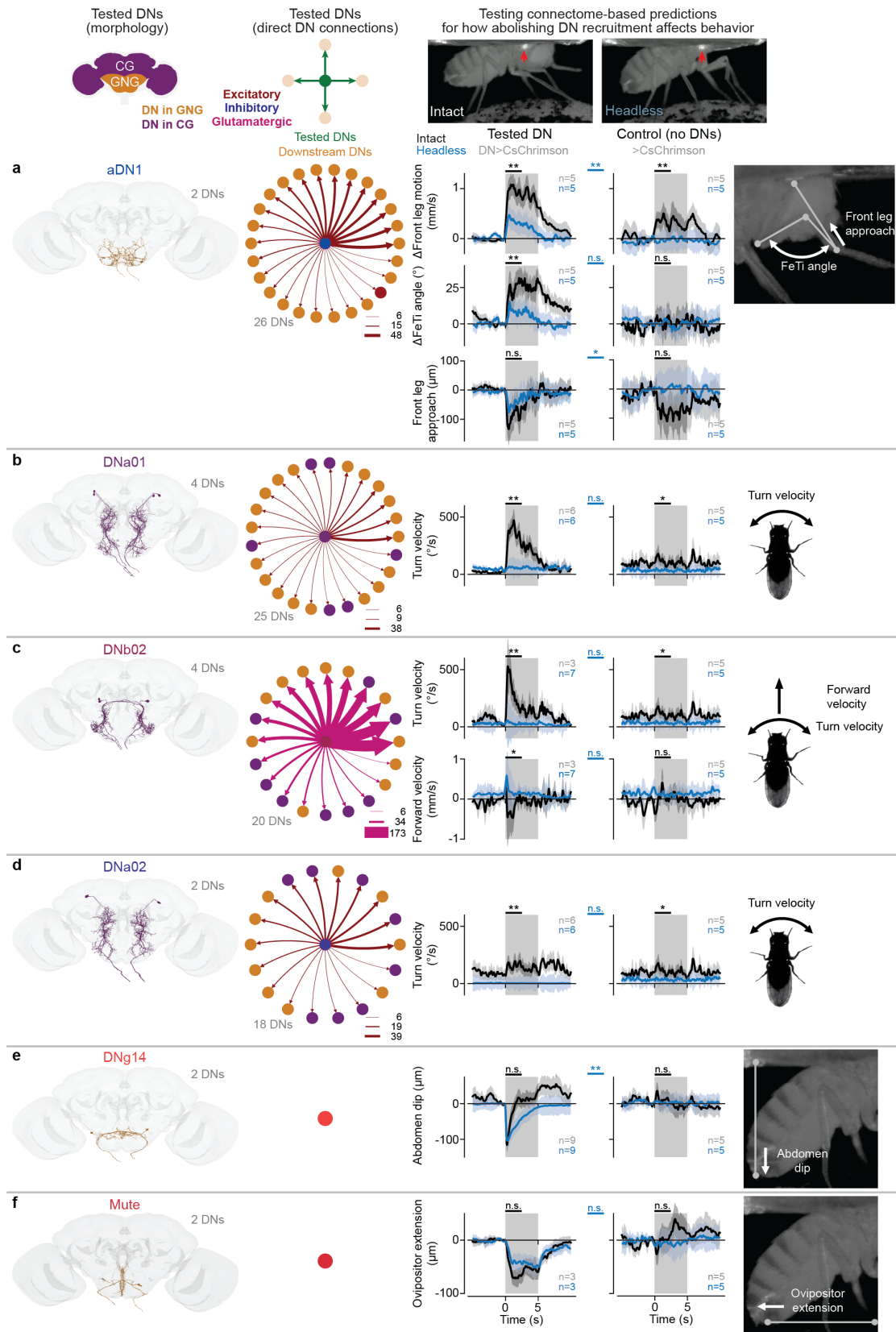
Figure S4.3 - See Figure Legend on next page.

Supplementary Figure S4.3: Testing connectome-based predictions of DN-driven behavioral flexibility and its dependence upon downstream DNs. (a-f) (first column) The morphology of tested DNs in the adult female brain connectome. DNs are color-coded based on their somata localization within the cerebral ganglia (purple) or gnathal ganglia (orange). The number of DNs is indicated. **(second column)** A network schematic of direct connections from tested to downstream DNs. Edge widths reflect the number of synapses and is consistent across plots. Edge colors denote excitatory (red), inhibitory (blue), or glutamatergic (pink) which can be excitatory or inhibitory depending on receptor type [258]. **(third column)** Quantitative analyses of optogenetically-driven behaviors and movements in intact (black traces) and headless animals (blue traces). The number of flies for each condition are indicated. Each fly is optogenetically stimulated ten times. Thus, the average and 95 % confidence interval of the mean for a total of $n * 10$ trials is shown. **(fourth column)** Identical behavioral analysis for control flies without DN opsin expression. Note that controls for different parameters include the same five animals. Mann-Whitney U tests comparing the trial mean of intact and headless animals (black bars, above each plot) and comparing headless experimental with headless control flies (blue, in between experimental and control plots) are shown (*** means p<0.001, ** means p<0.01, * means p<0.05, n.s. means p≥0.05; for exact p-values see Methods). **(fifth column)** An illustration of the behavioral parameter(s) being quantified. **(a)** aDN1 has monosynaptic connections to 26 other DNs and triggers grooming in intact animals. By contrast, headless animals produce mostly uncoordinated front leg movements. These occur more slowly at a lower frequency (top) with a smaller change in femur-tibia angle (middle). The 'front leg approach' to the head—the change in Euclidean distance between the neck and tibia-tarsus joint relative to 1 s before stimulus onset—is similar between intact and headless animals (bottom). **(b)** DNa01 has monosynaptic connections to 25 other DNs and triggers in place turning. This is quantified as an increase in turn velocity. This behavior is lost in headless animals. **(c)** DNb02 has monosynaptic connections to 20 other DNs and weakly triggers turning. This is quantified as an increase in turning velocity (top), a phenotype that is lost in headless animals. Instead, a flexion of the front legs can be observed in headless animals. This is quantified as a short spike in forward velocity (bottom). These data partially overlap with those in **Figure 4.5d-g**). **(d)** DNa02 has monosynaptic connections to 18 other DNs and weakly triggers turning. This is quantified as an increase in turning velocity. This behavior is lost in headless animals. **(e)** DNg14 has no monosynaptic connections to other DNs and triggers abdominal dipping and vibration in both intact and headless animals. This movement is quantified as a change in the vertical position of the anal plate relative to 1 s before stimulus onset. These are the same data as in **Figure 4.5d-f**). **(f)** The DN 'Mute' has no monosynaptic connections to other DNs and triggers ovipositor extension in both intact and headless animals. This movement is quantified as a change in the horizontal position of the ovipositor relative to the 1 s before stimulus onset.

4.7   Supporting Information Files

Supporting Information File 1 - Individual fly neural and behavioral responses to optogenetic stimulation (Ref. **Figure 4.2**)
Part 1: Flies were walking prior to stimulation. Each page is for a single genotype. Each row shows individual fly neural and behavioral results. The number of trials is indicated. The analyses and plots are as in **Figure 4.2a,c,d**. The bottom row summarizes data across all flies of the genotype as in **Figure 4.2**a,e,f. Flies were only used if they had at least 10 trials of forward walking before stimulation onset.
Part 2: Flies were resting prior to stimulation. Same as for **Part 1** except that flies were resting before to stimulation onset. Flies were only used if they had at least 10 trials of resting before stimulation onset.
Link to Supporting Information File 1

Supporting Information File 2 - DN cluster analysis (Ref. **Figure 4.6**)
Sheet 1: DN cluster behaviors. A list showing which DNs are in which particular cluster.
Sheet 2: DN cluster VNC projections. VNC projections for known DNs. Aside from MDN, these data were obtained from [35].
Sheet 3: Investigated DN clusters. A subset of sheet 1 showing the cluster associations for DNs investigated using optogenetics in this study: DNp09, aDN2, MDN, aDN1, DNa01, DNa02, DNb02, DNg14 and Mute.
Sheet 4: Equivalence DN names and root id. List of DNs, providing the known names for the root ids used in FAFB [50].
Sheet 5: DN literature aggregation Reported behavioral phenotypes for DNs, including citations.
Sheet 6: Connectivity statistics. Connectivity statistics in the DN-DN network for reported neurons.
Link to Supporting Information File 2

4.8   Supplementary Videos

Supplementary Video 4.1: DNp09-driven behavior and trial-averaged GNG-DN population activity. (top) Stimulus-triggered average of neural activity upon DNp09 optogenetic stimulation. Video shows $\Delta F/F$ processed GCaMP6s fluorescence. (bottom) Four instances of forward walking for one animal (fly in **Figure 4.2b-d**) upon DNp09 stimulation. Red circle indicates laser stimulation.
Link to Supplementary Video 1

Supplementary Video 4.2: aDN2-driven behavior and trial-averaged GNG-DN population activity. (top) Stimulus-triggered average of neural activity upon aDN2 optogenetic stimulation. Video shows $\Delta F/F$ processed GCaMP6s fluorescence. (bottom) Four instances of anterior grooming for one animal (fly in **Figure 4.2b-d**) upon aDN2 stimulation. Red circle indicates laser stimulation.
Link to Supplementary Video 2

Supplementary Video 4.3: MDN-driven behavior and trial-averaged GNG-DN population activity. (top) Stimulus-triggered average of neural activity upon MDN optogenetic stimulation. Video shows $\Delta F/F$ processed GCaMP6s fluorescence. (bottom) Four instances of backward walking for one animal (fly in **Figure 4.2b-d**) upon MDN stimulation. Red circle indicates laser stimulation.
Link to Supplementary Video 3

Supplementary Video 4.4: Control for light-driven behavior and trial-averaged GNG-DN population activity. (top) Stimulus-triggered average of neural activity upon optogenetic stimulation of a fly without a GAL4 driver. Video shows $\Delta F/F$ processed GCaMP6s fluorescence. (bottom) Four instances of behavior for one animal (fly in **Figure 4.2b-d**) upon light exposure. Red circle indicates laser exposure.
Link to Supplementary Video 4

Supplementary Video 4.5: Comparing GNG-DN population activity for DNp09-driven versus spontaneous forward walking. Forward walking (left) driven by optogenetic stimulation of DNp09 versus (right) spontaneously generated in the same animal (fly in **Figure S4.2**a). (top) Stimulus-triggered average of neural activity. Video shows $\Delta F/F$ processed GCaMP6s fluorescence. (bottom) Four instances of behavior time-locked to stimulation or forward walking onset. Red circle indicates laser stimulation. White circle indicates spontaneous forward walking detection.
Link to Supplementary Video 5

Supplementary Video 4.6: Comparing GNG-DN population activity for aDN2-driven versus puff-induced anterior grooming. Anterior grooming (left) driven by optogenetic stimulation of DNp09 versus (right) elicited by vapor-puff stimulation in the same animal (fly in **Figure S4.2**b). (top) Stimulus-triggered average of neural activity. Video shows $\Delta F/F$ processed GCaMP6s fluorescence. (bottom) Four instances of behavior time-locked to stimulation or anterior grooming onset. Red circle indicates laser stimulation. White circle indicates vapor puff stimulation.
Link to Supplementary Video 6

Supplementary Video 4.7: Comparing GNG-DN population activity for MDN-driven versus spontaneous backward walking. Backward walking (left) driven by optogenetic stimulation of MDN versus (right) spontaneously generated in the same animal on a cylindrical treadmill (fly in **Figure S4.2**c). (top) Stimulus-triggered average of neural activity. Video shows $\Delta F/F$ processed GCaMP6s fluorescence. (bottom) Four instances of behavior time-locked to stimulation or backward walking onset. Red circle indicates laser stimulation. White circle indicates spontaneous backward walking onset.
Link to Supplementary Video 7

Supplementary Video 4.8: DNp09-driven behavioral responses of animals that are intact, headless, or headless without ground contact. Responses to optogenetic stimulation of DNp09 for three flies (one animal per column). The same animal is studied intact on the spherical treadmill (top), headless on the spherical treadmill (middle), and headless while hanging without ground contact (bottom). Red circles indicate optogenetic laser stimulation.
Link to Supplementary Video 8

Supplementary Video 4.9: aDN2-driven behavioral responses of animals that are intact, headless, or headless without ground contact. Responses to optogenetic stimulation of aDN2 for three flies (one animal per column). The same animal is studied intact on the spherical treadmill (top), headless on the spherical treadmill (middle), and headless while hanging without ground contact (bottom). Red circles indicate optogenetic laser stimulation.
Link to Supplementary Video 9

Supplementary Video 4.10: MDN-driven behavioral responses of animals that are intact, headless, or headless without ground contact. Responses to optogenetic stimulation of MDN for three flies (one animal per column). The same animal is studied intact on the spherical treadmill (top), headless on the spherical treadmill (middle), and headless while hanging without ground contact (bottom). Red circles indicate optogenetic laser stimulation.
Link to Supplementary Video 10

Supplementary Video 4.11: Control animal behavioral responses to laser illumination of animals that are intact, headless, or headless without ground contact. Responses to laser illumination of animals without a GAL4 driver for three flies (one animal per column). The same animal is studied intact on the spherical treadmill (top), headless on the spherical treadmill (middle), and headless while hanging without ground contact (bottom). Red circles indicate laser illumination.
Link to Supplementary Video 11

Supplementary Video 4.12: DNb02-driven behavioral responses of animals that are intact, headless, or headless without ground contact. Responses to optogenetic stimulation of DNb02 for three flies (one animal per column). Animals are studied intact on the spherical treadmill (top), headless on the spherical treadmill (middle), or headless while hanging without ground contact (bottom). Red circles indicate optogenetic laser stimulation.
Link to Supplementary Video 12

Supplementary Video 4.13: DNa01-driven behavioral responses of animals that are intact, headless, or headless without ground contact. Responses to optogenetic stimulation of DNa01 for three flies (one animal per column). Animals are studied intact on the spherical treadmill (top), headless on the spherical treadmill (middle), or headless while hanging without ground contact (bottom). Red circles indicate optogenetic laser stimulation.
Link to Supplementary Video 13

Supplementary Video 4.14: DNa02-driven behavioral responses of animals that are intact, headless, or headless without ground contact. Responses to optogenetic stimulation of DNa02 for three flies (one animal per column). Animals are studied intact on the spherical treadmill (top), headless on the spherical treadmill (middle), or headless while hanging without ground contact (bottom). Red circles indicate optogenetic laser stimulation.
Link to Supplementary Video 14

Supplementary Video 4.15: aDN1-driven behavioral responses of animals that are intact, headless, or headless without ground contact. Responses to optogenetic stimulation of aDN1 for six flies (each animal identity is indicated). Animals are studied intact on the spherical treadmill (top), headless on the spherical treadmill (middle), or headless while hanging without ground contact (bottom). Red circles indicate optogenetic laser stimulation.
Link to Supplementary Video 15

Supplementary Video 4.16: DNg14-driven behavioral responses of animals that are intact, headless, or headless without ground contact. Responses to optogenetic stimulation of DNg14 for three flies (one animal per column). Animals are studied intact on the spherical treadmill (top), headless on the spherical treadmill (middle), or headless while hanging without ground contact (bottom). Red circles indicate optogenetic laser stimulation.
Link to Supplementary Video 16

Supplementary Video 4.17: Mute-driven behavioral responses of animals that are intact, headless, or headless without ground contact. Responses to optogenetic stimulation of Mute for six flies (each animal identity is indicated). Animals are studied intact on the spherical treadmill (top), headless on the spherical treadmill (middle), or headless while hanging without ground contact (bottom). Red circles indicate optogenetic laser stimulation.

Link to Supplementary Video 17

4.9 Data availability

Data are available at:
https://dataverse.harvard.edu/dataverse/dn_networks This repository includes processed
data required to reproduce the figures for each fly. Raw two-photon imaging data and
behavioral videos (~ 1 TB) are available upon request.

4.10 Code availability

Analysis code is available at: https://github.com/NeLy-EPFL/dn_networks

4.11 Acknowledgments

4.12 Author Contributions

J.B. - Conceptualization, Methodology, Software, Validation, Formal Analysis, Investigation,
Data Curation, Validation, Writing – Original Draft Preparation, Writing – Review & Editing,
Visualization.
Technical contributions: **Figure 4.1** visualisation; **Figure 4.2** experiments, analysis, visu-
alisation; **Figure 4.3** some visualisation; **Figure 4.4** experiments, analysis, visualisation;
Figure 4.5 some experiments, some data analysis, some visualisation.
F.H. - Conceptualization, Methodology, Software, Validation, Formal Analysis, Investigation,
Data Curation, Validation, Writing – Review & Editing, Visualization.
Technical contributions: **Figure 4.3** most connectomics data analysis, most visualisation;

Figure 4.5 most experiments, most data analysis, some visualisation; **Figure 4.6** connectomics modelling, visualisation.

S.W. - Conceptualization, Methodology, Software, Validation, Formal Analysis, Investigation, Data Curation, Validation, Writing – Review & Editing.

Technical contributions: **Figure 4.3**, **Figure 4.5** some connectomics data analysis

P.R. - Conceptualization, Methodology, Resources, Writing – Original Draft Preparation, Writing - Review & Editing, Supervision, Project Administration, Funding Acquisition.

4.13   Ethical compliance

All experiments were performed in compliance with relevant national (Switzerland) and institutional (EPFL) ethical regulations.

4.14   Declaration of Interests

The authors declare that no competing interests exist.

5 Discussion

Here, I presented scientific progress in two synergistically linked domains — advancing *in vivo* long-term neuronal recordings of Ascending Neurons (ANs) and Descending Neurons (DNs) and advancing our understanding of descending behavioural control:

In Chapter 3, we developed a toolkit to enable long-term imaging of the ventral nerve cord (VNC) and cervical connective in behaving adult *Drosophila*. As part of this work, we developed a flexible pipeline for combined two-photon microscopy and behavioural data processing, that can be easily adapted to different use cases. In both projects, it allowed us to rapidly inspect data despite the complex processing necessary to extract meaningful signals from such high-dimensional data. We showed that animals who underwent the dissection to insert a v-shaped implant and were sealed with a small window behave similar to control flies and can survive for multiple months. Using this toolkit, we observed ipsilateral mechanosensory nerve degradation in the VNC upon unilateral resection of a front-leg. We demonstrated that this toolkit allows imaging of neural population dynamics during and after feeding and observed waves of AN and DN activity after ingestion of high doses of caffeine. This toolkit paves the way for studies of neuronal activity during long-term motor adaptation or the progression of neurodegenerative diseases.

In Chapter 4, we provided a novel account of interactions between Descending Neurons (DNs) as a functional principle for flexible behavioural control. We found that command-like DNs activate many other DNs and do not act alone on the VNC. Analysing the brain connectome, we found that this recruitment may be explained by many monosynaptic connections between DNs in the brain. Interestingly, command-like DNs for flexible forward walking connect to more DNs than command-like DNs for stereotyped backward walking. We found that this DN recruitment is necessary for forward walking and grooming, but not for backward walking. Based on these results, we predicted that large networks of downstream DNs are required for flexible behaviours, but simple movements are maintained without DN recruitment, and confirmed this prediction with experiments on 6 additional DNs. Finally, we looked at descending control from a network perspective and studied the network that is formed by all DNs. Surprisingly, we found that DNs form excitatory clusters of neurons linked to specific behaviours. These clusters inhibit competing clusters, potentially

as a mechanism for action selection. Taken together, our novel model of descending behavioural control unifies the two previously conflicting models of command-like and population-based DN control: Networks of DNs are recruited to transform command-like signals into population-based behavioural control. DN recruitment may be a mechanism to construct flexible behaviours by combining multiple motor subroutines.

In the following, I will discuss implications of our second study on models of behavioural control, describe technical limitations of both studies, and will highlight ways to combine and follow-up on both advances.

5.1 Implications of interactions between DNs on models of behavioural control

5.1.1 Limitations of the command-like model of descending control

In the past, many studies have identified command-like DNs, often individual pairs of DNs (see Section 1.3). This command-like model of descending control implied a one-dimensional signal being sent from the brain to lower-level motor circuits. Our experiments demonstrate that this is only true for a subset of DNs, and is not a general rule of how DNs generate behaviour: For some command-like DNs — particularly those responsible for stereotyped behaviours such as backward walking — a one-dimensional signal is indeed sufficient for motor circuits in the VNC to generate a complete behaviour. However, most DNs do not act alone on the VNC but instead recruit other DNs through connections in the brain to create a higher-dimensional signal. Other command-like DNs — particularly those responsible for flexible behaviours such as forward walking — are not in itself sufficient and require recruitment of other DNs in the brain to execute complete behaviours. DNp09, a DN that triggers forward walking, was one of the examples we studied in detail and found that it requires connections to other DNs to elicit forward walking. A recent study showed that DNp09 activity correlates neither with rotational, nor forward velocity [87] further underlining the fact that DNp09 does not fulfil the formal definition of a 'command neuron' because it does not encode the behaviour it commands [64]. Additionally, Sapkal et al analysed the DN network downstream of DNp09 in more detail [286]: They found that certain DNs are responsible for the rotational component of DNp09 triggered walking, while other DNs are responsible for the translational component. A GNG interneuron that acts on the translational DNs can selectively suppress translation while keeping rotational movements intact [286].

Thinking of some DNs as command-like neurons is still a useful model, but rather than being a single-channel to the VNC, they may be thought of as entry points to sub-networks of DNs responsible for specific behaviours. Having such single neuron entry points with the unique ability to activate a behaviour may be useful for context-independent activation of specific behaviours. For example, the MDNs can be activated through visual inputs [98] or through touch information conveyed by an Ascending Neuron [99].

5.1.2   A foundation for the population model of descending control

In recent years, a population model of descending control has been proposed, mostly based on observational studies (see Section 1.4). Across different species, multiple studies showed that large populations of DNs are active during ongoing behaviours but it was not clear how this population recruitment was generated. Our study now provides a generative model that may explain why many DNs are co-active: They are connected to each other through synapses in the brain. While our study was performed with *Drosophila*, this principle may be conserved across species. In mammals, some corticospinal tract neurons form collaterals within the brainstem and the corticobulbar tract (even though it does not project to the spinal cord) links the two major populations of spinally projecting DNs in motor cortex and brainstem [28, 45, 46].

Populations of DNs instead of individual DNs may be active for different reasons: In work focused on primate motor cortex — root of many corticospinal DNs —, the principle of 'population control' is grounded in the idea that a population of neurons jointly encodes different parameters of movements [287]. This is evident in the fact that single-unit recordings are often hard to interpret and do not correlate with external variables, but population recordings provide the necessary statistical power to reliably decode movement intentions [14]. Additionally, similar population activity patterns are observed in motor cortex during tasks that require activation of different muscles, presumably as a sign of adaptability [288]. Thus, DN population control may be a mechanism for reliable, yet flexible descending control through nonlinear embedding of multiple variables in the joint activity of populations of DNs.

Alternatively, activity of populations of DNs may be the necessary substrate for fine-grained control of individual limb degrees of freedom or movement motifs. Aymanns et al. found that information about turning is spread across many DNs [96]. The recordings from many genetically identified DNs by Yang et al. confirmed that at least 5 pairs of DNs correlate with turning [87]. Additionally, they showed that individual DNs may control different "limb gestures": One DN attenuates the inside stride and another one extends the outside stride during turning. These findings argue for a model where populations of DNs may be recruited to provide finer-grained control by the brain. Similarly, a population of brainstem DNs gets recruited during skilled forelimb tasks and projects directly onto forelimb-innervating motor neurons [38]. Most fine-grained and skilled movements, such as grasping, feeding, or grooming are indeed performed with the forelimbs. The GNG is the brain region with the strongest projections to the front leg neuropil in *Drosophila* and itself receives input from 85% of all DNs [32]. Thus, the recruitment of additional populations of DNs, particularly in the GNG or brainstem, may also play an important role in fine-grained descending control of skilled motor behaviours.

5.1.3   Distributed action selection through interactions of DNs

In conventional models of action selection, higher order brain circuits such as the central complex [285] or mushroom body [289] implement action selection and then activate DNs to communicate their behavioural choice to motor circuits in the VNC. In mammals, inhibitory circuits in the basal ganglia contribute to action selection by "disinhibiting a selected motor program and inhibiting other competing actions" [290]. In particular, indirect projections from the basal ganglia are thought to differentially affect behaviour specific brain stem circuits [40].

Our analyses showed that DNs themselves are connected in behaviour-specific excitatory clusters that inhibit each other. This reciprocal inhibition is a hallmark of action selection circuits implementing a winner-takes-all mechanism [18, 291]. Our results suggest that action selection may not be limited to higher order brain circuits, but may instead be distributed across many hierarchical layers, one of which are the DNs. DNs are ideally positioned to fulfil this role because even individual DNs can integrate sensory information from multiple sources, for example MDN [98, 99] or DNp09 [79]. This is in line with observations in *Drosophila* larvae that action selection is implemented through convergence of multiple sensory pathways at different levels of sensorimotor transformation circuits [19, 292]. Overall, our results contribute to an increasing body of literature arguing for a distributed mechanism of action selection that is not finalised with the activation of DNs.

5.2   Technical limitations

5.2.1   Calcium imaging

While GCaMP is a powerful tool to study functional activity in genetically defined populations of neurons, its usage as a proxy of neuronal activity comes with multiple limitations: First, the slow decay kinematics of GCaMP6s preclude the analysis of correlations between neuronal activity and fast limb kinematics. In Chapter 4, we focused on whether neurons become active upon stimulation and not the encoding of neurons. Electrophysiological recordings of individual DNs that are recruited by command-like DNs may reveal a tighter correlation with the movement of individual limbs, movement parameters, or even joints. For example, the study of Yang et al revealed that DNa02 and DNg13 — the former being downstream of DNp09 and MDN — are responsible for different 'limb gestures' during turning [87]. This is consistent with the model that command-like DNs control higher level behaviours by hierarchically recruiting other DNs for more fine-grained control.

Second, the slow rise kinematics of GCaMP6s preclude us from determining whether connections from a command-like DN to other DNs are monosynaptic or multi-synaptic. We showed that the command-like neurons studied in Chapter 4 not only connect to many DNs monosynaptically, but also connect to more DNs across multiple synapses than an average DN. Thus, it is likely that among the recruited DNs in functional imaging, we can observe multi-synaptically activated neurons. This makes functional imaging a valuable

complement to connectomics, because it shows how many connections are actively used. As an example, both the forward walking command-like DN DNp09 and its backward walking counterpart MDN directly synapse onto DNa01 and DNa02, which are both involved in turning [91, 95]. We showed that they contact many DNs themselves, which are necessary for turning and may be visible in our functional recording of GNG DNs upon DNp09 or MDN stimulation.

Third, GCaMP does not reliably show inhibition of neurons. Thus, we do not claim that the de-activation we observe in some neurons is due to inhibition. Since the flies were walking before the stimulation onset, those neurons most likely encode walking (like many cerebral ganglia DNs in [96]) and became less active when the fly was not walking anymore. However, our analysis of DN-DN interaction in the connectome revealed inhibition between DN communities corresponding to different behaviours. Potentially, an analysis of the decay timescales upon optogenetic stimulation may allow us to discriminate between active inhibition and passive de-excitation of individual DNs.

These technical limitations of GCaMP may be reduced by using faster calcium sensors, such as GCaMP8f with a half-rise time of 2ms [135], or entirely overcome by the use of genetically encoded voltage indicators [136]. However, our two-photon recordings were not possible to speed-up beyond the current 16 Hz scan rate and will limit the meaningfulness of such recordings. Additionally, faster recordings will require indicators with high signal-to noise ratio because of the reduced pixel dwell time. Light-sheet microscope recordings of the cervical connective (e.g., a SCAPE microscope [142]) may alleviate this constraint by illuminating and acquiring an entire 2D plane at once instead of scanning over individual pixels. Alternatively, electrophysiological recordings may allow us to precisely understand the recruitment of selected, individual DNs and their relationship to fast time-scale behavioural parameters as a valuable complement to population recordings.

5.2.2 Split-GAL4 reagents

Split-GAL4 reagents do not always express in a single type of neurons. In particular, the aDN2 reagent we used in Chapter 4 (*aDN2-GAL4.2* [61]) contains two groups of additional neurons. One pair of neurons is on the anterior surface of the brain and, based on our control experiments, will likely not or only weakly be activated by the targeted neck stimulation and not at all by the thorax stimulation. Another group of neurons in the anterior VNC is labelled by this driver line. Other genetic driver lines targeting the aDN2 neurons with more, but other off-target neurons labelled have the same behavioural phenotype as the driver we used [61]. We performed some preliminary experiments with an additional driver line (*aDN2-GAL4.4* [61]). This driver line also contains additional neurons, but they do not overlap with the neurons in the *aDN2-GAL4.2* line we used originally. In particular, they do not contain cells in the anterior VNC. We observed that optogenetic activation of the *aDN2-GAL4.4* driver is less reliable than the *aDN2-GAL4.2* driver. Consistently across both driver lines, headless flies do not groom as intact flies. These results make us confident that the effects we observe are due to the aDN2 neurons themselves and not due to off-target expression of the driver line.

Different studies have found conflicting behavioural phenotypes for the activation of DNp09: Some found forward walking [79], others found stopping or freezing [81, 85]. We observed both: at our standard 10μW stimulation power, flies were mostly walking forward. However, sometimes flies would only transiently walk forward and then halt, or alternate rhythmically between walking and halting. For higher expression levels of CsChrimson (i.e., DNp09-GAL4 > UAS-CsChrimson homozygous animals) we observed mostly freezing.

5.2.3   Hox gene driver lines for targeted DN imaging

In Chapter 4, we chose the Hox-gene Dfd and an optical intersection to selectively record from GNG DNs. This does not include the entirety of all GNG DNs because two Hox-genes are expressed in the GNG [276]: Deformed (Dfd) and Sex combs reduced (Scr). Sterne et al. [44] estimate that 550 cells in the GNG are Dfd positive and 1100 Scr positive, with only a small fraction expressing both Hox genes. We showed, for example, that aDN2 is Dfd negative and thus most likely Scr positive (**Figure S4.1c**). We also attempted functional recording of Scr DNs while optogenetically activating command-like DNs, but it proved to be difficult because of Scr expression extending into the neck, anterior VNC and front-leg (**Figure 5.1a**, from [168]). Using the *Dfd-LexA* line, DNs are clearly visible as parallel axons in a volume recording of the cervical connective (**Figure 5.1b**). On the contrary, using the *Scr-LexA* line we observed strong expression of GCaMP in tissue surrounding the thoracic cervical connective, stronger than any expression in DNs, making it impossible to record functional activity of DN axons (**Figure 5.1c**). This expression could be in ensheathing glia that wraps the cervical connective [277]. Additionally, the expression of tdTomato under the *Scr-LexA* driver did not yield any viable progeny. We expect to see that some Scr positive DNs will be recruited by command-like DNs similar to Dfd positive DNs. Thus, the number of recruited GNG DNs that we report are likely underestimates.

Many Hox-gene lines have expression predominantly in a particular segment of the body and thereby a segment of the nervous system. For example, the Hox-gene Tsh is frequently used in intersectional strategies to suppress (using Tsh-GAL80) or restrict (using the Flp/FRT system) expression to the VNC. However, Tsh also expresses in some cells in the brain, making it an imperfect genetic reagent [168]. We showed that Dfd-LexA does not drive expression in cells in the adult VNC (**Figure S4.1b**). This was important to exclude the expression in Ascending Neurons (ANs), which project from the VNC to the brain and would have been visible in our functional recordings of axons in the cervical connective (CC). However, we observed weak expression in the leg and wing nerves, but not in the haltere nerves (see nerves attached to the VNC visible in **Figure S4.1a**). VNC nerves contain motor neurons, which do not ascend to the brain, and sensory neurons. Among the $\sim$ 6500 sensory neurons in nerves attached to the VNC, the vast majority ($\sim$ 6000) project only to the VNC. A small minority ($\sim$ 500) also ascend directly to the brain [177]. Only four particular types of sensory modalities ascend directly to the brain [47]: Haltere companiform sensilla (hcs), wing companiform sensilla (wcs), leg gustatory sensilla (lgs), and leg chordotonal organs (lco). We identified those sensory ascending (SA) neurons in
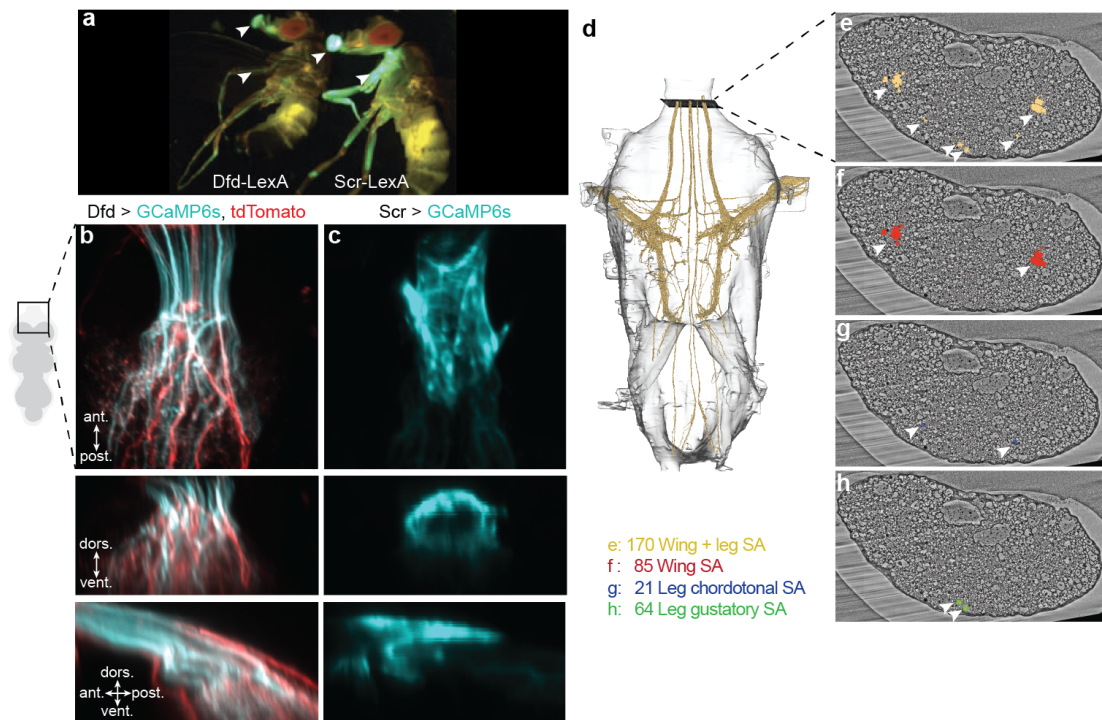
Figure 5.1: Limitations of Hox gene driver lines for targeted DN imaging. (a) Expression patterns of *Dfd-LexA* and *Scr-LexA* lines. Note the strong expression in the proboscis, the faint leg expression in Dfd, and the strong front-leg expression of Scr. Modified from [168]. **(b)** Three different mean projections of a volume recording of the cervical connective and T1 region of an anaesthetised fly expressing GCaMP6s and tdTomato in *Dfd-LexA*. **(c)** As (b) but for GCaMP6s expression in *Scr-LexA*. Note the strong expression in a sheath surrounding the cervical connective. **(d)** A rendering of all sensory ascending (SA) neurons in the wings and legs based on the male VNC connectome [177]. **(e)** An electron microscopy slice of the cervical connective with all wing and leg sensory ascending neurons indicated. **(f)** As (e), but only wing sensory ascending neurons indicated in red. **(g)** As (e), but only leg chordotonal ascending neurons indicated in blue. **(h)** As (e), but only leg gustatory ascending neurons indicated in green.

the male VNC connectome [177]: We found 315 hcs, 85 wcs, 64 lgs, and 21 lco neurons. Given that we see Dfd expression in the leg and wing nerves but not the haltere nerves, we cannot exclude that 170 SA neurons are also labelled and may be visible in the CC (**Figure 5.1d**). Thus, we identified their position in the CC. Interestingly, each sensory modality sends its ascending axons in a specific, symmetrically positioned ipsilateral tract of the CC. Each of those six tracts is formed by many thin axons from one sensory modality, that are in immediate proximity to each other (**Figure 5.1e**). Wing SA neurons ascend in two medio-lateral tracts (**Figure 5.1f**). Leg chordotonal SA neurons ascend in two ventro-lateral tracts (**Figure 5.1g**). Leg gustatory SA neurons ascend in two ventro-central tracts (**Figure 5.1h**). Given that these axons are so thin and close to each other, they likely each appear as a single ROI during functional imaging. These six tracts are outside of the main regions where we see activation upon DNp09, aDN2, and MDN stimulation (mostly

dorso-central and medio-central, see **Figure 4.2**). Only the ventro-central neurons activated upon DNp09 stimulation may spatially overlap with the leg-gustatory SA. However, if the activated neurons we observe were leg sensory neurons, we would also expect them to be activated during spontaneous forward walking, which is not the case (**Figure S4.2f**). Despite the limitations that come from the use of an imperfect genetic reagent labelling sensory ascending neurons in six tracts, this confirms that the strong activation we see in our imaging study is due to Descending Neurons, and not sensory ascending neurons.

5.2.4   Connectivity patterns of DN networks

In Chapter 4 we observed that many DNs are activated upon optogenetic activation of command-like DNs. We showed that monosynaptic connections in the brain from command-like DNs to other DNs may be a potential circuit mechanism. We also discussed how other circuit mechanisms may contribute to this observation: Multi-synaptic connections in the brain involving multiple DNs, or other brain neurons are likely contributing to the DN population recruitment. Additionally, connections involving synapses in the VNC and Ascending Neurons (ANs), for example a 'zigzag' motif (DN-AN-DN) [175] may be present. The fact that many ANs project to the GNG [48], where many DNs receive synaptic inputs, makes their existence plausible. To be sure that DN networks are only recruited through connections in the brain, and not the VNC, one could perform *ex-vivo* experiments with entire nervous system explants: After identifying DNs that are activated in functional recordings during optogenetic stimulation, one could prevent synaptic transmission in the VNC (by cutting the posterior cervical connective or by bathing the VNC in tetanus toxin) and repeat the optogenetic activation and functional recording. If DNs are still activated, their recruitment will have been solely through synapses in the brain. If DNs were not active anymore, their recruitment would have been through pathways involving synapses the VNC.

5.2.5   Automated ROI detection

The only step of the processing pipeline developed in Chapter 3 and used in Chapter 4 that requires manual intervention is the semi-automated ROI detection. Currently, a peak-detection algorithm suggests the location of individual ROIs (see Section 4.5.9), but the ROIs have to be manually approved or modified by the user. This process is subject to biases and takes around 30 minutes per fly. Fully automated ROI detection is challenging for multiple reasons: (1) Individual frames of two-photon recordings are very noisy. Thus, ROI detection is currently performed using summary images, such as the standard deviation projection of each pixel across time, the local correlation of a pixel with its neighbouring pixels, or the association of each pixel to a specific principal component of the entire data of one fly. Based on that, only one data-point is available per fly and large datasets that would be required for deep-learning tools are hard to attain. (2) Within one fly, individual ROIs may have very variable appearance in the summary images mentioned above. Their maximum values and size may vary based on how often a fly was performing a specific behaviour that a given neuron's activity correlates with. Neurons that were less active, are

often harder to spot. Based on that, quantitative heuristics that apply to all neurons of one fly are hard to design. (3) Across flies, the shape of the entire cervical connective and the signal-to-noise level varies, making it hard to apply a detection model trained on some flies to another fly's data. (4) Depending on the scientific questions, one can imagine recording from different types of neurons in the cervical connective: all ANs and DNs (as in Chapter 3), GNG DNs (as in Chapter 4), cerebral ganglia DNs [96], or ANs [48]. Expecting different numbers of neurons in different locations creates yet another domain gap that would need to be overcome by a fully automated algorithm. In a student project with Qianyi Xu, Bachelor student at Nanyang Technological University Singapore, we have explored the possibility of using deep learning to automate this process. We used auxiliary learning [293] to learn shared representations across different animals and test-time adaptation [294] to fine-tune the model for accurate ROI detection in a new fly. The results were promising, but generalisation across different flies was limited because of the small size of the available dataset. In the future, segmentation models that are trained across many different modalities, such as 'Segment Anything for Microscopy' [295] might be able to overcome the large domain gaps present in our data because they have been trained for even larger domain gaps.

5.2.6 Identifying individual DNs across recording time points and animals

One of the largest obstacles in interpreting functional recordings of populations of DNs in *Drosophila* is the fact that in most cases, individual DNs cannot be identified across animals. This is the case even though *Drosophila* neurons can be targeted individually and repeatedly across animals [75]. In our study in Chapter 4, this would have permitted to average individual neuron responses across flies and cross-identify individual DNs in the brain connectome. Instead, we made use of the stereotyped anatomy of the cervical connective (CC) and aligned the recordings of individual flies to each other to visualise global patterns of activation and observed specific loci of activation for different command-like DNs. A previous study with similar data managed to match a characteristic pair of DNs across flies based on its unique position and size [96]. We also showed that individual neurons strongly activated by DNp09 stimulation are in a similar position in the CC and may in fact be the same neurons (**Figure S4.2f**). In general, matching neurons across flies is challenging because despite some stereotypy, the anatomy of the CC is variable across flies: The cross-section of the CC varies in orientation, size, and shape, making it difficult to globally align them across flies. Within the CC, DNs travel in specific tracts [35], which constrains their position. However, based on observing characteristic DNs such as the giant fibres, the exact position of DNs within the CC appears surprisingly variable.

Nonetheless, we tried to tackle this problem in multiple ways. In a student project with Sara Djambazovska, Master student at EPFL, we used functional features (encoding of behaviours, activity level during behaviours) and anatomical features (position, size, morphology, ...) of each neuron to first match neurons across different time points in the recording of a single fly. Matching neurons across flies was possible with 70 % accuracy

for manually labelled characteristic neurons. However, testing the generalisation of this algorithm was impossible because of missing ground trough data for the remaining neurons. Such ground truth data may be acquired by expressing GCaMP in a large population of DNs (e.g., *Dfd-LexA*), and a red fluorescent protein in a small number of uniquely identifiable neurons. However, this approach would require large amounts of experiments.

In a student project with Chléa Schiff, Bachelor student at EPFL, we attempted to augment the features available for matching across flies by relying on 3D axon morphology. We used 3D volumes of the CC (like **Figure 5.1b**) acquired post-hoc during anaesthesia to avoid movement artifacts and segmented neurons in 3D to extract their morphology. We used this segmentation in a student project with Philippe Forero, Master student at EPFL, to match neurons within the same fly after the animal has undergone an experimental manipulation outside of the microscope set-up. Applying this method to matching neurons across flies would be the logical next step.

Recently, Brezovec et al. [266] developed a reference atlas of the *Drosophila* brain and alignment algorithms allowing to register data from different animals and different modalities to each other. Using a similar methodology for the cervical connective and the VNC may allow us to match DN recordings across flies, and to match them to existing VNC connectomes [176, 177]. Ultimately, this would allow us to precisely understand the relationship between DN connectivity, and functional DN recruitment during behaviours.

5.3   Future directions

5.3.1   Internal state modulation of VNC circuits through Descending Neurons

In Chapter 3 we demonstrated that the long-term imaging toolkit can be used to study neuronal dynamics of Ascending and Descending Neurons during and after feeding. We demonstrated large-scale changes in neuronal activity after ingesting high doses of caffeine. Limited by the fact the we were recording from Ascending and Descending Neurons at the same time and were not able to discriminate between them, we did not analyse in detail whether any smaller-scale changes happen during and after feeding. However, using more restricted genetics may permit us to ask specific questions about how internal state and sensory information are conveyed to the VNC.

The GNG receives gustatory sensory input from the proboscis [42], and 'Bract', a DN that projects from the GNG to the VNC, is active upon sugar, but not water sensation [52]. Besides processing sensory signals, the GNG also encodes internal states, such as starvation [54]. It has been shown that starvation induces changes in taste perception [296] and hyperactivity in flies [297]. Conversely, the taste of sugar suppresses locomotion [298]. Using the long-term imaging toolkit while recording exclusively from GNG DNs (*Dfd-LexA*, as in Chapter 4) would permit us to study how hunger hyperactivity is induced and reduced again once sugar is consumed. It may be that only some neuromodulatory DNs change their activity to signal hunger, but other descending signals remain unchanged. Alternatively,

gustatory DN signals may be used to modulate local VNC circuits. Lastly, starvation may only act on the brain and changes in DN signals may simply be explained by changes in movement parameters related to faster, and more frequent locomotion. Complementing this functional imaging study with a connectome analysis of pathways from gustatory neurons to DNs — beyond what is known about 'Bract' DNs [52] — would allow us to understand circuit mechanisms how internal states modulate descending circuits and ultimately the VNC.

5.3.2   Influence of ANs on DN signalling

We observed that many DNs are recruited during optogenetic activation of command-like DNs and that in general, DNs connect to each other in behaviour-specific clusters. Our analyses propose direct DN-DN connectivity as a possible explanans of DN recruitment, but other pathways may also contribute to it. So far, we have studied DN-DN connectivity in detail, but have not explored inputs do DNs from other types of neurons. Feed-forward inputs to specific command-like DNs have been studied previously: MDN receives input from visual projection neurons [98], DNp09 receives input from visual projection neurons and courtship-promoting neurons [79], and aDNs receive indirect input from Johnston's organ sensory neurons [61]. However, less is known about feedback connections. In order to coordinate ongoing actions and to switch between actions, feedback about the current behavioural state is critical. In *Drosophila*, Ascending Neurons (ANs) are well positioned to provide this feedback: Many of them project from the VNC to the GNG [48], where many DNs receive synaptic inputs [32] and different sensory modalities [41–44] and internal states are integrated to select different actions [54]. Individual ANs have already been shown to impact action selection: A pair of ANs influences the choice between feeding and locomotion [267]. The TwoLumps ANs project directly onto MDNs to initiate backward walking [99]. The moonwalker ascending neurons (MANs) promote persistent backward walking when activated together with MDNs [86] and promote halting when activated alone [286]. Activation of a group of six 'BRAKE' ANs causes flies to stop irrespective of whether the animal was walking forward or backward before stimulus onset [286]. In the case of MAN and BRAKE neurons, many DNs are only a few synapses downstream in the brain [286]. Understanding on a global scale how ANs connect to DNs in the brain, and in turn, how DNs connect to ANs in the VNC will allow us to gain a complete understanding of interactions between the brain and the VNC during motor control and action selection. Activating ANs using sparse genetic lines [48] while recording GNG DNs will permit us to understand their influence on DN dynamics. The identification of ANs in brain [50] and VNC connectomes [176, 177] will facilitate a comprehensive study of the effect of ANs on action selection and execution, potentially revealing general principles how ANs influence DN signalling.

Bibliography

1. Bernstein, N. A. *Dexterity and Its Development* ISBN: 978-1-4106-0335-7 (1996).

2. Profeta, V. L. S. & Turvey, M. T. Bernstein's levels of movement construction: A contemporary perspective. *Human Movement Science* 57, 111–133 (2018).

3. Bongers, R. M., Kyberd, P. J., Bouwsema, H., Kenney, L. P. J., Plettenburg, D. H. & Van der Sluis, C. K. Bernstein's Levels of Construction of Movements Applied to Upper Limb Prosthetics. *JPO: Journal of Prosthetics and Orthotics* 24, 67 (2012).

4. Rothwell, J. *Bernstein's Anatomical Levels of Construction* in *Bernstein's Construction of Movements* (2020). ISBN: 978-0-367-81679-7.

5. Bruton, M. & O'Dwyer, N. Synergies in coordination: a comprehensive overview of neural, computational, and behavioral approaches. *Journal of Neurophysiology* 120, 2761–2774 (2018).

6. Li, L., Xiong, W.-C. & Mei, L. Neuromuscular Junction Formation, Aging, and Disorders. *Annual Review of Physiology* 80, 159–188 (2018).

7. Heckman, C. J. & Enoka, R. M. Motor unit. *Comprehensive Physiology* 2, 2629–2682 (2012).

8. d'Avella, A., Saltiel, P. & Bizzi, E. Combinations of muscle synergies in the construction of a natural motor behavior. *Nature Neuroscience* 6, 300–308 (2003).

9. Tresch, M. C. & Jarc, A. The case for and against muscle synergies. *Current Opinion in Neurobiology* 19, 601–607 (2009).

10. Marshall, N. J., Glaser, J. I., Trautmann, E. M., Amematsro, E. A., Perkins, S. M., Shadlen, M. N., Abbott, L. F., Cunningham, J. P. & Churchland, M. M. Flexible neural control of motor units. *Nature Neuroscience* 25, 1492–1504 (2022).

11. MacKay-Lyons, M. Central pattern generation of locomotion: a review of the evidence. *Physical Therapy* 82, 69–83 (2002).

12. Wimalasena, L. N., Braun, J. F., Keshtkaran, M. R., Hofmann, D., Gallego, J. Á., Alessandro, C., Tresch, M. C., Miller, L. E. & Pandarinath, C. Estimating muscle activation from EMG using deep learning-based dynamical systems models. *Journal of Neural Engineering* 19, 036013 (2022).

13. Churchland, M. M., Cunningham, J. P., Kaufman, M. T., Foster, J. D., Nuyujukian, P., Ryu, S. I. & Shenoy, K. V. Neural population dynamics during reaching. *Nature* 487, 51–56 (2012).

14. Shenoy, K. V., Sahani, M. & Churchland, M. M. Cortical Control of Arm Movements: A Dynamical Systems Perspective. *Annual Review of Neuroscience* 36, 337–359 (2013).

15. Pandarinath, C., O'Shea, D. J., Collins, J., Jozefowicz, R., Stavisky, S. D., Kao, J. C., Trautmann, E. M., Kaufman, M. T., Ryu, S. I., Hochberg, L. R., Henderson, J. M., Shenoy, K. V., Abbott, L. F. & Sussillo, D. Inferring single-trial neural population dynamics using sequential auto-encoders. *Nature Methods* 15, 805–815 (2018).

16. Logiaco, L., Abbott, L. F. & Escola, S. Thalamic control of cortical dynamics in a model of flexible motor sequencing. *Cell Reports* 35, 109090 (2021).

17. Yokoi, A. & Diedrichsen, J. Neural Organization of Hierarchical Motor Sequence Representations in the Human Neocortex. *Neuron* 103, 1178–1190.e7 (2019).

18. Jovanic, T., Schneider-Mizell, C. M., Shao, M., Masson, J.-B., Denisov, G., Fetter, R. D., Mensh, B. D., Truman, J. W., Cardona, A. & Zlatic, M. Competitive Disinhibition Mediates Behavioral Choice and Sequences in Drosophila. *Cell* 167, 858–870.e19 (2016).

19. Masson, J.-B., Laurent, F., Cardona, A., Barré, C., Skatchkovsky, N., Zlatic, M. & Jovanic, T. Identifying neural substrates of competitive interactions and sequence transitions during mechanosensory responses in Drosophila. *PLOS Genetics* 16, e1008589 (2020).

20. Seeds, A. M., Ravbar, P., Chung, P., Hampel, S., Midgley Jr, F. M., Mensh, B. D. & Simpson, J. H. A suppression hierarchy among competing motor programs drives sequential grooming in Drosophila. *eLife* 3, e02951 (2014).

21. Kato, S., Kaplan, H. S., Schrödel, T., Skora, S., Lindsay, T. H., Yemini, E., Lockery, S. & Zimmer, M. Global Brain Dynamics Embed the Motor Command Sequence of Caenorhabditis elegans. *Cell* 163, 656–669 (2015).

22. Brooks, R. A robust layered control system for a mobile robot. *IEEE Journal on Robotics and Automation* 2, 14–23 (1986).

23. Merel, J., Botvinick, M. & Wayne, G. Hierarchical motor control in mammals and machines. *Nature Communications* 10, 1–12 (2019).

24. Tuthill, J.C. *Schematic of major descending pathways in mammals, Graphic on Wikipedia.* 2022.

25. Lassek, A. M. & Rasmussen, G. L. A comparative fiber and numerical analysis of the pyramidal tract. *Journal of Comparative Neurology* 72, 417–428 (1940).

26. Uematsu, J., Ono, K., Yamano, T. & Shimada, M. Development of corticospinal tract fibers and their plasticity I: Quantitative analysis of the developing corticospinal tract in mice. *Brain and Development* 18, 29–34 (1996).

27. Welniarz, Q., Dusart, I. & Roze, E. The corticospinal tract: Evolution, development, and human disorders. *Developmental Neurobiology* 77, 810–829 (2017).

28. Lemon, R. N. Descending Pathways in Motor Control. *Annual Review of Neuroscience* 31, 195–218 (2008).

29. Ueno, M., Nakamura, Y., Li, J., Gu, Z., Niehaus, J., Maezawa, M., Crone, S. A., Goulding, M., Baccei, M. L. & Yoshida, Y. Corticospinal Circuits from the Sensory and Motor Cortices Differentially Regulate Skilled Movements through Distinct Spinal Interneurons. *Cell reports* 23, 1286–1300.e7 (2018).

30. Gu, Z., Kalambogias, J., Yoshioka, S., Han, W., Li, Z., Kawasawa, Y. I., Pochareddy, S., Li, Z., Liu, F., Xu, X., Wijeratne, H. R. S., Ueno, M., Blatz, E., Salomone, J., Kumanogoh, A., Rasin, M.-R., Gebelein, B., Weirauch, M. T., Sestan, N., Martin, J. H. & Yoshida, Y. Control of species-dependent cortico-motoneuronal connections underlying manual dexterity. *Science* 357, 400–404 (2017).

31. Grad, L. I., Rouleau, G. A., Ravits, J. & Cashman, N. R. Clinical Spectrum of Amyotrophic Lateral Sclerosis (ALS). *Cold Spring Harbor Perspectives in Medicine* 7, a024117 (2017).

32. Namiki, S., Dickinson, M. H., Wong, A. M., Korff, W. & Card, G. M. The functional organization of descending sensory-motor pathways in Drosophila. *eLife* 7, e34272 (2018).

33. Davis, R. L. Mushroom bodies and drosophila learning. *Neuron* 11, 1–14 (1993).

34. Varga, A. G., Kathman, N. D., Martin, J. P., Guo, P. & Ritzmann, R. E. Spatial Navigation and the Central Complex: Sensory Acquisition, Orientation, and Motor Control. *Frontiers in Behavioral Neuroscience* 11 (2017).

35. Cheong, H. S. J., Eichler, K., Stuerner, T., Asinof, S. K., Champion, A. S., Marin, E. C., Oram, T. B., Sumathipala, M., Venkatasubramanian, L., Namiki, S., Siwanow-icz, I., Costa, M., Berg, S., Team, J. F. P., Jefferis, G. S. X. E. & Card, G. M. Transforming descending input into behavior: The organization of premotor circuits in the Drosophila Male Adult Nerve Cord connectome. *bioRxiv,* 2023.06.07.543976 (2023).

36. Liang, H., Paxinos, G. & Watson, C. Projections from the brain to the spinal cord in the mouse. *Brain Structure and Function* 215, 159–186 (2011).

37. Leiras, R., Cregg, J. M. & Kiehn, O. Brainstem Circuits for Locomotion. *Annual Review of Neuroscience* 45, 63–85 (2022).

38. Esposito, M. S., Capelli, P. & Arber, S. Brainstem nucleus MdV mediates skilled forelimb motor tasks. *Nature* 508, 351–356 (2014).

39. Ruder, L., Schina, R., Kanodia, H., Valencia-Garcia, S., Pivetta, C. & Arber, S. A functional map for diverse forelimb actions within brainstem circuitry. *Nature* 590, 445–450 (2021).

40. Arber, S. & Costa, R. M. Networking brainstem and basal ganglia circuits for movement. *Nature Reviews Neuroscience* 23, 342–360 (2022).

41. Kendroud, S., Bohra, A. A., Kuert, P. A., Nguyen, B., Guillermin, O., Sprecher, S. G., Reichert, H., VijayRaghavan, K. & Hartenstein, V. Structure and development of the subesophageal zone of the Drosophila brain. II. Sensory compartments. *Journal of Comparative Neurology* 526, 33–58 (2018).

42. Snell, N. J., Fisher, J. D., Hartmann, G. G., Zolyomi, B., Talay, M. & Barnea, G. Complex representation of taste quality by second-order gustatory neurons in Drosophila. *Current Biology* 32, 3758–3772 (2022).

43. Matsuo, E., Seki, H., Asai, T., Morimoto, T., Miyakawa, H., Ito, K. & Kamikouchi, A. Organization of projection neurons and local neurons of the primary auditory center in the fruit fly Drosophila melanogaster. *Journal of Comparative Neurology* 524, 1099–1164 (2016).

44. Sterne, G. R., Otsuna, H., Dickson, B. J. & Scott, K. Classification and genetic targeting of cell types in the primary taste and premotor center of the adult Drosophila brain. *eLife* 10, e71679 (2021).

45. Kita, T. & Kita, H. The subthalamic nucleus is one of multiple innervation sites for long-range corticofugal axons: a single-axon tracing study in the rat. *The Journal of Neuroscience* 32, 5990–5999 (2012).

46. Ugolini, G. & Kuypers, H. G. J. M. Collaterals of corticospinal and pyramidal fibres to the pontine grey demonstrated by a new application of the fluorescent fibre labelling technique. *Brain Research* 365, 211–227 (1986).

47. Tsubouchi, A., Yano, T., Yokoyama, T. K., Murtin, C., Otsuna, H. & Ito, K. Topological and modality-specific representation of somatosensory information in the fly brain. *Science* 358, 615–623 (2017).

48. Chen, C.-L., Aymanns, F., Minegishi, R., Matsuda, V. D. V., Talabot, N., Günel, S., Dickson, B. J. & Ramdya, P. Ascending neurons convey behavioral state to integrative sensory and action selection brain regions. *Nature Neuroscience* 26, 682–695 (2023).

49. Thomas M. Kandel, E. R. ; S. *Principles of Neural Science* 4th edition. ISBN: 978-0-07-112000-5 (2000).

50. Dorkenwald, S., Matsliah, A., Sterling, A. R., Schlegel, P., Yu, S.-c., McKellar, C. E., Lin, A., Costa, M., Eichler, K., Yin, Y., Silversmith, W., Schneider-Mizell, C., Jordan, C. S., Brittain, D., Halageri, A., Kuehner, K., Ogedengbe, O., Morey, R., Gager, J., Kruk, K., Perlman, E., Yang, R., Deutsch, D., Bland, D., Sorek, M., Lu, R., Macrina, T., Lee, K., Bae, J. A., Mu, S., Nehoran, B., Mitchell, E., Popovych, S., Wu, J., Jia, Z., Castro, M., Kemnitz, N., Ih, D., Bates, A. S., Eckstein, N., Funke, J., Collman, F., Bock, D. D., Jefferis, G. S. X. E., Seung, H. S., Murthy, M. & Consortium, t. F. Neuronal wiring diagram of an adult brain. *bioRxiv,* 2023.06.27.546656 (2023).

51. McKellar, C. E., Siwanowicz, I., Dickson, B. J. & Simpson, J. H. Controlling motor neurons of every muscle for fly proboscis reaching. *eLife* 9, e54978 (2020).

52. Shiu, P. K., Sterne, G. R., Engert, S., Dickson, B. J. & Scott, K. Taste quality and hunger interactions in a feeding sensorimotor circuit. *eLife* 11, e79887 (2022).

53.   Tastekin, I., Riedl, J., Schilling-Kurz, V., Gomez-Marin, A., Truman, J. W. & Louis, M. Role of the Subesophageal Zone in Sensorimotor Control of Orientation in Drosophila Larva. *Current Biology* 25, 1448–1460 (2015).

54.   Münch, D., Goldschmidt, D. & Ribeiro, C. The neuronal logic of how internal states control food choice. *Nature* 607, 747–755 (2022).

55.   Hartenstein, V., Omoto, J. J., Ngo, K. T., Wong, D., Kuert, P. A., Reichert, H., Lovick, J. K. & Younossi-Hartenstein, A. Structure and development of the subesophageal zone of the Drosophila brain. I. Segmental architecture, compartmentalization, and lineage anatomy. *Journal of Comparative Neurology* 526, 6–32 (2018).

56.   Ito, K., Shinomiya, K., Ito, M., Armstrong, J. D., Boyan, G., Hartenstein, V., Harzsch, S., Heisenberg, M., Homberg, U., Jenett, A., Keshishian, H., Restifo, L. L., Rössler, W., Simpson, J. H., Strausfeld, N. J., Strauss, R. & Vosshall, L. B. A Systematic Nomenclature for the Insect Brain. *Neuron* 81, 755–765 (2014).

57.   Emanuel, S., Kaiser, M., Pflueger, H.-J. & Libersat, F. On the Role of the Head Ganglia in Posture and Walking in Insects. *Frontiers in Physiology* 11, 135 (2020).

58.   Ridgel, A. L. & Ritzmann, R. E. Effects of neck and circumoesophageal connective lesions on posture and locomotion in the cockroach. *Journal of Comparative Physiology. A, Neuroethology, Sensory, Neural, and Behavioral Physiology* 191, 559–573 (2005).

59.   Gal, R. & Libersat, F. New vistas on the initiation and maintenance of insect motor behaviors revealed by specific lesions of the head ganglia. *Journal of Comparative Physiology. A, Neuroethology, Sensory, Neural, and Behavioral Physiology* 192, 1003–1020 (2006).

60.   Whelan, P. J. Control of locomotion in the decerebrate cat. *Progress in Neurobiology* 49, 481–515 (1996).

61.   Hampel, S., Franconville, R., Simpson, J. H. & Seeds, A. M. A neural command circuit for grooming movement control. *eLife* 4, e08758 (2015).

62.   Robie, A. A., Hirokawa, J., Edwards, A. W., Umayam, L. A., Lee, A., Phillips, M. L., Card, G. M., Korff, W., Rubin, G. M., Simpson, J. H., Reiser, M. B. & Branson, K. Mapping the Neural Substrates of Behavior. *Cell* 170, 393–406.e28 (2017).

63.   Wiersma, C. A. G. & Ikeda, K. Interneurons commanding swimmeret movements in the crayfish, Procambarus clarki (girard). *Comparative Biochemistry and Physiology* 12, 509–525 (1964).

64.   Kupfermann, I. & Weiss, K. R. The command neuron concept. *Behavioral and Brain Sciences* 1, 3–39 (1978).

65.   Eaton, R. C., Lee, R. K. K. & Foreman, M. B. The Mauthner cell and other identified neurons of the brainstem escape network of fish. *Progress in Neurobiology* 63, 467–485 (2001).

66. Chalfie, M., Sulston, J. E., White, J. G., Southgate, E., Thomson, J. N. & Brenner, S. The neural circuit for touch sensitivity in Caenorhabditis elegans. *The Journal of Neuroscience* 5, 956–964 (1985).

67. Nissanov, J., Eaton, R. C. & DiDomenico, R. The motor output of the Mauthner cell, a reticulospinal command neuron. *Brain Research* 517, 88–98 (1990).

68. Hedwig, B. Control of cricket stridulation by a command neuron: efficacy depends on the behavioral state. *Journal of Neurophysiology* 83, 712–722 (2000).

69. Jordan, L. M., Liu, J., Hedlund, P. B., Akay, T. & Pearson, K. G. Descending command systems for the initiation of locomotion in mammals. *Brain Research Reviews* 57, 183–191 (2008).

70. Kim, L. H., Sharma, S., Sharples, S. A., Mayr, K. A., Kwok, C. H. T. & Whelan, P. J. Integration of Descending Command Systems for the Generation of Context-Specific Locomotor Behaviors. *Frontiers in Neuroscience* 11 (2017).

71. Capelli, P., Pivetta, C., Soledad Esposito, M. & Arber, S. Locomotor speed control circuits in the caudal brainstem. *Nature* 551, 373–377 (2017).

72. Bouvier, J., Caggiano, V., Leiras, R., Caldeira, V., Bellardita, C., Balueva, K., Fuchs, A. & Kiehn, O. Descending Command Neurons in the Brainstem that Halt Locomotion. *Cell* 163, 1191–1203 (2015).

73. Brocard, F., Ryczko, D., Fénelon, K., Hatem, R., Gonzales, D., Auclair, F. & Dubuc, R. The Transformation of a Unilateral Locomotor Command into a Symmetrical Bilateral Activation in the Brainstem. *Journal of Neuroscience* 30, 523–533 (2010).

74. Cregg, J. M., Leiras, R., Montalant, A., Wanken, P., Wickersham, I. R. & Kiehn, O. Brainstem neurons that command mammalian locomotor asymmetries. *Nature Neuroscience* 23, 730–740 (2020).

75. Pfeiffer, B. D., Ngo, T.-T. B., Hibbard, K. L., Murphy, C., Jenett, A., Truman, J. W. & Rubin, G. M. Refinement of Tools for Targeted Gene Expression in Drosophila. *Genetics* 186, 735–755 (2010).

76. Ache, J. M., Namiki, S., Lee, A., Branson, K. & Card, G. M. State-dependent decoupling of sensory and motor circuits underlies behavioral flexibility in Drosophila. *Nature Neuroscience* 22, 1132–1139 (2019).

77. Dombrovski, M., Peek, M. Y., Park, J.-Y., Vaccari, A., Sumathipala, M., Morrow, C., Breads, P., Zhao, A., Kurmangaliyev, Y. Z., Sanfilippo, P., Rehan, A., Polsky, J., Alghailani, S., Tenshaw, E., Namiki, S., Zipursky, S. L. & Card, G. M. Synaptic gradients transform object location to action. *Nature* 613, 534–542 (2023).

78. McKellar, C. E., Lillvis, J. L., Bath, D. E., Fitzgerald, J. E., Cannon, J. G., Simpson, J. H. & Dickson, B. J. Threshold-Based Ordering of Sequential Actions during Drosophila Courtship. *Current Biology* 29, 426–434.e6 (2019).

79. Bidaye, S. S., Laturney, M., Chang, A. K., Liu, Y., Bockemühl, T., Büschges, A. & Scott, K. Two Brain Pathways Initiate Distinct Forward Walking Programs in Drosophila. *Neuron* 108, 469–485 (2020).

80. Namiki, S., Ros, I. G., Morrow, C., Rowell, W. J., Card, G. M., Korff, W. & Dickinson, M. H. A population of descending neurons that regulates the flight motor of Drosophila. *Current Biology* 32, 1189–1196 (2022).

81. Cande, J., Namiki, S., Qiu, J., Korff, W., Card, G. M., Shaevitz, J. W., Stern, D. L. & Berman, G. J. Optogenetic dissection of descending behavioral control in Drosophila. *eLife* 7, e34275 (2018).

82. Feng, K., Sen, R., Minegishi, R., Dübbert, M., Bockemühl, T., Büschges, A. & Dickson, B. J. Distributed control of motor circuits for backward walking in Drosophila. *Nature Communications* 11, 6166 (2020).

83. Guo, L., Zhang, N. & Simpson, J. H. Descending neurons coordinate anterior grooming behavior in Drosophila. *Current Biology* 32, 823–833.e4 (2022).

84. Lima, S. Q. & Miesenböck, G. Remote Control of Behavior through Genetically Targeted Photostimulation of Neurons. *Cell* 121, 141–152 (2005).

85. Zacarias, R., Namiki, S., Card, G. M., Vasconcelos, M. L. & Moita, M. A. Speed dependent descending control of freezing behavior in Drosophila melanogaster. *Nature Communications* 9, 3697 (2018).

86. Bidaye, S. S., Machacek, C., Wu, Y. & Dickson, B. J. Neuronal Control of Drosophila Walking Direction. *Science* 344, 97–101 (2014).

87. Yang, H. H., Brezovec, L. E., Capdevila, L. S., Vanderbeck, Q. X., Rayshubskiy, S. & Wilson, R. I. Fine-grained descending control of steering in walking Drosophila. *bioRxiv,* 2023.10.15.562426 (2023).

88. Von Philipsborn, A. C., Liu, T., Yu, J. Y., Masser, C., Bidaye, S. S. & Dickson, B. J. Neuronal Control of Drosophila Courtship Song. *Neuron* 69, 509–522 (2011).

89. Wang, F., Wang, K., Forknall, N., Patrick, C., Yang, T., Parekh, R., Bock, D. & Dickson, B. J. Neural circuitry linking mating and egg laying in Drosophila females. *Nature* 579, 101–105 (2020).

90. Von Reyn, C. R., Breads, P., Peek, M. Y., Zheng, G. Z., Williamson, W. R., Yee, A. L., Leonardo, A. & Card, G. M. A spike-timing mechanism for action selection. *Nature Neuroscience* 17, 962–970 (2014).

91. Rayshubskiy, A., Holtz, S. L., D'Alessandro, I., Li, A. A., Vanderbeck, Q. X., Haber, I. S., Gibb, P. W. & Wilson, R. I. Neural control of steering in walking Drosophila. *bioRxiv,* 2020.04.04.024703 (2020).

92. Schnell, B., Ros, I. G. & Dickinson, M. H. A Descending Neuron Correlated with the Rapid Steering Maneuvers of Flying Drosophila. *Current Biology* 27, 1200–1205 (2017).

93. Suver, M. P., Huda, A., Iwasaki, N., Safarik, S. & Dickinson, M. H. An Array of Descending Visual Interneurons Encoding Self-Motion in Drosophila. *Journal of Neuroscience* 36, 11768–11780 (2016).

94.   Tschida, K. & Bhandawat, V. Activity in descending dopaminergic neurons represents but is not required for leg movements in the fruit fly Drosophila. *Physiological Reports* 3, e12322 (2015).

95.   Chen, C.-L., Hermans, L., Viswanathan, M. C., Fortun, D., Aymanns, F., Unser, M., Cammarato, A., Dickinson, M. H. & Ramdya, P. Imaging neural activity in the ventral nerve cord of behaving adult Drosophila. *Nature Communications* 9, 4390 (2018).

96.   Aymanns, F., Chen, C.-L. & Ramdya, P. Descending neuron population dynamics during odor-evoked and spontaneous limb-dependent behaviors. *eLife* 11, e81527 (2022).

97.   Young, J. Z. The Functioning of the Giant Nerve Fibres of the Squid. *Journal of Experimental Biology* 15, 170–185 (1938).

98.   Sen, R., Wu, M., Branson, K., Robie, A., Rubin, G. M. & Dickson, B. J. Moonwalker Descending Neurons Mediate Visually Evoked Retreat in Drosophila. *Current Biology* 27, 766–771 (2017).

99.   Sen, R., Wang, K. & Dickson, B. J. TwoLumps Ascending Neurons Mediate Touch-Evoked Reversal of Walking Direction in Drosophila. *Current Biology* 29, 4337–4344.e5 (2019).

100.   Carreira-Rosario, A., Zarin, A. A., Clark, M. Q., Manning, L., Fetter, R. D., Cardona, A. & Doe, C. Q. MDN brain descending neurons coordinately activate backward and inhibit forward locomotion. *eLife* 7, e38554 (2018).

101.   Lee, K. & Doe, C. Q. A locomotor neural circuit persists and functions similarly in larvae and adult Drosophila. *eLife* 10, e69767 (2021).

102.   Edwards, D. H., Heitler, W. J. & Krasne, F. B. Fifty years of a command neuron: the neurobiology of escape behavior in the crayfish. *Trends in Neurosciences* 22, 153–161 (1999).

103.   Palmer, E. H., Omoto, J. J. & Dickinson, M. H. The role of a population of descending neurons in the optomotor response in flying Drosophila. *bioRxiv,* 2022.12.05.519224 (2022).

104.   Orger, M. B., Kampff, A. R., Severi, K. E., Bollmann, J. H. & Engert, F. Control of visually guided behavior by distinct populations of spinal projection neurons. *Nature Neuroscience* 11, 327–333 (2008).

105.   Severi, K. E., Portugues, R., Marques, J. C., O'Malley, D. M., Orger, M. B. & Engert, F. Neural Control and Modulation of Swimming Speed in the Larval Zebrafish. *Neuron* 83, 692–707 (2014).

106.   Berg, E. M., Mrowka, L., Bertuzzi, M., Madrid, D., Picton, L. D. & El Manira, A. Brainstem circuits encoding start, speed, and duration of swimming in adult zebrafish. *Neuron* 111, 372–386.e4 (2023).

107.   Lemon, R. Recent advances in our understanding of the primate corticospinal system. *F1000Research* 8, F1000 Faculty Rev–274 (2019).

108. Ruta, V., Datta, S. R., Vasconcelos, M. L., Freeland, J., Looger, L. L. & Axel, R. A dimorphic pheromone circuit in Drosophila from sensory input to descending output. *Nature* 468, 686–690 (2010).

109. Ache, J. M., Haupt, S. S. & Dürr, V. A Direct Descending Pathway Informing Locomotor Networks about Tactile Sensor Movement. *Journal of Neuroscience* 35, 4081–4091 (2015).

110. Stolz, T., Diesner, M., Neupert, S., Hess, M. E., Delgado-Betancourt, E., Pflüger, H.-J. & Schmidt, J. Descending octopaminergic neurons modulate sensory-evoked activity of thoracic motor neurons in stick insects. *Journal of Neurophysiology* 122, 2388–2413 (2019).

111. Krakauer, J. W., Ghazanfar, A. A., Gomez-Marin, A., MacIver, M. A. & Poeppel, D. Neuroscience Needs Behavior: Correcting a Reductionist Bias. *Neuron* 93, 480–490 (2017).

112. Fossum, E. R. CMOS image sensors: Electronic camera-on-a-chip. *IEEE transactions on electron devices* 44, 1689–1698 (1997).

113. Fujii, N., Hihara, S. & Iriki, A. Dynamic Social Adaptation of Motion-Related Neurons in Primate Parietal Cortex. *PLoS ONE* 2, e397 (2007).

114. Mathis, A., Mamidanna, P., Cury, K. M., Abe, T., Murthy, V. N., Mathis, M. W. & Bethge, M. DeepLabCut: markerless pose estimation of user-defined body parts with deep learning. *Nature Neuroscience* 21, 1281–1289 (2018).

115. Pereira, T. D., Aldarondo, D. E., Willmore, L., Kislin, M., Wang, S. S.-H., Murthy, M. & Shaevitz, J. W. Fast animal pose estimation using deep neural networks. *Nature Methods* 16, 117–125 (2019).

116. Günel, S., Rhodin, H., Morales, D., Campagnolo, J., Ramdya, P. & Fua, P. DeepFly3D, a deep learning-based approach for 3D limb and appendage tracking in tethered, adult Drosophila. *eLife* 8, e48571 (2019).

117. Pereira, T. D., Tabris, N., Matsliah, A., Turner, D. M., Li, J., Ravindranath, S., Papadoyannis, E. S., Normand, E., Deutsch, D. S., Wang, Z. Y., McKenzie-Smith, G. C., Mitelut, C. C., Castro, M. D., D'Uva, J., Kislin, M., Sanes, D. H., Kocher, S. D., Wang, S. S.-H., Falkner, A. L., Shaevitz, J. W. & Murthy, M. SLEAP: A deep learning system for multi-animal pose tracking. *Nature Methods* 19, 486–495 (2022).

118. Karashchuk, P., Rupp, K. L., Dickinson, E. S., Walling-Bell, S., Sanders, E., Azim, E., Brunton, B. W. & Tuthill, J. C. Anipose: A toolkit for robust markerless 3D pose estimation. *Cell Reports* 36, 109730 (2021).

119. Kabra, M., Robie, A. A., Rivera-Alba, M., Branson, S. & Branson, K. JAABA: interactive machine learning for automatic annotation of animal behavior. *Nature Methods* 10, 64–67 (2013).

120. Segalin, C., Williams, J., Karigo, T., Hui, M., Zelikowsky, M., Sun, J. J., Perona, P., Anderson, D. J. & Kennedy, A. The Mouse Action Recognition System (MARS) software pipeline for automated analysis of social behaviors in mice. *eLife* 10, e63720 (2021).

121. Bohnslav, J. P., Wimalasena, N. K., Clausing, K. J., Dai, Y. Y., Yarmolinsky, D. A., Cruz, T., Kashlan, A. D., Chiappe, M. E., Orefice, L. L., Woolf, C. J. & Harvey, C. D. DeepEthogram, a machine learning pipeline for supervised behavior classification from raw pixels. *eLife* 10, e63377 (2021).

122. Leng, X., Wohl, M., Ishii, K., Nayak, P. & Asahina, K. Quantifying influence of human choice on the automated detection of Drosophila behavior by a supervised machine learning algorithm. *PLOS ONE* 15, e0241696 (2020).

123. Berman, G. J., Choi, D. M., Bialek, W. & Shaevitz, J. W. Mapping the stereotyped behaviour of freely moving fruit flies. *Journal of The Royal Society Interface* 11, 20140672 (2014).

124. Whiteway, M. R., Schaffer, E. S., Wu, A., Buchanan, E. K., Onder, O. F., Mishra, N. & Paninski, L. Semi-supervised sequence modeling for improved behavioral segmentation. *bioRxiv,* 2021.06.16.448685 (2021).

125. Adrian, E. D. *The basis of sensation.* (W W Norton & Co, 1928).

126. Hubel, D. H. & Wiesel, T. N. Receptive fields of single neurones in the cat's striate cortex. *The Journal of Physiology* 148, 574–591 (1959).

127. O'Keefe, J. & Recce, M. L. Phase relationship between hippocampal place units and the EEG theta rhythm. *Hippocampus* 3, 317–330 (1993).

128. Steinmetz, N. A., Aydin, C., Lebedeva, A., Okun, M., Pachitariu, M., Bauza, M., Beau, M., Bhagat, J., Böhm, C., Broux, M., Chen, S., Colonell, J., Gardner, R. J., Karsh, B., Kloosterman, F., Kostadinov, D., Mora-Lopez, C., O'Callaghan, J., Park, J., Putzeys, J., Sauerbrei, B., Daal, R. J. J. v., Vollan, A. Z., Wang, S., Welkenhuysen, M., Ye, Z., Dudman, J. T., Dutta, B., Hantman, A. W., Harris, K. D., Lee, A. K., Moser, E. I., O'Keefe, J., Renart, A., Svoboda, K., Häusser, M., Haesler, S., Carandini, M. & Harris, T. D. Neuropixels 2.0: A miniaturized high-density probe for stable, long-term brain recordings. *Science* 372 (2021).

129. Murthy, M. & Turner, G. Whole-cell in vivo patch-clamp recordings in the Drosophila brain. *Cold Spring Harbor Protocols* 2013, 140–148 (2013).

130. Miyawaki, A., Llopis, J., Heim, R., McCaffery, J. M., Adams, J. A., Ikura, M. & Tsien, R. Y. Fluorescent indicators for Ca2+based on green fluorescent proteins and calmodulin. *Nature* 388, 882–887 (1997).

131. Dana, H., Mohar, B., Sun, Y., Narayan, S., Gordus, A., Hasseman, J. P., Tsegaye, G., Holt, G. T., Hu, A., Walpita, D., Patel, R., Macklin, J. J., Bargmann, C. I., Ahrens, M. B., Schreiter, E. R., Jayaraman, V., Looger, L. L., Svoboda, K. & Kim, D. S. Sensitive red protein calcium indicators for imaging neural activity. *eLife* 5, e12727 (2016).

132. Inoue, M., Takeuchi, A., Manita, S., Horigane, S.-i., Sakamoto, M., Kawakami, R., Yamaguchi, K., Otomo, K., Yokoyama, H., Kim, R., Yokoyama, T., Takemoto-Kimura, S., Abe, M., Okamura, M., Kondo, Y., Quirin, S., Ramakrishnan, C., Imamura, T., Sakimura, K., Nemoto, T., Kano, M., Fujii, H., Deisseroth, K., Kitamura, K. & Bito, H. Rational Engineering of XCaMPs, a Multicolor GECI Suite for In Vivo Imaging of Complex Brain Circuit Dynamics. *Cell* 177, 1346–1360.e24 (2019).

133. Chen, T.-W., Wardill, T. J., Sun, Y., Pulver, S. R., Renninger, S. L., Baohan, A., Schreiter, E. R., Kerr, R. A., Orger, M. B., Jayaraman, V., Looger, L. L., Svoboda, K. & Kim, D. S. Ultrasensitive fluorescent proteins for imaging neuronal activity. *Nature* 499, 295–300 (2013).

134. Dana, H., Sun, Y., Mohar, B., Hulse, B. K., Kerlin, A. M., Hasseman, J. P., Tsegaye, G., Tsang, A., Wong, A., Patel, R., Macklin, J. J., Chen, Y., Konnerth, A., Jayaraman, V., Looger, L. L., Schreiter, E. R., Svoboda, K. & Kim, D. S. High-performance calcium sensors for imaging activity in neuronal populations and microcompartments. *Nature Methods* 16, 649–657 (2019).

135. Zhang, Y., Rózsa, M., Liang, Y., Bushey, D., Wei, Z., Zheng, J., Reep, D., Broussard, G. J., Tsang, A., Tsegaye, G., Narayan, S., Obara, C. J., Lim, J.-X., Patel, R., Zhang, R., Ahrens, M. B., Turner, G. C., Wang, S. S.-H., Korff, W. L., Schreiter, E. R., Svoboda, K., Hasseman, J. P., Kolb, I. & Looger, L. L. Fast and sensitive GCaMP calcium indicators for imaging neural populations. *Nature* 615, 884–891 (2023).

136. Kannan, M., Vasan, G., Haziza, S., Huang, C., Chrapkiewicz, R., Luo, J., Cardin, J. A., Schnitzer, M. J. & Pieribone, V. A. Dual-polarity voltage imaging of the concurrent dynamics of multiple neuron types. *Science* 378, eabm8797 (2022).

137. Evans, S. W., Shi, D.-Q., Chavarha, M., Plitt, M. H., Taxidis, J., Madruga, B., Fan, J. L., Hwang, F.-J., van Keulen, S. C., Suomivuori, C.-M., Pang, M. M., Su, S., Lee, S., Hao, Y. A., Zhang, G., Jiang, D., Pradhan, L., Roth, R. H., Liu, Y., Dorian, C. C., Reese, A. L., Negrean, A., Losonczy, A., Makinson, C. D., Wang, S., Clandinin, T. R., Dror, R. O., Ding, J. B., Ji, N., Golshani, P., Giocomo, L. M., Bi, G.-Q. & Lin, M. Z. A positively tuned voltage indicator for extended electrical recordings in the brain. *Nature Methods* 20, 1104–1113 (2023).

138. Liu, Z., Lu, X., Villette, V., Gou, Y., Colbert, K. L., Lai, S., Guan, S., Land, M. A., Lee, J., Assefa, T., Zollinger, D. R., Korympidou, M. M., Vlasits, A. L., Pang, M. M., Su, S., Cai, C., Froudarakis, E., Zhou, N., Patel, S. S., Smith, C. L., Ayon, A., Bizouard, P., Bradley, J., Franke, K., Clandinin, T. R., Giovannucci, A., Tolias, A. S., Reimer, J., Dieudonné, S. & St-Pierre, F. Sustained deep-tissue voltage recording using a fast indicator evolved for two-photon microscopy. *Cell* 185, 3408–3425.e29 (2022).

139. Marvin, J. S., Borghuis, B. G., Tian, L., Cichon, J., Harnett, M. T., Akerboom, J., Gordus, A., Renninger, S. L., Chen, T.-W., Bargmann, C. I., Orger, M. B., Schreiter, E. R., Demb, J. B., Gan, W.-B., Hires, S. A. & Looger, L. L. An optimized fluorescent probe for visualizing glutamate neurotransmission. *Nature Methods* 10, 162–170 (2013).

140. Patriarchi, T., Cho, J. R., Merten, K., Howe, M. W., Marley, A., Xiong, W.-H., Folk, R. W., Broussard, G. J., Liang, R., Jang, M. J., Zhong, H., Dombeck, D., von Zastrow, M., Nimmerjahn, A., Gradinaru, V., Williams, J. T. & Tian, L. Ultrafast neuronal imaging of dopamine dynamics with designed genetically encoded sensors. *Science* 360, eaat4422 (2018).

141. Denk, W., Strickler, J. H. & Webb, W. W. Two-photon laser scanning fluorescence microscopy. *Science* 248, 73–76 (1990).

142. Bouchard, M. B., Voleti, V., Mendes, C. S., Lacefield, C., Grueber, W. B., Mann, R. S., Bruno, R. M. & Hillman, E. M. C. Swept confocally-aligned planar excitation (SCAPE) microscopy for high-speed volumetric imaging of behaving organisms. *Nature Photonics* 9, 113–119 (2015).

143. Voleti, V., Patel, K. B., Li, W., Perez Campos, C., Bharadwaj, S., Yu, H., Ford, C., Casper, M. J., Yan, R. W., Liang, W., Wen, C., Kimura, K. D., Targoff, K. L. & Hillman, E. M. C. Real-time volumetric microscopy of in vivo dynamics and large-scale samples with SCAPE 2.0. *Nature Methods* 16, 1054–1062 (2019).

144. Schaffer, E. S., Mishra, N., Whiteway, M. R., Li, W., Vancura, M. B., Freedman, J., Patel, K. B., Voleti, V., Paninski, L., Hillman, E. M. C., Abbott, L. F. & Axel, R. The spatial and temporal structure of neural activity across the fly brain. *Nature Communications* 14, 5572 (2023).

145. Musall, S., Kaufman, M. T., Juavinett, A. L., Gluf, S. & Churchland, A. K. Single-trial neural dynamics are dominated by richly varied movements. *Nature Neuroscience* 22, 1677–1686 (2019).

146. Heo, C., Park, H., Kim, Y.-T., Baeg, E., Kim, Y. H., Kim, S.-G. & Suh, M. A soft, transparent, freely accessible cranial window for chronic imaging and electrophysiology. *Scientific Reports* 6, 27818 (2016).

147. Wu, W., He, S., Wu, J., Chen, C., Li, X., Liu, K. & Qu, J. Y. Long-term in vivo imaging of mouse spinal cord through an optically cleared intervertebral window. *Nature Communications* 13, 1959 (2022).

148. Woller, A., Bandow, P., Aimon, S. & Kadow, I. C. G. Preparing Adult Drosophila melanogaster for Whole Brain Imaging during Behavior and Stimuli Responses. *JoVE (Journal of Visualized Experiments),* e61876 (2021).

149. Uzel, K., Kato, S. & Zimmer, M. A set of hub neurons and non-local connectivity features support global brain dynamics in C. elegans. *Current Biology* 32, 3443–3459.e8 (2022).

150. Lemon, W. C., Pulver, S. R., Höckendorf, B., McDole, K., Branson, K., Freeman, J. & Keller, P. J. Whole-central nervous system functional imaging in larval Drosophila. *Nature Communications* 6, 7924 (2015).

151. Schulze, L., Henninger, J., Kadobianskyi, M., Chaigne, T., Faustino, A. I., Hakiy, N., Albadri, S., Schuelke, M., Maler, L., Del Bene, F. & Judkewitz, B. Transparent Danionella translucida as a genetically tractable vertebrate brain model. *Nature Methods* 15, 977–983 (2018).

152. Hamada, F. N., Rosenzweig, M., Kang, K., Pulver, S. R., Ghezzi, A., Jegla, T. J. & Garrity, P. A. An internal thermal sensor controlling temperature preference in Drosophila. *Nature* 454, 217–220 (2008).

153. Boyden, E. S., Zhang, F., Bamberg, E., Nagel, G. & Deisseroth, K. Millisecond-timescale, genetically targeted optical control of neural activity. *Nature Neuroscience* 8, 1263–1268 (2005).

154. Klapoetke, N. C., Murata, Y., Kim, S. S., Pulver, S. R., Birdsey-Benson, A., Cho, Y. K., Morimoto, T. K., Chuong, A. S., Carpenter, E. J., Tian, Z., Wang, J., Xie, Y., Yan, Z., Zhang, Y., Chow, B. Y., Surek, B., Melkonian, M., Jayaraman, V., Constantine-Paton, M., Wong, G. K.-S. & Boyden, E. S. Independent Optical Excitation of Distinct Neural Populations. *Nature methods* 11, 338–346 (2014).

155. Mohammad, F., Stewart, J. C., Ott, S., Chlebikova, K., Chua, J. Y., Koh, T.-W., Ho, J. & Claridge-Chang, A. Optogenetic inhibition of behavior with anion channel-rhodopsins. *Nature Methods* 14, 271–274 (2017).

156. Vierock, J., Rodriguez-Rozada, S., Dieter, A., Pieper, F., Sims, R., Tenedini, F., Bergs, A. C. F., Bendifallah, I., Zhou, F., Zeitzschel, N., Ahlbeck, J., Augustin, S., Sauter, K., Papagiakoumou, E., Gottschalk, A., Soba, P., Emiliani, V., Engel, A. K., Hegemann, P. & Wiegert, J. S. BiPOLES is an optogenetic tool developed for bidirectional dual-color control of neurons. *Nature Communications* 12, 4527 (2021).

157. Tuthill, J. C. & Wilson, R. I. Parallel Transformation of Tactile Signals in Central Circuits of Drosophila. *Cell* 164, 1046–1059 (2016).

158. Shen, Y., Dana, H., Abdelfattah, A. S., Patel, R., Shea, J., Molina, R. S., Rawal, B., Rancic, V., Chang, Y.-F., Wu, L., Chen, Y., Qian, Y., Wiens, M. D., Hambleton, N., Ballanyi, K., Hughes, T. E., Drobizhev, M., Kim, D. S., Koyama, M., Schreiter, E. R. & Campbell, R. E. A genetically encoded Ca2+ indicator based on circularly permutated sea anemone red fluorescent protein eqFP578. *BMC biology* 16, 9 (2018).

159. Subach, O. M., Barykina, N. V., Chefanova, E. S., Vlaskina, A. V., Sotskov, V. P., Ivashkina, O. I., Anokhin, K. V. & Subach, F. V. FRCaMP, a Red Fluorescent Genetically Encoded Calcium Indicator Based on Calmodulin from Schizosaccharomyces Pombe Fungus. *International Journal of Molecular Sciences* 22, 111 (2020).

160. Packer, A. M., Russell, L. E., Dalgleish, H. W. P. & Häusser, M. Simultaneous all-optical manipulation and recording of neural circuit activity with cellular resolution in vivo. *Nature Methods* 12, 140–146 (2015).

161. Ronzitti, E., Ventalon, C., Canepari, M., Forget, B. C., Papagiakoumou, E. & Emiliani, V. Recent advances in patterned photostimulation for optogenetics. *Journal of Optics* 19, 113001 (2017).

162. Bergs, A. C. F., Liewald, J. F., Rodriguez-Rozada, S., Liu, Q., Wirt, C., Bessel, A., Zeitzschel, N., Durmaz, H., Nozownik, A., Dill, H., Jospin, M., Vierock, J., Bargmann, C. I., Hegemann, P., Wiegert, J. S. & Gottschalk, A. All-optical closed-loop voltage clamp for precise control of muscles and neurons in live animals. *Nature Communications* 14, 1939 (2023).

163. Azcorra, M., Gaertner, Z., Davidson, C., He, Q., Kim, H., Nagappan, S., Hayes, C. K., Ramakrishnan, C., Fenno, L., Kim, Y. S., Deisseroth, K., Longnecker, R., Awatramani, R. & Dombeck, D. A. Unique functional responses differentially map onto genetic subtypes of dopamine neurons. *Nature Neuroscience* 26, 1762–1774 (2023).

164. Muto, A., Ohkura, M., Kotani, T., Higashijima, S.-i., Nakai, J. & Kawakami, K. Genetic visualization with an improved GCaMP calcium indicator reveals spatiotemporal activation of the spinal motor neurons in zebrafish. *Proceedings of the National Academy of Sciences* 108, 5425–5430 (2011).

165. Duffy, J. B. GAL4 system in drosophila: A fly geneticist's swiss army knife. *genesis* 34, 1–15 (2002).

166. Lai, S.-L. & Lee, T. Genetic mosaic with dual binary transcriptional systems in Drosophila. *Nature Neuroscience* 9, 703–709 (2006).

167. Riabinina, O. & Potter, C. J. The Q-System: A Versatile Expression System for Drosophila. *Methods in molecular biology* 1478, 53–78 (2016).

168. Simpson, J. H. Rationally subdividing the fly nervous system with versatile expression reagents. *Journal of Neurogenetics* 30, 185–194 (2016).

169. Ashburner, M. *Drosophila : a laboratory handbook* in collab. with Internet Archive. ISBN: 978-0-87969-706-8 (2005).

170. White, J. G., Southgate, E., Thomson, J. N. & Brenner, S. The structure of the nervous system of the nematode Caenorhabditis elegans. *Philosophical Transactions of the Royal Society of London. B, Biological Sciences* 314, 1–340 (1986).

171. Karimi, A., Odenthal, J., Drawitsch, F., Boergens, K. M. & Helmstaedter, M. Cell-type specific innervation of cortical pyramidal cells at their apical dendrites. *eLife* 9, e46876 (2020).

172. Morgan, J. L. & Lichtman, J. W. An Individual Interneuron Participates in Many Kinds of Inhibition and Innervates Much of the Mouse Visual Thalamus. *Neuron* 106, 468–481.e2 (2020).

173. Scheffer, L. K. *et al.* A connectome and analysis of the adult Drosophila central brain. *eLife* 9, e57443 (2020).

174. Eichler, K., Li, F., Litwin-Kumar, A., Park, Y., Andrade, I., Schneider-Mizell, C. M., Saumweber, T., Huser, A., Eschbach, C., Gerber, B., Fetter, R. D., Truman, J. W., Priebe, C. E., Abbott, L. F., Thum, A. S., Zlatic, M. & Cardona, A. The complete connectome of a learning and memory centre in an insect brain. *Nature* 548, 175–182 (2017).

175. Winding, M., Pedigo, B. D., Barnes, C. L., Patsolic, H. G., Park, Y., Kazimiers, T., Fushiki, A., Andrade, I. V., Khandelwal, A., Valdes-Aleman, J., Li, F., Randel, N., Barsotti, E., Correia, A., Fetter, R. D., Hartenstein, V., Priebe, C. E., Vogelstein, J. T., Cardona, A. & Zlatic, M. The connectome of an insect brain. *Science* 379, eadd9330 (2023).

176. Phelps, J. S., Hildebrand, D. G. C., Graham, B. J., Kuan, A. T., Thomas, L. A., Nguyen, T. M., Buhmann, J., Azevedo, A. W., Sustar, A., Agrawal, S., Liu, M., Shanny, B. L., Funke, J., Tuthill, J. C. & Lee, W.-C. A. Reconstruction of motor control circuits in adult Drosophila using automated transmission electron microscopy. *Cell* 184, 759–774 (2021).

177. Marin, E. C., Morris, B. J., Stuerner, T., Champion, A. S., Krzeminski, D., Badala-mente, G., Gkantia, M., Dunne, C. R., Eichler, K., Takemura, S.-y., Tamimi, I. F. M., Fang, S., Moon, S. S., Cheong, H. S. J., Li, F., Schlegel, P., Berg, S., Team, F. P., Card, G. M., Costa, M., Shepherd, D. & Jefferis, G. S. X. E. Systematic annotation of a complete adult male Drosophila nerve cord connectome reveals principles of functional organisation. *bioRxiv,* 2023.06.05.543407 (2023).

178. Witvliet, D., Mulcahy, B., Mitchell, J. K., Meirovitch, Y., Berger, D. R., Wu, Y., Liu, Y., Koh, W. X., Parvathala, R., Holmyard, D., Schalek, R. L., Shavit, N., Chisholm, A. D., Lichtman, J. W., Samuel, A. D. T. & Zhen, M. Connectomes across development reveal principles of brain maturation. *Nature* 596, 257–261 (2021).

179. Cook, S. J., Jarrell, T. A., Brittin, C. A., Wang, Y., Bloniarz, A. E., Yakovlev, M. A., Nguyen, K. C. Q., Tang, L. T.-H., Bayer, E. A., Duerr, J. S., Bülow, H. E., Hobert, O., Hall, D. H. & Emmons, S. W. Whole-animal connectomes of both Caenorhabditis elegans sexes. *Nature* 571, 63–71 (2019).

180. Atanas, A. A., Kim, J., Wang, Z., Bueno, E., Becker, M., Kang, D., Park, J., Kramer, T. S., Wan, F. K., Baskoylu, S., Dag, U., Kalogeropoulou, E., Gomes, M. A., Estrem, C., Cohen, N., Mansinghka, V. K. & Flavell, S. W. Brain-wide representations of behavior spanning multiple timescales and states in C. elegans. *Cell* 186, 4134–4151.e31 (2023).

181. Shiu, P. K., Sterne, G. R., Spiller, N., Franconville, R., Sandoval, A., Zhou, J., Simha, N., Kang, C. H., Yu, S., Kim, J. S., Dorkenwald, S., Matsliah, A., Schlegel, P., Yu, S.-c., McKellar, C. E., Sterling, A., Costa, M., Eichler, K., Jefferis, G. S. X. E., Murthy, M., Bates, A. S., Eckstein, N., Funke, J., Bidaye, S. S., Hampel, S., Seeds, A. M. & Scott, K. A leaky integrate-and-fire computational model based on the connectome of the entire adult Drosophila brain reveals insights into sensorimotor processing. *bioRxiv,* 2023.05.02.539144 (2023).

182. Lee, W.-C. A., Bonin, V., Reed, M., Graham, B. J., Hood, G., Glattfelder, K. & Reid, R. C. Anatomy and function of an excitatory network in the visual cortex. *Nature* 532, 370–374 (2016).

183. Wanner, A. A. & Friedrich, R. W. Whitening of odor representations by the wiring diagram of the olfactory bulb. *Nature Neuroscience* 23, 433–442 (2020).

184. Haber, A., Wanner, A. A., Friedrich, R. W. & Schneidman, E. The structure and function of neural connectomes are shaped by a small number of design principles. *bioRxiv,* 2023.03.15.532611 (2023).

185. Lecoq, J., Oliver, M., Siegle, J. H., Orlova, N., Ledochowitsch, P. & Koch, C. Removing independent noise in systems neuroscience data using DeepInterpolation. *Nature Methods* 18, 1401–1408 (2021).

186. Seelig, J. D., Chiappe, M. E., Lott, G. K., Dutta, A., Osborne, J. E., Reiser, M. B. & Jayaraman, V. Two-photon calcium imaging from head-fixed Drosophila during optomotor walking behavior. *Nature Methods* 7, 535–540 (2010).

187. Moore, R. J. D., Taylor, G. J., Paulk, A. C., Pearson, T., van Swinderen, B. & Srinivasan, M. V. FicTrac: A visual method for tracking spherical motion and generating fictive animal paths. *Journal of Neuroscience Methods* 225, 106–119 (2014).

188. Denk, W., Delaney, K. R., Gelperin, A., Kleinfeld, D., Strowbridge, B., Tank, D. W. & Yuste, R. Anatomical and functional imaging of neurons using 2-photon laser scanning microscopy. *Journal of neuroscience methods* 54, 151–162 (1994).

189. Trachtenberg, J. T., Chen, B. E., Knott, G. W., Feng, G., Sanes, J. R., Welker, E. & Svoboda, K. Long-term in vivo imaging of experience-dependent synaptic plasticity in adult cortex. *Nature* 420, 788–794 (2002).

190. Kim, T. H., Zhang, Y., Lecoq, J., Jung, J. C., Li, J., Zeng, H., Niell, C. M. & Schnitzer, M. J. Long-term optical access to an estimated one million neurons in the live mouse cortex. *Cell reports* 17, 3385–3394 (2016).

191. Andermann, M. L., Gilfoy, N. B., Goldey, G. J., Sachdev, R. N., Wölfel, M., McCormick, D. A., Reid, R. C. & Levene, M. J. Chronic cellular imaging of entire cortical columns in awake mice using microprisms. *Neuron* 80, 900–913 (2013).

192. Goldey, G. J., Roumis, D. K., Glickfeld, L. L., Kerlin, A. M., Reid, R. C., Bonin, V., Schafer, D. P. & Andermann, M. L. Removable cranial windows for long-term imaging in awake mice. *Nature protocols* 9, 2515 (2014).

193. Maimon, G., Straw, A. D. & Dickinson, M. H. Active flight increases the gain of visual motion processing in Drosophila. *Nature neuroscience* 13, 393–399 (2010).

194. Seelig, J. D. & Jayaraman, V. Neural dynamics for landmark orientation and angular path integration. *Nature* 521, 186–191 (2015).

195. Pick, S. & Strauss, R. Goal-Driven Behavioral Adaptations in Gap-Climbing Drosophila. *Current Biology* 15, 1473–1478 (2005).

196. Asahina, K. Neuromodulation and strategic action choice in Drosophila aggression. *Annual review of neuroscience* 40, 51–75 (2017).

197. Pavlou, H. J. & Goodwin, S. F. Courtship behavior in Drosophila melanogaster: towards a 'courtship connectome'. *Current Opinion in Neurobiology* 23, 76–83 (2013).

198. Grover, D., Katsuki, T. & Greenspan, R. J. Flyception: imaging brain activity in freely walking fruit flies. *Nature Methods* 13, 569–572 (2016).

199. Huang, C., Maxey, J. R., Sinha, S., Savall, J., Gong, Y. & Schnitzer, M. J. Long-term optical brain imaging in live adult fruit flies. *Nature Communications* 9, 872 (2018).

200. Flores-Valle, A., Honnef, R. & Seelig, J. D. Automated long-term two-photon imaging in head-fixed walking Drosophila. *Journal of Neuroscience Methods* 368, 109432 (2022).

201. Holtmaat, A., Bonhoeffer, T., Chow, D. K., Chuckowree, J., De Paola, V., Hofer, S. B., Hübener, M., Keck, T., Knott, G., Lee, W.-C. A., *et al.* Long-term, high-resolution imaging in the mouse neocortex through a chronic cranial window. *Nature protocols* 4, 1128–1144 (2009).

202. Silbering, A. F., Bell, R., Galizia, C. G. & Benton, R. Calcium imaging of odor-evoked responses in the Drosophila antennal lobe. *Journal of visualized experiments: JoVE* 61, 2976 (2012).

203. Nelson, N. A., Wang, X., Cook, D., Carey, E. M. & Nimmerjahn, A. Imaging spinal cord activity in behaving animals. *Experimental neurology* 320, 112974 (2019).

204. Farrar, M. J., Bernstein, I. M., Schlafer, D. H., Cleland, T. A., Fetcho, J. R. & Schaffer, C. B. Chronic in vivo imaging in the mouse spinal cord using an implanted chamber. *Nature methods* 9, 297–302 (2012).

205. Tuthill, J. C. & Azim, E. Proprioception. *Current Biology* 28, R194–R203 (2018).

206. Bidaye, S. S., Bockemühl, T. & Büschges, A. Six-legged walking in insects: how CPGs, peripheral feedback, and descending signals generate coordinated and adaptive motor rhythms. *Journal of neurophysiology* 119, 459–475 (2018).

207. Kawata, S., Sun, H.-B., Tanaka, T. & Takada, K. Finer features for functional microdevices. *Nature* 412, 697–698 (2001).

208. Mendes, C. S., Rajendren, S. V., Bartos, I., Márka, S. & Mann, R. S. Kinematic Responses to Changes in Walking Orientation and Gravitational Load in Drosophila melanogaster. *PLOS ONE* 9, e109204 (2014).

209. Bavelier, D., Levi, D. M., Li, R. W., Dan, Y. & Hensch, T. K. Removing brakes on adult brain plasticity: from molecular to behavioral interventions. *Journal of Neuroscience* 30, 14964–14971 (2010).

210. Sugie, A., Marchetti, G. & Tavosanis, G. Structural aspects of plasticity in the nervous system of Drosophila. *Neural Development* 13, 14 (2018).

211. Ayaz, D., Leyssen, M., Koch, M., Yan, J., Srahna, M., Sheeba, V., Fogle, K. J., Holmes, T. C. & Hassan, B. A. Axonal Injury and Regeneration in the Adult Brain of Drosophila. *Journal of Neuroscience* 28, 6010–6021 (2008).

212. Hollis, E. R. Axon guidance molecules and neural circuit remodeling after spinal cord injury. *Neurotherapeutics* 13, 360–369 (2016).

213. Hunt, R. F., Scheff, S. W. & Smith, B. N. Synaptic Reorganization of Inhibitory Hilar Interneuron Circuitry after Traumatic Brain Injury in Mice. *Journal of Neuroscience* 31, 6880–6890 (2011).

214. Murphy, T. H. & Corbett, D. Plasticity during stroke recovery: from synapse to behaviour. *Nature Reviews Neuroscience* 10, 861–872 (2009).

215. Isakov, A., Buchanan, S. M., Sullivan, B., Ramachandran, A., Chapman, J. K., Lu, E. S., Mahadevan, L. & De Bivort, B. Recovery of locomotion after injury in Drosophila melanogaster depends on proprioception. *Journal of Experimental Biology* 219, 1760–1771 (2016).

216. Mamiya, A., Gurung, P. & Tuthill, J. C. Neural Coding of Leg Proprioception in Drosophila. *Neuron* 100, 636–650.e6 (2018).

217. Root, C. M., Masuyama, K., Green, D. S., Enell, L. E., Nässel, D. R., Lee, C.-H. & Wang, J. W. A presynaptic gain control mechanism fine-tunes olfactory behavior. *Neuron* 59, 311–321 (2008).

218. French, A. S., Geissmann, Q., Beckwith, E. J. & Gilestro, G. F. Sensory processing during sleep in Drosophila melanogaster. *Nature* 598, 479–482 (2021).

219. Hindmarsh Sten, T., Li, R., Otopalik, A. & Ruta, V. Sexual arousal gates visual processing during Drosophila courtship. *Nature* 595, 549–553 (2021).

220. Hoopfer, E. D., Jung, Y., Inagaki, H. K., Rubin, G. M. & Anderson, D. J. P1 interneurons promote a persistent internal state that enhances inter-male aggression in Drosophila. *Elife* 4, e11346 (2015).

221. Gibson, W. T., Gonzalez, C. R., Fernandez, C., Ramasamy, L., Tabachnik, T., Du, R. R., Felsen, P. D., Maire, M. R., Perona, P. & Anderson, D. J. Behavioral responses to a repetitive visual threat stimulus express a persistent state of defensive arousal in Drosophila. *Current Biology* 25, 1401–1415 (2015).

222. Shaw, P. J., Cirelli, C., Greenspan, R. J. & Tononi, G. Correlates of sleep and waking in Drosophila melanogaster. *Science* 287, 1834–1837 (2000).

223. Wu, M. N., Ho, K., Crocker, A., Yue, Z., Koh, K. & Sehgal, A. The effects of caffeine on sleep in Drosophila require PKA activity, but not the adenosine receptor. *Journal of Neuroscience* 29, 11029–11037 (2009).

224. Lin, F. J., Pierce, M. M., Sehgal, A., Wu, T., Skipper, D. C. & Chabba, R. Effect of taurine and caffeine on sleep-wake activity in Drosophila melanogaster. *Nature and Science of Sleep* 2, 221–231 (2010).

225. Harris, D. T., Kallman, B. R., Mullaney, B. C. & Scott, K. Representations of taste modality in the Drosophila brain. *Neuron* 86, 1449–1460 (2015).

226. Ribeiro, C. & Dickson, B. J. Sex Peptide Receptor and Neuronal TOR/S6K Signaling Modulate Nutrient Balancing in Drosophila. *Current Biology* 20, 1000–1005 (2010).

227. Wyman, R. J., Thomas, J. B., Salkoff, L. & King, D. G. *The Drosophila giant fiber system* in *Neural mechanisms of startle behavior* (1984), 133–161. ISBN: 978-1-4899-2288-5.

228. Mamiya, A., Gurung, P. & Tuthill, J. C. Neural coding of leg proprioception in Drosophila. *Neuron* 100, 636–650 (2018).

229. Fang, Y. & Bonini, N. M. Axon degeneration and regeneration: Insights from drosophila models of nerve injury. *Annual Review of Cell and Developmental Biology* 28, 575–597 (2012).

230. MacDonald, J. M., Beach, M. G., Porpiglia, E., Sheehan, A. E., Watts, R. J. & Freeman, M. R. The Drosophila Cell Corpse Engulfment Receptor Draper Mediates Glial Clearance of Severed Axons. *Neuron* 50, 869–881 (2006).

231. Shakiryanova, D., Klose, M. K., Zhou, Y., Gu, T., Deitcher, D. L., Atwood, H. L., Hewes, R. S. & Levitan, E. S. Presynaptic ryanodine receptor-activated calmodulin kinase II increases vesicle mobility and potentiates neuropeptide release. *Journal of Neuroscience* 27, 7799–7806 (2007).

232. Feany, M. B. & Bender, W. W. A Drosophila model of Parkinson's disease. *Nature* 404, 394–398 (2000).

233. Jang, Y.-H., Chae, H.-S. & Kim, Y.-J. Female-specific myoinhibitory peptide neurons regulate mating receptivity in Drosophila melanogaster. *Nature Communications* 8, 1630 (2017).

234. Sinha, S., Liang, L., Ho, E. T. W., Urbanek, K. E., Luo, L., Baer, T. M. & Schnitzer, M. J. High-speed laser microsurgery of alert fruit flies for fluorescence imaging of neural activity. *Proceedings of the National Academy of Sciences* 110, 18374 LP –18379 (2013).

235. Savall, J., Ho, E. T. W., Huang, C., Maxey, J. R. & Schnitzer, M. J. Dexterous robotic manipulation of alert adult Drosophila for high-content experimentation. *Nature methods* 12, 657–660 (2015).

236. Duffy, D. C., McDonald, J. C., Schueller, O. J. & Whitesides, G. M. Rapid prototyping of microfluidic systems in poly(dimethylsiloxane). *Analytical Chemistry* 70, 4974–4984 (1998).

237. Sum, T. C., Bettiol, A. A., Rao, S. V., van Kan, J. A., Ramam, A. & Watt, F. *Proton beam writing of passive polymer optical waveguides* in *Micromachining Technology for Micro-Optics and Nano-Optics II* 5347 (2003), 160–169.

238. Johansson, A., Calleja, M., Rasmussen, P. A. & Boisen, A. SU-8 cantilever sensor system with integrated readout. *Sensors and Actuators, A: Physical* 123-124, 111–115 (2005).

239. Qin, D., Xia, Y. & Whitesides, G. M. Soft lithography for micro- and nanoscale patterning. *Nature Protocols* 5, 491–502 (2010).

240. Weibel, D. B., DiLuzio, W. R. & Whitesides, G. M. Microfabrication meets microbiology. *Nature Reviews Microbiology* 5, 209–218 (2007).

241. Laermer, F., Schilp, A., Funk, K. & Offenberg, M. Bosch deep silicon etching: Improving uniformity and etch rate for advanced MEMS applications. *Proceedings of the IEEE Micro Electro Mechanical Systems (MEMS),* 211–216 (1999).

242. Satoshi, K., Hong-Bo, S., Tomokazu, T. & Kenji, T. Finer features for functional microdevices. *Nature* 412, 697–698 (2001).

243. Liu, Y., Campbell, J. H., Stein, O., Jiang, L., Hund, J. & Lu, Y. Deformation Behavior of Foam Laser Targets Fabricated by Two-Photon Polymerization. *Nanomaterials* 8, 498 (2018).

244. Sridhar, V. H., Roche, D. G. & Gingins, S. Tracktor: Image-based automated tracking of animal movement and behaviour. *Methods in Ecology and Evolution* 10, 815–820 (2019).

245. Paszke, A., Gross, S., Massa, F., Lerer, A., Bradbury, J., Chanan, G., Killeen, T., Lin, Z., Gimelshein, N., Antiga, L., Desmaison, A., Kopf, A., Yang, E., DeVito, Z., Raison, M., Tejani, A., Chilamkurthy, S., Steiner, B., Fang, L., Bai, J. & Chintala, S. *PyTorch: An Imperative Style, High-Performance Deep Learning Library* in *Advances in Neural Information Processing Systems 32* (2019), 8024–8035.

246. Nair, V. & Hinton, G. E. *Rectified linear units improve restricted boltzmann machines* in *International Conference on Machine Learning (ICML)* (2010), 807–814.

247. Srivastava, N., Hinton, G., Krizhevsky, A., Sutskever, I. & Salakhutdinov, R. Dropout: a simple way to prevent neural networks from overfitting. *The Journal of Machine Learning Research* 15, 1929–1958 (2014).

248. Kingma, D. P. & Ba, J. *Adam: A method for stochastic optimization* in *The International Conference on Learning Representations (ICLR)* (2015).

249. Schindelin, J., Arganda-Carreras, I., Frise, E., Kaynig, V., Longair, M., Pietzsch, T., Preibisch, S., Rueden, C., Saalfeld, S., Schmid, B., Tinevez, J.-Y., White, D. J., Hartenstein, V., Eliceiri, K., Tomancak, P. & Cardona, A. Fiji: an open-source platform for biological-image analysis. *Nature Methods* 9, 676–682 (2012).

250. Lowe, D. G. Distinctive image features from scale-invariant keypoints. *International Journal of Computer Vision* 60, 91–110 (2004).

251. Chen, C.-L., Hermans, L., Viswanathan, M. C., Fortun, D., Aymanns, F., Unser, M., Cammarato, A., Dickinson, M. H. & Ramdya, P. Imaging neural activity in the ventral nerve cord of behaving adult Drosophila. *Nature communications* 9, 1–10 (2018).

252. Muijres, F. T., Elzinga, M. J., Melis, J. M. & Dickinson, M. H. Flies Evade Looming Targets by Executing Rapid Visually Directed Banked Turns. *Science* 344, 172–177 (2014).

253. Hoopfer, E. D. Neural control of aggression in Drosophila. *Current Opinion in Neurobiology* 38, 109–118 (2016).

254. Hedwig, B. Pulses, patterns and paths: neurobiology of acoustic behaviour in crickets. *Journal of Comparative Physiology A* 192, 677–689 (2006).

255. Ijspeert, A. J., Crespi, A., Ryczko, D. & Cabelguen, J.-M. From Swimming to Walking with a Salamander Robot Driven by a Spinal Cord Model. *Science* 315, 1416–1420 (2007).

256. Cruz, T. L. & Chiappe, M. E. Multilevel visuomotor control of locomotion in Drosophila. *Current Opinion in Neurobiology* 82, 102774 (2023).

257. Dorkenwald, S., McKellar, C. E., Macrina, T., Kemnitz, N., Lee, K., Lu, R., Wu, J., Popovych, S., Mitchell, E., Nehoran, B., Jia, Z., Bae, J. A., Mu, S., Ih, D., Castro, M., Ogedengbe, O., Halageri, A., Kuehner, K., Sterling, A. R., Ashwood, Z., Zung, J., Brittain, D., Collman, F., Schneider-Mizell, C., Jordan, C., Silversmith, W., Baker, C., Deutsch, D., Encarnacion-Rivera, L., Kumar, S., Burke, A., Bland, D., Gager, J., Hebditch, J., Koolman, S., Moore, M., Morejohn, S., Silverman, B., Willie, K., Willie, R., Yu, S.-c., Murthy, M. & Seung, H. S. FlyWire: online community for whole-brain connectomics. *Nature Methods* 19, 119–128 (2022).

258. Liu, W. W. & Wilson, R. I. Glutamate is an inhibitory neurotransmitter in the Drosophila olfactory system. *Proceedings of the National Academy of Sciences* 110, 10294–10299 (2013).

259. Eckstein, N., Bates, A. S., Champion, A., Du, M., Yin, Y., Schlegel, P., Lu, A. K.-Y., Rymer, T., Finley-May, S., Paterson, T., Parekh, R., Dorkenwald, S., Matsliah, A., Yu, S.-C., McKellar, C., Sterling, A., Eichler, K., Costa, M., Seung, S., Murthy, M., Hartenstein, V., Jefferis, G. S. X. E. & Funke, J. Neurotransmitter Classification from Electron Microscopy Images at Synaptic Sites in Drosophila Melanogaster. *bioRxiv,* 2020.06.12.148775 (2023).

260. Harris, R. M., Pfeiffer, B. D., Rubin, G. M. & Truman, J. W. Neuron hemilineages provide the functional ground plan for the Drosophila ventral nervous system. *eLife* 4, e04493 (2015).

261. Miesenböck, G. Lighting up the Brain. *Scientific American* 299, 52–59 (2008).

262. Barabási, A.-L. & Albert, R. Emergence of Scaling in Random Networks. *Science* 286, 509–512 (1999).

263. Broido, A. D. & Clauset, A. Scale-free networks are rare. *Nature Communications* 10, 1017 (2019).

264. Blondel, V. D., Guillaume, J.-L., Lambiotte, R. & Lefebvre, E. Fast unfolding of communities in large networks. *Journal of Statistical Mechanics: Theory and Experiment* 2008, P10008 (2008).

265. Aimon, S., Cheng, K. Y., Gjorgjieva, J. & Grunwald Kadow, I. C. Global change in brain state during spontaneous and forced walk in Drosophila is composed of combined activity patterns of different neuron classes. *eLife* 12, e85202 (2023).

266. Brezovec, L. E., Berger, A. B., Hao, Y. A., Lin, A., Ahmed, O. M., Pacheco, D. A., Thiberge, S. Y., Murthy, M. & Clandinin, T. R. BIFROST: a method for registering diverse imaging datasets. *bioRxiv,* 2023.06.09.544408 (2023).

267. Mann, K., Gordon, M. D. & Scott, K. A Pair of Interneurons Influences the Choice between Feeding and Locomotion in Drosophila. *Neuron* 79, 754–765 (2013).

268. Kien, J. The Initiation and Maintenance of Walking in the Locust: An Alternative to the Command Concept. *Proceedings of the Royal Society of London. Series B, Biological Sciences* 219, 137–174 (1983).

269. Flash, T. & Hochner, B. Motor primitives in vertebrates and invertebrates. *Current Opinion in Neurobiology* 15, 660–666 (2005).

270. Thoroughman, K. A. & Shadmehr, R. Learning of action through adaptive combination of motor primitives. *Nature* 407, 742–747 (2000).

271. Stroud, J. P., Porter, M. A., Hennequin, G. & Vogels, T. P. Motor primitives in space and time via targeted gain modulation in cortical networks. *Nature Neuroscience* 21, 1774–1783 (2018).

272. Mussa-Ivaldi, F. A., Giszter, S. F. & Bizzi, E. Linear combinations of primitives in vertebrate motor control. *Proceedings of the National Academy of Sciences* 91, 7534–7538 (1994).

273. Heinrich, R. Impact of descending brain neurons on the control of stridulation, walking, and flight in orthoptera. *Microscopy Research and Technique* 56, 292–301 (2002).

274. Tadres, D., Shiozaki, H. M., Tastekin, I., Stern, D. L. & Louis, M. An essential experimental control for functional connectivity mapping with optogenetics. *bioRxiv,* 2022.05.26.493610 (2022).

275. Akin, O., Bajar, B. T., Keles, M. F., Frye, M. A. & Zipursky, S. L. Cell-type-Specific Patterned Stimulus-Independent Neuronal Activity in the Drosophila Visual System during Synapse Formation. *Neuron* 101, 894–904.e5 (2019).

276. Hirth, F., Hartmann, B. & Reichert, H. Homeotic gene action in embryonic brain development of Drosophila. *Development* 125, 1579–1589 (1998).

277. Awasaki, T., Lai, S.-L., Ito, K. & Lee, T. Organization and Postembryonic Development of Glial Cells in the Adult Central Brain of Drosophila. *Journal of Neuroscience* 28, 13742–13753 (2008).

278. Hermans, L., Kaynak, M., Braun, J., Ríos, V. L., Chen, C.-L., Friedberg, A., Günel, S., Aymanns, F., Sakar, M. S. & Ramdya, P. Microengineered devices enable long-term imaging of the ventral nerve cord in behaving adult Drosophila. *Nature Communications* 13, 5006 (2022).

279. Pereira, T. D., Shaevitz, J. W. & Murthy, M. Quantifying behavior to understand the brain. *Nature Neuroscience* 23, 1537–1549 (2020).

280. Virtanen, P., Gommers, R., Oliphant, T. E., Haberland, M., Reddy, T., Cournapeau, D., Burovski, E., Peterson, P., Weckesser, W., Bright, J., van der Walt, S. J., Brett, M., Wilson, J., Millman, K. J., Mayorov, N., Nelson, A. R. J., Jones, E., Kern, R., Larson, E., Carey, C. J., Polat, İ., Feng, Y., Moore, E. W., VanderPlas, J., Laxalde, D., Perktold, J., Cimrman, R., Henriksen, I., Quintero, E. A., Harris, C. R., Archibald, A. M., Ribeiro, A. H., Pedregosa, F. & van Mulbregt, P. SciPy 1.0: fundamental algorithms for scientific computing in Python. *Nature Methods* 17, 261–272 (2020).

281. Matsliah, A., Sterling, A., Dorkenwald, S., Kuehner, K., Morey, R., Seung, H. & Murthy, M. *Codex: Connectome Data Explorer* (2023).

282. Schlegel, P., Yin, Y., Bates, A. S., Dorkenwald, S., Eichler, K., Brooks, P., Han, D. S., Gkantia, M., Santos, M. d., Munnelly, E. J., Badalamente, G., Capdevila, L. S., Sane, V. A., Pleijzier, M. W., Tamimi, I. F. M., Dunne, C. R., Salgarella, I., Javier, A., Fang, S., Perlman, E., Kazimiers, T., Jagannathan, S. R., Matsliah, A., Sterling, A. R., Yu, S.-c., McKellar, C. E., Consortium, F., Costa, M., Seung, H. S., Murthy, M., Hartenstein, V., Bock, D. D. & Jefferis, G. S. X. E. A consensus cell type atlas from multiple connectomes reveals principles of circuit stereotypy and variation. *bioRxiv*, 2023.06.27.546055 (2023).

283. Hagberg, A. A., Schult, D. A. & Swart, P. J. *Exploring Network Structure, Dynamics, and Function using NetworkX* in *Proceedings of the 7th Python in Science Conference* (2008).

284. Lacin, H., Chen, H.-M., Long, X., Singer, R. H., Lee, T. & Truman, J. W. Neurotransmitter identity is acquired in a lineage-restricted manner in the Drosophila CNS. *eLife* 8, e43701 (2019).

285. Hulse, B. K., Haberkern, H., Franconville, R., Turner-Evans, D., Takemura, S.-y., Wolff, T., Noorman, M., Dreher, M., Dan, C., Parekh, R., Hermundstad, A. M., Rubin, G. M. & Jayaraman, V. A connectome of the Drosophila central complex reveals network motifs suitable for flexible navigation and context-dependent action selection. *eLife* 10, e66039 (2021).

286. Sapkal, N., Mancini, N., Kumar, D. S., Spiller, N., Murakami, K., Vitelli, G., Bargeron, B., Maier, K., Eichler, K., Jefferis, G. S. X. E., Shiu, P., Sterne, G. R. & Bidaye, S. S. Neural circuit mechanisms underlying context-specific halting in Drosophila. *bioRxiv*, 2023.09.25.559438 (2023).

287. Georgopoulos, A. P., Schwartz, A. B. & Kettner, R. E. Neuronal Population Coding of Movement Direction. *Science* 233, 1416–1419 (1986).

288. Gallego, J. A., Perich, M. G., Naufel, S. N., Ethier, C., Solla, S. A. & Miller, L. E. Cortical population activity within a preserved neural manifold underlies multiple motor behaviors. *Nature Communications* 9, 4233 (2018).

289. Aso, Y., Sitaraman, D., Ichinose, T., Kaun, K. R., Vogt, K., Belliart-Guérin, G., Plaçais, P.-Y., Robie, A. A., Yamagata, N., Schnaitmann, C., Rowell, W. J., Johnston, R. M., Ngo, T.-T. B., Chen, N., Korff, W., Nitabach, M. N., Heberlein, U., Preat, T., Branson, K. M., Tanimoto, H. & Rubin, G. M. Mushroom body output neurons encode valence and guide memory-based action selection in Drosophila. *eLife* 3, e04580 (2014).

290. Stephenson-Jones, M., Samuelsson, E., Ericsson, J., Robertson, B. & Grillner, S. Evolutionary conservation of the basal ganglia as a common vertebrate mechanism for action selection. *Current biology: CB* 21, 1081–1091 (2011).

291. Wang, X.-J. Decision Making in Recurrent Neuronal Circuits. *Neuron* 60, 215–234 (2008).

292. Ohyama, T., Schneider-Mizell, C. M., Fetter, R. D., Aleman, J. V., Franconville, R., Rivera-Alba, M., Mensh, B. D., Branson, K. M., Simpson, J. H., Truman, J. W., Cardona, A. & Zlatic, M. A multilevel multimodal circuit enhances action selection in Drosophila. *Nature* 520, 633–639 (2015).

293. Liebel, L. & Körner, M. *Auxiliary Tasks in Multi-task Learning* 2018. arXiv: 1805. 06334[cs].

294. Karani, N., Erdil, E., Chaitanya, K. & Konukoglu, E. Test-time adaptable neural networks for robust medical image segmentation. *Medical Image Analysis* 68, 101907 (2021).

295. Archit, A., Nair, S., Khalid, N., Hilt, P., Rajashekar, V., Freitag, M., Gupta, S., Dengel, A., Ahmed, S. & Pape, C. Segment Anything for Microscopy. *bioRxiv,* 2023.08.21.554208 (2023).

296. Inagaki, H. K., Panse, K. M. & Anderson, D. J. Independent, reciprocal neuromodulatory control of sweet and bitter taste sensitivity during starvation in Drosophila. *Neuron* 84, 806–820 (2014).

297. Yu, Y., Huang, R., Ye, J., Zhang, V., Wu, C., Cheng, G., Jia, J. & Wang, L. Regulation of starvation-induced hyperactivity by insulin and glucagon signaling in adult Drosophila. *eLife* 5, e15693 (2016).

298. Jacobs, R. V., Wang, C. X., Lozada-Perdomo, F. V., Nguyen, L., Deere, J. U., Uttley, H. A. & Devineni, A. V. Overlap and divergence of neural circuits mediating distinct behavioral responses to sugar. *bioRxiv,* 2023.10.01.560401 (2023).

JONAS BRAUN
Data Scientist - Neuroscientist

As an experienced data scientist, neuroscientist, and passionate mountaineer, I am a structured explorer at heart: I proactively find data and critically analyse it to generate insights and lay out a roadmap with pivotal decision points and alternative solutions. Clearly communicating this strategy with my team helps me to archieve goals collaboratively.

SKILLS

- Data analysis & visualisation
- Problem solving
- Public speaking
- Project management (AgilePM)
- Workshop organisation
- Literature research
- Programming (Python, Matlab, C)

LANGUAGES

- German – native
- English – business fluent (C2)
- French – conversational (B2)

AWARDS

- Boehringer Ingelheim Fonds: PhD fellowship
- BMW: Undergraduate traineeship
- German National Scholarship Foundation: Graduate Scholarship

PERSONAL

- PhD student representative
- Mountaineering
- Ski touring
- Travelling

RELEVANT EXPERIENCE

02.2020 - 01.2024 | EPFL, Lausanne (CH)
Doctoral researcher
- Design & management of a collaborative neuroscience project
- Supervision of students
- Teaching programming to life scientists
- Organisation of seminars and workshops

02.2018 - 01.2020 | Technical University Munich (DE)
Research and teaching assistant
- Analysis of biological data from varied sources
- Teaching mathematics to life scientists

07.2018 - 09.2018 | Emory University, Atlanta (US)
Research internship
- Computational modelling of biological data using deep learning

12.2016 - 04.2017 | Siemens Healthineers, Erlangen (DE)
Bachelor thesis
- Acquisition and analysis of Magnetic Resonance Imaging data
- Industrial research

09.2013 – 11.2016 | BMW Group, Munich (DE)
Traineeship including multiple internships, total 8 months
- Control and modelling of fuel cells and electrical engines
- Agile development team work: Scrum master

EDUCATION

2020 - 2024 | PhD Neuroscience
École Polytechnique Fédéral de Lausanne (CH)

2017 - 2020 | Master Neuroengineering
Technical University Munich (DE)

2013 - 2017 | Bachelor Electrical Engineering
University of Applied Sciences Esslingen (DE)

2015 - 2016 | Visiting student: Biomedical Engieneering
University of Cambridge, Trinity College (UK)

jonasfbraun@gmail.com

in